

# **THESE**

Présentée par

Oran F. K. Mc Grath

pour obtenir le titre de

**Docteur**

de l'Université Joseph Fourier - Grenoble 1  
(arrêtés ministériels du 5 juillet 1984 et du 30 mars 1992)

(Spécialité : Physique)

## **STRUCTURAL AND MAGNETIC PROPERTIES OF EPITAXIAL W / Fe / W AND Gd / Fe FILMS GROWN BY PULSED LASER DEPOSITION**

Soutenue le : 8 Novembre 1994

### **Composition du Jury :**

Président :	D. Bloch
Rapporteurs :	P. Bruno R. Coehoorn
Examineurs :	C. Fermon D. Givord C. Lacroix

Thèse préparée au sein du Laboratoire de Magnétisme Louis Néel  
CNRS - Grenoble



## ACKNOWLEDGEMENTS

I am deeply indebted to D. Givord for the supervision he has given me during the course of this thesis work. Words alone cannot express my gratitude to him, but suffice it to say that thanks to him this thesis has been a most formative, rewarding and enjoyable experience.

I am honoured by the presence of D. Bloch as president of the examining jury and I thank him.

I am very grateful to P. Bruno and R. Coehoorn who accepted the task of refereeing this manuscript. I appreciate the magnitude of the task involved and I thank them most sincerely. I would also like to thank C. Fermon and C. Lacroix for participating as members of the examining jury.

I wish to acknowledge the assistance of the following people who have contributed to the work described in this manuscript ; K. Mackay - PLD (Ch. 1), A. Liénard - X -ray analysis (Ch. 3), E. du Trémolet de Lacheisserie - pair model calculations (Ch. 4), C. Pinettes and C. Lacroix - spin wave calculations (Ch. 4), V. Passyuk and H. Lauter - spin polarised neutron reflectivity (Ch. 5) and C. Fermon - spin polarised neutron reflectivity with spin analysis (Ch. 6).

I am grateful to the Commission of the European Communities for financing this thesis.

A special word of thanks to F. Robaut, N. Cherief and P. David.

Finally, I would like to thank the personnel in the laboratory for making my stay so pleasant and for fear of forgetting anybody I shall name nobody but thank everybody.



## INTRODUCTION

Les grandeurs importantes caractérisant un matériau magnétique sont l'amplitude des moments magnétiques, la nature de l'ordre, la température au-dessous de laquelle cet ordre existe et l'anisotropie magnétique. Ces grandeurs dépendent de divers paramètres tels que la coordination atomique, la symétrie et la dimensionnalité du système. Les couches ultra-minces, d'épaisseur comprise entre 1 et 50 plans atomiques, apparaissent de plus en plus comme des systèmes modèles pour l'étude du magnétisme. D'une part la brisure de symétrie et la réduction de coordination se produisant aux surfaces entraînent une modification des propriétés rencontrées pour un échantillon massif; pour des couches d'épaisseur suffisamment faible, ces effets de surface peuvent être détectés et par suite permettre une meilleure compréhension de l'influence de la symétrie et de la coordination sur le comportement magnétique d'un matériau. Il y est d'autre part possible d'étudier la portée des interactions d'échange ou les excitations thermiques, de longueur caractéristique du même ordre que l'épaisseur de la couche. Les couches ultra-minces permettent donc l'étude, à l'échelle atomique, des processus les plus fondamentaux du magnétisme.

Par ailleurs, les propriétés spécifiques des couches minces peuvent être exploitées pour diverses applications. L'anisotropie de surface, par exemple, peut entraîner une aimantation perpendiculaire à la couche et ouvre donc la possibilité de stockage de données à haute densité. Citons également les effets de couplage entre couches qui peuvent induire une forte magnétorésistance, intéressante pour le développement de têtes de lecture.

Des progrès technologiques récents dans les techniques d'élaboration et de caractérisation très fine des couches minces ouvrent des possibilités nouvelles pour l'étude du magnétisme des couches ultra-minces. En conséquence, plusieurs laboratoires ont démarré une nouvelle activité de recherche, centrée sur les couches ultra-minces magnétiques. Ce travail de thèse présente le développement d'un tel thème de recherche au laboratoire Louis Néel.

La technique de dépôt par laser pulsé a été choisie pour ses caractéristiques très prometteuses. Au début de ce travail, la connaissance de cette technique était peu avancée et nous avons démarré notre recherche en étudiant la physique de l'ablation des métaux.

Après avoir développé la méthode de dépôt par laser pulsé, nous l'avons utilisée pour étudier la croissance épitaxiale de trois systèmes. En règle générale, l'élaboration de couches épitaxiées ultra-minces est difficile et la compréhension de leur croissance nécessite une bonne connaissance de leurs propriétés structurales. Une telle connaissance est également importante pour mieux comprendre le lien existant entre les propriétés structurales et magnétiques d'un échantillon. Pour cette raison, nous avons fait une étude systématique des propriétés structurales des couches élaborées, pendant et après la croissance.

Nous avons tout d'abord étudié la croissance de W sur des substrats de corindon. Les trois objectifs étaient: tester la pertinence de la technique de dépôt par laser pulsé pour élaborer des films métalliques épitaxiés; en optimiser les paramètres (orientation et température du substrat, épaisseur du dépôt...) afin d'utiliser ce système comme couche tampon; étudier le mécanisme de croissance de cette couche.

Les autres systèmes élaborés ont été choisis comme étant des systèmes modèles pour étudier quelques aspects fondamentaux du magnétisme des couches ultra-minces.

Une étude du moment magnétique, de l'anisotropie planaire et des excitations thermiques a été entreprise sur des couches de W / Fe (110) / W. Ce système a été choisi car le fer est le plus simple et le mieux connu des éléments ferromagnétiques. Par ailleurs, il avait déjà été établi que le fer s'épitaxie sur le tungstène. Le premier objectif de cette étude était de déterminer la valeur du moment magnétique du fer dans ce système au zéro absolu. Les mesures macroscopiques d'aimantation dans les couches ultra-minces étant très difficiles, nous avons préféré la technique de réflectométrie de neutrons polarisés, mieux adaptée pour une telle étude.

La compréhension de l'anisotropie magnétique dans des couches ultra-minces reste toujours insuffisante malgré les nombreuses études réalisées dans ce domaine. Une meilleure compréhension de l'anisotropie s'appuie sur l'analyse des résultats expérimentaux. Il nous a semblé que des facteurs importants avaient été négligés dans des études antérieures sur l'anisotropie, en particulier l'influence des effets de dimensionalité. Nous nous sommes donc efforcés de comprendre l'anisotropie planaire dans les couches de W / Fe / W en développant une technique d'analyse des résultats expérimentaux qui prend en compte ces effets de dimensionalité. L'analyse de la variation thermique de l'aimantation nous a permis l'étude de la variation des excitations thermiques en fonction de l'épaisseur de la couche.

Le deuxième système magnétique étudié était formé de bi-couches monocristallines de Gd (0001) / Fe (110). Cette étude a permis une compréhension du couplage interfacial 3d-4f entre le fer et le gadolinium. Pour analyser ce couplage on a d'abord effectué des mesures d'aimantation macroscopique. Les résultats, inattendus, ont été complétés par ceux obtenus par des mesures originales de réflectométrie de neutrons polarisés avec analyse de polarisation.

Le plan de ce travail est le suivant: Le premier chapitre est consacré au mécanisme de l'ablation de métaux par laser pulsé. La croissance des couches par épitaxie est présentée dans le deuxième chapitre. La croissance et la caractérisation structurale des trois systèmes cités ci-dessus sont décrites dans le troisième chapitre. Dans le quatrième chapitre nous discutons, d'une manière générale, du moment magnétique, de l'anisotropie et des excitations thermiques dans des couches ultra-minces; les résultats expérimentaux obtenus dans le cas des couches de W / Fe / W sont exposés dans le cinquième chapitre. Enfin, dans le dernier chapitre, nous discutons des résultats de notre étude sur le couplage interfacial dans les bi-couches Gd / Fe.

## INTRODUCTION

The most important parameters which characterise the magnetism of materials are the magnitude of the magnetic moment, the type of magnetic order, the temperature below which order exists and the magnetic anisotropy. These properties depend on various parameters such as atomic co-ordination, symmetry, and system dimensionality. It is becoming more and more evident that ultra-thin films, of typical thicknesses of 1 - 50 atomic layers, are model systems for the study of magnetism. This is because, on the one hand, the symmetry breaking and reduced atomic co-ordination which occurs at surfaces modifies the magnetic properties of these surface layers. For films sufficiently thin, these surface effects can be detected and thus provides a greater insight into the influence of symmetry and co-ordination on magnetism. On the other hand, as the perpendicular film dimension is of the order of the characteristic length of exchange interactions, the range of these interactions can be probed. This is also the case for thermal excitations. Ultra-thin films therefore enable the most fundamental interactions involved in magnetism to be studied at an atomic scale.

In addition the specific properties of thin films can be exploited for applications. Surface anisotropies, for example, offer the possibility of perpendicular magnetisation and therefore high density magnetic recording. Exchange coupling effects can give rise to giant magnetoresistance which can be exploited in recording heads.

Recent technical progress, both in the domain of film deposition techniques and ultra-sensitive characterisation techniques, has opened up new vistas for the study of magnetism of ultra-thin films. Several laboratories therefore recently started a research activity centred around ultra-thin film magnetism. The work described in this thesis corresponds to the development of such a research activity in the Laboratoire Louis Néel.

The technique of pulsed laser deposition was chosen because its technical characteristics (congruent evaporation, versatility ...) were very promising. At the outset, however, pulsed laser deposition was poorly understood and in order to optimise the technique we performed an investigation of the physical mechanisms of the ablation process.

After having studied the technique of pulsed laser deposition we then used it to study the epitaxial growth of three systems. As a general rule, the fabrication of ultra-thin films is difficult and a detailed characterisation of the structural properties is essential to understand film growth. In addition, such characterisation is essential to understand the subtle interplay between structural and magnetic properties. It was for this reason that we undertook a systematic study of the structural properties of the prepared films, both during and after growth.

The first system studied was W on  $\text{Al}_2\text{O}_3$ , for which the objectives were threefold ; to investigate the possibility of applying the technique of pulsed laser deposition to the epitaxial deposition of metals; to isolate the experimental parameters (substrate orientation, deposition temperature, film thickness) necessary to optimise this system as a buffer layer; to study the epitaxial mechanism of the optimum system.

The other systems were chosen as they are model systems for studying some fundamental aspects of thin film magnetism.

A study of the magnetic moment, in-plane anisotropy and thermal excitations of Fe in W / Fe (110) / W tri-layers was undertaken. This system was chosen because Fe is one of the most simple and best characterised ferromagnets and it had already been established that Fe can be epitaxially grown on W. The first objective of this study was to determine an absolute value for the ground state Fe moment in the films. Accurate measurements of the macroscopic magnetisation of ultra-thin films is extremely difficult and it was for this reason that we chose a more appropriate technique - polarised neutron reflectometry. The understanding of ultra-thin film anisotropy, despite the vast body of experimental work devoted to this subject, still remains un-satisfactory. A crucial element to this end is the analysis of experimental results in order to extract the true value of surface anisotropy. It occurred to us from the outset that some important factors had been neglected, in particular dimensionality effects on thin film anisotropy had never been considered. We therefore concentrated more particularly on a detailed analysis of the in-plane anisotropy in W / Fe (110) / W films, taking into account these dimensionality effects on volume, magnetoelastic and surface anisotropy.

The above-mentioned analysis of magnetic moment and anisotropy requires a knowledge of the temperature dependence of the magnetisation in thin films. This was determined for our W / Fe / W films and this was used to analyse these dimensionality effects.

The second system studied was Gd / Fe epitaxial bi-layers, with the aim of investigating 3d - 4f interfacial exchange coupling. To analyse these effects macroscopic magnetisation measurements were initially performed. The results were intriguing and it was decided to determine the magnetic moment configuration in this system by means of polarised neutron reflectometry with polarisation analysis.

The organisation of this thesis manuscript is as follows : The physics of laser ablation of metals is discussed in the first chapter. Epitaxial growth is reviewed in the second chapter. The epitaxial growth and structural characterisation of the three systems studied is discussed in the third chapter. In the fourth chapter, ground state moments, anisotropy and thermal excitations in ultra-thin films are reviewed. In the fifth chapter, the magnetism of Fe in our W / Fe (110) / W films is discussed. In the sixth and last chapter, we present our results on Gd / Fe bi-layers and discuss these in terms of interface coupling.



## TABLE OF CONTENTS

Acknowledgements	1
Introduction (français)	3
Introduction (english)	5
Table of contents	7
Chapter 1 - Pulsed laser deposition	9
Chapter 2 - Thin film growth	33
Chapter 3 - Deposition and structural characterisation of epitaxial W, W / Fe / W and Gd / Fe	57
Chapter 4 - Ground state moments, anisotropy and thermal excitations in ultra-thin films	97
Chapter 5 - Ground state moments, anisotropy and thermal excitations of Fe in W / Fe / W	137
Chapter 6 - Exchange coupling in epitaxial Gd / Fe bi-layers	169
Conclusion (français)	191
Conclusion (english)	193



# CHAPTER ONE

## PULSED LASER DEPOSITION (PLD)

### Table of contents to chapter 1

1.1 Introduction	11
1.2 Experimental set-up	12
1.3 Physics of PLD	14
1.3.1 Laser-target interaction	14
1.3.2 Laser - evaporant interaction	17
1.3.2.1 Saturation effects	17
1.3.2.2 - Ion energies and ionic state	17
1.3.2.3 - Ion fraction	19
1.3.3 Expansion	21
1.4 Stoichiometric evaporation	24
1.5 PLD and film quality	25
1.5.1 Influence of high energy ions	25
1.5.2 Droplets	25
1.6 Discussion and conclusion	28
1.7 References	30

## RÉSUMÉ

La technique de dépôt laser pulsé (DLP) est discutée dans ce chapitre. Les processus mis en jeu pendant l'ablation des métaux, qui se présente en trois étapes, sont : l'interaction laser-cible, l'interaction laser-matériau évaporé et la dilatation du plasma. L'interaction laser-cible résulte d'une évaporation thermique et rapide de la cible. Ces espèces évaporées commencent à absorber l'énergie du faisceau laser créant un plasma. La dilatation du plasma dépend de sa géométrie initiale et puisqu'il peut être considéré comme bidimensionnel la dilatation est très directionnelle. Pendant DLP, la vitesse d'évaporation est telle que la stoechiométrie des cibles polyvalentes est conservée pendant l'évaporation. Néanmoins, pendant le vol entre la cible et le substrat, une séparation des éléments constitutifs peut se produire car leur vitesse asymptotique est inversement proportionnelle à leur masse. La dilatation des espèces plus légères est donc plus directionnelle. L'un des inconvénients majeur du DLP est que les couches sont souvent polluées. Deux types de polluant sont observés. La pression du laser sur une région fondue de la cible conduit à une éjection des gouttelettes fondues qui se condensent sur le substrat. Le deuxième type de polluant est dû à une usure inhomogène de la cible qui permet une expulsion des particules solides de la cible ; celles-ci se déposent également sur le substrat. Différents moyens pour éliminer ces contaminants sont discutés. A la fin du chapitre, les avantages et les inconvénients du DLP sont également présentés.

## SUMMARY

The technique of pulsed laser deposition (PLD) is discussed in this chapter. The ablation process is described as a three step process, which are : the laser-target interaction, the laser-evaporant interaction and plasma expansion. The laser-target interaction results essentially in rapid thermal evaporation. These evaporated species then start to absorb the laser energy resulting in a laser driven plasma. The plasma expansion towards the substrate depends on the initial geometry of the plasma and as it is very two dimensional, the plasma expansion is very directional. Another interesting feature of PLD is that during evaporation the stiochiometry of polycomponent targets is conserved. During the expansion from the target to the substrate a segregation of elements can however occur because the asymptotic velocities of each constituent elements is inversely proportional to their mass. The expansion of heavier elements is therefore less directional than that of lighter elements. One of the major drawbacks of PLD is that the films are often found to be polluted by particulates. Two classes of particulate contamination occurs. Firstly, the radiation pressure of the laser on the molten region of the target causes an expulsion of molten droplets from the target which condense on the substrate. The second type of particulate contamination arises due to inhomogeneous usure of the target resulting in pieces of the target being removed from the target in the solid state. Different methods of contamination elimination are discussed in the text. Finally the advantages and disadvantages of the technique are discussed at the end of the chapter.

## 1.1 Introduction

Pulsed laser deposition (PLD) is a thin film deposition technique in which a high powered pulsed laser is focused onto a target material to be ablated, causing the evaporation of material. The evaporated material is then collected on a substrate placed in front of the target, resulting in the growth of a thin film.

The advent of PLD came about shortly after the development of the first pulsed lasers [1]. Development of the technique was subsequently very slow until the discovery, in the late eighties, of the suitability of the technique for the deposition of epitaxial congruent high  $T_c$  superconductor thin films [2].

The use of PLD for the deposition of metallic thin films is still quite rare, especially epitaxial films. Optimisation of the technique for the epitaxial deposition of metals requires a knowledge of the physics of the ablation process.

In this chapter the various aspects of PLD are discussed. The experimental set-up for epitaxial deposition is briefly described. The physics of PLD is discussed by analysing experimental results. Finally, certain aspects of the technique which influence the film quality are discussed.

## 1.2 Experimental set-up

The experimental PLD set-up used for epitaxial deposition is schematically shown in figure 1.1. It consists of two ultra-high vacuum chambers, a chamber for film deposition and a chamber for sample analysis and storage. Both chambers are pumped by an ion pump and a titanium sublimation pump. The base pressure in both chambers is  $3 \times 10^{-11}$  Torr. Three targets can be accommodated in the deposition chamber at any one time. The target holder is continuously rastered in front of the laser beam during film preparation. A quartz micro balance is used for the calibration of deposition rates. The substrate holder is continuously rotated during deposition in order to minimise film inhomogeneities. For film deposition, a target-substrate distance of 8 cm is used. A tungsten filament is mounted onto the substrate holder which enables the substrate to be heated to 800°C. The deposition chamber is equipped with an electron gun for RHEED analysis. The electron beam is focused onto the substrate with an angle of incidence of  $3^\circ$ . The electron diffraction patterns are monitored on a fluorescent screen.

A pulsed Quantel Nd:YAG Laser is used, with a pulse duration of 9 ns and a pulse frequency of 10 Hz. The radiation wavelength used in almost all circumstances is 5320 Å (frequency doubling of the Nd:YAG fundamental), with a maximum energy per pulse of  $3 \times 10^6$  erg. The beam is focused onto the target by means of a pair of lenses mounted ex-situ. The laser-beam energy is monitored by a Joule meter placed ex-situ. The laser beam is focused onto the target at an angle of incidence of  $40^\circ$ .

All samples are entered and exited by means of an insertion lock placed on the analysis chamber. A pair of manipulators enables samples to be transferred from one chamber to another. The analysis chamber contains a sample carousel which is used to store up to 4 substrates and four targets at any one time. A vacuum suitcase is mounted onto the analysis which enables samples to be transported under UHV. An electron gun and a multi-channel analyser mounted on the analysis chamber enables Auger analysis to be performed.

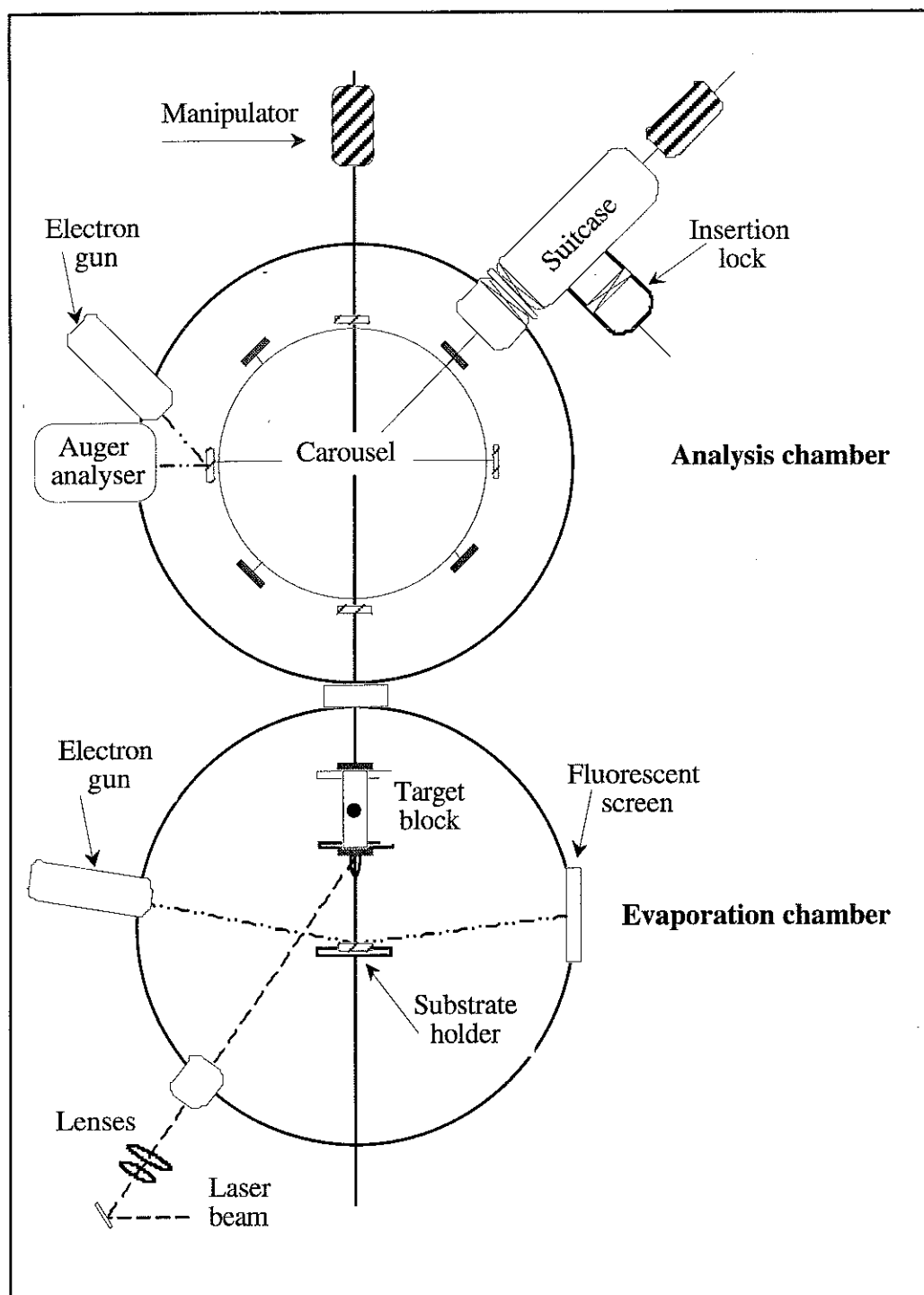


Figure 1.1. Schematic representation of the PLD set-up for epitaxial deposition

### 1.3 Physics of PLD

The deposition of films by pulsed laser ablation can be described as a three step process, which are: the laser-target interaction, the laser-evaporant interaction and plasma expansion. These three steps are schematised in figure 1.2.

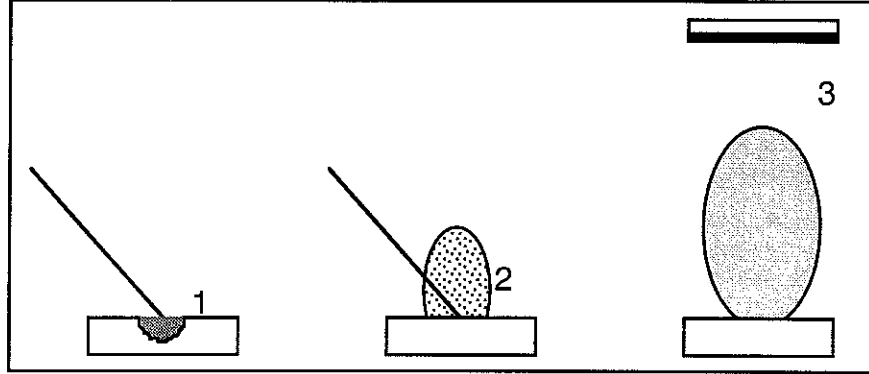


Fig. 1.2 - Schematic representation of the three step process during pulsed laser deposition.

#### 1.3.1 Laser-target interaction

The laser-target interaction can be understood in the first instances by measuring the deposition rate as a function of fluence (fig. 1.3 for Co). The ablation rate is negligibly small until a threshold fluence ( $F_{th}$ ) is reached. This varies from  $7.5 \times 10^6 \text{ erg.cm}^{-2}$  for Y to  $25 \times 10^6 \text{ erg.cm}^{-2}$  for W. Above  $F_{th}$  the ablation rate increases rapidly up to a typical value of the order of 5 to 10 times  $F_{th}$ . Above this value the evaporation rate tends to saturate. Such saturation effects are usually observed in the ablation deposition process [1] , [2].

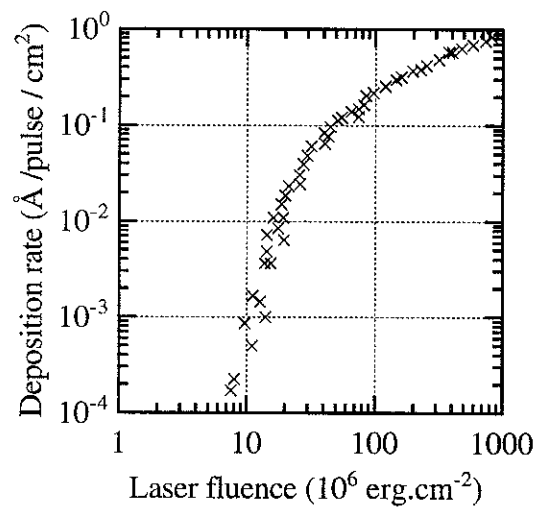


Fig. 1.3 - Evaporation rate per unit area vs. fluence, for Co .



In metals, the absorption of photons causes electron excitations which are converted to thermal energy (characteristic time of  $10^{-16}$  -  $10^{-15}$  s) through electron-phonon interactions in times of the order of  $10^{-14}$  s which are orders of magnitude faster than a ns laser pulse. Thus why laser ablation of metals is expected to be a thermal process and one may try to explain the above results from simple considerations of the thermal properties of metals.

The transfer of energy from a laser beam to a metal depends on the reflectivity ( $r$ ) of the metal target. The proportion of incident laser beam absorbed is given by:

$$I = I_0 (1-r) \quad (1.1)$$

For metals,  $r$  increases, in general with increasing wavelength ( $\lambda$ ) and decreases with increasing temperature. The value of  $r$  for  $\lambda = 5320 \text{ \AA}$  and for room temperature are shown in table 1.1 for some metals.

	W	Fe	Co	Ni	Y
$r$	49%	33%	68%	62%	50%*
$L_t (\mu\text{m})$	1.1	0.6	0.7	0.6	0.5
$F_{th} (10^6 \text{ erg.cm}^{-2})$	8.0	2.0	6.0	4.0	1.0
$U_i (\text{eV})$	7.98	7.90	7.86	7.63	6.50

Table 1.1 - Reflectivity ( $r$ ) values (for  $\lambda = 5320 \text{ \AA}$  for room temperature at normal incidence (\* estimated)), thermal diffusion lengths ( $L_t$ ) {for 9 ns laser pulses}, threshold fluences ( $F_{th}$ ) {for a spot of 1 mm diameter} and first ionisation potentials ( $U_i$ ) for some metals .

The target volume heated during laser ablation is characterised by the thermal diffusion length,  $L_t$ , which is given by:

$$L_t = \sqrt{2K.\tau} \quad (1.2)$$

where  $\tau$  is the pulse duration and  $K$  is the thermal diffusivity. The value of  $L_t$  for some metals for 9 ns pulses are quoted in table 1 and are found to be of the order of a micron. It is striking that the value of  $L_t$  is much larger than the optical absorption depth of metals ( $\sim 200 \text{ \AA}$ ), this is due to the extremely fast diffusivity of heat in metals.

Assuming that the temperature in the target layer of thickness  $L_t$  is constant, the energy necessary for the heated layer to reach a mean temperature  $\bar{T}$  can be estimated as:

$$E = C_v S L_t \rho (\bar{T} - 300) \quad (1.3)$$

where  $S$  is the spot size,  $C_v$  is the specific heat and  $\rho$  is the density. It may be assumed that the threshold fluence for laser ablation corresponds to the target surface reaching the boiling point ( $T_b$ ). The mean temperature  $\bar{T}$  in the heated region is then expected to be approximately  $T_b / 3$  [3]. The values of the threshold fluence ( $F_{th}$ ) then deduced from relation 1.3 are listed in table 1.1. They are of the order of magnitude of experimental values.

For thermal evaporation the material removal rate is expected to scale with vapour pressure. Equation 1.3 relates temperature in a volume  $SL_t$  to a fluence ( $F = E/S^2$ ). Therefore from vapour pressure versus temperature plots, the vapour pressure can be plotted as a function of fluence. This is shown in figure 1.4 for Co with the data of figure 1.3 superimposed.

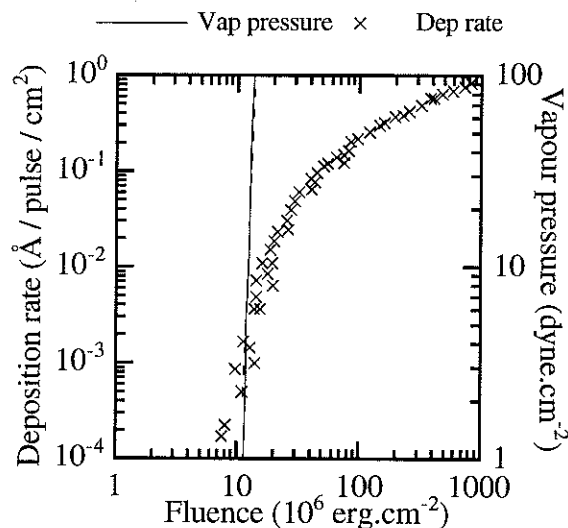


Fig. 1.4 - Vapour pressure data for Co plotted as a function of fluence with deposition rate as a function of measured fluence superimposed.

For fluences in the  $10\text{--}20 \times 10^6 \text{ erg.cm}^{-2}$  region (figure 1.3) the deposition rate is found to follow an approximate thermal evaporation behaviour as it shows the same rate of change with fluence as the vapour pressure. For fluences greater than  $2 \times 10^6 \text{ erg.cm}^{-2}$  the deposition rate data deviates significantly from the vapour pressure. A simple explanation of these saturation effects during PLD is that the depth of heated material is limited by the thermal properties of the metal. As the laser fluence increases above threshold, an excess of energy is accumulated in this region, but the volume of evaporated material does not increase in proportion. There is however a more important factor which results from significant laser absorption by the evaporated species and these laser evaporant interactions are described in the next section.

### 1.3.2 Laser - evaporant interaction

The second step of the process involves an interaction of the laser beam with the evaporated species. The absorption of the laser beam results in the formation of a plasma. This plasma can be seen as a glowing gas near the target surface. This is an essential feature which differentiates PLD from thermal evaporation.

This laser-evaporant interaction determines ;

- the saturation effects
- the ion energies and ionic state
- the ion fraction

and each are discussed in turn in the following.

#### 1.3.2.1 Saturation effects

The transition from a neutral plume to a plasma occurs initially through thermionic emission from the target surface and through multi-photon absorption by evaporated neutrals [4]. In a second stage the free electrons in the plume absorb photons, through inverse bremsstrahlung, and their energy increases. In a third stage these hot electrons collide with neutrals in the plume causing ionisation and finally reaches a density where the laser beam is fully absorbed by the plasma. This absorption obviously results in a reduction of the laser energy which is absorbed by the target. This is the main cause of the saturation effects.

#### 1.3.2.2 - Ion energies and ionic state

A series of experiments was carried out by the collaborators of the ALADIN project (EC Brite-Euram project for the developpment of PLD) in order to analyse the spectrum of ions emitted during PLD.

A quadrupole mass spectrometer was coupled to a cylindrical mass analyser in a vacuum chamber. The entrance to the analyser was placed in front of an Fe target which was ablated with a frequency doubled Nd:YAG laser. The emitted ions were energy analysed according to ionic order from singly ionised to quadruply ionised species, as a function of laser fluence. The experimental limit for ion detection was 500 eV. The spectra obtained for four fluences, 6, 700, 1300 and 2900  $10^6 \text{ erg.cm}^{-2}$  are shown in figure 1.4 [5].

At a fluence close to the threshold,  $6 \times 10^6 \text{ erg.cm}^{-2}$ , the only detected ions are  $\text{Fe}^+$  with an energy distribution centred at 25 eV.

$\text{Fe}^{2+}$  ions are detected with an energy distribution centred at 190 eV for a fluence of  $700 \times 10^6 \text{ erg.cm}^{-2}$ . The  $\text{Fe}^+$  spectrum shows a double peak at 10 eV and 160 eV. This suggests that the second  $\text{Fe}^+$  peak is due to  $\text{Fe}^{2+}$  recombination just before detection.

At laser fluences of  $1300 \times 10^6 \text{ erg.cm}^{-2}$   $\text{Fe}^{3+}$  ions are detected with an energy distribution centred at 200 eV and the  $\text{Fe}^+$  and  $\text{Fe}^{2+}$  spectra are identical to those for fluences of  $700 \times 10^6 \text{ erg.cm}^{-2}$ .

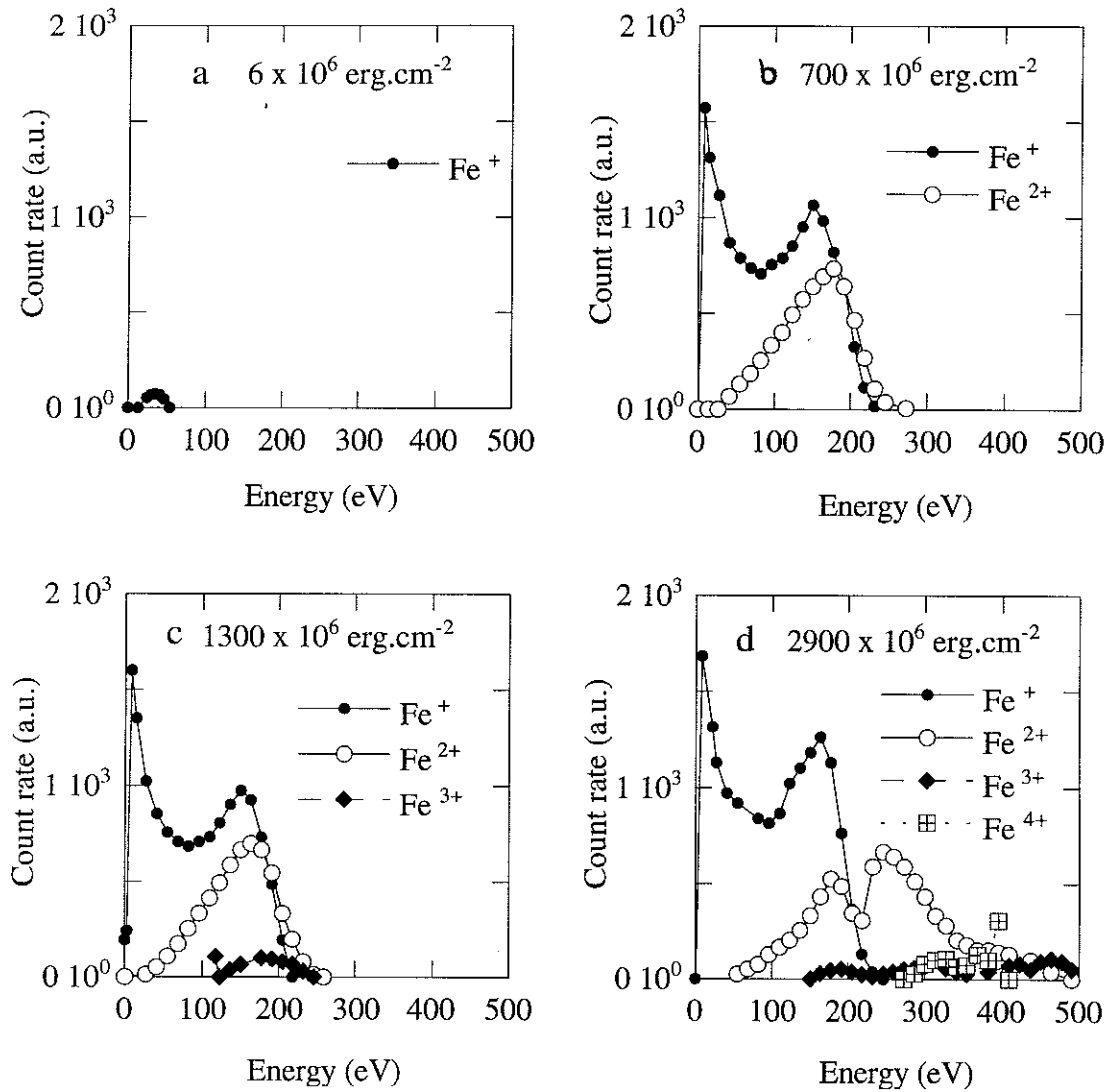


Fig. 1.4 - The energy spectra of Fe ions laser fluences of a - 6, b - 700, c - 1300 and d - 2900  $\times 10^6 \text{ erg.cm}^{-2}$ .

At maximum fluence,  $2900 \times 10^6 \text{ erg.cm}^{-2}$ , the  $\text{Fe}^+$  spectrum remains virtually unchanged. The  $\text{Fe}^{2+}$  and  $\text{Fe}^{3+}$  spectrum are found to contain a double peak. The first peak is identical to that for lower fluences the second peak is found up to energies of 500 eV, suggesting again the occurrence of re-combination.  $\text{Fe}^{4+}$  ions are detected with energies ranging from 300-400 eV.

The above analysis shows that as the laser fluence is increased the ion energy increases rapidly. This can be understood from the fact that as the temperature of a neutral gas is increased the elements will gradually become ionised. The energy necessary to singly ionise some elements is shown in table 1.1.

Similar results have been found for the ablation of Cu by excimer laser. Time of flight studies performed in UHV and for fluences of  $30 \times 10^6 \text{ erg.cm}^{-2}$  revealed the existence of three ion energy peaks at 45 eV, 20 eV and 2.5 eV [8]. Optical measurements [6] indicate that the ion energy is 80 eV and the energy of the neutral is 8 eV for the same operating conditions. In earlier TOF measurements [7], the ion energy and neutral energy was found to be 6.7 eV and 2.3 eV respectively. The differences between different authors is possibly due to the difficulty in accurately determining the laser fluence.

The ablation of FeSiGaRu by excimer lasers in UHV has also been investigated by time of flight measurements [8]. At the threshold fluence ( $19 \times 10^6 \text{ erg.cm}^{-2}$ ) the energy of the neutrals was found to be 25 eV: the ion signal was too weak to be detected. For fluences three times the threshold fluence ( $60 \times 10^6 \text{ erg.cm}^{-2}$ ) the energy of the neutrals was found to increase to 50 eV.

### 1.3.2.3 - Ion fraction

For a gas in equilibrium at a temperature  $T$  one can calculate the percentage of ions by applying a Maxwell-Boltzmann distribution law. If  $n_n$  and  $n_i$  are the number density of neutrals and ions and  $U_i$  is the first ionisation potential, then the degree of ionisation is given by [9]:

$$r = \frac{n_i}{n_n} = \left( \frac{2\pi m_e k_B T}{h^2} \right)^{\frac{3}{2}} n_i^{-1} \exp\left( \frac{U_i}{k_B T} \right) \quad (1.4)$$

Equation 1.4 is often referred to as the Saha equation. The percentage ionisation of Fe as a function of temperature for values of the total particle density ( $n_t = n_n + n_i$ ) ranging from  $10^{15} \text{ particles.cm}^{-3}$  to  $10^{25} \text{ particles.cm}^{-3}$  is shown in figure 1.6.

The total particle density can be estimated as follows. Coupling of the laser energy to the evaporated gas occurs mainly in a region close to the target surface and its volume can be estimated as :

$$V = \frac{S}{\alpha} \quad (1.5)$$

where  $S$  is the laser spot area and  $\alpha$  is the inverse bremsstrahlung absorption coefficient [10]. Typically this volume is of the order of  $1 \times 10^{-8} \text{ cm}^3$ . The number of atoms ablated per laser pulse near the threshold is found experimentally to be of the order of  $1 \times 10^{14}$  atoms [11]. The atom density is therefore of the order of  $10^{22} \text{ atoms.cm}^{-3}$ . For comparison, the solid density is  $2.5 \times 10^{23} \text{ atoms.cm}^{-3}$ .

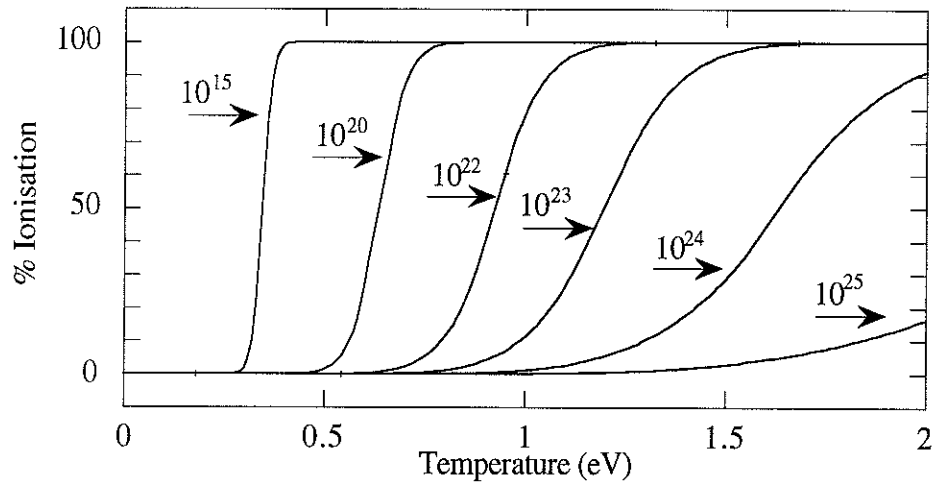


Fig. 1.6 - Percentage ionisation for Fe as a function of gas temperature for particle densities ranging from  $10^{15} \text{ atoms.cm}^{-3}$  to  $10^{25} \text{ atoms.cm}^{-3}$ .

Figure 1.6 shows that 100% ionisation of the evaporated species can occur for gas temperatures less than the first ionisation potential of Fe (i.e. 7.9 eV). This striking result effect is a well known gas ionisation effect. It is due to the fact that the degeneracy factor of an ion-electron pair is much larger than the degeneracy factor of a neutral atom. The temperature window for the transition from 0% ionisation to 100% is very narrow. It increases as the atomic density of the gas increases. For densities of  $10^{22} \text{ atoms.cm}^{-3}$ , ionisation will start for temperatures greater than 0.6 eV and 100% ionisation will occur for temperatures greater than 1.3 eV.

In order to estimate the fluence range for which a high ion fraction is expected one must estimate the gas temperature at a given fluence. This can be obtained by solving the heat diffusion equation for the system. Rough estimations can however be made by means of the analysis in the previous section. Firstly, for fluences close to the threshold, the gas temperature can be assumed to be equal to the boiling temperature of metals and therefore of the order of 0.3 eV. From fig. 1.5 and for gas densities of  $10^{22} \text{ atoms.cm}^{-3}$

the ion fraction is expected to be negligible. As the density of the gas is approximately ten times less than in the target, then the mean temperature ( $\bar{T}$ ) for a fluence equal to five times the threshold fluence, is:

$$\bar{T} \sim 10 \times 5 \times \frac{T_b}{3} \sim 2.5 \times 10^5 \text{ K} \sim 25 \text{ eV}$$

Therefore, full ionisation will have occurred for fluences even as low as five times the threshold fluence, i.e. fluences of the order of  $30 \times 10^6 \text{ erg.cm}^{-2}$  for metals.

The above analysis is in good agreement with published results. An analysis of the ablation of Cu by an excimer laser showed the ion fraction to be negligible at fluences close to the threshold ( $25 \times 10^6 \text{ erg.cm}^{-2}$ ) [6]. As the fluence was increased from  $30$  to  $40 \times 10^6 \text{ erg.cm}^{-2}$  the ion fraction was found to increase by a factor 20 [12].

In summary the interaction of the laser beam with the evaporated species results in the formation of ions and a saturation of the deposition rate. As the laser fluence is increased the plasma temperature increases leading to an exponential increase in the ion fraction. For fluences close to the threshold the mean ion energy is of the order of tens of eV and the ion fraction is negligible. In addition, it appears that the energy of the neutrals depends on the laser fluence.

### 1.3.3 Expansion

The third and final step of the ablation process involves the expansion of the plasma. After the extinction of the laser pulse, the plasma temperature decreases and the plasma expands adiabatically. Singh et al. [4] modelled the expanding plasma by supposing that it behaves like an ideal gas. This is justified as, in the absence of an external field, the motion of the charged particles is effected by collisions with neutral species similar to those of an ideal gas. The equation of flow can be written as:

$$\begin{aligned} X(t) \left[ \frac{d^2 X}{dt^2} \right] &= Y(t) \left[ \frac{d^2 Y}{dt^2} \right] = Z(t) \left[ \frac{d^2 Z}{dt^2} \right] \\ &= \frac{KT_0}{M} \left[ \frac{X_0 Y_0 Z_0}{X(t) Y(t) Z(t)} \right]^{\gamma-1} \end{aligned} \quad (1.6)$$

where  $X_0$ ,  $Y_0$  and  $Z_0$  are the initial dimensions of the plasma just after the extinction of the laser pulse.  $X_0$ ,  $Y_0$  are defined to lie in the plane of the target and  $Z_0$  is perpendicular.  $T_0$  is the initial temperature of the plasma,  $M$  the mass of the constituent elements in the plasma and  $\gamma$  is the ratio of the specific heat capacities of the plume at constant pressure and volume. From (1.6) it follows that:

$$\frac{\frac{d^2X}{dt^2}}{\frac{d^2Z}{dt^2}} = \frac{Z(t)}{X(t)} \quad (1.7)$$

Thus equation 1.7 shows that the acceleration of the species in the plasma is greatest along the direction of smallest initial dimension. The X and Y dimensions are determined by the laser spot size and are of the order of a mm, the Z dimension is of the order of a  $\mu\text{m}$ . Therefore plasma expansion occurs predominantly perpendicular to the target surface. This is the origin of the highly directional nature of PLD.

In addition, from equation 1.7, one would expect the deposit to become more isotropic as the spot size is decreased. In figure 1.7b, the angular distribution of deposit from a spot size of  $0.3 \text{ mm}^2$  is compared to that of a spot of  $3 \text{ mm}^2$ . A more isotropic distribution is obtained from the smaller spot. As the spot size is increased the deposit becomes more directional. The consequence of this is that for a smaller spot size the deposition rate measured in the straight-through position is found to rise slower than for a larger spot size, with increasing fluence (fig1.7a).

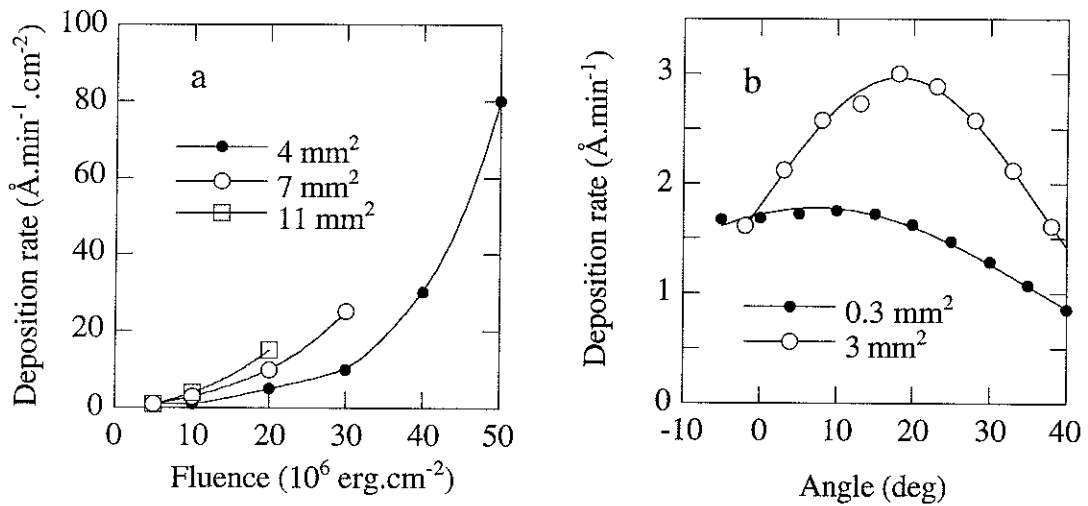


Figure 1.7a Deposition rate as a function of laser fluence. The lower deposition rate at a given fluence for a smaller spot size can be explained by 1.6b which shows the angular distribution of deposition rate for a spot size of  $0.3 \text{ mm}^2$  and  $3 \text{ mm}^2$ .

The maximum deposition rate for a given spot size is not found at  $\theta = 0^\circ$ , i.e. in the straight through position. For the  $0.3 \text{ mm}^2$  spot it is found at almost  $\theta = 10^\circ$ , whereas for the  $3 \text{ mm}^2$  spot it is found at  $\theta = 20^\circ$  (fig 1.7b). This corresponds to a tilt of the plume towards the direction of the incident laser beam. This arises due to the fact that the laser beam is not incident on the target at normal incidence which results in the formation of tilted target craters.



At  $10^\circ$  from the position of maximum deposition rate ( $\theta = 20^\circ$  for  $0.3 \text{ mm}^2$  and  $\theta = 30^\circ$  for  $3 \text{ mm}^2$ , fig 1.7b) the deposition rate is found to have decreased to 90% and 85%, which corresponds approximately to a  $\text{Cos}^5\theta$  and a  $\text{Cos}^{10}\theta$  deposition rate dependence for the  $0.3 \text{ mm}^2$  and  $3 \text{ mm}^2$  spot respectively.

The angular dependence of thermal evaporation ( $\text{Cos } \theta$ ) is compared to that of a  $\text{Cos}^{10}\theta$  dependence in figure 1.8a. For  $\theta = 25^\circ$  the plot indicates that a PLD film deposited by ablation with a  $3 \text{ mm}^2$  spot would have a thickness of 40 % of the thickness at the centre of the film, unlike thermal evaporation which would show a 90 % thickness at this point.

The area of homogeneous deposition can be increased by increasing the target substrate distance (fig. 1.8b) or by rastering the laser beam over the target surface.

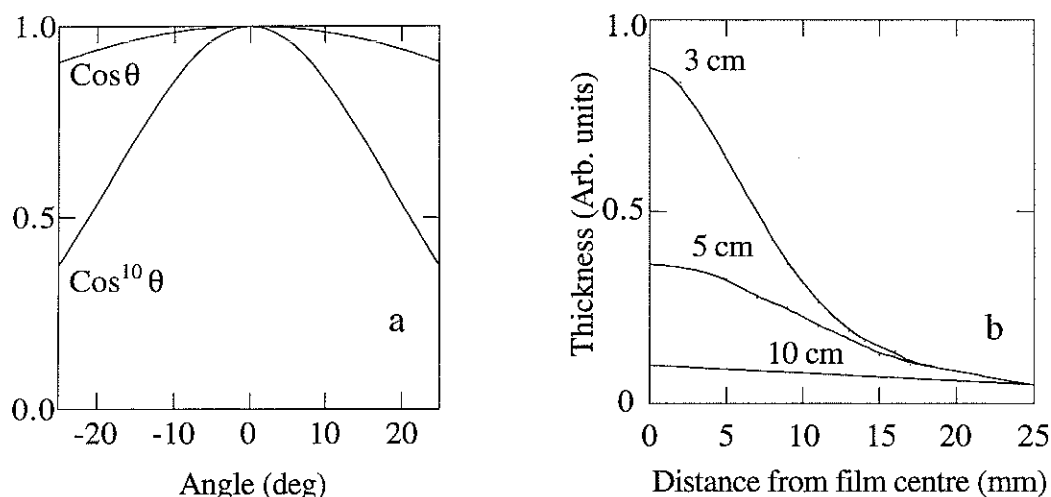


Fig. 1.8a - A comparison of the angular deposition of PLD with the angular distribution of thermal evaporation. 1.8b The influence of thickness inhomogeneities for target-substrate distances of 3 cm, 5cm and 10 cm.

#### 1.4 Stoichiometric evaporation

As discussed in the previous section, the depth of target heated during a 9 ns laser pulse is of the order of a  $\mu\text{m}$ . Assuming as before that at the melting temperature  $T_m$  (for metals  $T_b \sim 3T_m$ ) the corresponding volume is heated for a time of approximately  $3^2 \times \tau$ , which is of the order of 100 ns. Atomic displacement during this time is of the order of :

$$\sqrt{2L_a 3^2 \tau} \sim 20 \text{ \AA}$$

which is negligible compared with  $L_t$ . Thus atomic segregation does not occur in most cases during PLD.

Metallic films deposited by laser ablation, with target-substrate distances of 3 cm were found to be stoichiometrically equivalent to the target [13]. However for depositions with target-substrate distances of 7 cm, deposited films were found not to have the same stoichiometric composition as the target. For example, ablation of an  $\text{YCo}_5$  target at a distance of 7 cm from the substrate resulted in a film which was a mixture of  $\text{YCo}_5$  and  $\text{Y}_2\text{Co}_{17}$  phases.

Therefore during laser ablation congruent evaporation does not imply congruent deposition. The above results indicate that a certain segregation of evaporated species occurs during the flight from the target to the substrate.

This can be understood by examining equation 1.6 which shows that the asymptotic velocities of the ablated species are inversely proportional to the masses of evaporated species. Heavier evaporated species are therefore expected to be less directional compared with lighter species resulting in the straight-through position being richer in the lighter species. In the case of  $\text{YCo}_5$  the evaporated plume is expected to be Co-rich in the centre. This agrees with the experimental findings.

Equation 1.6 also suggests that the acceleration of the evaporated species is directly proportional to the temperature in the plasma. Assuming that the plasma temperature is proportional to the laser fluence, one expects a greater stoichiometric deviation at low fluences. Increasing stoichiometric deviations with decreasing fluences have been reported in the literature [14].

## 1.5 PLD and film quality

### 1.5.1 Influence of high energy ions

As discussed above, high energy ions are formed during PLD. From the point of view of film deposition the energies of the evaporated species play an important role in the resulting film quality. Muller [15] reported that as the kinetic energy of the adatoms is increased the films become more dense, have less defects and more ordered. Although high energy species are favourable for epitaxial growth overly energetic species can be destructive.

When an ion collides with a film surface, the resulting kinetic energy transfer can cause one of the following effects:

- heating of the surface ( $E \sim 10^{-1}$  eV)
- atomic re-arrangement ( $E \sim 10^{-1}$  eV)
- ejection of material from the surface ( $E \sim 10^1$ -  $10^2$  eV)
- implantations of ions in the surface ( $E \sim 10^3$  eV)

The first two effects are favourable for epitaxial deposition, the last two are destructive. For example, the threshold ion energy for the removal of Fe atoms from a surface is 22 eV for Ne ions and 25 eV for Kr ions.

Recent results suggest that deposition at high fluences can cause re-sputtering of the growing film [16]

### 1.5.2 Droplets

Microscope studies on films deposited by PLD reveal the existence of particulates. Two forms of particulates are observed.

The first have a uniform shape, are of the order of a micron (figure 1.9a). Their form (figure 1.9b) suggests that they arise due to the condensation of molten material on the film. Their origin can be attributed to the influence of radiation pressure acting on a region of molten target. The density of these molten droplets increases as the laser fluence increases. For depositions performed at low laser fluence, droplet contamination is negligible (figure 1.9c). Droplet contamination at high fluences depends on the nature of the material being ablated. Y and rare earth targets give rise to a large droplet density. Fe targets yield a smaller density and W yields almost droplet free films.

Many solutions have been proposed for high fluence droplet elimination, such as scattering from a heated screen [17] and employing two plumes at 90° to each other, with each plume being at 45° from the target-substrate axis [18]. Attempts to eliminate droplets by using electric fields have been unsuccessful as a large proportion of droplets are neutral [19].

The velocities of these droplets when travelling from the target to the substrate are of the order of 100 - 1000 ms<sup>-1</sup> [20] and therefore order(s) of magnitude lower than that of atomic or ionic species (10<sup>4</sup> - 10<sup>5</sup> ms<sup>-1</sup>). Thus the target-substrate distance acts in itself as a time filter, the faster atomic and ionic species arriving at the substrate long before the slower droplets. A rotating pallet, placed in the target-substrate path and synchronised with the laser firing yielded a 0.2% droplet contamination compared with a 20% contamination for deposition without a filter [21].

For depositions performed on heavily used targets, even at low fluences, a second type of particulate contamination may be observed (figure 1.9d). They have irregular shapes and sizes. They do not have a molten aspect. The origin of these particulates can be understood by examining the morphology of a heavily used target (figure 1.9e). As the use time increases, the target morphology deteriorates leading to the possibility of pieces of the target breaking away from the surface which then arrive on the substrate. Careful rastering of the laser beam on the target surface and regular polishing of the target surface eliminates this problem. The homogeneity of the laser beam is another critical parameter.

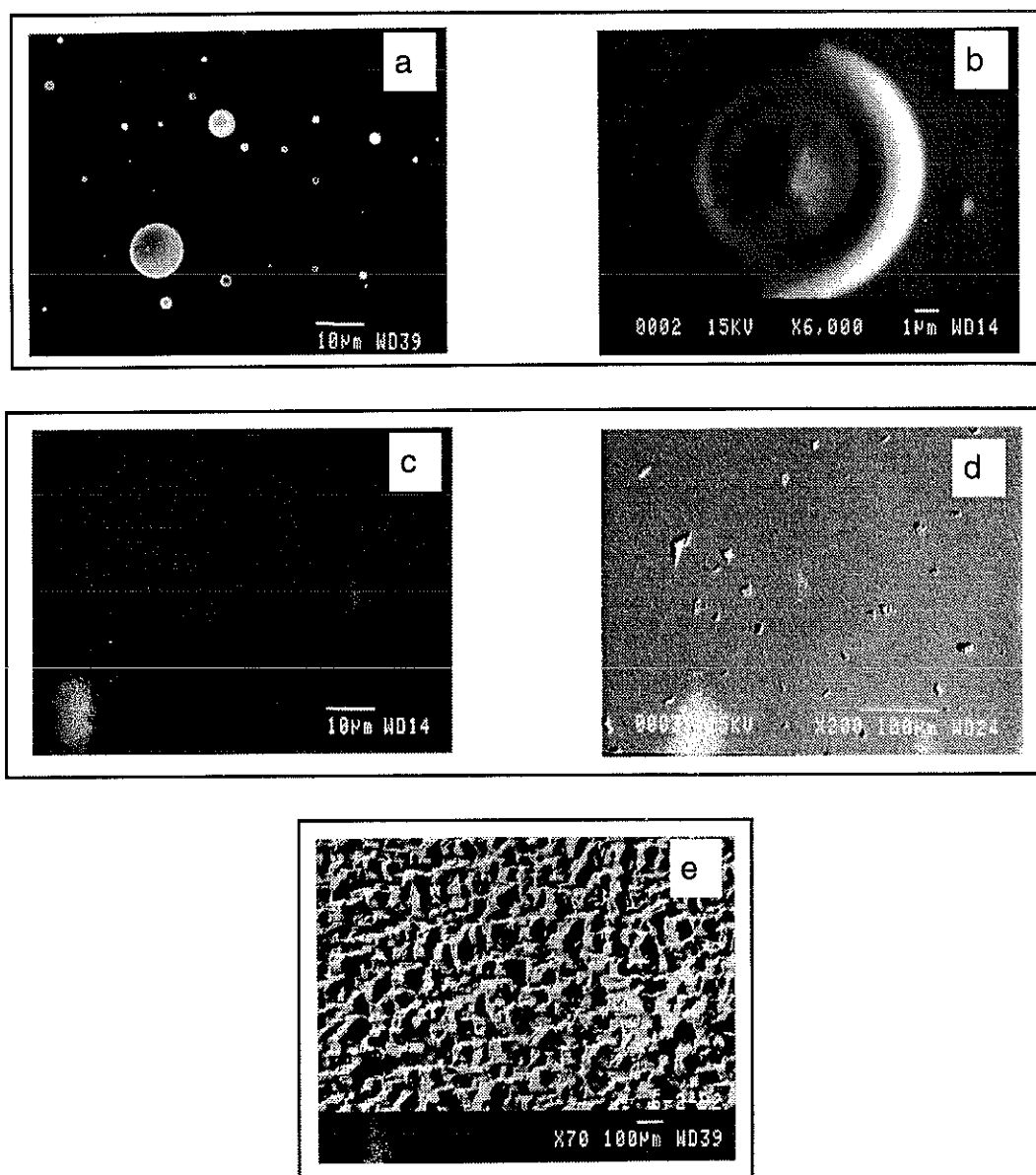


*Fig. 1.9a - SEM photograph of a film deposited by PLD at large fluences showing droplet contamination; 1.9b - close-up of a molten droplet ; 1.9c film deposited at low fluence ; 1.9d film deposited from a heavily used target and 1.9e morphology of a heavily used target.*

## 1.6 Discussion and conclusion

The quantity of matter heated during PLD depends on the laser energy, the pulse duration and the thermal properties of the material being evaporated. The initial stages of evaporation of metals appears to be governed by thermal processes. The high reflectivity of metals limits the efficiency of the process and is wavelength dependent.

The evaporated gas absorbs the incoming laser beam. This process appears to be proportional to the gas density and therefore increases as the laser fluence increases. This absorption leads to an increase in the gas temperature and ionisation occurs. The ion fraction in the plasma and the ion energy is a very sensitive function of laser fluence. The energy of the neutral species also increases as the laser fluence is increased.

The optimum fluences for film deposition correspond to fluences close to the threshold fluence. For such fluences, the energy of the evaporated species assists film growth without causing film damage. The deposition rates at such conditions are however much lower than other deposition techniques. High laser fluences leading to highly energetic species can lead to film re-sputtering.

The thermal properties of metals are such that the heated depth is orders of magnitude less than the area of material heated and this leads to a highly directional evaporated plume. This effect is more pronounced for large laser spots and limits the size of film that can be deposited without a homogeneous thickness. Rastering the laser beam over the target enables larger films to be deposited.

Droplet contamination can be avoided by working at fluences close to the threshold fluence and by limiting the build-up of target inhomogeneities by continuously rotating the target during ablation. Mechanical filters can also be employed to eliminate droplet contamination at high fluences.

Stoichiometric evaporation occurs during PLD. The directional nature of the evaporated plume is mass dependent leading to elemental segregation during the time of flight from the target to the substrate. This segregation can be limited by working at small target-substrate distances and by reducing the laser beam waist. Preferential re-sputtering can occur at high fluence and thus alters the film composition.

Compared with the other established techniques, such as MBE and sputtering, PLD offers the following advantages :

- UHV compatible
- can be employed for the deposition of any material
- no crucible employed
- versatile
- stoichiometric evaporation
- evaporated species of high energy
- laser located ex-situ

The disadvantages of the technique are :

- droplet contamination of deposited films
- presence of overly energetic species

In particular, for the deposition of magnetic films, such as transition metals, rare earth metals and transition metal rare earth alloys, PLD is most suitable for research work when the operating conditions are optimised. The versatility of the technique enable a large series of materials to be readily deposited. The composition of an alloy can be conserved. Finally, reactivity problems with crucibles etc. can be avoided.

## 1.7 References

---

- [1] H. W. Smith and A. F. Turner  
Appl. Optics, 4 (1965) 417.
- [2] D. Dijkkamp, T. Venkatesan, X. D. Wu, S. A. Shaheen,  
N. Jisrawi, Y. H. Min Lee, W. L. Mc Lean and M. Croft,  
Appl. Phys. Lett., 51 (1987) 619.
- [3] L. Weil, "Elements d'échange thermiques",  
Gauthier Villars publishers, Paris, 1965.
- [4] R.K. Singh and J. Narayan,  
Phys. Rev. B ,41 ,843 , 1990.
- [5] N. Cherief, D. Givord, O.F.K. Mc Grath, Y. Otani and F. Robaut,  
JMMM 126 (1993) 225.
- [6] K. L. Saenger,  
J. Appl. Phys., 66 (1989) 4435.
- [7] R. Viswanathan, I. Hussla,  
"Laser Processing and Diagnostics" D. Bäuerle (ed.),  
Springer Ser. Chem. Phys., Vol. 39 (Springer, Berlin 1984).
- [8] E. van de Riet, J.C.S. Kools and J. Dieleman,  
J. Appl. Phys., 73 1993) 8290.
- [9] W. B. Thomson,  
"An introduction to plasma physics", pp 17-20, Addison Wesley publishers, USA, 1962.
- [10] see for example; C. Phipps and R. W. Dreyfus,  
"Laser Microprobe Mass analysis", John Wiley and sons (pub), New York, USA, 1994.
- [11] J. C. S. Kools, S. H. Brongersman, E. van de Riet and J. Dielman,  
Appl. Phys. B53 (1991) 125.
- [12] R. W. Dreyfus,  
J. Appl. Phys., 69 (1991) 1721.
- [13] J.P. Gavigan, D. Givord, A. Liénard, O.F.K. Mc Grath, J.P. Rebouillat and Y. Souche,  
Mat. Res. Soc. Symp. Proc., 1990.



- 
- [14] T.P. O'Brien, J.F. Lawlor, J.G. Lunney and W.J. Blau,  
Mats. Sci. and Eng., B13, 9-13, 1992.
- [15] K.H. Muller,  
Surf. Sci. Letts., 184,,375 ,1987.
- [16] R. Jordan, D. Cole, J. G. Lunney, K. Mackay and D. Givord,  
to appear in proc. of E-MRS symposium, Strasbourg 1994, Elsevier Publishers.
- [17] S. V. Gapanov, A. A. Gudkov, B. M. Luskin and N.N. Salashchenko,  
Sov. Tech. Phys., 26 (1980) 598.
- [18] M. D. Strikovsky, E. B. Klyuenkov, S. V. Gapanov, J. Schubert and C. A. Copetti,  
Appl. Phys. Lett., 63 (1993) 1146 and references therein.
- [19] J.P. Rebouillat, B.Michelutti, Y. Souche, J.P. Gavigan, D. Givord, A. Liénard.,  
Mat. Res. Soc. Symp. Proceedings, 151 (1989) 259.
- [20] H. Dupendant, J.P. Gavigan, D. Givord, A. Liénard, J.P. Rebouillat and Y. Souche,  
Appl. Surf. Sci., 43 (1989) 639.
- [21] N. Cherief, D. Givord, A. Liénard, K. Mackay,  
O.F.K. Mc Grath, J.P. Rebouillat, F. Robaut and Y. Souche ,  
JMMM, 121 (1993) 94.



# CHAPTER TWO

## THIN FILM GROWTH

### Table of contents to chapter 2

2.1 Introduction	35
2.2 Epitaxy	36
2.2.1 Epitaxial misfit	36
2.2.2 Epitaxial relationship	37
2.2.3 Strain relief	41
2.3 Growth modes	42
2.3.1 Thermodynamics	42
2.3.2 Kinetics	43
2.4 Thin film characterisation	45
2.4.1 RHEED	46
2.4.2 Auger analysis	48
2.4.3 X-ray analysis	50
2.5 References	53

## RÉSUMÉ

Dans ce chapitre on discute de la croissance des couches minces. La croissance des couches minces monocristallines se fait en utilisant le phénomène d'épitaxie où la couche adopte une structure cristalline qui est reliée à celle du substrat. Jusqu'à présent il n'existe pas de théorie qui permette de prévoir la relation d'épitaxie de n'importe quel système, seules quelques tendances sont en train d'émerger. Une des conséquences de la croissance épitaxiale est que souvent la couche prend des paramètres de maille qui diffèrent de ceux de l'échantillon massif. En général, lorsque l'épaisseur de la couche augmente, la couche se relaxe vers les paramètres du massif. Trois modes de croissance peuvent être observés. A l'équilibre thermique, la formation d'une première monocouche continue est attendue quand l'énergie de surface du substrat est plus importante que celle de la couche. Quand l'énergie cinétique des adatoms augmente, la probabilité d'obtenir une structure unique augmente aussi. La compréhension de la croissance des couches repose sur une caractérisation structurale détaillée. Parmi les techniques les mieux adaptées pour cela il y a la diffraction rasante des électrons de haute énergie, l'analyse Auger et l'analyse de rayons X en diffraction et réflexion. Ces trois techniques sont exposées à la fin du chapitre.

## SUMMARY

The essential elements of thin film growth are reviewed in this chapter. Single crystalline thin films can be grown by exploiting the phenomenon of epitaxy whereby the growing film adopts a structural orientation which is related to that of the substrate. Although no theory exists which enables the epitaxial orientation of any given system to be predicted, some trends are beginning to emerge. Epitaxy often results in the film adopting a lattice parameter which is different from its equilibrium lattice parameter. In general as the film thickness increases the film relaxes to its equilibrium lattice parameter. Three types of growth modes can occur during film growth. At thermal equilibrium, the formation of a continuous first monolayer is expected when the surface energy of the substrate is greater than that of the film. As the kinetic energy of the adatoms is increased the probability of the film adopting a unique structure increases. The understanding of thin film growth requires a detailed structural characterisation. Amongst the most suitable techniques are : RHEED and Auger analysis which are performed in-situ and X-ray analysis (diffraction and reflection) which is usually performed ex-situ. These three techniques are briefly discussed at the end of the chapter.

## 2.1 Introduction

Thin films are generally grown by inducing a vapour flux removal from a source material. A support, called the substrate, is placed in the path of the flux upon which the vapour condenses leading to the formation of a solid film. For the deposition of metals the flux incident rate (deposition rate) is orders of magnitude greater than the re-evaporation rate.

The most important structural characteristics of a thin film are its crystallinity and its morphology.

The crystalline structure can vary from amorphous, to polycrystalline to single crystalline. Each structure can be identified according to the mean crystallite size and the relative orientation between the crystallites. Often, the crystallite size is too small to be measured by X-ray techniques and the term X-ray amorphous is often employed. In polycrystalline structures no common orientation between the crystallites can be defined in all directions. In thin films, a common orientation is often induced along the growth direction and this structure is termed textured. Finally, in single crystalline films, a common orientation is induced in all three directions.

The structural properties of a film depend on the structural properties of the substrate and on the kinetic energy of the adatoms. Amorphous films are deposited on amorphous substrates and the kinetic energy of the adatoms is quenched during deposition, usually by cooling the substrate. Polycrystalline films are usually deposited on polycrystalline or glass substrates, held at ambient temperature. Single crystal films are deposited on single crystalline substrates and by exploiting the phenomenon of epitaxy.

Thin film morphologies can be divided into two main classes ; continuous films, where the thickness is homogenous across the whole film, and island films, where abrupt thickness inhomogeneities are present.

The objective of the remainder of this chapter is to analyse the most important parameters which determine the outcome of a deposition in terms of crystalline structure and morphology. Such analysis enables the pertinent experimental conditions to be controlled in order to engineer the desired film quality. The film quality of interest in this work corresponds to single crystalline continuous (flat) films. Finally the characterisation of thin films is discussed.

## 2.2 Epitaxy

The original meaning of the word epitaxy was the growth on a crystalline substrate of a crystalline substance that mimics the orientation of the substrate. To-day, the word epitaxy is used in a more general sense, and describes the growth of single crystalline films where, usually, a relationship exists between the structure of the film and the substrate. Epitaxial depositions of metals were first reported by Lassen [1] and Bruck [2] in 1934.

The oriented growth of a material on itself is referred to as auto-epitaxy and on another material as hetero-epitaxy. It is interesting to note that oriented growth of a solid film on an amorphous or liquid surface has been observed, such a phenomenon is called rheotaxy, for example Si (111) on Mg [3] .

Although epitaxy is usually thought of as atomic engineering, it can occur in nature, as for example Rutile which grows on olgiste ( $\text{Fe}_2\text{O}_3$ ) with their [001] axes parallel.

Besides being a very challenging subject in itself, the motivations for studying epitaxial depositions are essentially twofold. Firstly epitaxial films provide a means of studying the properties of matter at surfaces and in reduced dimensions in a controlled manner. Secondly epitaxy provides a means of engineering structures that do not occur naturally.

### 2.2.1 Epitaxial misfit

The difference in lattice parameters between the substrate and the deposit is commonly referred to as the epitaxial misfit, which is defined as follows:

$$M = \frac{a(\text{hkl})_s - a(\text{hkl})_f}{a(\text{hkl})_f} \quad (2.1)$$

where  $a(\text{hkl})_s$  is the interplanar distance of the substrate and  $a(\text{hkl})_f$  is that of the film. It is a common misconception that a small lattice misfit is a necessary pre-condition for epitaxy. In the pioneering work of Royer [4] he defined the maximum permissible lattice misfit to be 15%. Recent developments in epitaxial depositions have shown this to be untrue. For instance Ce has been epitaxied on V despite a lattice misfit of 28% [6]. It is however true to say that the probability of successful epitaxy decreases with increasing misfit.

For the case of epitaxial deposition of a film on a substrate with a different crystallographic structure, for example Gd on W, the misfit will be anisotropic.

### 2.2.2 Epitaxial relationship

The relative orientation of the crystallographic axes of the substrate with those of the film is referred to as the epitaxial orientation. It is governed by ; an interplay between the difference in the crystallographic structure of the film and the substrate, the misfit and the differences in the chemical nature of the interface atoms.

A knowledge of the preferred epitaxial orientation of a film enables the correct choice of substrate orientation to be made. No unique theory exists which can however, for a given system, predict the epitaxial relationship. An analysis of experimental findings for films and substrates of the same chemical nature (i.e. metal on metal or semiconductor on semiconductor) indicate that some trends are beginning to emerge.

If the film and substrate have the same crystallographic structure then the epitaxial orientation will be such that all axes of the film are parallel to those of the substrate regardless of the misfit. Such a relationship is referred to as direct epitaxy and is schematised in figure 2.1a. Examples of direct epitaxy include : bcc Fe (110) on bcc W (110), or of fcc Ni (100) on fcc Cu (100).

If the film and substrate have a different structure then two possible outcomes occur.

Firstly, the growing film abandons its equilibrium structure and adopts the structure of the substrate. This situation is referred to as metastable epitaxy. Fe, for example, although at room temperature its equilibrium structure is bcc, is found to grow fcc when deposited on fcc Cu substrates [5]. The probability of meta-stable epitaxy occurring is limited by the cohesion energy difference between the equilibrium structure and the meta-stable structure [6] and on the kinetics of the adatoms [7].

Secondly and more commonly, the film grows according to its normal stable structure but orients itself in such a way as to minimise the misfit. For example Fe, with a lattice parameter of  $a = 2.86 \text{ \AA}$  can grow on Ag (fcc), lattice parameter  $a = 4.08 \text{ \AA}$  by rotation of the cube edges of Fe by  $45^\circ$  with respect to those of Ag (fig. 2.1b). This results in a misfit of 0.1% compared with 42% without rotation.

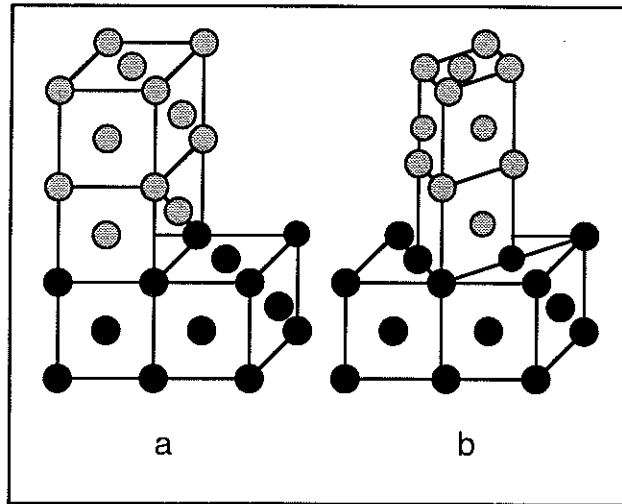


Figure 2.1 Schematic representation of : a - direct epitaxy and b - indirect epitaxy.

It appears that the density of the film plane and the substrate plane play an important rôle. The most dense planes of bcc, fcc and hcp structures are the (110), (111) and the (0001) planes respectively. For depositions of a film on one of these planes, there is a large probability that the film plane will also be a dense plane. This is because the most dense planes have the lowest surface energy and are therefore the most stable (see further on). For example, the epitaxial plane of hcp Gd when deposited on bcc Fe (110) is the (0001) plane (see chapter 4).

For the growth of a film on a substrate with a different crystallographic structure, the prediction of the in-plane epitaxial orientation is not as straightforward. Because the structures are different, lattice matching can occur along one direction only.

Consider the case of an hcp (0001) (equivalent to an fcc (111) plane) deposited on a bcc (110) plane. The hcp (0001) (and fcc (111)) plane has a hexagonal arrangement of the atoms in the plane (fig. 2.2b) and the bcc (110) plane has a pseudo-hexagonal arrangement in plane (2.2a).

Row matching can be achieved for two cases, depending on the difference in the atomic diameters.

If the diameter of the hcp atoms is greater than the bcc atoms by 13% then coherence along the [001] axis of the bcc structure can be obtained (figure 2.2C) when the  $[1\bar{1}00]$  axis of the hexagonal film is parallel to the [001] axis of the bcc substrate.

If the other hand, the diameter of the hcp atoms is greater than the diameter of the bcc atoms by 35%, then coherence along the  $[1\bar{1}1]$  axis of the bcc structure can be obtained when the  $[11\bar{2}0]$  axis of the hexagonal film is parallel to the  $[1\bar{1}1]$  of the bcc substrate.



This corresponds to a rotation of the hcp structure by  $5^\circ$  with respect to the previous case.

These two solutions are, with one exception [8], the only epitaxial relations reported for such faces in the literature to-date. The orientation in fig. 2.2c is commonly referred to as the Nishiyama [9]-Wasserman [10] (NW) orientation. This is the epitaxial orientation found for the growth of the rare earths on W (110) [11]. The second orientation is commonly referred to as the Kurdjumov-Sachs [12] (KS) orientation.

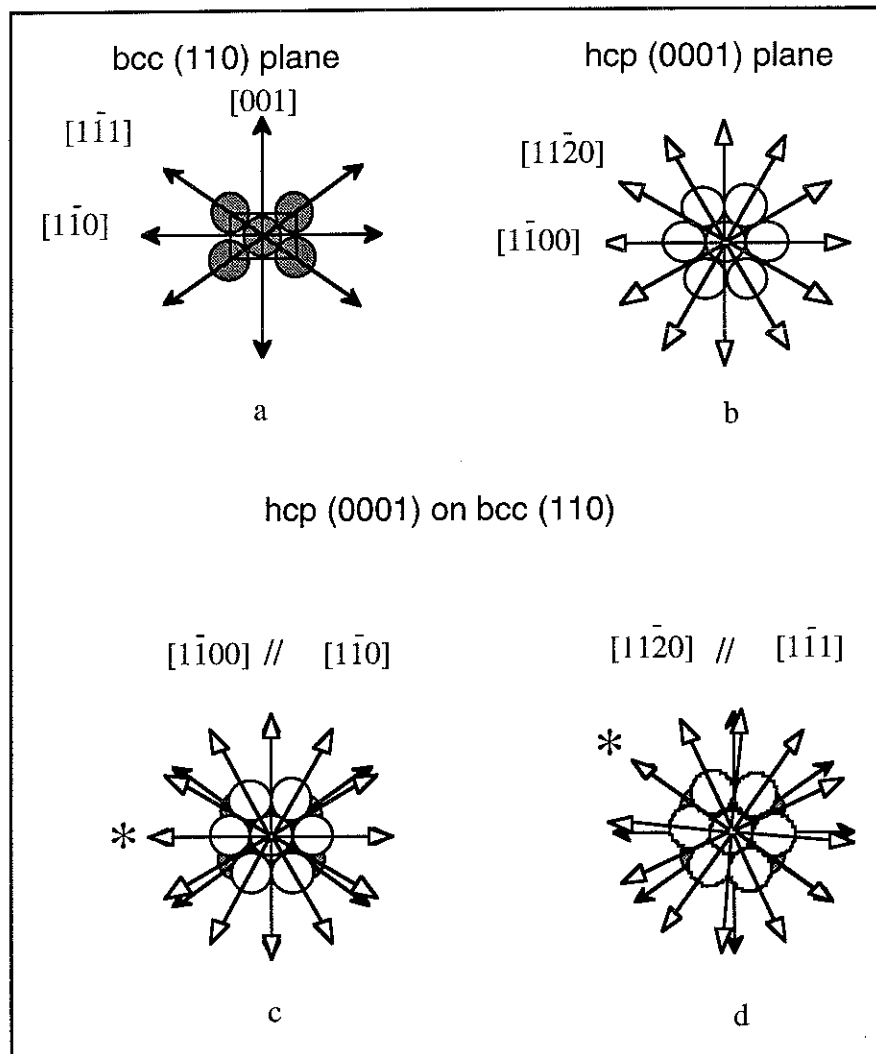


Fig. 2.2 - Schematic representation of - (a) bcc (110) plane, (b) hcp (0001), (c) hcp (0001) on bcc (110) with a NW orientation and (d) hcp (0001) on bcc (110) with a KS orientation.

The axis of row matching is indicated by \*.

A greater understanding of the origin of these relationships can be obtained by examining energy calculations where the epitaxy is modelled by assuming that both planes are rigid [13]. The interaction energy between the film and the substrate is taken

to be a Lennard Jones interaction. The calculations are performed by varying the angle ( $\theta$ ) between the  $[1100]$  of the film and  $[001]$  of the substrate. For each value of  $\theta$ , the energy is calculated as a function of the ratio of the atomic diameters ( $P$ ) (fig. 2.3).

For  $\theta = 0^\circ$  an energy minimum is found at  $P=1.13$  (fig. 23). This is in good agreement with experimental observations and corresponds to the NW orientation. For  $\theta = 5.26^\circ$  the calculation shows a minimum at  $P=1.32$ . This also agrees with experimental observations and corresponds to the KS orientation.

The energy minimum for  $\theta = 0^\circ$  (NW) is not as deep as that for  $\theta = 5.26^\circ$  (KS) and therefore suggesting that KS epitaxy is more stable than NW epitaxy. This arises due to the fact that in the KS orientation, coincidence is obtained along the most dense axis of the substrate ( $[1\bar{1}1]$ ), whereas in NW epitaxy coincidence is obtained along the second most dense axis of the substrate ( $[001]$ ).

No energy minima are found for row-matching along the  $[1\bar{1}0]$  axis of the bcc structure, which is the least dense axis in the plane. In addition, no energy minima were found for any other values of  $\theta$ .

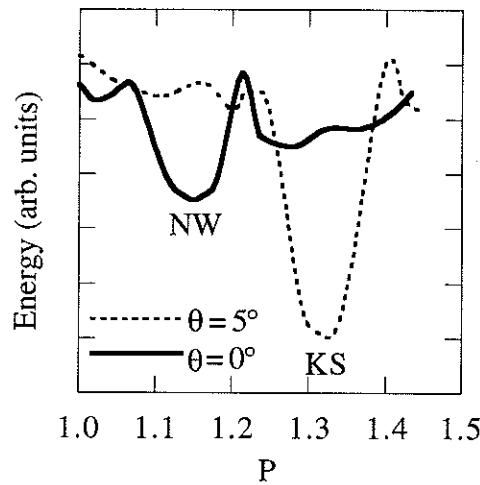


Fig. 2.3 - Energy calculations as a function of the adatom to substrate atom ratio ( $P$ ) for arrangement of a hcp (0001) lattice on a bcc (110) substrate for two different orientations ( $\theta = 0^\circ$  and  $\theta = 5^\circ$ ).

In summary, for the case of densely packed planes and for metal-metal epitaxy, the epitaxial relations can be determined by simple row-matching criteria with the most stable orientation being row matching along the most dense axes. If the lattice mismatch does not permit this then the next most stable orientation is row matching along the second most dense axes.

### 2.2.3 Strain relief

A competition occurs between the deposit-deposit interactions which tend to adjust the lattice parameters as in the bulk and the deposit-substrate interactions which tend to adjust the lattice parameters in such a way as to achieve registry between film and substrate. The former is dominated in the bulk of the film, the latter is dominant close to the interface. The outcome depends on the extent of the misfit, the thickness and the elastic properties of the film.

For zero misfit, then one can expect the film to be lattice matched with the substrate (fig. 2.4a). For larger misfits, then coherence at the interface can be conserved with the growing film being strained (fig. 2.4b). Such film growth is termed pseudomorphism. The energy cost of the strain is proportional to the film volume. For thicknesses greater than a certain critical thickness,  $d_c$ , then strain relief will occur through the formation of interface dislocations (fig. 2.4c). In general the greater the misfit the smaller the critical thickness.

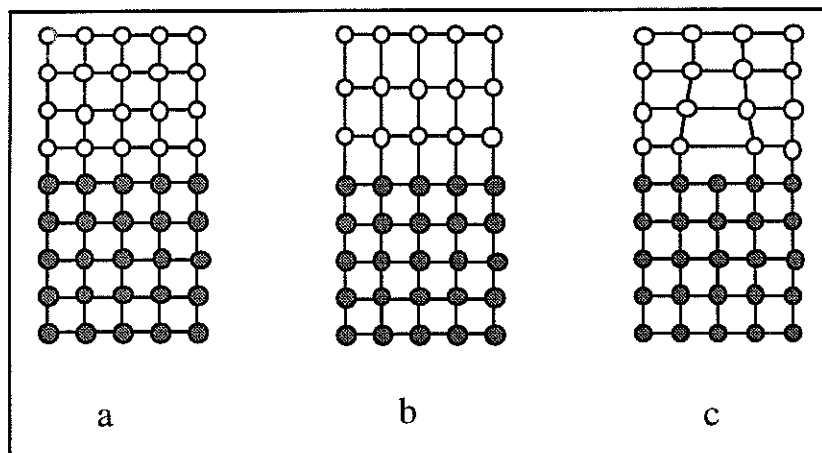


*Fig. 2.4 - Schematic illustration of (a) lattice matched heteroepitaxy, (b) coherently strained lattice mismatched heteroepitaxy and (c) strain relieved lattice mismatched heteroepitaxy through the formation of interface dislocations.*

## 2.3 Growth modes

The growth mode of a thin film depends on thermodynamical and kinetic energy considerations.

### 2.3.1 Thermodynamics

From a thermodynamical perspective the two most important parameters to be considered are surface and interface energies. The surface atoms of a material experience an increase in potential energy due to surface co-ordination reduction. This energy increase is defined as the surface energy. Surface energies are not known exactly as both experimental determination and calculations are difficult. [14].

In general the surface energy is proportional to the latent heat of sublimation and inversely proportional to the bulk co-ordination [15]. The most dense crystal faces have the lowest surface energies and are therefore more stable. For example, for bcc structures, the surface energy follows the following order :  $(111) > (002) > (110)$ . Typically for metals, surface energies range from  $10^2 - 10^3 \text{ erg.cm}^{-2}$ .

The interface energy ( $E_i$ ) is the energy cost of putting two surfaces in contact with each other, and in general for metals is one order of magnitude less than surface energies.

The stability of a monolayer on a substrate with a 100 % coverage can for equilibrium conditions at  $T = 0$  be determined by a spreading factor  $S$ , which is given by [16]:

$$S = E_s - E_f - E_i \quad (2.2)$$

If  $S$  is positive then a monolayer will be stable on the substrate and complete wetting of the substrate by the film occurs. This results in a 2D growth mode which is commonly referred to as Frank-Van der Merwe (FM) growth mode [17] (fig. 2.5). If however  $S$  is negative, then the film will deposit itself in such a way as to minimise its exposed surface and coalesces in the form of 3D nuclei, resulting in incomplete and non-uniform coverage of the substrate. This 3D growth mode is referred to as Volmer -Weber (VW) [18] (fig. 2.5).

A transition from initial 2D growth to island growth can occur in strained films which are elastically hard. The transition thickness corresponds to thicknesses, less than [19], or equal to [16], the critical thickness for the onset of misfit dislocations. Such a growth mode is termed Stranski-Krastanov [20].

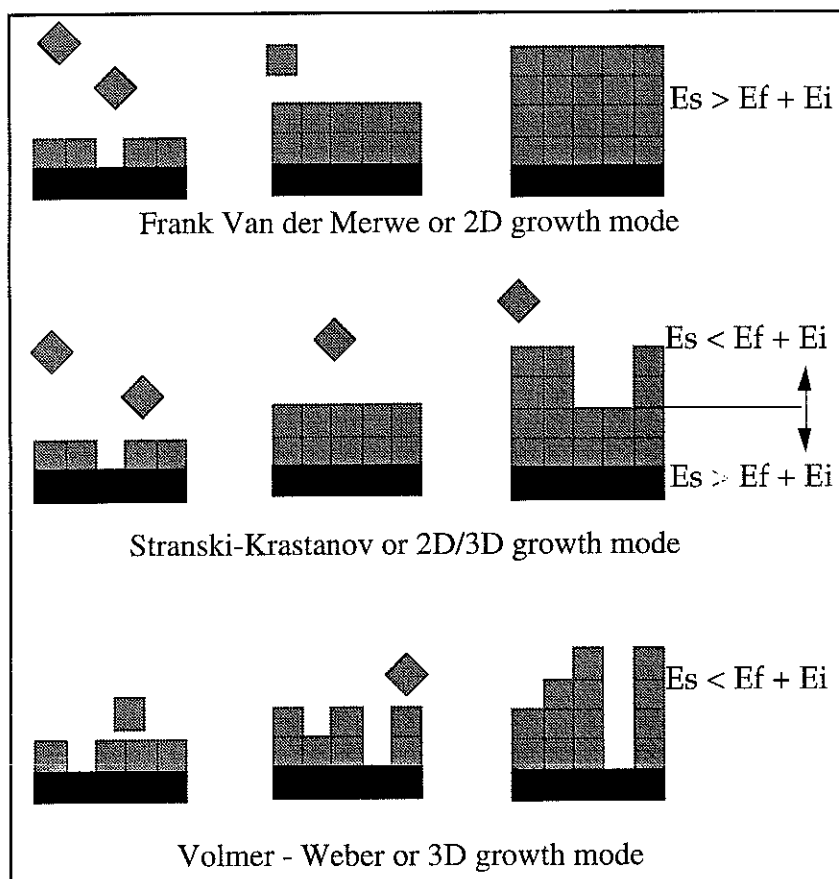


Fig. 2.5 - Schematic representation of the different growth modes of a thin film.

The ideal growth mode during deposition is that of a 2D one. It is for this reason that W is a very attractive buffer layer as it has one of the highest surface energies of all metals ( $E_s = 3468 \text{ erg.cm}^{-2}$ ). Therefore, depositions of Fe on W, for example, are expected to grow according to a 2D growth mode as the surface energy of Fe ( $E_s = 2938 \text{ erg.cm}^{-2}$ ) is less than that of W.

### 2.3.2 Kinetics

The above discussion assumes that the growing film is in equilibrium. This is rarely the case. In order for an adatom to reach its equilibrium it must have sufficient adatom mobility.

Both the crystalline quality and the growth mode depend on the kinetic energy of the arriving atoms. The kinetics of film growth depend on the substrate temperature and on the deposition rate.

If an atom requires an amount of energy  $E$  to move to a different site on the substrate, then the time required to jump to this site is:

$$t = t_0 \exp\left(\frac{-E}{k_B T}\right) \quad (2.3)$$

Surface mobility therefore increases with increasing substrate temperature, and consequently, so too does the probability of the film adopting a unique orientation.

For epitaxial growth to occur, the arrival time between atoms should be greater than  $t$ . For the deposition of Ge onto  $\text{CaF}_2$ , for example, it was found that increasing the deposition rate lead to a transition from the film being single crystalline to it being amorphous [21]. The single crystallinity was recovered by increasing the substrate temperature.

In many instances, a growth mode other than that predicted by energy minimum conditions may occur during film growth because supersaturation, induced by high deposition rates and low substrate temperatures, prevents equilibrium from being reached. Forced layer growth can therefore be obtained and Stranski-Krastanov growth can be prevented according to the experimental conditions employed.

For depositions of Fe on Cu, for example, the higher surface energy of Fe compared with Cu indicates that this system should grow by means of island formation. Experimentally, layer by layer growth was obtained by either lowering the substrate temperature or increasing the depositions rate [22]. Such a reduction in adatom mobility can be expected to decrease the crystallographic quality.

The stability of layer by layer growth in all systems decreases as the film thickness is increased [23]. The optimum experimental conditions for the deposition of flat epitaxial films with thicknesses of some tens of monolayers is therefore a compromise between high deposition rates and low substrate temperatures which favour flat films and low deposition rates and high substrate temperatures which favour epitaxy. These conditions can also be expected to be thickness dependent. As no theory can predict these conditions precisely for a given system the scientific approach has to be one of trial and error. To this end, the structural characterisation of films during and after growth is essential.

## 2.4 Thin film characterisation

A complete characterisation of an epitaxial thin film requires knowledge of :

- the crystallinity (crystal orientation, interplanar spacing, grain size and misorientation)
- planarity (film thickness, interface quality, morphology)
- chemical composition (contamination)

Structural characterisation can be divided into two categories ; in-situ characterisation and ex-situ characterisation.

For in-situ techniques, it is essential that the characterisation time be as short as possible so as to limit contamination. For a coherent analysis the contamination limit must be less than 1% of a monolayer. In a vacuum of  $1 \times 10^{-10}$  Torr such contamination will have occurred within 4 minutes. The ideal in-situ characterisation technique corresponds to one with instantaneous acquisition time. In addition instantaneous techniques enable measurements to be made at the same time as the film growth.

Reflection high energy electron diffraction (RHEED) is an ideal in-situ technique from this point of view. It is also extremely surface sensitive and yields information about both the structure and morphology of thin films. It is however more qualitative than quantitative.

Auger analysis is another in-situ technique par excellence. It enables the chemical composition of a film to be determined from one monolayer to some tens of monolayers. It can in principle detect 1% of a monolayer. It is however not instantaneous. The typical acquisition time is about 15 minutes.

Ex-situ analysis can be performed by protecting the film with another protective film prior to its removal from the vacuum chamber. This approach enables many different techniques to be used and leads to a greater knowledge of the structural properties of a given film.

The best ex-situ technique for detailed structural analysis is x-ray analysis. A detailed exploration of the reciprocal space enables the results obtained during RHEED analysis to be quantified. In addition specular X-ray reflectivity enables a precise knowledge of the film thickness and a limited knowledge of the interface roughness to be obtained.

The majority of the structural characterisation performed during this thesis work was done by means of the above three techniques (RHEED, Auger and x-ray analysis). Each technique is discussed in more detail in the following.

### 2.4.1 RHEED

Reflection high energy electron diffraction (RHEED) is an ideal in-situ analysis technique for the monitoring of epitaxial growth. During RHEED analysis a beam of electrons (of 10 keV energy in the present work) is focused onto a film at an angle of incidence of  $3^\circ$ .

It is the reflection geometry used during RHEED that enables qualitative analysis of both the structure and morphology to be performed. This geometry however renders quantitative analysis difficult due to inelastic scattering processes and an insufficient knowledge of the dynamical processes involved.

For 10 keV electrons with an incidence angle of  $3^\circ$  the perpendicular penetration depth of the electron beam is of the order of a few monolayers. Therefore RHEED operated under such conditions is very surface sensitive.

In the usual conditions, where a symmetry axis is perpendicular to the film plane, the perpendicular momentum transfer vector ( $\mathbf{q}_z$ ) is always tangential to the Ewald sphere. Due to the very large radius of the Ewald sphere, Bragg reflections are always observed.

The width of a diffracted beam is inversely proportional to the number of diffracting planes ( $N$ ). For the case of a 3D sample,  $N$  is infinite. The reciprocal lattice map observed on the fluorescent screen would consist of an array of spots, as schematised in figure 2.6a. The distance between the diffraction spots along the two directions of the screen is inversely proportional to the distance between the diffracting planes along the sample normal and in the plane of the sample. The constant of proportionality depends on the distance of the screen from the sample and is called the camera length.

Due to small penetration depth of the electrons during RHEED,  $N$  along the film normal is finite and the diffraction spot therefore tends to infinity along this direction. The diffraction pattern observed on the screen is then composed of a series of streaks, as schematised in figure 2.6b. Information about the lattice parameter along the growth direction is subsequently lost.



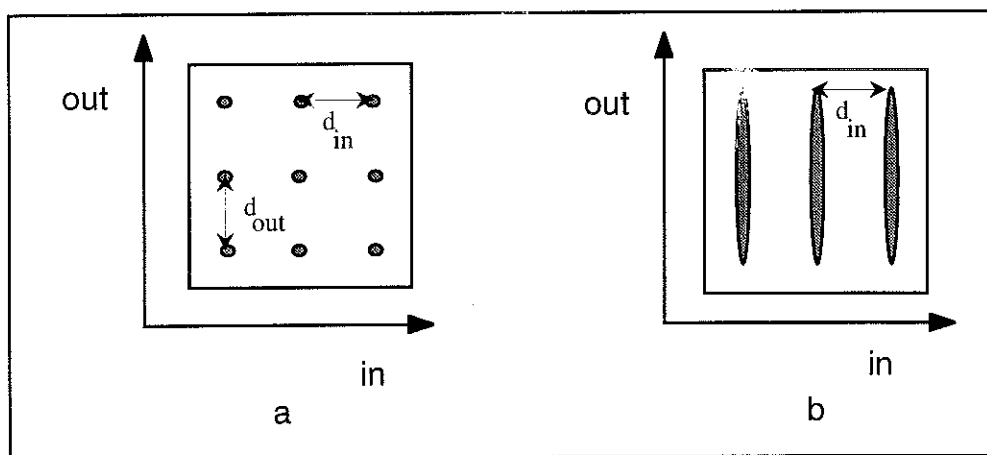


Fig. 2.6 - a - Schematic representation of a 3D (transmitted) diffraction pattern and b - a 2D (reflected) diffraction pattern.

Streaking of a diffraction pattern will only occur for a flat surface (fig. 2.7a). A rough surface will give rise to reflected and transmitted intensities (fig. 2.7b). As the effective number of diffracting planes along the film normal is increased the observed diffraction pattern will be a convolution of 2D and 3D intensities (i.e. streaks with intensity modulations). For the case of very rough surfaces, 2D diffraction is lost altogether and one obtains a pure 3D diffraction pattern. As the coherence length of the electron beam, for  $\lambda = 0.01 \text{ \AA}$ , is of the order of  $100 \text{ \AA}$  then if the in-plane thickness modulations are greater than  $100 \text{ \AA}$ , this will not be observed during RHEED. For example, a film consisting of an island structure, where the width of each island is greater than the coherence length of the electron beam, will yield a 2D diffraction pattern and therefore appear flat.

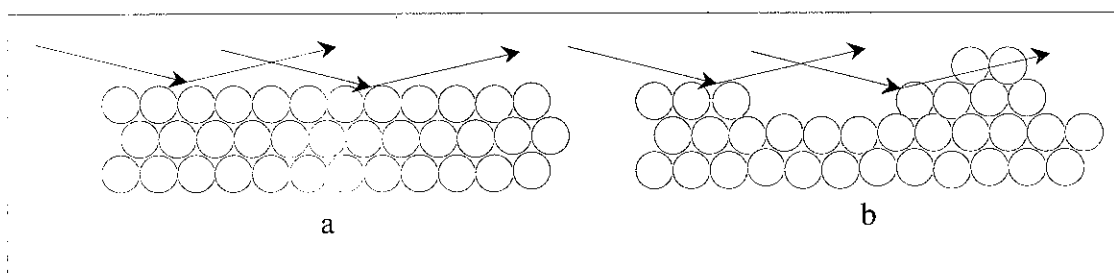


Fig. 2.7 Schematic representation of the influence of surface roughness on the diffraction pattern. a - a perfectly flat surface will give rise to 2D diffraction only; b - a rough surface will induce a transmitted component in the diffracted beam giving rise to 3D diffraction.

In addition to the major structure of the diffraction pattern discussed above, many fine structures are observed in during RHEED analysis.

The propagation of the electron beam in the crystal leads to multiple reflections. These reflections can sometimes be diffracted from other net planes apart from the main diffracting net planes, giving rise to additional diffraction streaks. These additional lines are called Kikuchi lines and are a signature of good crystalline quality.

Faceted surfaces can also be detected during RHEED analysis. Such surfaces give rise to additional diffraction streaks which are oriented at an angle  $\theta$  from the main diffraction streaks where  $\theta$  is directly related to facetting angle.

#### 2.4.2 Auger analysis

Auger analysis is performed by bombarding the sample to be investigated with a beam of electrons, resulting in the occurrence of the emission of an electron whose energy is characteristic of the energy levels from which it came. A scan of the energy spectrum of emitted Auger electrons enables all the elements in the sample to be identified. This experimental technique is called after Pierre Auger who in 1923 explained the physical processes [24].

The events leading up to the emission of an Auger electron are schematised in figure 2.8.

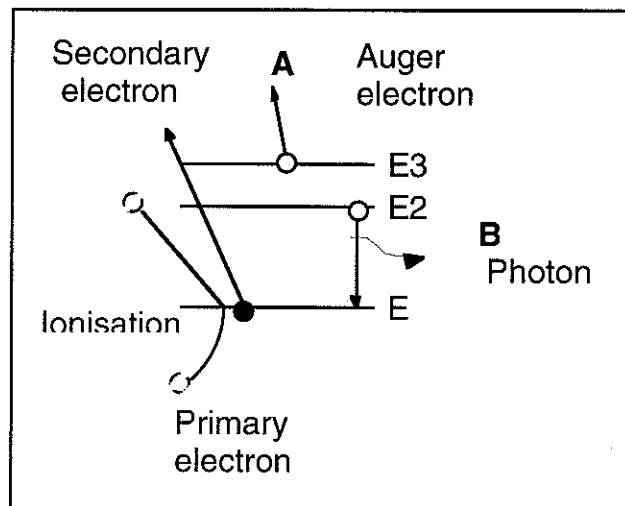


Fig. 2.8 - Schematic principle of the emission of an Auger electron

An incident electron undergoes an in-elastic collision, loses a part of its energy ( $\Delta E$ ) and continues travelling through the film with a slight deviation in its path,  $\Delta\theta = \text{Arc sin } (\Delta E/E)^{-1/2}$ . The transfer of energy results in the emission of an electron (usually referred to as a secondary electron) from an energy level  $E_1$ . The kinetic energy of the secondary electron is given by :

$$E_{se} = \Delta E - E_1 \quad (2.4)$$

After ionisation, the ion relaxes when an electron from a higher energy level,  $E_2$ , fills the vacancy in  $E_1$  created by the emission of the secondary electron. The excess energy is given by:

$$E_{excess} = E_1 - E_2 \quad (2.5)$$

and can result in the occurrence in one of the following:

- a) The emission of a photon X of energy  $E_{excess}$
- b) The emission of a third electron, called the Auger electron, from an energy level  $E_3$  ( $E_3 \geq E_2$ ). The kinetic energy of the Auger electron is given by:

$$E_{Auger} = E_{excess} - E_3 \quad (2.6)$$

and is independent of the incident electron energy. The Auger electron is labelled according to the energy levels involved in the transition, according to X-ray notation, i.e. K, L<sub>1</sub>, L<sub>2</sub>... The relaxation of external energy levels occurs principally by Auger emission, 99% of the time for energy levels less than 1000 eV and 95% for energy levels less than 2000 eV [25].

The effective probe depth during Auger analysis does not depend on the incident electron energy but on the escape depth of the Auger electrons. The escape depth of some elements are shown in figure 2.9.

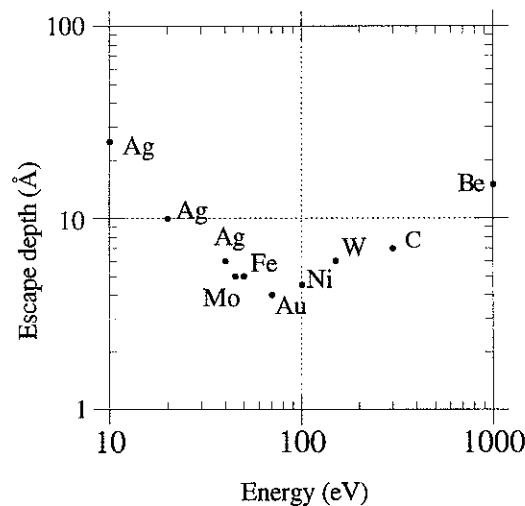


Fig. 2.9 - Escape depth of Auger electrons for some elements as a function of their energy

The Auger electrons of Fe  $L_1$ MM transitions, for example have energies of 500 eV. Their escape depth is thus determined to be of the order of 10 Å, which corresponds to a probe of five atomic layers from the surface.

### 2.4.3 X-ray analysis

Three different geometries are usually employed for the analysis of epitaxial thin films by X-rays, as schematised in figure 2.10. These geometries correspond to out-of plane diffraction (OPD) (fig. 2.10a), specular reflection (SR) (fig. 2.10b) and grazing incidence diffraction (GID) (fig. 2.10c).

The difference in the three geometries is the direction of the momentum transfer vector ( $\mathbf{q}$ ) and the angle of incidence.

For out of plane diffraction  $\mathbf{q}$  lies along the film normal and the angle of incidence is large and varied during acquisition ( $\theta - 2\theta$ ). In this geometry the diffracting planes are parallel to the film surface. For ultra-thin films, the number of diffracting planes is small and therefore this geometry can only be applied to relatively thick films (typically 20 monolayers or more). This geometry enables the epitaxial plane to be determined.

One of the interesting peculiarities of out plane diffraction is that due to the finite film thickness, oscillations can be observed in the intensity of the Bragg peak, if the planarity of the film is sufficiently good.

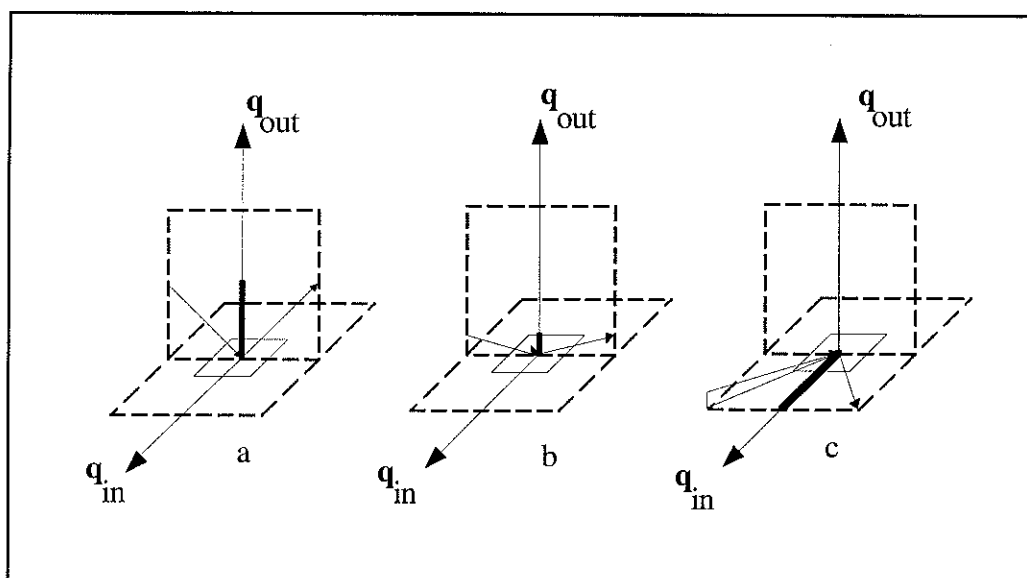


Fig. 2.10 - Schematic representation of the three main geometries employed for the analysis of thin films by X-rays : a- out of plane diffraction, b - specular reflection and c - grazing incidence diffraction.

For the other two geometries (SR and GID), the angle of incidence is small. For angles of incidence ( $\alpha$ ) of some tens of degrees the penetration depth of the x-rays into the film is of the order of some tens of a  $\mu\text{m}$ . As  $\alpha$  decreases the penetration depth decreases, as shown in figure 2.11 for  $\text{Al}_2\text{O}_3$ . For  $\alpha \leq \alpha_c$ , total reflection is observed and the penetration depth is determined by the penetration depth of the evanescent wave (fig. 2.11).

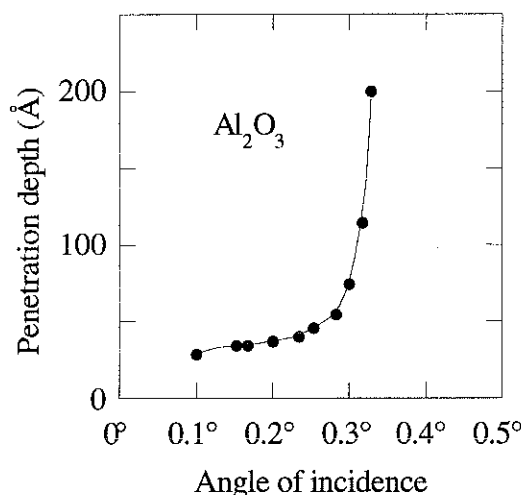


Fig. 2.11 - The penetration depth of x-rays as a function of incidence angle for  $\text{Al}_2\text{O}_3$  substrates (from [26]).

In the same way that thickness oscillations are observed around a Bragg peak, thickness oscillations are observed around the total reflective peak. SR analysis involves performing a very fine scan around this peak. The oscillation period is inversely proportional to the film thickness. For films composed of different films, i.e.  $\text{W} / \text{Fe} / \text{W}$ , then four oscillation periods will be observed corresponding to the total thickness and the thickness of each layer. For the case of a rough surface then reflection will occur away from  $\mathbf{q}_{\text{out}}$ , i.e. non specular reflection. Data analysis is performed during SR by modelling the refractive index as a function of film depth and fitting the calculated reflections to the experimental findings. For a film containing  $N$  individual films (i.e.  $N = 3$  for  $\text{W} / \text{Fe} / \text{W}$ ) then there are  $3N + 2$  fitting parameters, corresponding to refractive index ( $n$ ), thickness ( $d$ ) and thickness modulations ( $\partial d$ ) for each film plus  $n$  and  $\partial d$  for the substrate.

For grazing incidence diffraction, the angle of incidence is as small as possible and  $\mathbf{q}$  lies in the plane of the sample (fig. 2.7c). It therefore enables net planes perpendicular to the film plane to be explored by performing in-plane Bragg scans. It is the in-plane analogue of out of plane diffraction. As the number of diffracting planes in this geometry is not thickness dependent, this geometry can be applied to very thin films. The width of the diffraction peaks ( $\Delta 2\theta$ ) enables the number of coherently scattering planes and hence the in-plane crystallite size ( $D$ ) to be estimated by applying the Scherrer equation [27]:

$$D = \frac{\lambda}{\Delta 2\theta \cos \theta} \quad (2.7)$$

where  $\Delta 2\theta$  is the FWHM in radians of  $2\pi$ . In addition, the average orientation spread between these crystallites ( $\Delta D$ ) can be estimated by performing a rocking curve about the Bragg peak maximum. The peak width,  $\Delta \pi$ , of the rocking curve, enables  $\Delta D$  to be determined directly, after having corrected for the crystallite size broadening,  $(\Delta \pi)_s$  given by the following formula:

$$(\Delta \pi)_s = \frac{\lambda}{2D \sin \theta} \quad (2.8)$$

It must be noted that variations in interplanar spacing and instrumental imperfections will also contribute to line broadening effects. The values of  $D$  and  $\Delta D$  can therefore be taken to be minimum and maximum respectively.

Diffraction analysis can also be performed in geometries where  $\mathbf{q}$  lies in directions between the in-plane direction and the out of plane direction. This enables complicated film structures, such as intermetallic alloys, to be determined [28].

## 2.5 References

---

- [1] H. Lassen,  
Physik. Z 35 (1934) 172.
- [2] H. Lassen and L. Bruck,  
Ann. Physik, 22 (1935) 233.
- [3] G.L. Bailey,  
Proc. Royal Soc. London, 50 (1938) 63.
- [4] L. Royer,  
Bull. Soc. Franc. Mineral., 51 (1928) 7.
- [5] J. G. Wright,  
Philos. Mag. 24 (1971) 217.
- [6] V. L. Moruzzi, P.M. Marcus, K. Schwarz and P. Mohn,  
Phys. Rev. B34 (1986) 1784.
- [7] G. Prinz,  
Phys. Rev. Lett., 54 (1985) 1051.
- [8] H. Homma, K.Y. Yang and Ivan K. Schuller,  
Phys. Rev. B36 (1987) 9435.
- [9] Z. Nishiyama,  
Sci. Rep. Tohoku Univ. 23 (1934) 638.
- [10] G. Wasserman,  
Arch. Eisenhüttenw., 126 (1933) 647.  
  
Z. Nishiyama,  
Sci. Rep. Tohoku Univ. 23 (1934) 638.
- [11] J. Kwo, M. Hong, and S. Nakahara,  
Appl. Phys. Lett., 49 (1986) 319.
- [12] G. Kurdjumov and G. Sachs,  
Z. Phys., 64 (1930) 325.
- [13] R. Ramirez, A. Rahman, and Ivan K. Schuller,  
Phys. Rev. B30 (1984) 6208.

- 
- [14] see for example L. Z. Mezey and J. Giber,  
Surf. Sci., 117 (1982) 220.
- [15] J. M. Blakely,  
“Introduction to the properties of crystal surfaces”, Pergamon Press, Oxford, 1973.
- [16] E. Bauer,  
Z. Kristallogr., 110 (1958) 372.
- [17] F. C. Frank and J. H. van der Merwe,  
Proc. Roy. Soc. Lon., A198 (1949) 205.
- [18] M. Volmer and A. Weber,  
Z. Phys. Chem., 119 (1926) 277.
- [19] D. J. Eaglesham and M. Cerullo,  
Phys. Rev. Lett., 64 (1990) 1943.
- [20] I. N. Stranski and V. L. Krastanov,  
Akad. Wiss. Litt. Mainz Math.-Natur. KI 116 (1939) 797.
- [21] B.W. Sloope and C.O. Tillier,  
J. Appl. Phys., 36 (1965) 3174.
- [22] U. Gradmann and P. Tillmanns,  
Phys. Stat. Solidi, A44 (1977) 539.
- [23] M. Tikhov and E. Bauer,  
Surf. Sci. 232 (1990) 73.
- [24] P. Auger,  
C.R. Acad. Sci., 177 (1923) 169.
- [25] R. Weissman and K. Muller,  
Surf. Sci. Rep., 105 (1981) 251.
- [26] M. Brunel and F. de Bergevin,  
Acta. Crista, A42 (1986) 299.



- 
- [27] C.S. Barret and T.B. Massalski,  
"Structure of metals", Mc Graw-Hill publishers, New York, 1966.
- [28] F. Robaut, N. Cherief, P. Mikuluk, O.F.K. Mc Grath, T. Baumbach and D. Givord,  
to be published.



# CHAPTER THREE

## DEPOSITION AND STRUCTURAL CHARACTERISATION OF EPITAXIAL METALLIC FILMS

### Table of contents to chapter 3

3.1 Introduction	61
3.2 Al <sub>2</sub> O <sub>3</sub> substrates	61
3.3 W / Al <sub>2</sub> O <sub>3</sub>	62
3.3.1 Experimental conditions	63
3.3.2 In-situ analysis	63
3.3.3 Ex-situ analysis	64
3.3.4. Discussion	67
3.4 Fe / W (110) / Al <sub>2</sub> O <sub>3</sub> (11 $\bar{2}$ 0)	71
3.4.1 Experimental conditions	72
3.4.2 In-situ analysis	72
3.4.3 Ex-situ analysis	79
3.4.4 Discussion	83
3.5 Rare earth / Fe bi-layers	85
3.5.1 Experimental conditions	85
3.5.2 In-situ analysis	85
3.5.3 Ex-situ analysis	91
3.5.4 Concluding remarks	93
3.6 References to chapter three	94

## RÉSUMÉ

La technique du DLP a été utilisée pour épitaxier les trois systèmes suivants: W / Al<sub>2</sub>O<sub>3</sub>, W / Fe / W et Gd / Fe. La croissance de W sur Al<sub>2</sub>O<sub>3</sub> est étudiée en utilisant trois orientations de Al<sub>2</sub>O<sub>3</sub> : (0001), (1 $\bar{1}$ 00) et (11 $\bar{2}$ 0) pour lesquelles nous avons observé les relations d'épitaxie suivantes: W (111) // Al<sub>2</sub>O<sub>3</sub> (0001), W (112) // Al<sub>2</sub>O<sub>3</sub> (1 $\bar{1}$ 00) et W (110) // Al<sub>2</sub>O<sub>3</sub> (11 $\bar{2}$ 0). Les raies de diffraction obtenues par analyse RHEED pour des conditions optimales de dépôt suggèrent que la croissance soit bi-dimensionnelle. La qualité des couches de W(110) est systématiquement meilleure que celles de W(112) et W(111); ceci motive le choix de W (110) comme couche tampon pour la suite de notre travail. Nous présentons une étude détaillée de la structure de W (110). Notons, en particulier, que l'épitaxie de W peut être expliquée par l'occupation des sites octaédraux vacants de Al<sub>2</sub>O<sub>3</sub>. D'autre part, dans certains cas, la couche de W (110) est maclée. L'évolution des propriétés structurales de Fe (110) dans W (110) / Fe (110) / W (110) est analysée en fonction de la température du substrat et de l'épaisseur de la couche de Fe. Une croissance épitaxiale de Fe (110) est observée pour des températures du substrat entre 300 K et 1100 K. La morphologie de la couche de Fe dépend fortement de la température du substrat ( $T_s$ ). Pour  $T_s < 500$  K, l'analyse RHEED montre que la couche est rugueuse à l'échelle atomique. Pour  $T_s > 500$  K, selon l'analyse RHEED, les couches sont planes à une échelle inférieure à 100 Å, mais il résulte de l'analyse Auger, ainsi que de l'analyse par microscopie électronique à balayage, que les couches sont composées d'îlots dont la taille et la densité augmentent lorsque  $T_s$  diminue. La température optimale de dépôt pour ces couches est donc  $T_s = 500$  K. Pour des dépôts à  $T_s = 500$  K, les paramètres de maille, la densité de dislocations interfaciales, la taille et la désorientation des cristallites évoluent continûment lorsque l'épaisseur de la couche augmente. La croissance épitaxiale de Gd (0001) sur Fe (110) a été obtenue pour la première fois. Quand la température du substrat est élevée le Gd s'épitaxie sur le Fe mais la couche de Gd est décomposée en îlots. Au contraire, pour des dépôts à température ambiante, la couche de Gd est plane mais elle ne cristallise pas. En déposant la première monocouche de Gd à 500 K et en déposant la suite à 300 K, il est néanmoins possible d'élaborer des couches épitaxiées qui sont planes. La relation d'épitaxie correspond à la relation de Nishiyama-Wasserman.

## SUMMARY

The technique of PLD was used to grow three epitaxial systems which are :W on  $\text{Al}_2\text{O}_3$  , W / Fe / W and Gd / Fe. The epitaxial growth of W on  $\text{Al}_2\text{O}_3$  was studied by employing three different orientations, namely (0001),  $(1\bar{1}00)$  and  $(11\bar{2}0)$ . The following epitaxial relations were deduced: W (111) //  $\text{Al}_2\text{O}_3$  (0001), W (112) //  $\text{Al}_2\text{O}_3$   $(1\bar{1}00)$  and W (110) //  $\text{Al}_2\text{O}_3$   $(11\bar{2}0)$ . In all cases the RHEED patterns showed streaking for deposition at optimum conditions suggesting 2D growth for large coverages. The quality of W(110) films was found to be systematically better than W(112) and W (111) and it was therefore determined to be the best system for use as a buffer layer. A detailed study of W (110) was performed. The epitaxy was explained in terms of W atoms sitting into vacant octahedral sites of  $\text{Al}_2\text{O}_3$ . Twinning of W (110) was observed in some cases. The evolution of the structural properties of Fe (110) in W (110) / Fe (110) / W (110) tri-layers is analysed as a function of substrate deposition temperature and as a function of Fe film thickness. Epitaxial growth of Fe on W is obtained for all substrate temperatures from 300 K to 1100 K. The film morphology is found to be critically dependent on the substrate temperature. For substrate temperatures less than 500 K, RHEED analysis suggests that the films are rough on an atomic scale. For depositions at  $T > 500$  K, RHEED analysis suggests that the films are flat on a scale up to 100 Å, whereas Auger and scanning electron microscopy analysis suggests that the films are formed of islands, the size and density of which decreases as the substrate temperature increases. The optimum deposition temperature of Fe on W is therefore determined to be 500 K. For depositions at 500 K, the lattice parameter, the interface dislocation density, the minimum crystallite size and the maximum crystallite misorientation continuously evolve as the film thickness increases. The epitaxial growth of Gd on Fe was realised for the first time. Optimum film quality is obtained by depositing a first seed monolayer of Gd on Fe (110) at 500 K and the remaining layers at 300 K. The epitaxial orientation of Gd is found to be (0001) and the epitaxial relationship is found to follow the well known Nishiyama-Wasserman relationship.



### 3.1 Introduction

Epitaxial growth, by PLD, and structural characterisation of thin metallic films is discussed in this chapter. The chapter is divided into four main sections.

All depositions discussed here were performed on sapphire ( $\text{Al}_2\text{O}_3$ ) substrates and in the first section (3.2) the crystallinity of  $\text{Al}_2\text{O}_3$  is reviewed followed by a brief description of the preparation of the substrates prior to deposition.

In the second section (3.3) the epitaxial deposition and structural characterisation of W on  $\text{Al}_2\text{O}_3$  is described.

In the third section (3.4), Fe films deposited on W (110) /  $\text{Al}_2\text{O}_3$  are discussed.

Finally, in the last section (3.5) the growth of rare earth metals (Gd and Tb) on Fe (110) / W (110) /  $\text{Al}_2\text{O}_3$  is discussed.

### 3.2 $\text{Al}_2\text{O}_3$ substrates

$\text{Al}_2\text{O}_3$  has a melting point of 2355 K and a hardness of 8.8 on the Moh's scale. It is thus suitable for high temperature depositions and ensures good mechanical stability. It is diamagnetic with a susceptibility per  $\text{cm}^3$  of  $-0.23 \times 10^{-6}$ .

$\text{Al}_2\text{O}_3$  crystallises in a hcp structure with the  $\text{O}^{2-}$  ions (radius 1.4 Å) forming the hcp array with a stacking sequence of ABAB and the  $\text{Al}^{3+}$  ions (radius 0.53 Å) occupying two thirds of the octahedral sites (fig. 3.1). The stacking sequence of the  $\text{Al}^{3+}$  ions is abc. The total stacking sequence is therefore AaBbAcBaAbBc. One third of the octahedral sites are vacant. The lattice parameters are  $a = 4.759 \text{ Å}$  and  $c = 12.991 \text{ Å}$ . The c to a ratio is 2.73 compared to 2.828 for an ideal hcp structure.

Good quality single crystalline commercial substrates are readily available. Three orientations were used, (0001), (1 $\bar{1}$ 00) and (11 $\bar{2}$ 0). Prior to deposition the substrate orientation was verified by Laue diffraction. They were de-greased in an ultra-sonic bath. Chemical etching was performed with the following solution;  $\text{H}_2\text{SO}_4 + \text{H}_2\text{O}_2 + \text{H}_2\text{O}$ . The substrates were then rinsed with de-ionised water and then placed in the vacuum chamber where they were annealed at 1100 K for 60 minutes. The crystallinity and contamination was then verified by RHEED and Auger analysis.

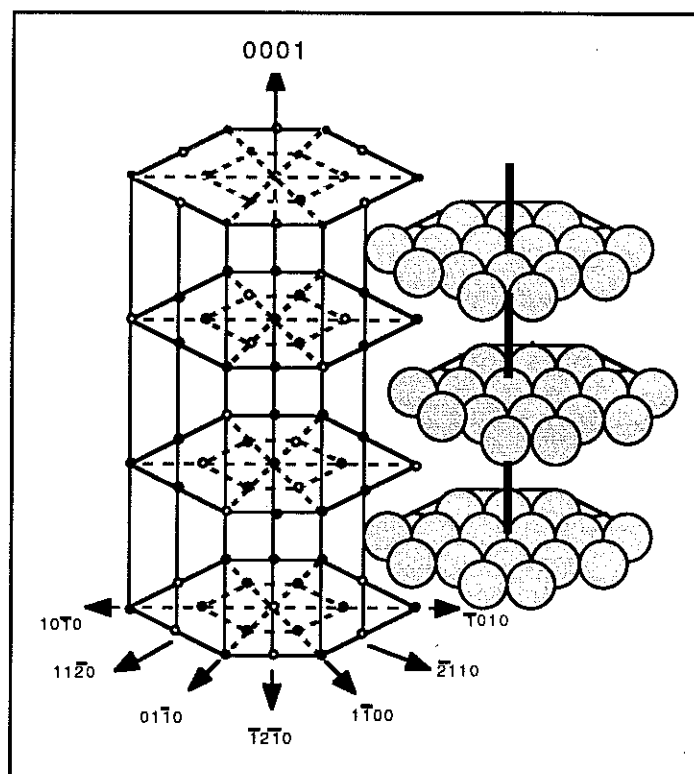


Fig. 3.1 -  $\text{Al}_2\text{O}_3$  half unit cell along the  $c$  axis . Small black spheres :  $\text{Al}^{3+}$  , small white circles: vacant octahedral sites and large shaded spheres:  $\text{O}^{2-}$  . For clarity the O layers are displaced to the right of the Al layers.

### 3.3 W / $\text{Al}_2\text{O}_3$

The epitaxial deposition of refractory metal films on ceramic substrates has been widely studied [1],[2] . Due to the inert nature of the refractory metals, they enable good quality epitaxial films to be prepared and they serve as excellent buffer layers for the subsequent deposition of other metals [3],[4].

From the point of view of epitaxial growth, Nb depositions on  $\text{Al}_2\text{O}_3$  is the best system due to an excellent matching of lattice parameters and thermal properties [5]. From the point of view of using such depositions as buffer layers for the subsequent deposition of transition metals, W is a better choice as it has a higher surface energy compared with Nb.

In view of the above we conducted a study of the epitaxial deposition of W on  $\text{Al}_2\text{O}_3$ . Epitaxial depositions of W had not been studied prior to this work, with the exception of W (001) on  $\text{Al}_2\text{O}_3$  ( $1\bar{1}02$ ) [6]. The objectives of the study were threefold. Firstly, to investigate the possibility of applying the technique of pulsed laser deposition to the epitaxial deposition of metals. Secondly, to isolate the experimental parameters (substrate orientation, deposition temperature, film thickness) necessary to optimise this



system as a buffer layer. Finally, to study the epitaxial mechanism of the optimum system.

### 3.3.1 Experimental conditions

W targets of 15 mm diameter were cut by electro-erosion from W foils, and were fixed onto the target holder by high vacuum glue (Torr-seal by Varian). The targets were degassed in an oven at 500 K for one hour and then entered into the deposition chamber.

The targets were etched by laser ablation until the evaporated plume was found to be contaminant free, as investigated by Auger analysis.

In order to determine the optimum laser conditions, W depositions were performed on glass substrates at varying laser conditions. The film quality was subsequently investigated by SEM. Depositions performed at high laser fluences were found to be contaminated by  $\mu\text{m}$  sized droplets of W. The droplet density was found to decrease as the fluence was decreased and for depositions close to the threshold droplet-free films were obtained.

The morphology of the target was also found to influence the film quality. As the target use increased its morphology deteriorated and the deposited films were found to be contaminated by W particulates of irregular shape. In addition the impact of these particulates on the substrate created film damage in the form of holes. This problem was eliminated by rastering the target in front of the laser beam and by regularly repolishing the target surface.

The optimum laser fluence was thus determined to be  $20 \text{ Jcm}^{-2}$  yielding a deposition rate of  $2 \text{ \AA} \cdot \text{min}^{-1}$  as measured by a quartz microbalance.

For epitaxial depositions the  $\text{Al}_2\text{O}_3$  substrates were placed at 10 cm in front of the target and were heated up to 1100 K during deposition. In-situ analysis was performed by RHEED and Auger analysis.

### 3.3.2 In-situ analysis

Three different orientations of  $\text{Al}_2\text{O}_3$  were used, namely (0001), (1 $\bar{1}$ 00) and (11 $\bar{2}$ 0). The following epitaxial relations were deduced from RHEED analysis:

- W (111) //  $\text{Al}_2\text{O}_3$  (0001)
- W (112) //  $\text{Al}_2\text{O}_3$  (1 $\bar{1}$ 00)
- W (110) //  $\text{Al}_2\text{O}_3$  (11 $\bar{2}$ 0)

These epitaxial relationships are the same as those found for Nb deposited on  $\text{Al}_2\text{O}_3$  [3]. In all cases the RHEED patterns showed streaking for deposition at optimum conditions suggesting 2D growth for large coverages (see below). The quality of the RHEED patterns of the W(110) films was found to be systematically better than W(112) and W(111). This can be attributed to the fact that the (110) plane of a bcc structure is the most dense and therefore the one of minimum surface energy. W(110) on  $\text{Al}_2\text{O}_3$  ( $11\bar{2}0$ ) was therefore determined to be the best system for use as a buffer layer and a detailed study was subsequently pursued.

Films deposited on ( $11\bar{2}0$ ) substrates held at temperatures between 300 K and 700 K were found from RHEED analysis to be polycrystalline. The RHEED patterns were characteristic of crystallites oriented at random in the film plane with a  $[1\bar{1}0]$  orientation perpendicular to the film plane. For substrate temperatures above 700 K and up to 1100 K the films were single crystalline with a (110) orientation. For film thicknesses less than approximately 20 Å the RHEED patterns consisted of diffraction spots indicative of 3D growth. This initial 3D growth can be attributed to a surface roughness of the substrate due to acid etching [7]. A gradual transition to streaking along the growth direction was observed with increasing film thickness. The intensity and sharpness of these patterns was found to increase up to approximately 100 Å (fig. 3.2). No further improvement was found for thicker films.

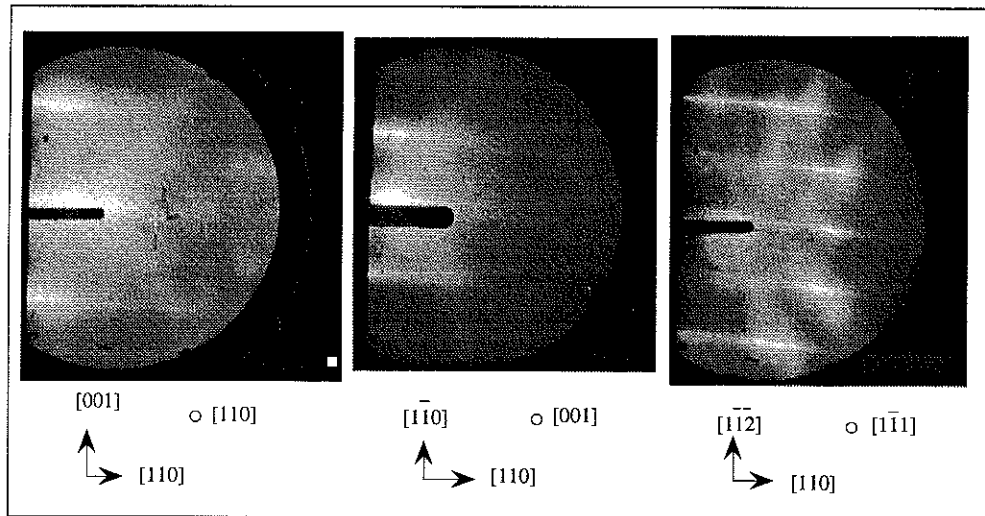


Fig. 3.2 - RHEED patterns for a 300 Å W(110) film taken with the electron beam parallel to the main in-plane crystallographic axes.

### 3.3.3 Ex-situ analysis

Symmetrical X-ray diffraction was performed ex-situ using  $\text{CuK}\alpha$  ( $\lambda = 1.54$  Å) radiation. The observed reflections were  $\text{Al}_2\text{O}_3$  ( $11\bar{2}0$ ) and ( $22\bar{4}0$ ) {equivalent to (110) and (220) respectively} and W(110) and (220), as shown in figure 3.3a, thus confirming the epitaxial relations deduced from the RHEED patterns. The values of the

W Bragg angles correspond to those expected for bulk W, thus indicating that the films are essentially un-strained at all thicknesses studied (100 Å - 500 Å). Intensity oscillations were found at the foot of the W (110) reflection (fig. 3.3b), indicative of good quality crystallinity. In a detailed analysis performed separate to this work [8], the W (110) reflection was found not to be perfectly symmetrical, from which it was deduced that the W (110) plane is inclined at 0.04° with respect to the Al<sub>2</sub>O<sub>3</sub> (11 $\bar{2}$ 0) plane.

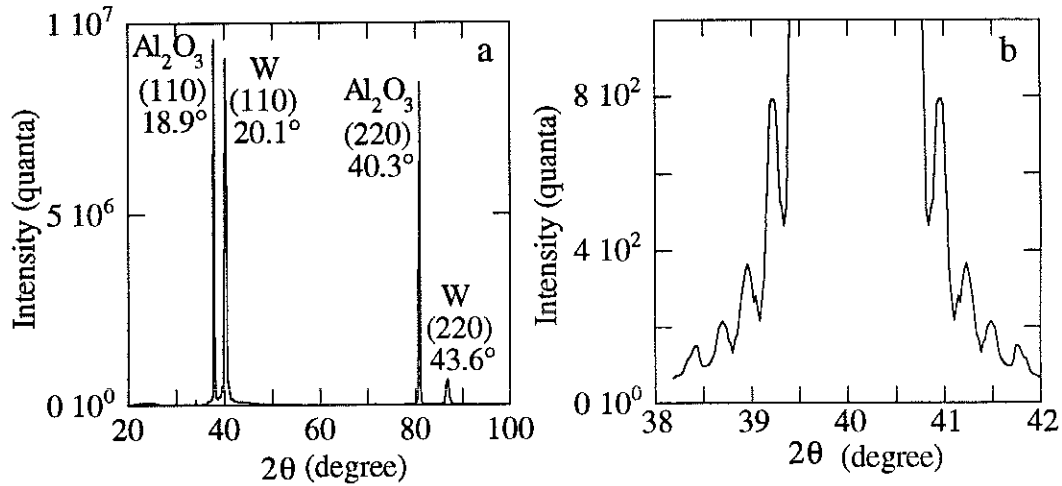


Fig. 3.3a - Symmetrical diffraction pattern of a 300 Å W (110) film and 3.3b - close up of the foot of the W (110) peak.

The in-plane crystallinity was also analysed by grazing incidence diffraction (GID) (angle of incidence = 0.5°) by performing  $\theta$ -2 $\theta$  scans along the [1 $\bar{1}$ 0] and [002] directions. In all samples measured, the FWHM of both directions, were found to be 0.27° - 0.30°, from which in-plane isotropic grain sizes of 18.6 nm - 16.8 nm were deduced. The misorientation of these in-plane crystallites, as measured from the FWHM of  $\omega$ -scans ( $\omega$  = rotation about film normal) was found to be typically 0.9°- 1.2°. The films were also found to be unstrained in-plane for all thicknesses studied (10 nm - 50 nm).

The in-plane epitaxial relations were also deduced from GID. In a series of examined films two epitaxial relations were observed:

Case A:            - W [1 $\bar{1}$ 1] // Al<sub>2</sub>O<sub>3</sub> [0001]  
                       - W [ $\bar{1}$ 12] // Al<sub>2</sub>O<sub>3</sub> [1 $\bar{1}$ 00]

and                Case B:            - W [1 $\bar{1}$  $\bar{1}$ ] // Al<sub>2</sub>O<sub>3</sub> [0001]  
                       - W [1 $\bar{1}$ 2] // Al<sub>2</sub>O<sub>3</sub> [1 $\bar{1}$ 00]

These relations are schematised in figure 3.4a and 3.4b.

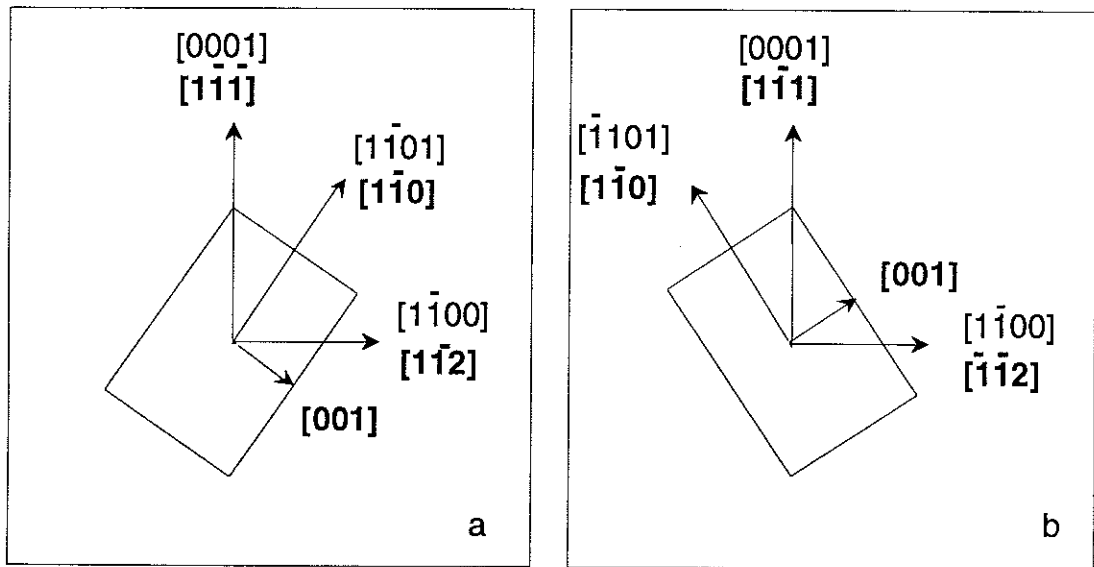


Fig. 3.4 - For W (110) films deposited on  $\text{Al}_2\text{O}_3$  two in-plane epitaxial relationships were found as schematised in a and b. The  $\text{Al}_2\text{O}_3$  axes are shown by plain numerals and the W axes are shown by bold numerals.

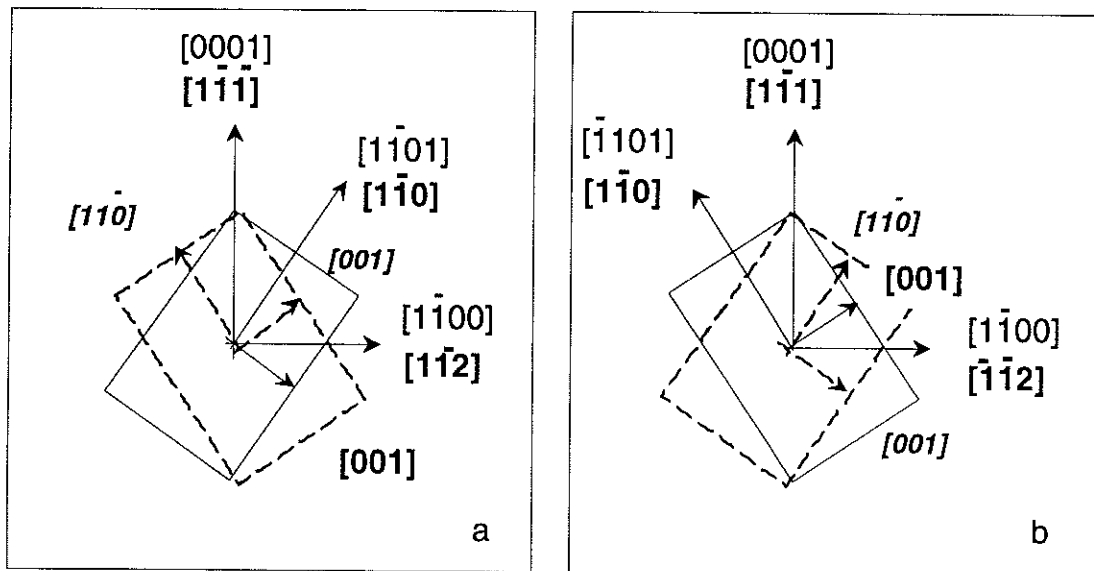


Fig. 3.5 - In some samples both epitaxial relationships were found in the same sample (twinning). The twinned configuration for case Aepitaxy is shown in figure a and that for case B in figure b. The minor population in both cases is shown by the dashed lines with the corresponding minor axes shown in italics.

Finally, in some samples two epitaxial arrangements were found in the same sample (twinning). In general a major and minor population was observed in twinned samples. For case A epitaxy the major population was found to be  $W [1\bar{1}2] // Al_2O_3 [1\bar{1}00]$  and the minor was  $W [\bar{1}12] // Al_2O_3 [1\bar{1}00]$  (fig. 3.5a) and for case B epitaxial relation the major population was found to be  $W [\bar{1}12] // Al_2O_3 [1\bar{1}00]$  and the minor population was found to be  $W [1\bar{1}2] // Al_2O_3 [1\bar{1}00]$  (i.e. the reverse for case A epitaxy (fig. 3.5b)).

The minor population of either case was not observed during RHEED analysis. It was observed by GID where two  $(1\bar{1}0)$  peaks were found at an angle of  $\omega = 110^\circ$  or  $\omega = 70^\circ$  from each other. In the example shown in figure 3.6, the relative populations are 80:20.

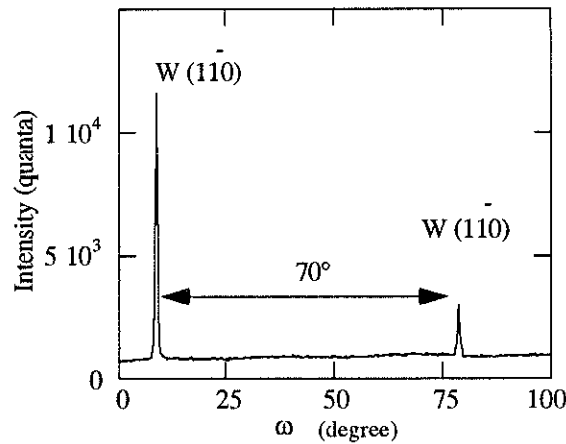


Fig. 3.6 - Grazing incidence diffraction (angle of incidence  $0.5^\circ$ ) spectrum of a twinned  $W (110)$  film showing two  $(1\bar{1}0)$  reflections at  $\omega = 70^\circ$  apart. The angle  $\omega$  corresponds to a rotation about the film normal.

### 3.3.4. Discussion

The existence of two epitaxial relationships is curious and in an attempt to understand this phenomenon Laue diffraction was performed on all films after deposition. For all films which were found to grow according to type A epitaxy a Laue pattern as shown in figure 3.7a was obtained whereas for all films which were found to grow according to type B epitaxy the pattern in figure 3.7b was obtained. By comparing 4.6a with 4.6b it can be seen that they are mirror images of each other. This arises due to the fact that the same indexation is used for planes which are mirror images of each other. The choice of plane for film deposition was determined by the substrate which was polished by the supplier. The difference between the two faces of the substrate is the orientation of the vacant octahedral sites in Al planes which are parallel to the  $[1\bar{1}01]$  direction as can be seen by comparing figure 3.7a with 3.7b.

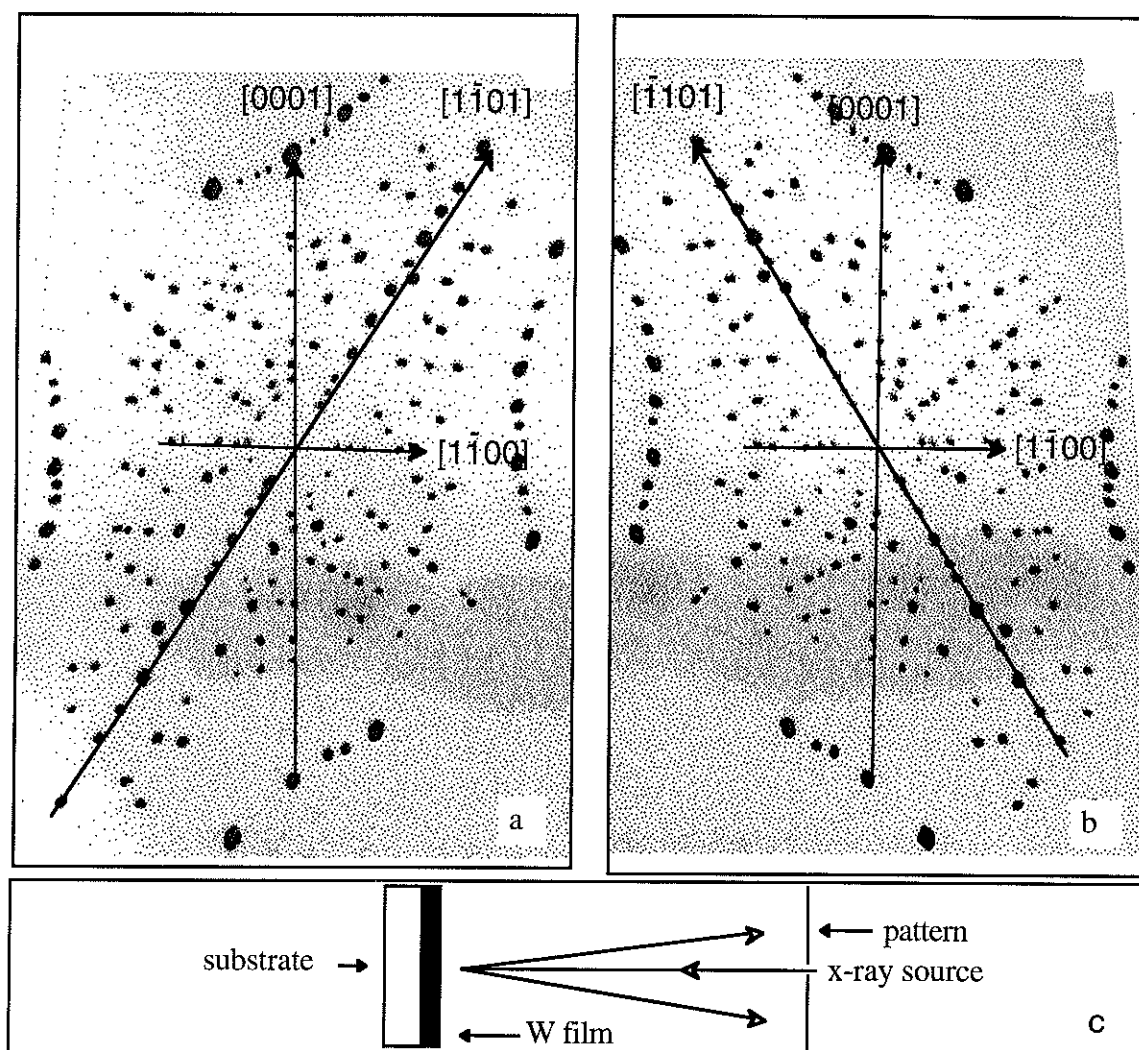


Fig. 3.7 - Laue diffraction patterns obtained for all films of type A epitaxy (a) and type B epitaxy (b). The geometrical orientation of the substrate and film with respect to the x-ray beam and plate is shown in c.

The orientation of the W lattice on the  $\text{Al}_2\text{O}_3$  lattice as deduced from grazing incidence diffraction is shown in figures 3.8a and 3.8b. Comparison of the two figures shows that in both cases the  $[1\bar{1}0]$  axis of W is parallel to the  $\text{Al}_2\text{O}_3$  axis containing the vacant octahedral sites. This suggests that the  $(11\bar{2}0)$  termination plane is an Al plane. Energy calculations for the termination plane are not available for the  $(11\bar{2}0)$  plane. Calculations for the  $(0001)$  plane indicate that an Al termination plane is the one of minimum energy [9].

This observation suggests that the vacant octahedral sites determine the epitaxial orientation which occurs through a W atom sitting into a vacant octahedral site, as one would expect from electronegativity considerations. However our hypothesis cannot account for the position of the W atom at the centre of the bcc unit cell.

The observation of twinning is difficult to explain. However, in twinned films, as the orientation of the major population corresponded to the one expected for the substrate face employed, it appears that the existence of the minor population is not due to two degenerate epitaxial relationships. Twinning has also been observed in other refractory metals deposited on  $\text{Al}_2\text{O}_3$ , for example Nb [10] and Mo [11].

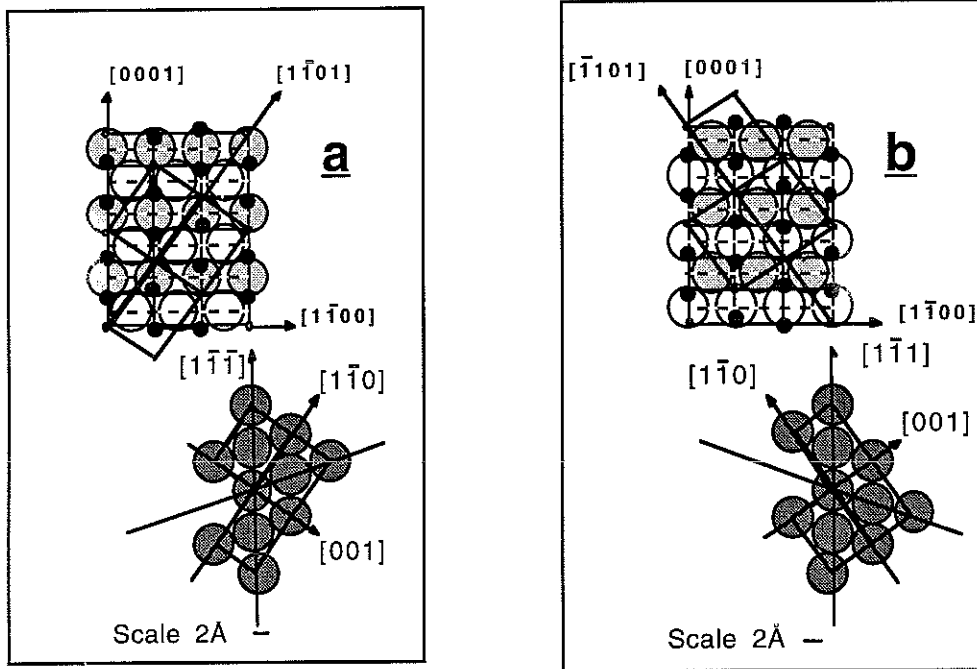


Figure 3.8a and 3.8b Schematic representation of the two faces of an Al termination  $(11\bar{2}0)$  plane showing the epitaxial arrangement of W thereon. The Al atoms are shown as black circles. The underlying two rows of O atoms are shown as large white open circles and large shaded circles respectively. The vacant octahedral sites are shown as small white circles. Figure 3.8a corresponds to the epitaxial relations described as case A in the text and figure 3.8b corresponds to the epitaxial relations described as case B in the text.

Having established the geometrical arrangement of the W lattice on the  $\text{Al}_2\text{O}_3$  lattice it is interesting to address the problem of misfit accommodation. All films studied were found to have bulk W lattice parameters to within experimental error. The W (110) lattice is a rectangular one of dimensions  $4.46 \text{ \AA} \times 3.16 \text{ \AA}$  ( $a \times \sqrt{2}a$ ). It sits into a rectangle on the  $\text{Al}_2\text{O}_3$   $(11\bar{2}0)$  plane of dimensions  $4.1 \text{ \AA} \times 5.1 \text{ \AA}$ . The misfit along the W  $[001]$  axis is therefore 9.7 % and 12.5 % along the W  $[110]$  axis. The existence of un-strained films can therefore be explained by supposing that misfit dislocations are formed at the interface. From geometrical considerations the misfit period along the  $[110]$  axis should be 5 to 6 atomic rows, as shown in figure 3.9. Recent TEM observations on these films have confirmed the existence of periodic dislocations at the interface [12].

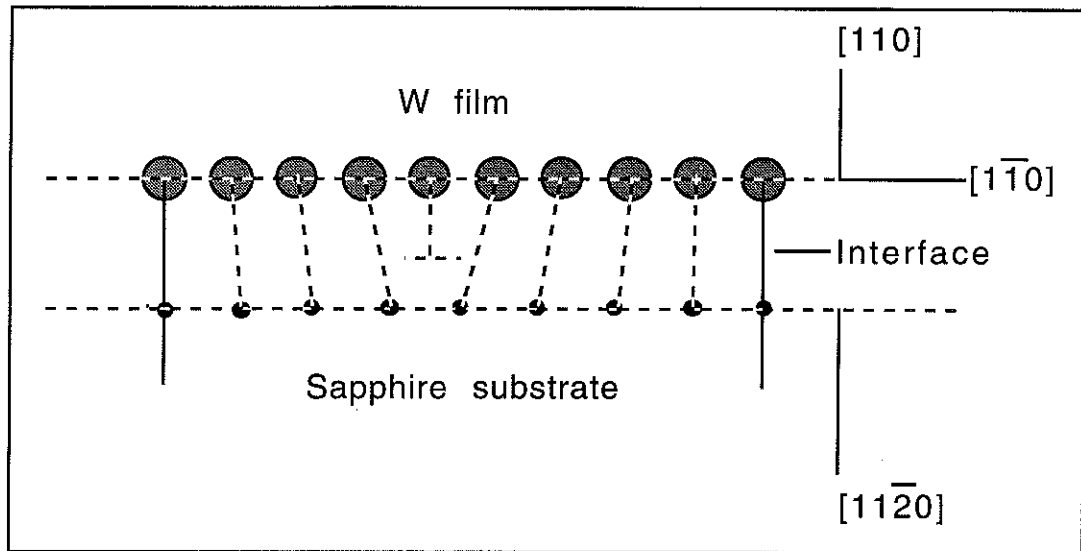


Fig. 3.9 - A possible misfit dislocation along the W  $[1\bar{1}0]$ . The figure shows an extra W row of atoms every five to six atomic layers.



### 3.4 Fe / W (110) / Al<sub>2</sub>O<sub>3</sub> (11 $\bar{2}$ 0)

The epitaxial growth of Fe films has been extensively studied in the recent past. The various substrates used can be divided into four classes and specific features of the resulting epitaxy can be attributed to each class of substrate, as shown in the following :

1. Non metallic substrate, ex. GaAs [13], MgO and Al<sub>2</sub>O<sub>3</sub> [14].

- interface chemical reaction
- possible layer by layer growth

2. Large lattice parameter fcc metals ( $a = 4\text{\AA}$ ), ex. Ag [15] and Au [16].

- bcc Fe
- small misfit
- island growth

3. Small lattice parameter fcc metals ( $a < 4\text{\AA}$ ) , ex. Cu [17]

- fcc Fe
- complex growth mode

4. Refractory metals, ex. W [18] and Mo [19].

- bcc Fe
- large misfit
- layer by layer growth

The above analysis indicates that for bcc Fe with a layer by layer growth the optimum substrate is a refractory metal.

The epitaxial depositions of Fe on W (110) / Al<sub>2</sub>O<sub>3</sub> (11 $\bar{2}$ 0) was therefore studied and the results are presented in this section.

The objective of the study was, firstly, to determine the optimum deposition conditions for the realization of a series of high quality Fe films of various thickness. Secondly to characterize the structural properties and analyse the evolution of these properties as a function of film thickness.

### 3.4.1. Experimental conditions

Targets of dimensions 10 mm diameter and 3 mm thickness were made in an induction furnace from Fe of purity 5N. The targets were mechanically polished and placed under vacuum. The targets' surfaces prior to depositions were etched by the laser, as in the case of W.

W(110) buffer layers were deposited as explained above. In order to avoid droplet contamination and film damage due to overly energetic ions, all Fe depositions were conducted at laser fluences close to the ablation threshold. The laser was operated at full power and the beam was de-focused to give a deposition rate of  $0.8 \text{ \AA} \cdot \text{min}^{-1}$  as measured on a quartz micro-balance. The vacuum during deposition was  $5 \times 10^{-10}$  Torr.

### 3.4.2. In-situ analysis

Fe films were deposited on substrates held at temperatures ranging from 300 K to 500 K. RHEED analysis showed that these films were single crystalline. Indexation of these RHEED patterns revealed the [002],  $[1\bar{1}0]$  and  $[1\bar{1}1]$  axes of Fe to be parallel to the W axes of same index, thus indicating that direct epitaxy of Fe (110) on W (110) occurs. Streaking of the RHEED patterns was obtained for all temperatures. Sharper RHEED patterns were obtained for depositions on substrates held at 500 K compared to 300 K but no improvement was found for higher substrate temperatures. In figure 3.10 the RHEED patterns of a  $30 \text{ \AA}$  film deposited at 300 K is compared with that of a  $30 \text{ \AA}$  film deposited at 500 K. The FWHM of the diffraction along the  $[1\bar{2}1]$  in-plane axis is less for the film deposited at higher temperature. In addition the diffraction spectra along the growth direction [110] shows intensity modulations at points in the reciprocal lattice for the film deposited at 300 K whereas the film deposited at 500 K does not. The above results indicate that the crystalline quality and the planarity of the film increases as the substrate temperature is increased.

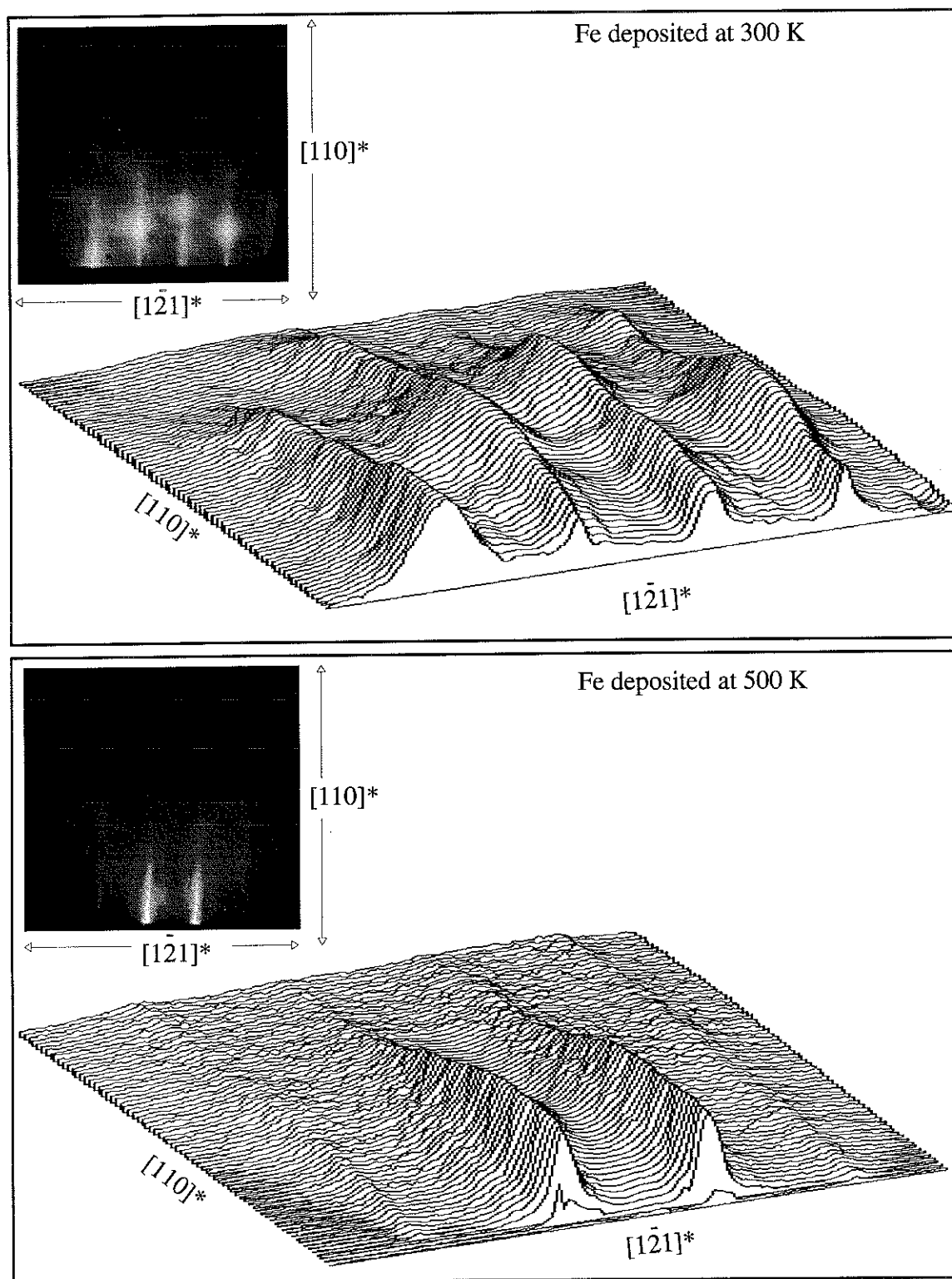


Fig. 3.10 - RHEED analysis of an Fe film deposited on a substrate held at 300 K and 500 K.

The coverage of the films was analysed by performing Auger analysis on films deposited at different substrate temperatures. In figure 3.11 the Auger spectrum acquired from a 30 Å film deposited at 500 K (fig. 3.11a) is compared with that acquired from a 30 Å film deposited at 600 K (fig. 3.11b). For the film deposited at 500 K, the W CVV peak is absent, indicating complete coverage of the buffer layer. For depositions at higher substrate temperatures, the W CVV peak is clearly present, indicating that island formation occurs at high substrate temperatures; the W signal arises from the spaces between the islands. It may seem surprising that these islands were not detected during RHEED analysis. This suggests that the lateral dimension of these islands is greater than the coherence length of the electrons.

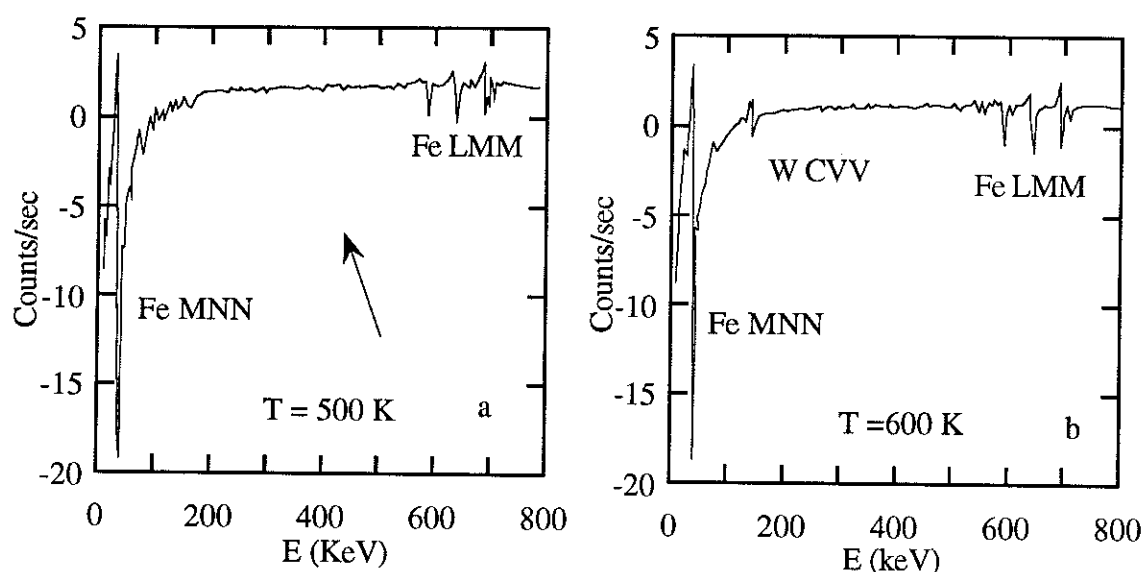


Fig. 3.11 - Auger differentiated spectra for an Fe film deposited at 500 K (a) and at 600 K (b), showing the apparition of a W CVV transition peak at 600 K which can be attributed to the clustering of the film into islands.

The optimum deposition temperature was thus determined to be 500 K.

In order to investigate the thickness dependence of the Fe lattice parameter, Fe depositions were performed at 500 K and RHEED patterns were taken as a function of thickness after the film had cooled to 300 K. (fig. 3.12). The Fe lattice parameter was then obtained from the inter-streak spacing of the RHEED patterns. The magnification factor of the RHEED patterns is  $1\text{cm} = 0.323 \text{ \AA}^{-1}$ . Assuming the distance between several diffraction streaks (sampling width of 10 cm) can be measured to within 0.5 mm, the error in the lattice parameter measurement is  $0.035 \text{ \AA}$  or 1.2% of the bulk value.

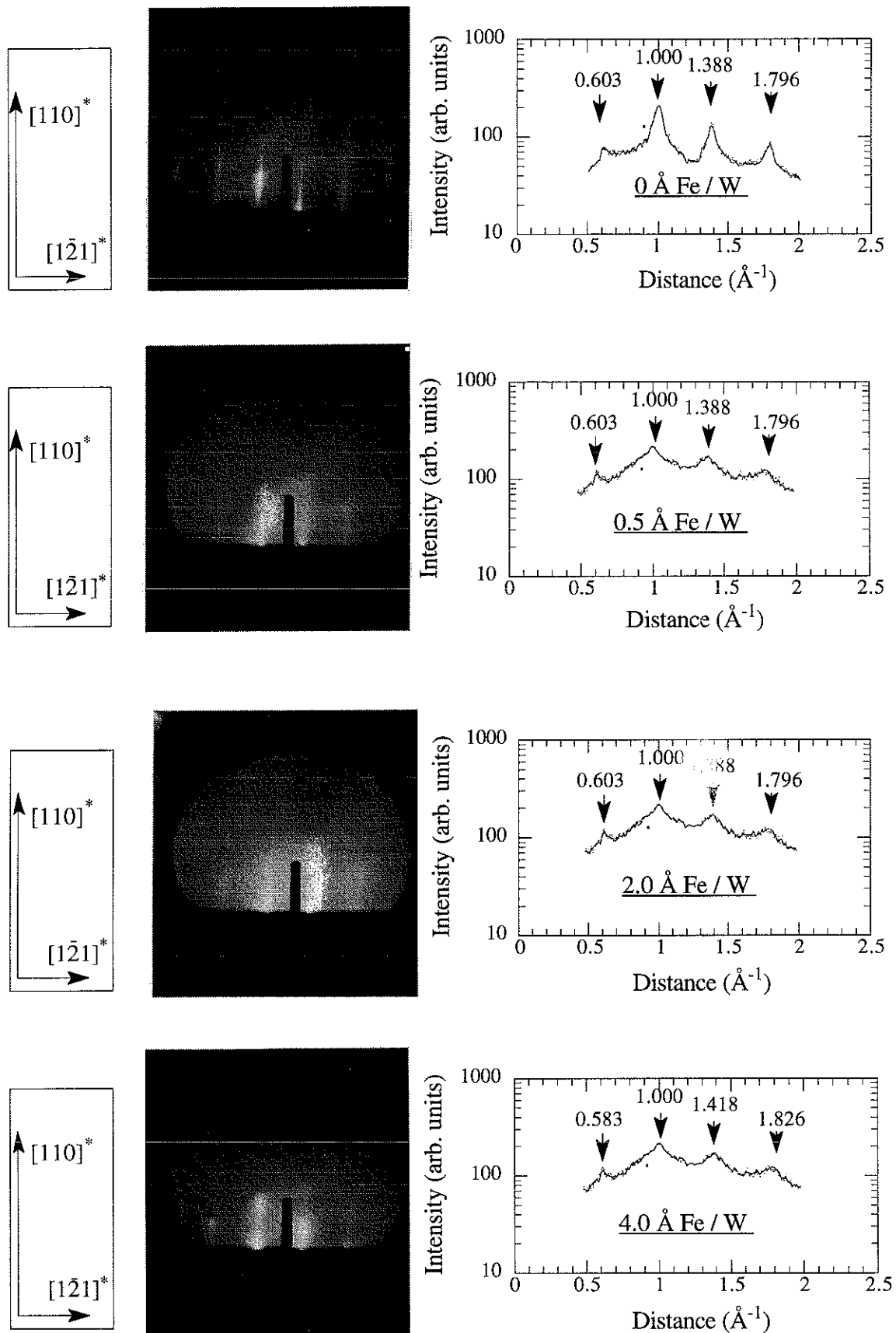


Fig. 3.12 - The thickness variation of the Fe RHEED streaks indicating that the Fe film adopts the W bulk lattice parameters for thicknesses up to 2  $\text{\AA}$  approximately and relaxes thereafter.

The Fe film was found to adopt the lattice parameter of bulk W (3.16 Å) for thicknesses up to 2 Å approximately. This indicates that the film nucleates through the formation of a pseudomorphic first monolayer. The stability of such a pseudomorphic monolayer of Fe (110) deposited on bulk W has been previously reported [20]. As the thickness is increased the lattice parameter decreases. No anisotropy of the lattice parameters in the plane of the films was detected. No analysis of the lattice parameter along the growth direction can be made due to the 2D diffraction along this direction.

The percentage strain ( $\epsilon$ ) of the film is related to the measured lattice parameter  $d$  as :

$$(\epsilon) = \frac{d - 2.886}{2.886} \times 100 \quad (3.1)$$

where 2.886 Å corresponds to the bulk lattice parameter of Fe. From the RHEED analysis the thickness dependence of the film strain was evaluated, as shown in figure 3.13. The strain is initially very large at small thicknesses and then relaxes to a value of 1% by approximately 10 monolayers.

As discussed in chapter two, a lattice mismatch between W and Fe may be relaxed by different mechanisms. The energy of a homogeneous strain is proportional to the volume of the film whereas the energy cost of dislocations is proportional to the area of the film. In the case of large mismatch, as in the case of Fe on W, one can expect pseudomorphism at low thicknesses and dislocations at greater thicknesses. A simple geometrical model for the prediction of the thickness variation of strain was formulated by Bruno and Renard [21].

The strain energy in a thin film is :

$$E_s = V \frac{1}{2} C \epsilon^2 \quad (3.2)$$

where  $V$  is the volume and  $C$  is an elastic constant. The dislocation energy, neglecting the interaction between dislocations is:

$$E_d = A \alpha \mu |d^{-1} - d_w^{-1}| \quad (3.3)$$

where  $A$  is the area of the film,  $\alpha$  (which is of the order of 1) is a numerical factor which depends on the geometry of the dislocations,  $\mu$  is the dislocation energy per unit length,  $d$  is the lattice parameter of the Fe film,  $d_w$  is the W lattice parameter. The minimum state is found by minimising the total energy  $E_s + E_d$  with respect to strain. Below a critical thickness,  $t_c$ , which is given by:

$$t_c \approx \frac{\alpha\mu}{dC |\epsilon_m|} \quad (3.4)$$

pseudomorphism is favoured, i.e.  $d = d_W$ . For film thicknesses greater than  $t_c$  misfit dislocations are expected resulting in a reduction of strain. The strain as a function of thickness,  $\epsilon_t$  for  $t > t_c$  is given by:

$$\epsilon_t \approx \epsilon_m \frac{t_c}{t} \quad (3.5)$$

where  $\epsilon_m$  is the misfit. The above RHEED analysis suggests that  $t_c = 2\text{\AA}$ . The strain as a function of film thickness was fitted to equation 5.5 and is shown in figure 3.13. A very reasonable agreement is found between the experimental data and the model.

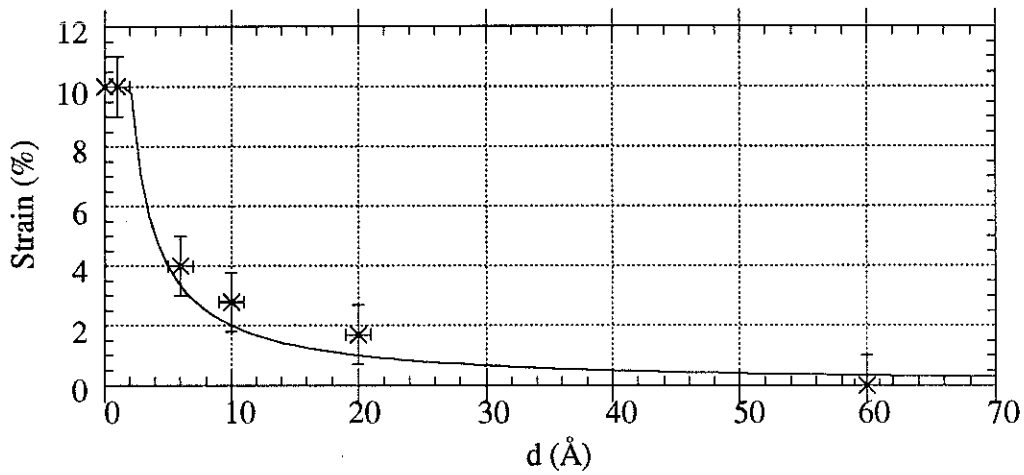


Fig. 3.13 - Thickness ( $d$ ) dependence of Fe strain as measured by RHEED (data points) compared with a  $1/d$  relaxation for  $d > 2\text{\AA}$  (continuous line).

The Fe films were protected by the subsequent deposition of  $50\text{\AA}$  of W. The W capping layers were deposited at room temperature to minimise islanding effects. This W capping layer was found to epitaxy directly on the Fe with all W axes parallel to those of Fe of the same indices, from RHEED analysis. The diffraction patterns of such films (fig. 3.14) were found to be intermediate between 2D and 3D diffraction and the FWHM of the diffraction maxima were found to be larger than the underlying Fe film. Complete coverage of the Fe film was verified by Auger analysis.

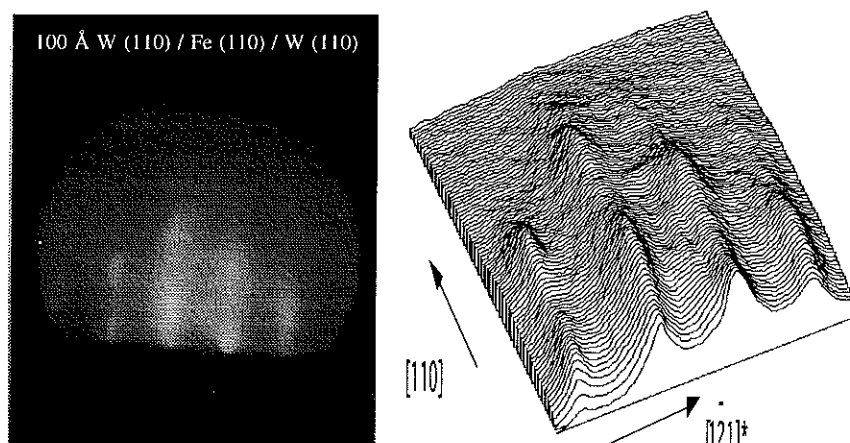


Fig. 3.14 - A typical RHEED diffraction pattern of a 100 Å W (110) film deposited on an Fe (110) film.

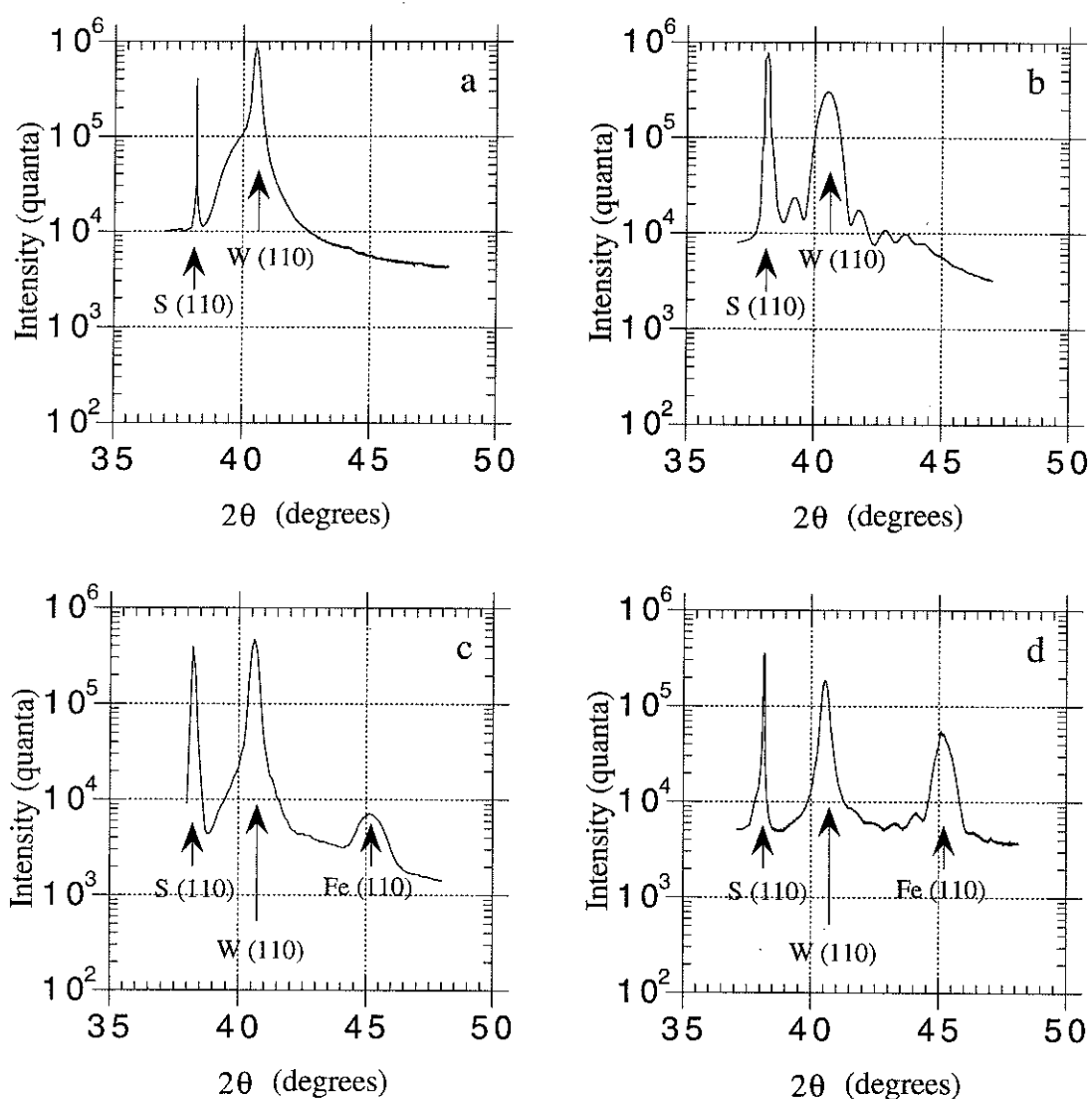


Fig. 3.15 - Zoom ( $2\theta$  from  $35^\circ$  to  $50^\circ$ ) of symmetrical diffraction spectra from net planes parallel to the film plane. The thickness of the Fe layers are;  $a = 6\text{Å}$ ,  $b = 20\text{Å}$ ,  $c = 90\text{Å}$  and  $d = 120\text{Å}$ , the substrate ( $\text{Al}_2\text{O}_3$ ) is denoted by S.



### 3.4.3 Ex-situ analysis

Ex-situ x-ray symmetrical diffraction ( $\theta$ - $2\theta$ ) was performed on all films. For scans of  $2\theta$  from  $20^\circ$  to  $100^\circ$  on thick films only the (110) and (220) reflections of  $\text{Al}_2\text{O}_3$ , W and Fe were observed, thus confirming the single crystallinity and orientation of these films. For film thicknesses of 20 Å and less, no diffraction from Fe planes could be detected (fig. 5.6). The Bragg angles were found to correspond to bulk Bragg angles to within experimental error ( $0.1^\circ$ ).

The in-plane crystallinity of the Fe films was investigated by grazing incidence diffraction. Two scans were systematically performed,  $\chi$ -scans (i.e. Bragg scans about the net planes perpendicular to the film plane) and  $\omega$ -scans (rotational scans about the film normal).

The experiments were performed by initially determining the  $\omega$  position of the W (002) peak by performing  $\omega$  scans from  $0 - 180^\circ$ . Knowing the epitaxial relations for the films, the expected position of all diffraction planes can therefore be calculated, as shown in figure 3.16.

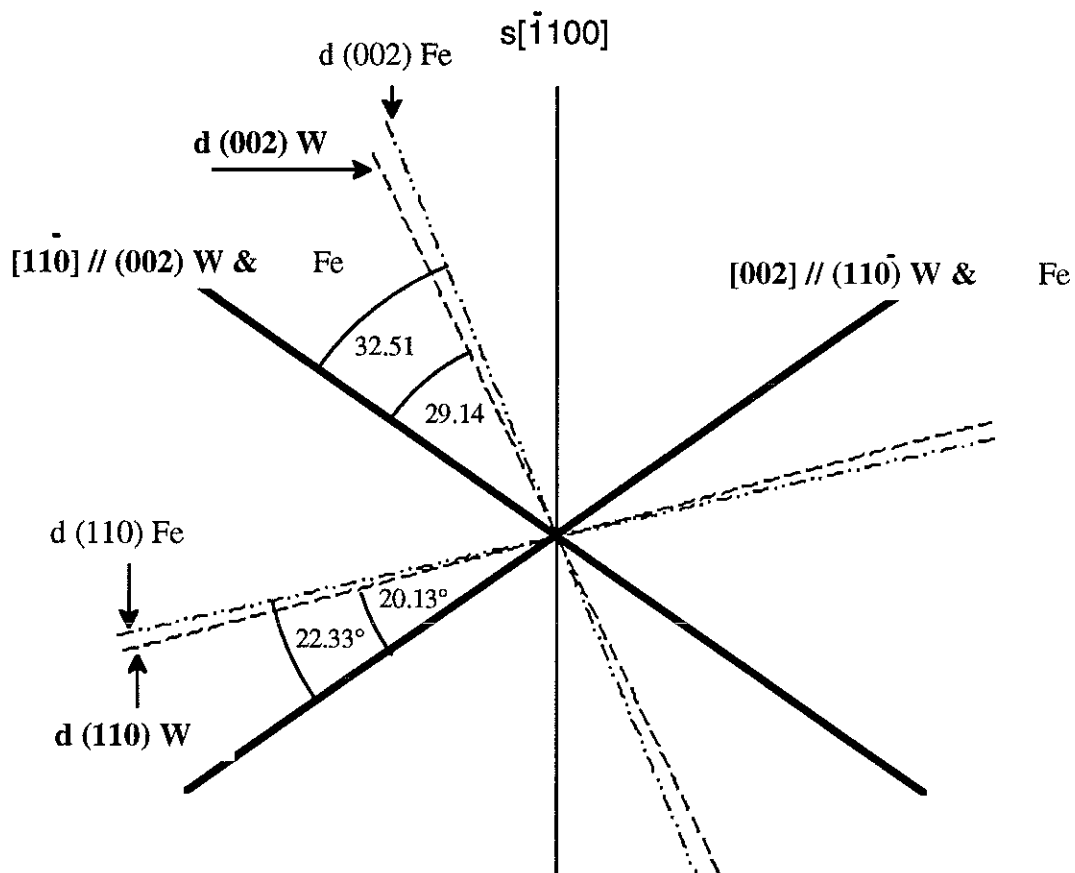


Fig. 3.16 - Schematic representation of the angular rotation ( $\omega$ ) between the diffracting planes of Fe and W for grazing incidence diffraction.

The  $\omega$  position of maxima intensity for Fe (002) and (1  $\bar{1}$  0) diffraction from all films studied was found to correspond to that expected for the case of direct epitaxy of Fe on W. The mean crystallite size (D) and misorientation ( $\Delta D$ ) were obtained from the FWHM of  $\chi$  -scans and  $\omega$  -scans respectively for films of different thicknesses (d). The results are reported in table 3.1.

Reflection	d (Å)	$\Delta\chi$ (°)	$\Delta\omega$ (°)	D (Å)	$\Delta D$ (°)
(002)	20	0.9	1.9	50	1.9
	90	0.6	1.6	80	1.5
	130	0.4	1.5	120	1.4
(1 $\bar{1}$ 0)	20	0.8	1.8	50	1.8
	90	0.5	1.6	100	1.5
	130	0.3	1.4	170	1.3

*Table 3.1 - Mean crystallite size (D) and mean misorientation ( $\Delta D$ ) as a function of Fe thickness (d) for in-plane (002) and (1  $\bar{1}$  0) diffraction as evaluated from the FWHM of the Bragg scans ( $\Delta\chi$ ) and from the FWHM of rocking curves around the Bragg maxima ( $\Delta\omega$ ).*

The analysis indicates the mean crystallite size is small and appears to be approximately equal to the film thickness. As the film thickness increases, misorientation between the crystallites decreases.

The exact thickness of the Fe layers and the W buffer layers and protective layers were determined by specular reflectivity analysis. The specular reflectivity curve was measured by performing low angle  $\theta$ - $2\theta$  scans, as shown in figure 3.17a for a film of 6 Å thickness and 3.18a for a film of 120 Å thickness. The x-ray beam is totally reflected for angles up to the critical angle and for higher angles the intensity falls rapidly. The experimental results were fitted by taking the refractive index thickness profile as a fitting parameter. The results of the best fit are shown alongside the experimental data and the obtained refractive index profile is shown in figure 3.17b and 3.18b for the 6Å and 120Å film respectively.

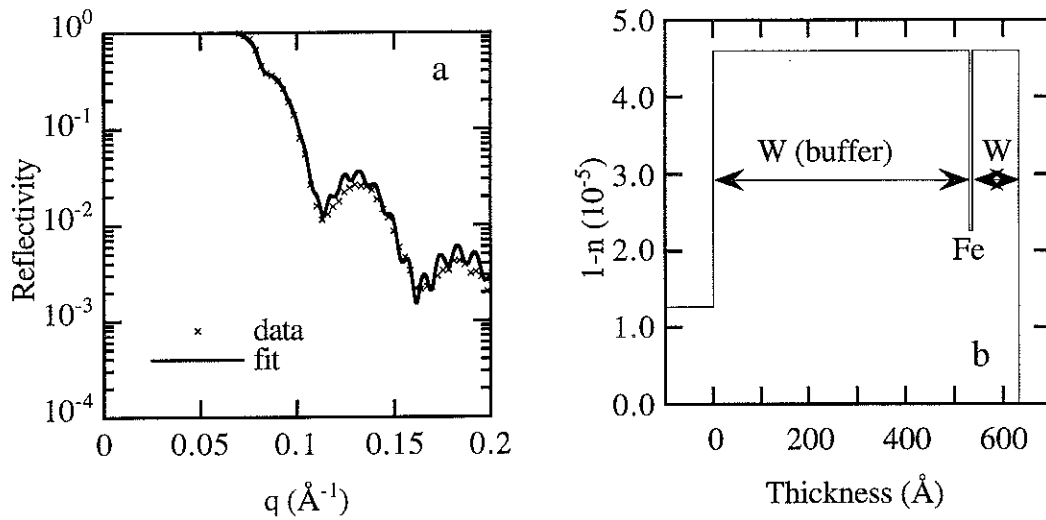


Fig. 3.17a Specular x-ray reflectivity and fit for a 6  $\text{\AA}$  Fe film, b - the deduced refractive index profile.

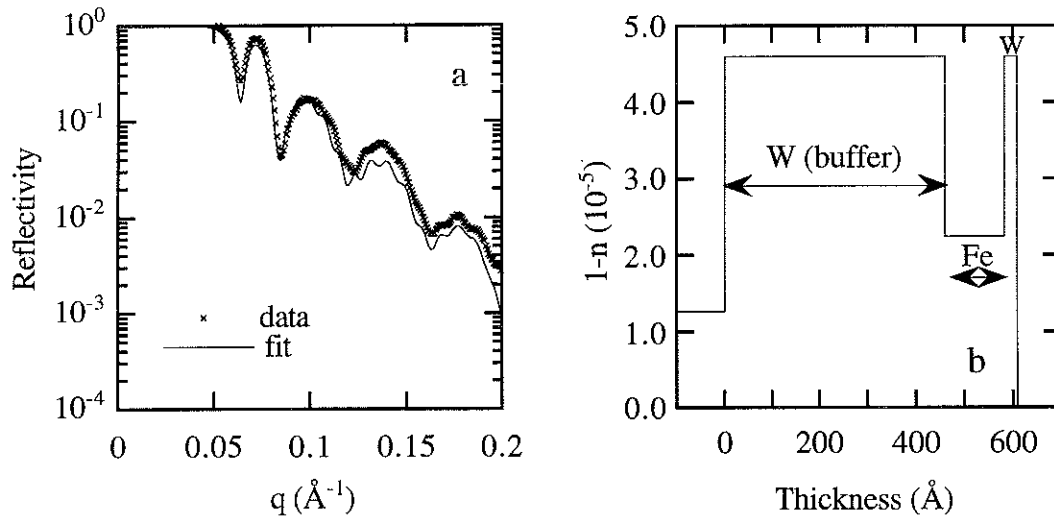


Fig. 3.18a Specular x-ray reflectivity and fit for a 120  $\text{\AA}$  Fe film, b - the deduced refractive index profile.

Due to the fact that the refractive index of Fe ( $1-n = 2.248 \times 10^{-5}$ ) is less than that of W ( $1-n = 4.602 \times 10^{-5}$ ), the specular reflectivity of such films is dominated by the W layers. Even very thin Fe layers can however be detected. The above results show that such a technique is quite powerful for the determination of the thickness of films composed of different materials.

The second fitting parameter is the interface roughness. In order to achieve this one must model such roughness. A perfect interface can be described as one where an abrupt termination of the film occurs (fig. 3.19a). A real interface can be expected to have a certain intermixing at the interface (fig. 3.19b).

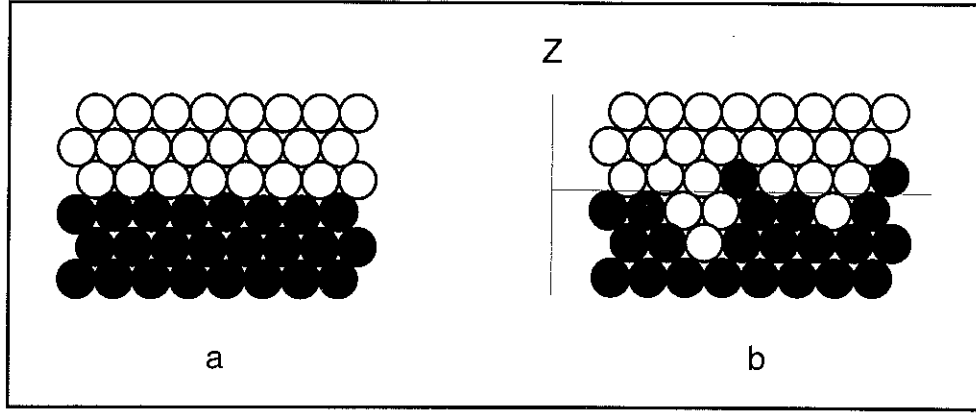


Fig. 3.19 a- Schematic representation of a perfect interface and b - an imperfect interface.

At any position in the film, one can define its roughness by the amplitude of the deviations from the perfect case. Consider the Z direction as defined in figure 3.19 and let the roughness amplitude be given by  $a_z$ . A root mean square roughness ( $\sigma$ ) can be defined as :

$$\sigma = \sqrt{\overline{(a_z)^2}} \quad (3.6)$$

The roughness amplitude in the other two directions (x and y) is usually termed the correlation length. In the case of specular reflectivity, as the momentum transfer in a layer is perpendicular to the surface, only roughness in the Z direction contributes to the specular reflectivity. For fitting purposes one can assume that the distribution function of  $a(z)$  follows a Gaussian distribution given by :

$$a(z) = \frac{e^{\frac{-z^2}{2\sigma^2}}}{\sigma\sqrt{2\pi}} \quad (3.7)$$

In the framework of the Distorted Born Wave Approximation (DBWA) [22], the scattering potential in each layer is divided into two parts  $V = V_1 + V_2$  where  $V_1$  is the potential of a perfect layer and  $V_2$  is a perturbation due to the roughness. By following such a procedure the best fits of the experimental results enabled the roughness at each interface to be evaluated as shown in table 3.2.

Interface	6Å film (fig. 3.17) $\sigma$ (Å)	120Å film (fig. 3.18) $\sigma$ (Å)
W (capping) / air	3	5
Fe / W (capping)	8	3
W (buffer) / Fe	9	7
Substrate / W (buffer)	6	11

*Table 3.2 - Root mean square interface roughness ( $\sigma$  (Å)) obtained from fitting of x-ray reflectivity data for a 6Å (fig. 3.17) and 120Å (fig. 3.18) Fe film.*

The obtained values indicate that the mean thickness fluctuations are of the order of some 3 - 10 Å. As the in-plane correlation is not known a direct physical interpretation is not possible. If the correlation length is the sample width then the films are of excellent interface quality. If, for the other extreme, the in-plane correlation length is of the order of some monolayers, then the interface quality is poor.

#### **3.4.4. Discussion**

The results of this section show that the epitaxial growth of Fe on W is quite straightforward. The influence of the substrate temperature is typical of most epitaxial systems, i.e. high temperatures results in better crystallinity but leads to islanding.

The main structural properties that evolve with thickness are the strain, the mean crystallite size and the mean misorientation. As the thickness increases, the strain and misorientation decrease whilst the crystallite size increases. Evaluation of the thickness dependence of the interface quality is difficult. This is due to the experimental difficulty of detecting thickness fluctuations of the order of a monolayer and due to the fact that as the film thickness increases the interface to volume ratio also increases, i.e. sensitivity to the interface is lost.

It is interesting to compare the above results with Fe depositions by other techniques, such as thermal evaporation (Fe (110) deposited on bulk W (110) [17] and magnetron sputtering (Fe (110) deposited on Mo (110) buffer layers [18].

The findings for the growth and coverage during the initial stages of deposition for PLD compare favourably with the findings for thermal evaporation, notably 2D growth up to substrate temperatures of 500 K and the improvement of crystallinity with increasing substrate temperature. The deposition conditions, i.e. vacuum and deposition rate were similar for both the thermally evaporated and the PLD films. Although in the case of PLD the time averaged deposition rate was  $8.3 \times 10^{-3} \text{ Å.s}^{-1}$ , the instantaneous deposition rate is of the order of  $9 \times 10^6 \text{ Å.s}^{-1}$ . This difference does not

appear to effect the epitaxial depositions. No information regarding the growth for the sputtered film was reported.

Some differences in the relaxation mechanisms appear between the three techniques, although all agree on the formation of a pseudomorphic first monolayer. At 5ML the strain observed in the sputtered film (3-5%) is within experimental error of the PLD films. The thermally evaporated films appear to have no strain at this thickness, as determined by LEED analysis however satellites in the LEED patterns were attributed to periodic lattice distortions which were observed for thicknesses greater than 20 Å. In the sputtered films the deposition was stopped every ML or so to perform GID showing a very gradual relief of strain as a function of thickness. By 20 Å a strain of 1% is detected, which is similar to the PLD films.

As no reports of the crystalline quality appear in the literature a comparison is not possible.

### 3.5 Rare earth / Fe bi-layers

The epitaxial deposition of rare earths has attracted much less attention compared with other metals. This is probably due to the reactive nature of these metals.

The heavy rare earth metals from Gd to Tm have very similar structural and thermal properties. They all crystallise in a hcp structure with a basal plane lattice parameter ranging from 3.63Å to 3.54Å. From the point of view of epitaxial deposition the same behaviour can therefore be expected for these metals.

These rare earths (RE) have been epitaxied in the past on W (110) [23] and on Nb (110) [24] and the epitaxial plane was found to be the (0001) plane.

Prior to this work, no reports have appeared in the literature for the epitaxial deposition of rare earth metals on 3d transition metals. It was therefore decided to attempt such an epitaxy and the results of these studies are presented in this section. The epitaxial deposition of RE on Fe is not however straightforward due to their different crystallographic and chemical structure.

#### 3.5.1 Experimental conditions

Fe films were deposited on W buffer layers as described in the previous sections. Gd targets were cut from 4N bulk Gd and subsequently polished. Prior to deposition, the target face was etched with the laser until a contaminant free deposition, detected by Auger was obtained. The total etch time was found to be two hours running at a deposition rate of 1 Å.min<sup>-1</sup>.

For depositions the laser was focused onto the Gd target until a deposition rate of 0.6Å.min<sup>-1</sup> was obtained.

#### 3.5.2 In-situ analysis

The influence of substrate temperature was investigated by performing depositions at temperatures of ambient, 400 K and 500 K and by performing RHEED in real time.

For depositions at 300 K the RHEED patterns of Fe were found to gradually disappear as the deposition progressed. After approximately 10Å of deposition (15 minutes) the Fe pattern had completely disappeared and no diffraction pattern was observed. A homogenous diffuse intensity was observed on the fluorescent screen, indicating the formation of either amorphous Gd or polycrystalline Gd with crystallite dimensions less than 100Å.

For depositions on the substrate held at 400 K the disappearance of the Fe pattern was followed by the appearance of very faint diffraction streaks barely distinguishable from the background intensity.

For depositions at 500 K sharp diffraction streaks started to appear alongside the Fe  $[1\bar{1}0]$  streaks after 1.5 Å of Gd deposition ( fig. 3.20a). By 10 Å of deposition only one set of diffraction streaks are visible which are characteristic of Gd (fig. 3.20b).

A comparison of the Auger spectrum acquired on a 40Å Gd film deposited at ambient temperature (fig. 3.21a) and on a 40Å film deposited at 500 K (fig. 3.21b) shows that complete coverage of the Fe has occurred at ambient temperature, whereas incomplete coverage has occurred for the film deposited at 500 K as indicated by the presence of a relatively sharp Fe LMM transition peak. Thus as in the case of Fe on W, depositions at higher substrate temperature favours epitaxy but leads to islanding.

In the present case, however, it is not possible to grow Gd at low substrate temperatures, as no epitaxy is observed. In order to achieve epitaxial deposition and to avoid islanding, the following conditions were employed. The substrate temperature was held at 500 K for the deposition of the first monolayer of Gd and then decreased to 300 K for the remainder of the deposition.

Auger analysis revealed complete coverage of the Fe by the Gd when deposited under these optimum conditions.

The RHEED patterns for deposition under optimum conditions are shown in figure 3.22, at thicknesses of 5Å, 15Å and 75Å. Clear diffraction streaks are obtained for all thicknesses. As the film thickness increases the width of the diffraction streaks increases. The same pattern, with an interstreak spacing of 17 mm is obtained by rotating the film by 60° around the film normal. A second series of diffraction patterns are obtained at 30° from the first with an interstreak spacing of 10 mm ; this pattern is also obtained every 60°. No evolution of the interstreak spacing is observed with increasing thickness.



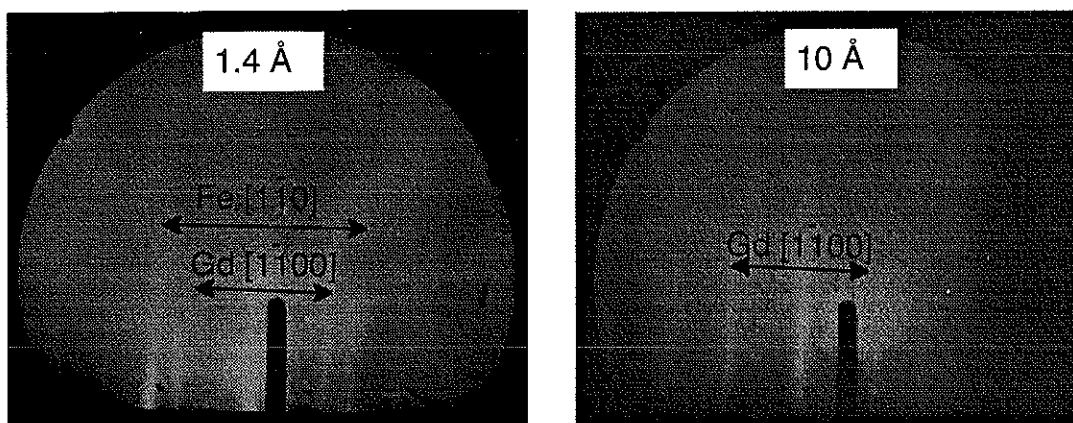


Fig. 3.20 - RHEED patterns obtained from a Gd film deposited on Fe (110) at 500 K as a function of film thickness ; a- 1.5Å, b - 10Å.

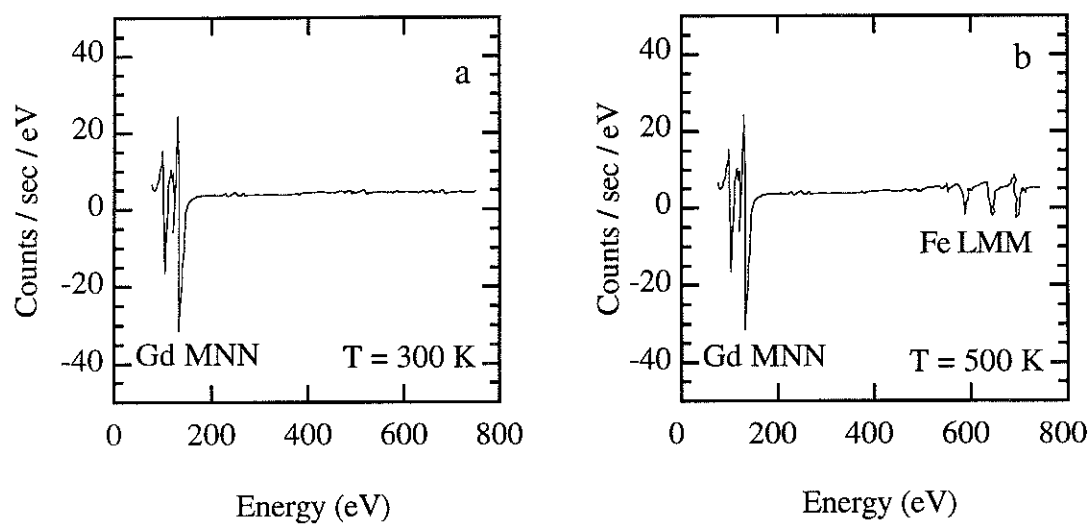


Fig. 3.21 - Auger analysis spectra for a 40Å Gd film deposited on Fe (110) at different temperatures; a - ambient substrate temperature and b - 500 K.

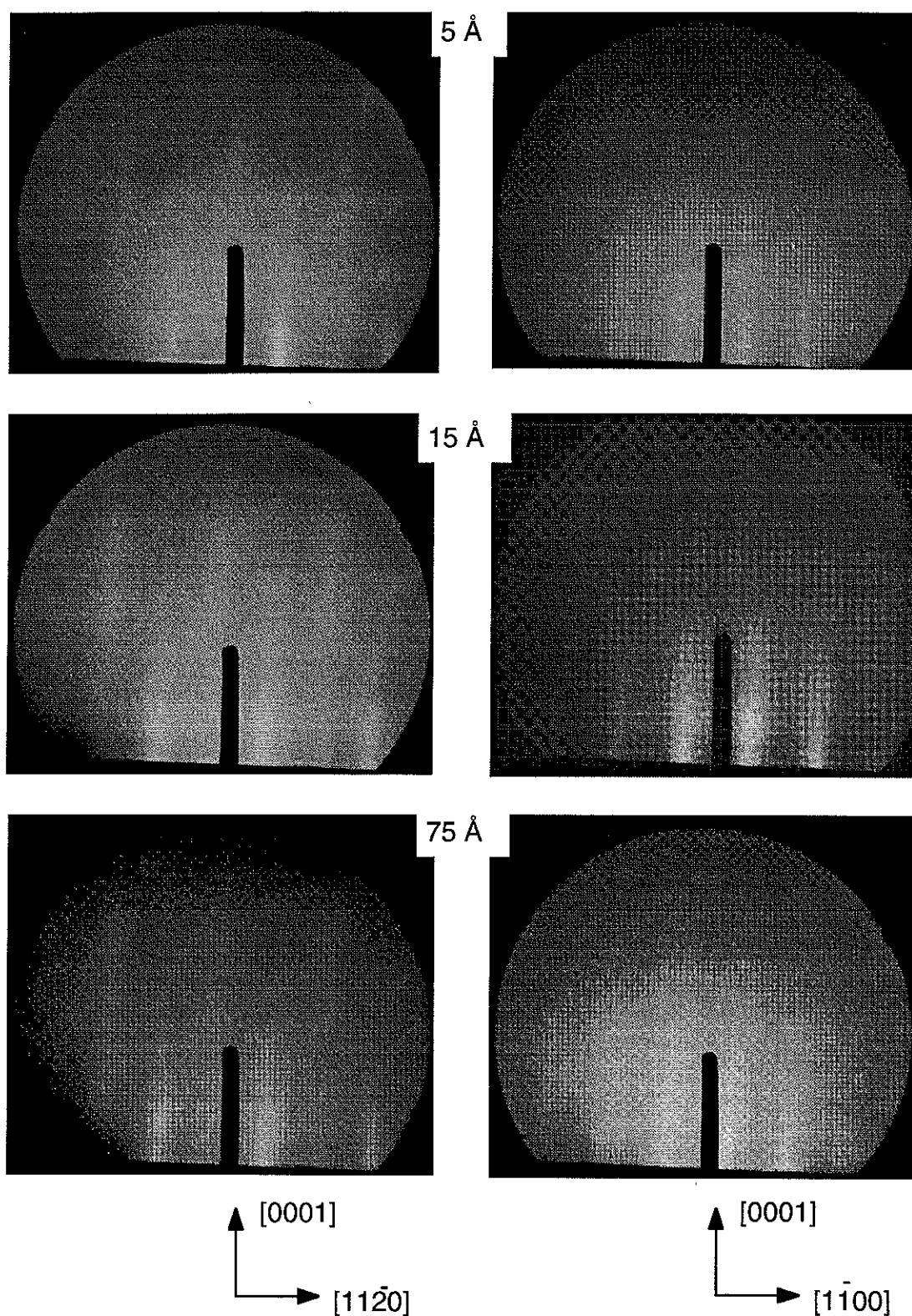


Fig. 3.22 - RHEED patterns obtained from Gd deposited on Fe with the substrate temperature initially held at 500 K for the first 5 Å of deposit and then dropped to 300 K for the remainder. Only two different diffraction patterns are obtained a and b which are 30° apart. Each pattern is found every 60°.

The above symmetry is characteristic of an hexagonal plane with the c axis perpendicular, i.e. an hcp (0001) plane. It has two-in plane non equivalent axes,  $[1\bar{1}00]$  and  $[11\bar{2}0]$  which are  $30^\circ$  apart and repeat every  $60^\circ$ . The Gd a lattice parameter can be evaluated from the inter-streak spacing :

$$d_{[1\bar{1}00]} = \frac{2}{a\sqrt{3}M} = 1\text{cm}$$

$$\Rightarrow a = 3.6\text{\AA}$$

$$d_{[11\bar{2}0]} = \frac{2}{aM} = 1.7\text{cm}$$

$$\Rightarrow a = 3.6\text{\AA}$$

As the same value of a is obtained along the two directions this confirms that the epitaxial plane is a (0001) plane. Following the discussion in chapter 2, this result is not surprising as it corresponds to the epitaxy of the most dense Gd plane on the most dense Fe plane. In addition, the obtained value of the Gd lattice parameter is identical to the bulk parameter (3.63\AA) to within experimental accuracy. The growing film therefore appears to be-unstrained, to within the detection limit of RHEED, from the very early stages of growth.

The in-plane epitaxial relationships were deduced from RHEED and found to be :

$$[1\bar{1}0] \text{ Fe} // [1\bar{1}00] \text{ Gd}$$

$$[002] \text{ Fe} // [11\bar{2}0] \text{ Gd}$$

The above epitaxial relationship corresponds to the Nishiyama -Wasserman (NW) orientation (see chapter 2) and is schematised in figure 3.23a.

The nearest neighbour distance mismatch along the two main hcp axes for the Gd / Fe system with the NW relationship is shown in table 3.3. The minimum mismatch is along the Gd  $[1\bar{1}00]$  direction (parallel to the  $[001]$  of Fe) and it is 12 %.

It is interesting to note that if the bcc double lattice were rotated by  $90^\circ$  with respect to the NW orientation (fig. 3.22b) then a smaller mismatch of 7.5% would have been obtained (table 3.3). It therefore appears that the parallelism along dense axes dominates over mismatch considerations in this system.

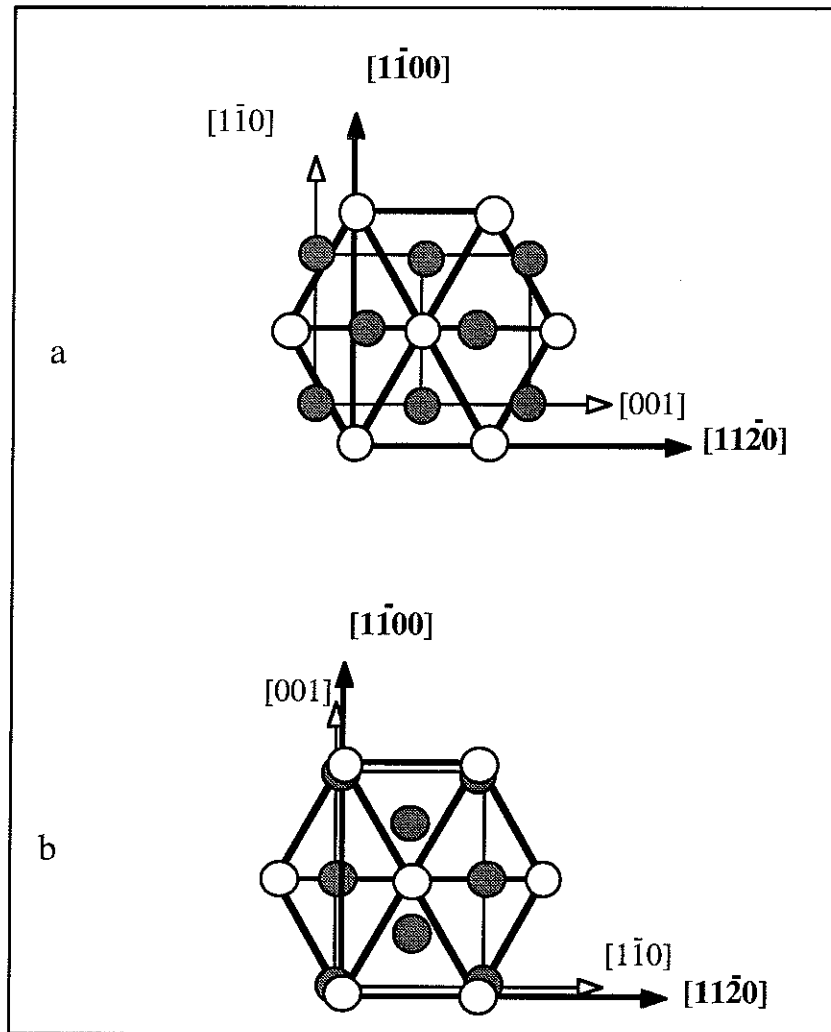


Fig 3.23a - Schematic diagram showing the epitaxial relationship for Gd / Fe which corresponds to the NW relationship. The Gd hcp unit cell is shown in bold and a double Fe bcc unit cell is shown in plain (to scale). The grey spheres represent the Fe atomic sites and the white spheres represent the Gd atomic sites (not to scale). A smaller mismatch would have been obtained for the epitaxial relationship schematized in figure 3.22b where the bcc double unit cell is rotated by  $90^\circ$  with respect to the NW orientation.

	$[11\bar{2}0]$	$[1\bar{1}00]$
Gd / Fe NW	21 %	12 %
Gd / Fe NW + $90^\circ$	12 %	7.5 %

Table 3.3 The nearest neighbour distance mismatch along the two main axes of the hcp cell for the epitaxial relationship found for Gd deposited on Fe (i.e. NW orientation). The same calculations are performed for a hypothetical relationship where the double bcc cell is rotated by  $90^\circ$  with respect to the NW orientation (NW +  $90^\circ$ ).

The RE / Fe bi-layers were protected depositions of either W or Y, with the substrate temperature held at ambient temperature for both cases. Complete coverage of the bi-layer was verified by Auger analysis.

For the case of Y, RHEED analysis revealed that direct epitaxy of Y occurs with all the crystallographic axes of Y being parallel to the underlying RE. The in-plane lattice parameter of Y is found to be as in the bulk ( $a = 3.65 \text{ \AA}$ ). The nominal thickness of the Y coating layer was  $300 \text{ \AA}$ .

For the case of W, no diffraction pattern was obtained.

Depositions of Tb on Fe were similarly performed. The same substrate temperature dependence as Gd / Fe was found for Tb / Fe. In addition the epitaxial relationships are also identical.

Having isolated the necessary conditions for the epitaxial deposition of RE on Fe the reverse epitaxy was attempted, i.e. Fe deposited on RE.

Gd was deposited on W (110) buffer layers with the substrate temperature held at ambient temperature. RHEED analysis revealed the epitaxial plane to be the (0001) plane of Gd. The in-plane lattice parameters, as deduced from RHEED analysis, were found to be as in the bulk. The epitaxial relationship was found to be the same as for Gd deposited on Fe (as schematised in figure 3.23a). This is in agreement with previous results of Gd deposited on W (110) [21] and Gd deposited on Nb (110) [22].

Fe was subsequently deposited on the Gd (0001) film at ambient temperature. A 3D diffraction pattern was obtained. The same pattern was obtained for all rotations of the film about its normal. The inter-spot spacing along the growth direction corresponded to [110] axis of Fe. This indicates that the film is polycrystalline with a (110) texturing.

### **3.5.3 Ex-situ analysis**

The morphology of RE / Fe bi-layers were examined by scanning electron microscopy. RE / Fe bi-layers deposited at 500 K were found to have an island morphology (fig. 3.24a) whereas films deposited under optimum conditions appear flat (fig. 3.24b), in agreement with the Auger analysis.

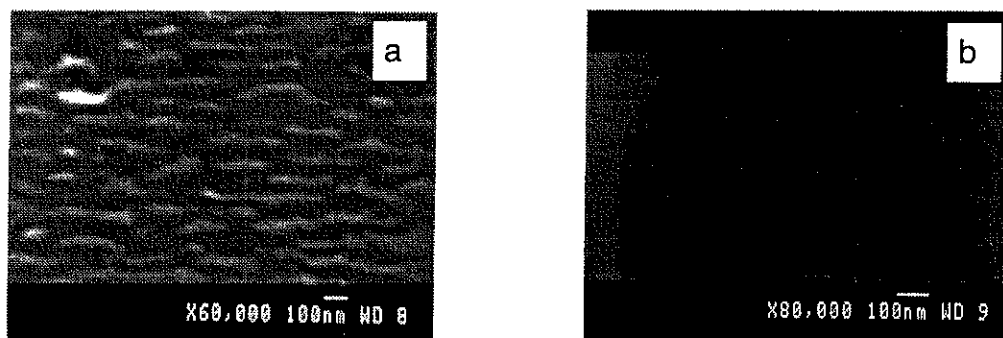


Fig. 3.24 Scanning electron micrographs for ; a- a RE / Fe bi-layer deposited at 500 K and b - a RE / Fe bi-layer where the first 5Å was deposited at 500 K and the remainder was deposited at 300 K.

Out of plane symmetrical diffraction confirmed the epitaxial orientation deduced by RHEED. In scans of  $2\theta$  from  $20^\circ$  -  $50^\circ$  (fig. 3.25) four peaks were observed ; Rare earth (0002),  $\text{Al}_2\text{O}_3$  (11 $\bar{2}$ 0) (denoted as S (110) in figure 3.25), W (110) and Fe (110). No additional peaks were observed.

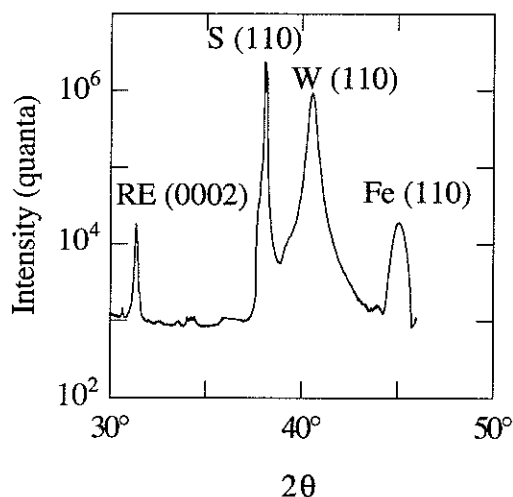


Fig. 3.25 - Out of plane symmetrical diffraction spectra obtained from a Y (0001) / Tb (0001) / Fe (110) / W (110) /  $\text{Al}_2\text{O}_3$  (11 $\bar{2}$ 0) film.

The exact thicknesses of all layers was determined by X-ray reflectivity, as shown in figure 3.26a for a Y (0001) / Gd (0001) / Fe (110) / W (110) /  $\text{Al}_2\text{O}_3$  (11 $\bar{2}$ 0) film, with the results of a best fit included. The corresponding thickness profile of the refractive index is shown in figure 26b.

Fitting of the data was found to be extremely difficult due to the large number of different films in the overall film. The obtained fit is reasonable and although intensity fluctuations between the experimental data and the fit are present the oscillation periods are in good agreement.

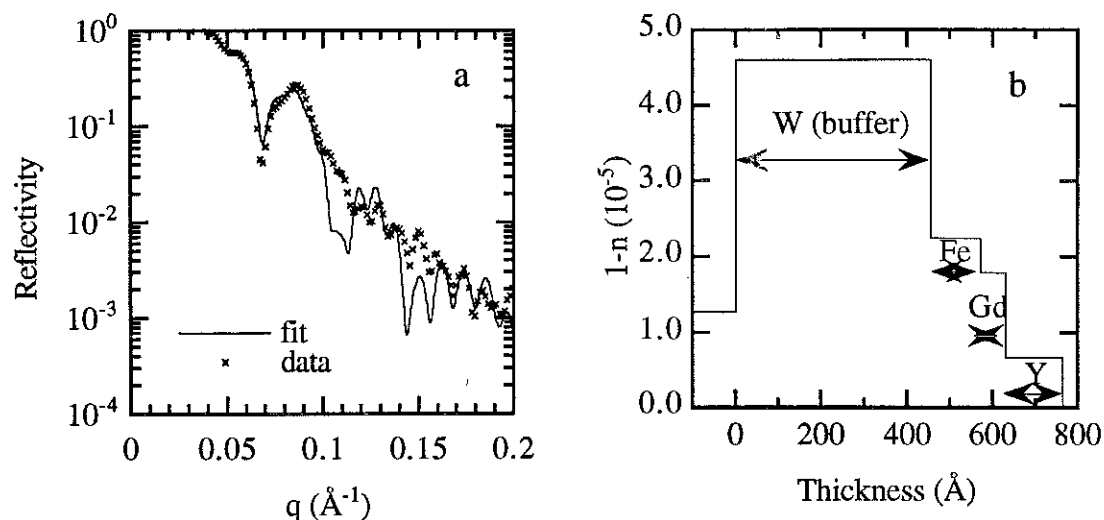


Fig. 3.26a - X-ray specular reflectivity and fit for a Y (0001) / Gd (0001) / Fe (110) / W (110) /  $\text{Al}_2\text{O}_3$  (11 $\bar{2}$ 0) film and b- the corresponding thickness profile of the refractive index.

The mean square interface roughnesses for the fit shown in figure 3.26a are shown in table 3.4.

Interface	$\sigma$ ( $\text{\AA}$ )
Y / air	30
Gd / Y	8
Fe / Gd	0
W / Fe	0
Substrate / W	9

Table 3.4 - Root mean square interface roughnesses ( $\sigma$  ( $\text{\AA}$ )) for a Gd / Fe bi-layer

The large value of the roughness obtained at the surface of the film can be attributed to usure of the surface during various experiments. In general the interface quality appears to be good although it must be stressed that the fit is poor.

### 3.5.4 Concluding remarks

Some interesting points arise from the results in this section. Firstly, the epitaxial behaviour for Gd and Tb is found to be identical, as expected. Secondly, RE can be epitaxied on Fe and the epitaxial orientation is found to be the same as for RE on W. For the case of Fe, the difference in the atomic diameters is 30%, whereas for the case of W it is 23%. The epitaxial orientation found in both cases does not correspond to that which allows minimum mismatch. Thirdly, the RE, whether on W or on Fe appear to adopt their bulk lattice parameter from the very early stages of deposition. Finally, it is not possible to epitaxy Fe on RE (0001)

### 3.6 References to chapter three

---

- [1] M. Rühle, A. G. Evans, M. F. Ashby and J. P. Firth (editors),  
"Metal-Ceramic Interfaces", Pergamon Press, New York, 1990.
- [2] S. M. Durbin, J. E. Cunningham, M. E. Mochel and C. P. Flynn,  
J. Phys. F11 (1981) L223.
- [3] U. Gradmann and G. Waller,  
Surf. Sci., 116 (1982) 539.
- [4] J. Kwo, E.M. Gyorgy, D.B. Mc Whan,  
M. Hong, F.J. DiSalvo, C. Vettier and J. E. Bower,  
Phys. Rev. Lett., 55 (1985) 1402.
- [5] J. Mayer, G. Gutekunst, G. Möbus, J. Dura, C.P. Flynn and M. Rühle,  
Acta. Meta. Mater., S217 (1992) 40.
- [6] J. H. Souk, Armin Segmüller and J. Angilello,  
J. Appl. Phys., 62 (1987) 509.
- [7] Ch. Chatillion and J. Massies,  
Mat. Sci. Forum, 59 (1990) 229.
- [8] P. Mikulik, private communication.
- [9] J. Guo, H.L.M. Chang and D.J. Lam,  
Appl. Phys. Lett., 61 (1992) 3116.
- [10] F. J. Lamelas, Hui He and Roy Clarke,  
Phys. Rev. B38 (1988.) 6334.
- [11] R. Osgood, private communication.
- [12] F. Robaut, private communication.
- [13] G.A. Prinz, G.T. Rado and J.J. Krebbs,  
J. Appl. Phys., 53 (1982) 2082.
- [14] N. Metoki, M. Hofelich, Th. Zeidler, T. Mughe, Ch. Morawe and H. Zabel,  
JMMM, 121 (1993) 137.



- 
- [15] G.C. Smith, G.A. Padmore and C. Norris,  
Surf. Sci. 119 (1982) L287.
- [16] G. Luggert and G. Bayreuther,  
Thin Solid Films, 175 (1989) 311.
- [17] J. G. Wright,  
Philos. Mag., 24 (1971) 217.
- [18] U. Gradmann and G. Waller,  
Surf. Sci., 116 (1982) 539.
- [19] B. M. Clemens, R. Osgood, A.P. Payne, B.M. Lairson, S. Brennen  
R.L. White and W.D. Nix,  
JMMM 121 (1993) 37.
- [20] M. Przybylski, I. Kaufmann, U. Gradmann,  
Phys. Rev. B40, 8631, 1989.
- [21] P. Bruno and J.P. Renard,  
Appl. Phys. A49, 499, 1989.
- [22] V. Holy, J. Kubena, I. Ohlidal, K. Lischka and W. Plotz,  
Phys. Rev., B47 (1993) 2064.
- [23] M. Farle and W. A. Lewis,  
J. Appl. Phys., 75 (1994) 5604.
- [24] J. Kwo, M. Hong and S. Nakahara,  
Appl. Phys. Lett., 49 (1986) 319.



# CHAPTER FOUR

## GROUND STATE MOMENTS, ANISOTROPY AND THERMAL EXCITATIONS IN ULTRA-THIN FILMS

### Table of contents to chapter 4

4.1 Introduction	99
4.1.1 Ground state moment	99
4.1.2 Exchange interactions	100
4.1.3 Dipolar interactions	100
4.1.4 Magnetocrystalline anisotropy	101
4.1.5 Thermal excitations	102
4.2 Surface ground state moments	105
4.2.1 Introduction	105
4.2.2 Experimental results	106
4.2.3 Theoretical results	107
4.2.4 Concluding remarks	108
4.3 Thin film anisotropy	109
4.3.1 Sources of anisotropies	109
4.3.2 Experimental analysis	112
4.3.3 Experimental results	113
4.3.4 Theoretical results	115
4.3.5 Discussion	121
4.3.6 Concluding remarks	121
4.4 Thermal excitations	122
4.4.1 Introduction	122
4.4.2 Experimental results	122
4.4.3 Theoretical results	124
4.5 Conclusion	130
4.6 References	131

## RÉSUMÉ

Dans ce chapitre nous discutons du moment magnétique, de l'anisotropie et des excitations thermiques des couches ultra-minces. Nous présentons un résumé de la littérature expérimentale et une perspective théorique y compris notre contribution. A la surface d'une couche mince d'un métal de transition, la bande d'énergie 3d est modifiée. Pour une surface libre, il en résulte que l'amplitude du moment magnétique à 0K ainsi que l'anisotropie est augmentée par rapport au massif. A une interface, l'amplitude du moment magnétique à 0K peut être diminuée et l'anisotropie peut être modifiée par rapport à une surface libre. L'étude expérimentale de ces effets est rendue difficile par des déformations de maille et par une rugosité aux interfaces. Une déformation modifie les propriétés magnétiques de toute la couche, y compris les atomes de surface. Puisque la déformation varie souvent en fonction de l'épaisseur de la couche, une séparation de l'anisotropie de surface de l'anisotropie totale est difficile. La thermodynamique de l'ordre ferromagnétique dépend fortement de l'épaisseur de la couche. Pour une couche monoatomique c'est l'anisotropie et les interactions dipolaires qui stabilisent l'ordre ferromagnétique à longue portée. Lorsque l'épaisseur de la couche augmente, l'ordre ferromagnétique à longue portée devient plus stable.

## SUMMARY

In this chapter we discuss ground state moments, anisotropy and thermal excitations of ultra-thin films giving both an experimental overview of the literature and a theoretical perspective including some of our own work. At the surfaces of a transition metal film, the energy band of the 3d electrons is modified. For the case of free surfaces, it results in an enhanced ground state moment and in an enhanced anisotropy energy per surface atom. At interfaces the above phenomenon may be influenced by hybridisation effects. These may lead to a reduction in ground state moments and changes in the anisotropy energy compared with a free surface. The experimental study of the above surface effects is further complicated by interface roughness and strains. Interface roughness can influence the ground state moment and the anisotropy. Lattice strains influence the magnetic properties of all layers in the film, including the surface / interface layers. As strains often vary as  $1/d$  where  $d$  is the film thickness a separation of surface / interface is often not possible. The thermodynamics of ferromagnetism in thin films is strongly thickness dependent. For a monolayer, long range ferromagnetic order is stabilised by anisotropy and dipolar interactions. As the film thickness increases ferromagnetic order becomes progressively more stable.

## 4.1 Introduction

The two most important ground state properties characteristic of a ferromagnetic material are its magnetic moment and anisotropy. As the temperature of a ferromagnet is raised above 0 K, these start to differ from their ground state values due to thermally induced magnetic excitations.

As ferromagnetism is a co-operative phenomenon, all interactions can be characterised by an interaction length scale. The thickness of a film at which one expects a specific magnetic property to be different compared with bulk materials depends on the characteristic length scale at the origin of the magnetic property in question.

Real films are often highly strained and have a certain degree of interface roughness. In addition, at least one surface is in contact with another material (i.e. the substrate). These effects (roughness, strain and interface effects) can be expected to greatly modify the magnetic properties of ultra-thin films. The task of understanding their magnetic properties is thus rendered quite challenging.

In the remainder of this introduction we briefly outline the fundamental magnetic properties of 3D ferromagnets. In the subsequent three sections we discuss ground state moments, anisotropy and thermal excitations of ultra-thin films giving both an experimental overview of the literature and a theoretical perspective including some of our own work.

### 4.1.1 Ground state moment

Magnetism is a phenomenon which arises from an exchange term in the electrostatic interactions between electrons and concerns only unfilled electron shells. Two main series of magnetic elements exist ; the transition metal elements (un-filled 3-d shell) and the elements of the rare earth series (un-filled 4f shell).

The 3-d electrons are itinerant and form a band whose width is typically 5 eV. Exchange interactions favour the occupancy of states belonging to a sub-band with the same spin state. Kinetic energy considerations favour equal occupancy of both sub-bands. A net de-localised magnetic moment will exist if the occupancy of one sub-band is greater than the other. The intra-atomic exchange interactions are much larger than the inter-atomic exchange interactions, therefore intra-atomic exchange interactions dominate the band splitting and lead to the formation of a moment, as in the case of localised electron systems. In Fe, for example, the density of states corresponds to a moment of  $4.7 \mu_B$  / atom in the majority spin band and to  $-2.5 \mu_B$  / atom in the minority spin band leading to a net magnetic moment of  $2.2 \mu_B$  [1]. The essential parameter for determining the magnetic moment is the band width. This is essentially determined by the nearest neighbour co-ordination.

The 4-f shell on the other hand is localised and shell filling follows Hund's rules :  $S = S_{\max}$  and  $L = L_{\max}$ . The resulting total angular momentum,  $J$  is equal to  $L - S$  for the rare earth elements of the first half of the series (Ce to Sm or Eu) and equal to  $L + S$  for the second half of the series (Gd to Yb). The corresponding magnetic moment is defined as  $g\mu_B J$ . In Gd, for example the 4f shell is half full and the magnetic moment is therefore  $7 \mu_B$  [2]. The total angular momentum  $J$  is entirely determined by inter-atomic exchange interactions. The magnetic moment  $g\mu_B J$  results from a competition between exchange and crystalline electric field interactions for which the characteristic lengths are some atomic distances and on-site respectively (see further on).

#### 4.1.2 Exchange interactions

A convenient formalism for expressing the exchange energy of an ensemble of spins is:

$$E_{\text{ex}} = -2J(r)\sum_{i,j} S_i S_j \quad (4.1)$$

where  $S_i$  and  $S_j$  are the spin quantum numbers of atoms  $i$  and  $j$  respectively and  $J(r)$  is a nearest neighbour coupling constant ( $J > 0$  for ferromagnets) which is assumed to be independent of  $i$  and  $j$ . The above model is referred to as the Heisenberg model [3].

The magnetic moments on different atomic sites are coupled through exchange interactions. For 3-d electrons it is their itinerant nature that ensures direct coupling between spins and the exchange energy is typically 10 - 100 meV / atom. These direct exchange interactions are very short ranged and are typically of the order of atomic distances.

For 4-f electrons, coupling occurs through the spin polarisation of the 5d and 6s conduction electrons. This indirect exchange mechanism is spatially oscillatory in nature and can lead to many forms of coupling such as parallel, anti-parallel and helical. These indirect exchange interactions are more long ranged than direct exchange interactions and are typically of the order of a few atomic distances.

#### 4.1.3 Dipolar interactions

An ensemble of spins stores energy through the magnetic field it creates and therefore spin correlations will exist in order to minimise this magnetostatic energy. These correlations between two spins,  $s_i$  and  $s_j$  can be calculated by assuming that they act as dipoles and it can be shown that the dipolar interaction energy is given by :

$$E_{ij} = \frac{\mathbf{m}_i \cdot \mathbf{m}_j}{r_{ij}^3} - \frac{3(\mathbf{m}_i \cdot \mathbf{r}_{ij})(\mathbf{m}_j \cdot \mathbf{r}_{ij})}{r_{ij}^5} \quad (4.2)$$

where  $\mathbf{m}_i = \mu_B g \mathbf{s}_i$ ,  $g$  is the Landé factor and  $\mathbf{r}_{ij}$  is a unit vector joining  $\mathbf{m}_i$  and  $\mathbf{m}_j$ . As dipolar interactions decay as  $r^{-3}$  and the number of neighbouring atoms to a given atom varies as  $r^3$ , all moments in a given sample must be taken into account in the evaluation of dipolar interactions at each atomic site.

#### 4.1.4 Magnetocrystalline anisotropy

Due to crystalline electric field effects, the orbitals tend to adopt the symmetry of the lattice. Through the action of spin-orbit coupling, the ground state configuration of a ferromagnet corresponds to spin and orbital alignment along a given lattice direction. The energy cost of alignment along another direction is termed the magnetocrystalline anisotropy energy and it is a very sensitive function of the material symmetry.

The anisotropy energy density can be written phenomenologically as :

$$E_a = k_0 + \sum_{i,j} k_{ij} \alpha_i \alpha_j + \sum_{i,j,k,l} k_{ijkl} \alpha_i \alpha_j \alpha_k \alpha_l + \dots \quad (4.3)$$

where in a classical approach of constant moments the  $\alpha$ 's are the direction cosines of the magnetisation vector with respect to the crystal lattice and the  $k$ 's are energy density coefficients. The relationships between the various coefficients are obtained from symmetry (time reversal and crystal) arguments. For cubic symmetry, 4.3 becomes :

$$E_a = K_1 s + K_2 p + K_3 s^2 + K_4 s p + \dots \quad (4.4)$$

where  $s = \alpha_1^2 \alpha_2^2 + \alpha_2^2 \alpha_3^2 + \alpha_3^2 \alpha_1^2$  and  $p = \alpha_1^2 \alpha_2^2 \alpha_3^2$ .

Such a description is more appropriate for transition metals where the orbitals are weak and the modulus of the total moment is approximately constant. Anisotropy energies are typically of the order of a  $\mu\text{eV}$  / atom and therefore orders of magnitude less than exchange energies.

For the case of 4f systems, where the orbital and spin moments are strongly coupled, the anisotropy energy can be expressed as :

$$E = \sum_{n,m} B_n^m \langle O_n^m \rangle \quad (4.5)$$

where  $O_n^m$  are the Stevens operators which describe the successive moments of the 4f shell in a given environment and  $n$  and  $m$  describe the symmetry order of the considered moment ( $2 \leq n \leq 6$ ,  $0 \leq m \leq n$ ). In 4f systems the anisotropy energy may reach values of the order of  $100 \mu\text{eV}$  / atom.

Anisotropy interactions can, to a first approximation, be considered to be on-site interactions i.e. they are extremely short ranged.

#### 4.1.5 Thermal excitations

As the temperature of a ferromagnet is raised above 0K thermal spin excitations occur which tend to destroy the spin alignment. From a quantum mechanical point of view, an injection of thermal energy will cause a spin to flip into a higher energy state, i.e. a reversed spin state as schematised in figure 4.1a for a spin of a half. Such an excitation will not be confined to one lattice site but will travel through the whole crystal as a spin-wave. Classically one can picture each spin precessing around its ground state position with a distinct phase relation with neighbouring spins (fig. 4.1b). At the Curie temperature ( $T_C$ ) the thermal energy equals the exchange energy and ferromagnetism is lost.

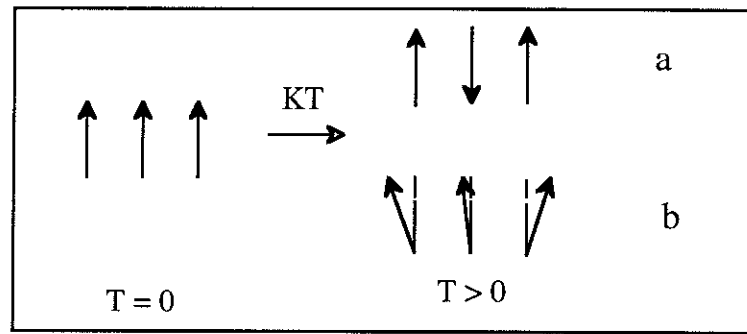


Fig. 4.1 - Schematic description of the influence of thermal energy on a ferromagnetic arrangement of spins from a quantum mechanical (a) and classical perspective (b).

Consider a ferromagnet of  $N$  atoms with spin  $S$  per atom and a ground state exchange given by (4.1). The total spin, at  $T = 0$  K, is  $NS$ . The first excited state has a spin number of  $NS-1$ . The energy of this first excited state depends on the number of sites over which this spin deviation is distributed ; the longer the wavelength, the lower the energy. It can be shown that for a cubic lattice ( lattice parameter =  $a$ ) the energy of a given state of wavevector  $q$  is [4]

$$E_q = 2JSa^2q^2 \equiv Dq^2 \quad (4.6)$$

where  $D$  is the stiffness constant and where it is assumed that  $qa \ll 1$  (i.e. long-wavelength limit).

The average occupation number of each mode at temperature  $T$  is:

$$\langle n_q \rangle = \frac{1}{\exp(E_q / k_B T) - 1} \quad (4.7)$$



and the total magnetisation at T can be written as :

$$M(T) = M(0) \left[ 1 - \frac{1}{NS} \sum_q \langle n_q \rangle \right] \quad (4.8)$$

From (4.6), (4.7) and (4.8) it follows that at low temperatures:

$$\frac{M(T)}{M(0)}(3D) = 1 - \frac{1}{M(0)} \frac{a^3}{(2\pi)^3} \int_0^\infty \frac{4\pi q^2 dq}{\exp(Dq^2 / k_B T) - 1}$$

evaluating the integral leads to [3] :

$$\frac{M(T)}{M(0)}(3D) = 1 - BT^{3/2}$$

where

$$B = 2.612 \frac{a^3}{M(0)} \left( \frac{k_B}{4\pi D} \right)^{3/2} \quad (4.9)$$

and thus showing that a  $T^{3/2}$  thermal dependence of magnetisation is expected for 3D ferromagnets.

The above spin wave analysis is only valid for the temperature range over which (4.6) is valid. This corresponds to long wavelength non-interacting spin waves and, as a rule of thumb, the upper limit can be estimated as  $T_c / 3$ . The thermal variation of the spontaneous magnetisation of most ferromagnets is found to follow a  $T^{3/2}$  behaviour at low temperatures, as expected from (4.9). In Fe, for example, B is found to be  $3.4 \times 10^{-6} \text{ K}^{-3/2}$  [3].

The spin wave dispersion curve of Fe along the main crystallographic axes, as measured by inelastic neutron scattering at  $T = 300 \text{ K}$ , is shown in figure 4.2a (from ref. [5]) . The experimental data follows a dispersion given by (4.5) with  $D = 281 \text{ meV} \cdot \text{\AA}^2$  in the low  $q$  range. At a given temperature, the spin waves that are thermally excited have energies of the order of  $k_B T$  (see 4.7). From this one sees that at  $300 \text{ K}$ , the typical wavelength for magnetic excitations is  $> 20 \text{ \AA}$ .

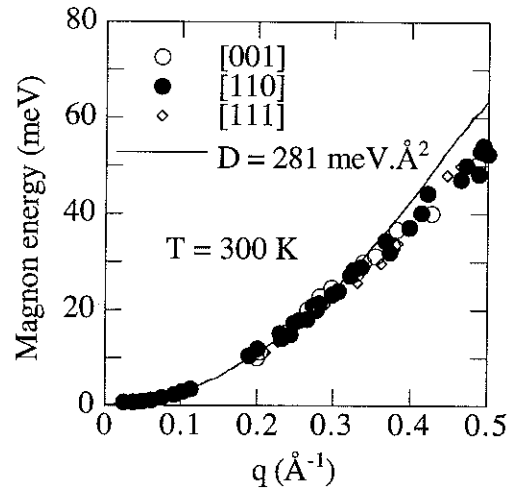


Fig. 4.2 - Magnon dispersion energy for Fe at 300 K measured by inelastic neutron scattering along the main crystallographic axes with a fit to expression (4.6) yielding a value of  $D = 281 \text{ meV.Å}^2$  (from reference [5]).

## 4.2 Surface ground state moments

### 4.2.1 Introduction

The magnetic moment at the surface / interface of a thin film may be significantly different compared with its value in bulk materials. Due to the more delocalised character of the 3d electrons compared with the 4f electrons, one expects transition metals to be more susceptible to surface effects than rare earth metals.

The influence of surface effects on the ground state magnetic moment of transition metals can be understood by considering the modifications to the band structure. Due to the reduction in co-ordination at the surface, the electrons become more localised leading to a narrowing of the surface 3d band ( $W_s$ ) compared with that of the bulk ( $W_b$ ) which can be estimated as [6] :

$$W_s = \left( \frac{z_s}{z_b} \right)^{\frac{1}{2}} W_b \quad (4.10)$$

where  $z_s$  and  $z_b$  is the co-ordination of the surface and bulk respectively. The thus induced band narrowing is schematised in figure 4.3. The magnetic moment ( $\mu$ ) can be estimated as :

$$\mu \approx \mu_B \int_{E_{\min}}^{E_f} (n^+ - n^-) dE \quad (4.11)$$

and therefore the magnetic moment at the surface is expected to be enhanced with respect to the bulk. Considerable enhancement can only occur for weak ferromagnets in that there must exist holes in the majority d-band which can be polarised. One would therefore expect enhancement to follow the following order; Fe > Co > Ni.

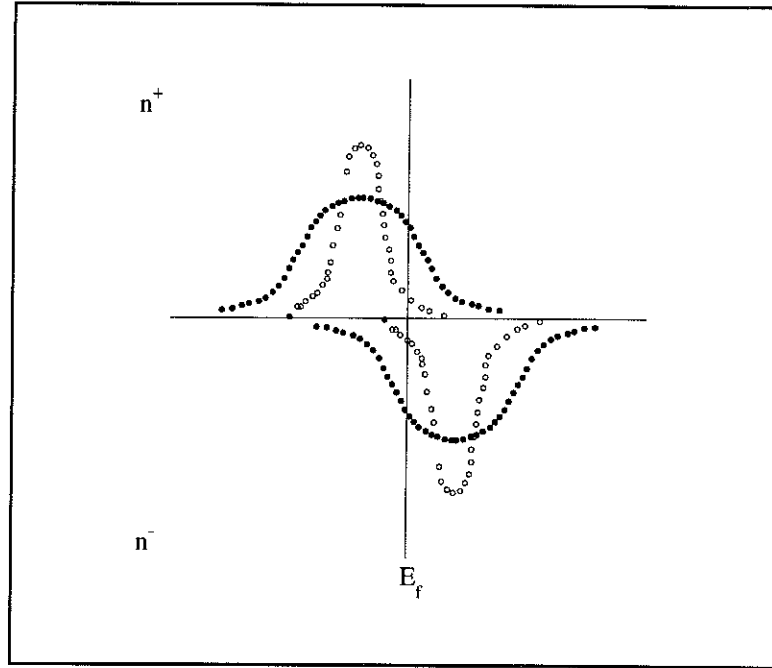


Fig. 4.3 - Schematic density of states of a spin split ( $n^+$  and  $n^-$ ) 3d band showing a narrowing of the surface states (open points) compared to the bulk states (full points).  $E_f$  is the Fermi level.

In addition to band narrowing at the surface, hybridisation effects between the film and the substrate may occur. For the case of hybridisation with s and p electrons of the substrate, this can be expected to cause band broadening and therefore moment reduction.

Conversely, for magnetic overlayers on 4d and to a lesser extent 5d substrates, 3d-4d and 3d-5d hybridisation effects may lead to the induction of a substantial polarisation on 4d and 5d atoms.

#### 4.2.2 Experimental results

Experimental data on directly measured moments is rare due to experimental difficulties and only a handful of publications exist. The main experimental techniques employed to-date are spin polarised low energy electron diffraction (SPLEED), magnetometry measurements and more recently, polarised neutron reflectivity (PNR).

SPLEED measurements are limited to free surfaces and evaluation of the magnetic moment is difficult [7]. It has been applied to an investigation of the surface moment of Fe and Ni. Surface moment enhancement is found to be larger for Fe (110) (38 +/- 2 %) compared with Ni (001) (5 +/- 5 %) [7], which is in agreement with the fact that Fe is a weak ferromagnet and Ni is a strong ferromagnet, as discussed above.

Magnetometry measurements enable moments to be measured directly but corrections for substrate contributions are often difficult. Results of magnetisation measurements

on a one monolayer and two layer Fe (110) film deposited on W (110) and coated by Ag [8] are reported in table 4.1. An enhancement of 14% and 11% respectively is observed for the ground state moment compared with the bulk. The value extrapolated to 0 K is enhanced by 14 % and 11 % with respect to the bulk value for the one monolayer and two layer film respectively.

Magnetometry measurements have also been employed to determine the existence of a Cr moment of  $3 \mu_B$  in a monolayer of Cr on Fe (100) [9].

PNR is currently being developed [10] and appears to be a promising technique for moment determination in ultra-thin films. Recently, PNR results for bcc Fe films deposited on Ag (001) with different coatings have been reported [11], as shown in table 4.1. A significant moment enhancement was again observed (table 4.1) and coatings with Ag and Cu did not lead to a significant change.

Substrate	Fe thickness	Capping	Fe moment ( $\mu_B$ )	T (K)	Ref
W (110)	1 ml	Ag	$2.53 \pm 0.12$	0 K	[8]
W (110)	2 ml	Ag	$2.46 \pm 0.15$	0 K	[8]
Ag (001)	5.5 ml	Ag	$2.58 \pm 0.09$	300 K	[11]
Ag (001)	5.8 ml	Cu	$2.48 \pm 0.09$	300 K	[11]
Ag (001)	5.7 ml	Cu	$2.50 \pm 0.10$	300 K	[11]

*Table 4.1 - Experimentally determined magnetic moments in ultra-thin Fe films.*

In the case of Pd / Co / Pd sandwich structures with Co thicknesses around 20 Å, PNR results [12] were interpreted by assuming  $\mu_{Co} = 1.84 \mu_B$  which corresponds to a  $0.1 \mu_B$  enhancement with respect to bulk Co. However, it is also possible to assume a polarisation of  $0.5 \mu_B$  in a 5 Å layer at each Co / Pd interface.

Finally surface roughness, or stepped surfaces have been found to lead to moment enhancement. For example annealing of a rough Fe surface to induce a smooth surface was found, by magnetometry measurements, to reduce the magnetic moment by  $0.5 \mu_B$  [13].

#### 4.2.3 Theoretical results

Unlike experimental results, many theoretical results exist for ground state moments in ultra-thin films. The most commonly used method is ab initio energy band calculations employing mainly the full potential linearised augmented plane wave method (FLAPW) based on local spin density (LSD) functional theory (for an overview of this procedure see [14]). It is believed that this method is accurate in predicting ground state moments.

Calculations for a 7 layer Fe (001) free standing film [15] enable the thickness dependence of surface perturbation to be evaluated, as shown in table 4. Moment enhancement is found to decrease rapidly away from the surface layer.

Layer no.	S	S - 1	S -2	C
Moment ( $\mu_B$ )	2.98	2.35	2.39	2.25

*Table 4.2 - Calculated ground state moment profile in a seven layer Fe (001) film ; S denotes the surface layer and C denotes the centre layer, from ref. [15].*

Theoretical calculations predict that moment enhancement is less for densely packed planes, as can be seen from expression (4.9). For example the moment on a Fe (100) surface is expected to be enhanced by 30% [16], [17] but only by 20% for a clean Fe (110) surface [18], [19].

Hybridisation effects have been considered by calculating the moment in a monolayer film deposited on various substrates or non-magnetic overlayers on magnetic substrates. These hybridisation effects can have two consequences. Firstly, a reduction in the interface moment of a magnetic film. Secondly, a polarisation of the substrate or the overlayer. At an Fe / W interface, for example the Fe moment is reduced to  $2.17 \mu_B$  and a weak W polarisation of  $0.05 \mu_B$  is induced [14]. In general, hybridisation effects are negligible for Ag and Au substrates but more significant for non-magnetic transition metal substrates (Cu, W ..) and for paramagnetic transition metals (Pt, Pd ..) [20]. A large moment induction in Cr ( $3.6 \mu_B$ ) is found for a Cr overlayer on Fe [21].

Epitaxial strain can also influence the ground state magnetic moment and it is even possible that a lattice expansion greater than 5% can cause a transition to ferromagnetism in Pd [22] and fcc Co can become non-magnetic by a 4% lattice contraction [14].

#### **4.2.4 Concluding remarks**

- Experimental measurements for surface / interface ground state moments have been limited until now by technical difficulties. Such measurements are important in order to understand thin film magnetism.
- Theoretical calculations assume that films are ideal. Roughness and interface mixing has not been considered theoretically. Such calculations are essential in order to attain a better contact between experiment and theory.

### 4.3 Thin film anisotropy

The magnetic anisotropy has been one of the most widely studied properties of ultra-thin films to-date. It is often found to be much greater than in bulk materials and found to be thickness dependent. In this section we shall firstly discuss the various sources of anisotropy in a thin film. We shall then examine how these various contributions can be deduced experimentally and go on to present an overview of experimental results. Finally, we examine the origin of surface and interface anisotropy from a theoretical perspective.

#### 4.3.1 Sources of anisotropies

In order to understand experimental results, one must consider all sources of anisotropy which contribute to the total magnetic anisotropy.

- volume magnetocrystalline anisotropy

In all layers except the surface / interface layers (i.e. volume layers), the local environment of each atom is the same as in the bulk. As magnetocrystalline anisotropy is essentially an on-site interaction, it can be assumed that the magnetocrystalline anisotropy, at 0 K, of the atoms in the volume layers is the same as in the bulk. For a cubic film, for example, the magnetocrystalline anisotropy of the volume layers is given by (4.4).

- shape anisotropy

Due to the long range of dipolar interactions, calculation of these interactions is a formidable task. It is common to define fictitious magnetic charges (analogous to electrostatic charges) and the dipolar interactions are determined by surface and volume charges. For the case of uniform magnetisation, only surface charges need to be considered and they are equal to:

$$\mathbf{M} \cdot \mathbf{n} \quad (4.12)$$

where  $\mathbf{M}$  is the magnetisation vector and  $\mathbf{n}$  is a unit vector normal to the surface at a considered point. From this, it is defined that the dipolar energy ( $E_{\text{dip}}$ ) of a uniformly magnetised thin film is :

$$E_{\text{dip}} = -2\pi M^2 \sin^2 \phi \quad (4.13)$$

where  $\phi$  is the angle between  $\mathbf{M}$  and the film normal. Relation (4.13) shows that thin films will have a shape anisotropy, which is quantified by the second order shape anisotropy constant ( $K_{\text{dip}}$ ) :

$$K_{\text{dip}} = -2\pi M^2 \quad (4.14)$$

Shape anisotropy favours in-plane magnetisation (this can be seen directly from the basic expression for dipolar interactions given in expression (4.2)). Note that, for ultra-thin films, (4.13) can still be applied even when the magnetisation is not saturated because the lateral dimensions of the magnetic domains are usually much greater than the film thickness. In 3d materials, the shape anisotropy is in general much larger than cubic magnetocrystalline anisotropy (see fig. 4.4 for a comparison for Fe).

- Surface magnetocrystalline anisotropy

Due to the loss of co-ordination at a surface, the surface atoms are sitting in sites of reduced symmetry which gives rise to surface anisotropy. Surface anisotropy may have both an in-plane and an out-of-plane character. For the case of surfaces such as hcp (0001), cubic (001) and (111), only out-of-plane anisotropy is involved to second order. The surface anisotropy energy between the film normal and the film plane ( $E'_s$ ) may be expressed phenomenologically as a function of the angle between the total magnetic moment and the film normal ( $\phi$ ):

$$E_s = K'_s \sin^2\phi \quad (4.15)$$

where  $K'_s$  is the second order out-of-plane surface anisotropy constant with units of energy per unit area. For a cubic (110) surface, both out-of-plane and in-plane anisotropies are present to second order, and the anisotropy energy in this case is :

$$E_s = K'_s \sin^2\phi + K_s \sin^2\phi \sin^2\theta \quad (4.16)$$

where  $\theta$  is the angle between the total magnetic moment and the in-plane [001] axis and  $K_s$  is the in-plane surface anisotropy constant. Typically, transition metal surface anisotropy energies are of the order of 0.1 meV / atom (see fig. 4.4 for Fe (110)).

- Magnetoelastic anisotropy

The magnetoelastic energy of a crystal is that part of the energy which arises from an interaction between the magnetisation and the mechanical strain of the lattice. For an unstrained lattice, the magnetoelastic energy is defined as being equal to zero. The presence of large epitaxial strains in ultra-thin films induces a large magnetoelastic anisotropy energy [23]. If one assumes that all layers are uniformly strained, then the expression for the magnetoelastic energy is the same as in the bulk. The magnetoelastic energy expressions for all symmetries are given in reference [24]. Two important examples, which we shall use further on, are :



1. - the out of plane magnetoelastic anisotropy for a cubic (001) film is :

$$E_s = K'_{mel} \sin^2\phi$$

where, the out of plane magnetoelastic anisotropy constant ( $K'_{mel}$ ) is :

$$K'_{mel} = (B\gamma,2) (\epsilon_{out} - \epsilon_{in}) \quad (4.17)$$

2. the in-plane magnetoelastic anisotropy for a cubic (110) film is :

$$E_{mel} = K_{mel} \sin^2\theta$$

where the in-plane magnetoelastic anisotropy constant ( $K_{mel}$ ) is :

$$K_{mel} = (B\gamma,2 - B\epsilon,2) (\epsilon_{in} - \epsilon_{out}) \quad (4.18)$$

In (4.17) and (4.18),  $\epsilon_{in}$  and  $\epsilon_{out}$  are the in-plane and out-of-plane strains respectively (assumed to be isotropic in the plane) and  $B\gamma,2$  and  $B\epsilon,2$  are the magnetoelastic constants.  $B\gamma,2$  and  $B\epsilon,2$  describe the magnetoelastic energy associated with strains along the cube edges and cube diagonals respectively [24]. The value of  $K_{mel}$ , for example, for an Fe film with a 5 % strain is 0.375 meV / atom (fig. 4.4).

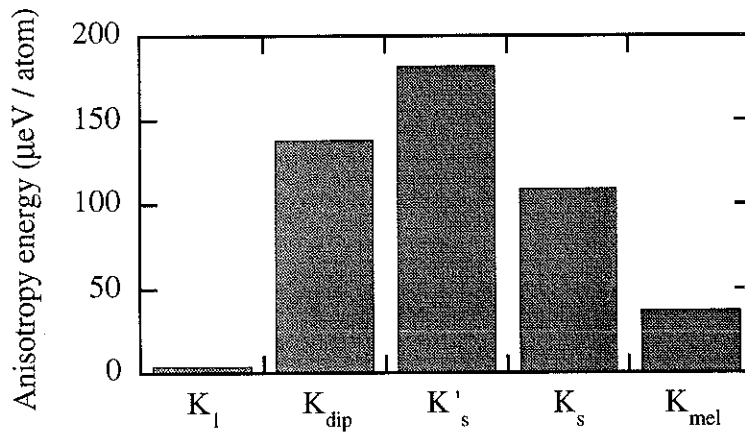


Fig. 4.4 - Typical absolute values of the anisotropy constants in Fe (110) films on W (110) ;  $K_l$ ,  $K_{dip}$  from bulk data at 300K [3],  $K_{mel}$  from bulk data for a planar expansive 5% strain [24] and  $K'_s$  and  $K_s$  at 300 K [25].

### 4.3.2 Experimental analysis

The understanding of the various contributions to experimentally measured thin film anisotropies requires a subtle analysis. Consider, first, the case of an un-strained cubic (001) film. The anisotropy energy per unit volume between the film normal and the film plane ( $K'_{\text{tot}}$ ) is the sum of volume magnetocrystalline, dipolar and surface magnetocrystalline contributions :

$$K'_{\text{tot}} = K_{\text{dip}} + \frac{K_1}{2} + \frac{2 K'_s}{d} \quad (4.19)$$

where all anisotropy terms are limited to their lowest order and  $d$  is the film thickness. The last term represents the contribution of the surface magnetocrystalline anisotropy per unit volume to the total anisotropy and it is assumed that the surface anisotropy is the same for both surfaces (interfaces). If all anisotropy constants are thickness independent, then  $K'_{\text{tot}}d$  varies linearly with  $d$  ; the slope is determined by the volume contributions ( $K_{\text{dip}} + K_1/2$ ) and the intercept is determined by the surface contribution ( $2K'_s$ ) (figure 4.5a for  $2K'_s < 0$ ). (Alternatively, for a plot of  $K'_{\text{tot}}$  versus  $1/d$ , the intercept is determined by the volume contributions and the slope is determined by the surface contributions).

In real epitaxial films, the presence of strains is such that it is essential to include magnetoelastic terms in the analysis of thin film anisotropy. As discussed in chapter 3, for thicknesses below a critical thickness ( $d_c$ ), the epitaxial strain is constant, then :

$$K'_{\text{tot}} d = \left( \frac{K_1}{2} + K_{\text{dip}} + K'_{\text{mel}} \right) d + 2K'_s \quad (4.20)$$

i.e.,  $K'_{\text{mel}}$  will contribute to  $K'_{\text{tot}}d$  as a volume term and the intercept of  $K'_{\text{tot}}d$  will yield  $2K'_s$ , as in the case of an un-strained film (fig. 4.5b). For  $d > d_c$ , however, the strain is expected to vary as  $1/d$  (see expression 3.5), then :

$$K'_{\text{tot}} d = \left( \frac{K_1}{2} + K_{\text{dip}} \right) d + K'_{\text{mel}}(d_c)d_c + 2K'_s \quad (4.21)$$

where  $K'_{\text{mel}}(d_c)$  is the value of the magnetoelastic anisotropy constant for the coherently strained region. In this case, the magnetoelastic term will appear to be a surface term and the intercept of the slope of  $K'_{\text{tot}} d$  will yield an effective surface anisotropy constant  $2K'_s{}^{\text{eff}}$ , which is given by :

$$2K'_s{}^{\text{eff}} = 2K'_s + K'_{\text{mel}}(d_c)d_c \quad (4.22)$$

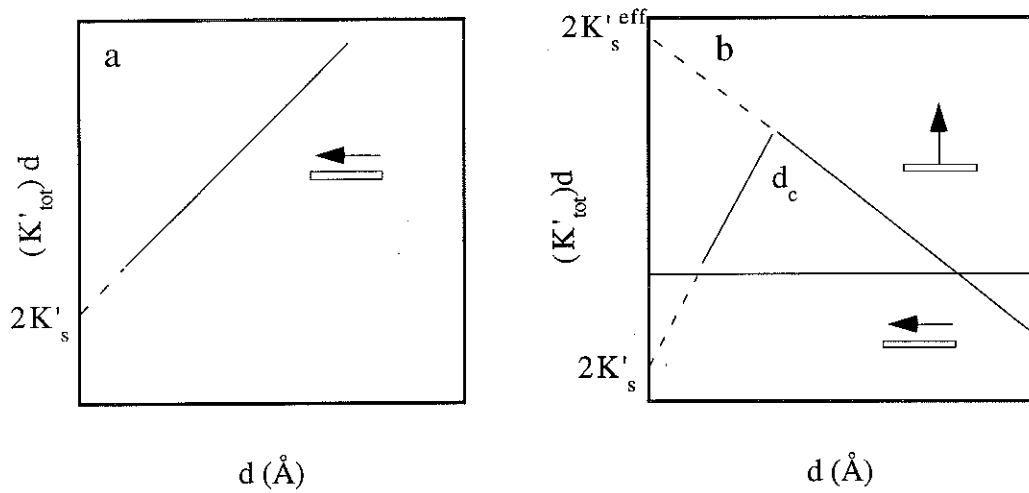


Fig. 4.5 a - For an un-strained film, the intercept  $K'_{tot}d$  as a function of  $d$  enables  $2K'_s$  to be determined ; b - For a strained film, for  $d < d_c$ , the strain is constant, and  $2K'_s$  can be obtained from the intercept but for  $d > d_c$  the strain varies as  $1/d$  and the intercept yields an effective surface anisotropy constant ( $2K'_s{}^{eff}$ ).

#### 4.3.3 Experimental results

In Ni (111) films deposited on Cu (111) [26], the easy axis (plane) of magnetisation was found to vary as a function of thicknesses. For  $d > 25 \text{ \AA}$ , the magnetisation was in-plane, for  $10 \text{ \AA} < d < 25 \text{ \AA}$ , the magnetisation was along the film normal and for  $d < 10 \text{ \AA}$ , the magnetisation was again in-plane. This was the first experimental observation of perpendicular magnetisation in thin films. It was later observed in Co / Pd multilayers [27] and in many systems subsequently (see table 4.3).

In Fe (110) films on GaAs (110) substrates [28], for  $d > 50 \text{ \AA}$ , an in-plane [001] easy axis of magnetisation was observed, but for  $d < 50 \text{ \AA}$ , the easy axis of magnetisation was found to be the in-plane  $[1\bar{1}0]$  axis. This was later interpreted as being the first experimental observation of in-plane surface anisotropy [29]. In-plane surface anisotropy was later found in Fe (110) films deposited on W (110) [25].

The difficulty in these studies is the evaluation of  $K_s$  (or  $K'_s$ ). The recent analysis of magnetic anisotropy in Ni (100) wedged structures deposited on Cu (100) [30] constitutes a paradigm for the evaluation of surface anisotropy (fig. 4.6). The variation of  $K'_{tot}d$  as a function of  $d$  shows a behaviour similar to that of figure 4.5 with  $d_c = 47 \text{ \AA}$ . (fig. 4.6). The intercept of the data for  $d < d_c$  enables  $2K'_s$  to be deduced as  $-0.7 \text{ erg.cm}^{-2}$ . The intercept of the data for  $d > d_c$  enables  $2K'_s{}^{eff}$  to be deduced and from (4.22) one finds  $K'_{mel}(d_c) = 2.7 \times 10^6 \text{ erg.cm}^{-3}$ .

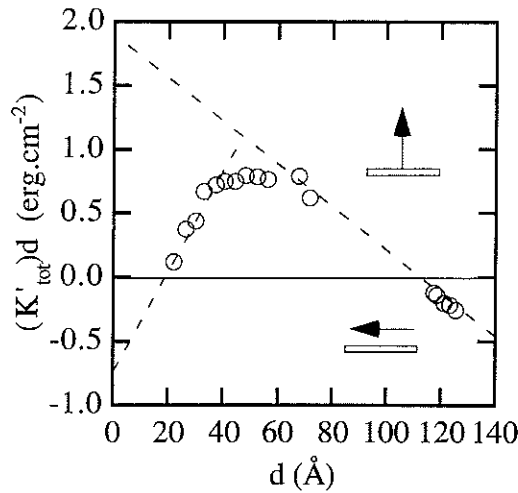


Figure 4.6 -  $K'_{tot}d$  as a function of  $d$  for Ni (100) deposited on Cu (from ref. [30])

In most cases, however,  $d_c$  is small ( i.e.  $2\text{\AA}$  for Fe (110) on W (110), as discussed in chapter 3) and  $K'_s$  (or  $K_s$ ) cannot be directly deduced from experimental measurements. One generally obtains an effective surface anisotropy constant to which the exact contribution of  $K'_s$  ( $K_s$ ) or  $K'_{mel}$  ( $K_{mel}$ ) are not known. Reviews of such analysis can be found in reference [31] for ultra-thin epitaxial Fe, Co and Ni films and in [32] for Co / X multilayers, where X = Ag, Au, Mo, Pd and Pt.

The most significant results of effective surface anisotropies are gathered in table 4.3. From this it appears that free Ni surfaces have an easy plane anisotropy, X / Ni interfaces all show in-plane anisotropy with the exception of X = W. Free Co surfaces show easy plane anisotropy, whereas X / Co interfaces show perpendicular easy axis. Free Fe surfaces show perpendicular anisotropy as well as most X / Fe interfaces with the exception of X = W.

An interesting feature of interface anisotropy has recently been observed in X / Co / Y tri-layers, where X and Y are Ag, Au, Cu or Pd [33]. In these systems, the film normal is an easy axis of magnetisation for small Co thicknesses. The anisotropy energy between the film normal and the film plane is found to be maximum for coatings of a monolayer thickness, which is attributed to electronic effects.

Surface / interface roughness is found in general to lead to a decrease in surface anisotropy [34]. Surface steps, on the other hand have been found to have a higher surface anisotropy at 300 K compared with a flat surface [35].

System	X	$K_s^{\text{eff}}$ (erg.cm <sup>-2</sup> )	$K_s^{\text{eff}}$ (erg.cm <sup>-2</sup> )	Ref.
X / Ni (111)	UHV	-0.48		[31]
	Cu	-0.22		[31]
	Pd	-0.22		[31]
	Re (0001)	-0.19		[31]
	W (110)	+0.02		[31]
Ni / Co (X) / Ni	(001)	+0.23		[36]
	(110)	<+0.19		[36]
	(111)	+0.42		[36]
X / Co (0001)	UHV	-0.46		[37]
	Au	+0.35		[38]
	Pd	+0.60		[38]
	Pt	+0.70		[38]
	Cu	+0.15		[38]
X / Fe (001)	UHV	+0.89		[31]
	Au	+0.29		[31]
	Ag	+0.55		[31]
X / Fe (110) / W (110)	UHV	-1.0	-0.30	[32]
	Cu	-0	-0.38	[31]
	Ag	-1.4	-0.29	[31]
	Pd	-	-0.29	[31]
	Au	-1.2	+0.05	[31]
X / Fe (110)	Au	+0.71 (4K)		[31]
	Ag	+		[31]

Table 4.3 - Example of some experimentally determined effective surface / interface anisotropy constants of epitaxial films (in units of erg.cm<sup>-2</sup>).

#### 4.3.4 Theoretical results

In this section we shall address the problem of the physical origin of surface anisotropy. Phenomenologically, it is easy to understand that as the symmetry of the surface is different from the volume so too should the magnetic anisotropy be different. That surface anisotropy should be much larger than bulk anisotropies can be understood from the fact that the lower the symmetry the higher the anisotropy energy.

These ideas were first discussed by Néel [39] when he developed a simple phenomenological model for anisotropy calculations. At the time of Néel's calculations, epitaxial films did not exist and he did not show how strain and interface

effects can also contribute to interface anisotropy. In the following section we show how these effects contribute within the framework of the Néel model.

The Néel model is however based on symmetry arguments only and it cannot account for the fact that not only is the symmetry of a given site dependent on its co-ordination but so too is its band structure. Therefore, for the case of transition metals especially, the Néel model cannot be expected to give a full explanation for surface anisotropy. For a complete understanding of surface anisotropy one must turn to band structure calculations which are rather more complicated and less transparent. For bulk materials, the accuracy of band structure calculations is not yet sufficient to guarantee that even the correct sign of anisotropy is obtained because bulk anisotropies in cubic 3d metals are less than 5  $\mu\text{eV}$  / atom. As surface anisotropies are of the order of 100  $\mu\text{eV}$  / atom, band structure calculations are more reliable.

Following our discussion of the Néel model we shall discuss the results of band structure calculations for monolayers in an attempt to discern the relationship between the band structure and anisotropy. Following that we shall look at band structure calculations for interfaces.

#### •Néel model

The model considers an ensemble of parallel localised moments. The central idea is that the magnetic anisotropy at a given atomic site may be decomposed into a sum of pair interactions with neighbouring atoms. The pair energy is written as a phenomenological function of the orientation of the moments with respect to the pair axis and the total anisotropy is obtained by summing over all pairs. The model provides an elegant method for deriving a phenomenological anisotropy expression for any symmetry. For example, it shows that the second order anisotropy energy for cubic symmetry averages to zero except at the surface due to the fact that a surface atom has an asymmetrical arrangement of pairs around it. The model also shows how strains will induce a second order anisotropy in cubic crystals. Indeed, Néel used this fact in order to evaluate his phenomenological parameters from measured cubic magnetoelastic anisotropy constants.

Consider a pair of atoms  $i$  and  $j$  with a moment of  $\mathbf{M}_i$  and  $\mathbf{M}_j$  oriented at an angle  $\phi$  to a line ( $r_{ij}$ ) joining their centres (fig. 4.7). The pair interaction energy,  $w_{ij}$ , to second order, can be written as:

$$\begin{aligned} w_{ij} &= (\mathfrak{J} + \mathfrak{M} \partial r) P_2(\cos \phi) \\ &= (\mathfrak{J} + \mathfrak{M} r_0 \epsilon_{ij}) \left( \cos^2 \phi - \frac{1}{3} \right) \end{aligned} \quad (4.23)$$

where  $r_0$  is the distance between atoms  $i$  and  $j$ ,  $\mathfrak{K}$  is a phenomenological magnetocrystalline anisotropy constant,  $\mathfrak{M}_{r_0}$  is a phenomenological magnetoelastic anisotropy constant and  $\epsilon_{ij}$  is the strain along the bond axis.

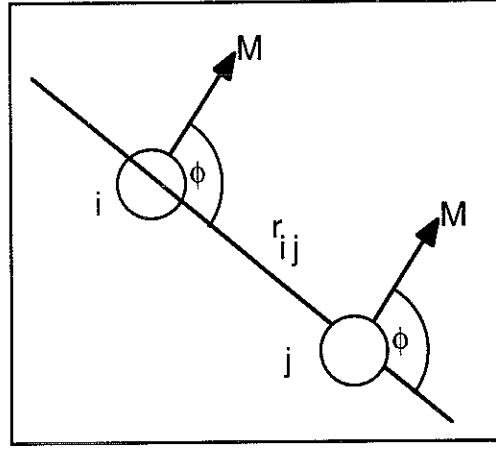


Fig.4.7 - Schematic drawing of the pair model for anisotropy calculations.

The total energy is obtained by summing all pair interactions over first nearest neighbours (neglecting interactions with second and higher nearest neighbours). For the surface of a cubic (110) lattice and neglecting strain, Néel showed the surface anisotropy to be [39] :

$$\begin{aligned}
 M // [1\bar{1}0] &\Rightarrow E = \frac{1}{6} \mathfrak{K} \\
 M // [001] &\Rightarrow E = 0 \\
 M // [110] &\Rightarrow E = -\frac{1}{6} \mathfrak{K}
 \end{aligned} \tag{4.24}$$

According to the sign of  $\mathfrak{K}$ , either the  $[1\bar{1}0]$  or the  $[110]$  will be an easy axis. The  $[001]$  axis, which is the easy direction in cubic Fe, is not expected to be favoured by surface anisotropy.

We have extended Néel's calculation by including an interface contribution and a strain contribution [40]. For an un-strained A bcc (110) / B bcc (110) interface, where A is a magnetic material and B is a non-magnetic material, the magnetocrystalline interface anisotropy is now :

$$\begin{aligned}
 M // [1\bar{1}0] &\Rightarrow E = \frac{1}{6} (\mathfrak{K}_{AA} - \mathfrak{K}_{AB}) \\
 M // [001] &\Rightarrow E = 0 \\
 M // [110] &\Rightarrow E = -\frac{1}{6} (\mathfrak{K}_{AA} - \mathfrak{K}_{AB})
 \end{aligned} \tag{4.25}$$

where  $\mathfrak{Z}_{AA}$  represents the magnetocrystalline anisotropy at A sites due to other A sites and  $\mathfrak{Z}_{AB}$  represents the magnetocrystalline anisotropy at A sites due to B sites. (4.25) shows that the presence of the B layer can cause the easy axis to change compared with the free surface case (4.24), as observed experimentally for some X / Fe (110) interfaces (see table 4.3).

For the case of an isotropically strained interface, i.e.  $\varepsilon_{\xi\xi} = \varepsilon_{\eta\eta} = \varepsilon_{\zeta\zeta} = \varepsilon$ , one finds that the interface anisotropy is now :

$$\begin{aligned} M // [1\bar{1}0] &\Rightarrow E = \frac{1}{6}(\mathfrak{Z}_{AA} - \mathfrak{Z}_{AB}) + \frac{1}{6}(\mathfrak{M}_{AA} - \mathfrak{M}_{AB})r_0\varepsilon \\ M // [001] &\Rightarrow E = 0 - \frac{1}{6}(\mathfrak{M}_{AA} - \mathfrak{M}_{AB})r_0\varepsilon \\ M // [110] &\Rightarrow E = \frac{-1}{6}(\mathfrak{Z}_{AA} - \mathfrak{Z}_{AB}) - \frac{2}{6}(\mathfrak{M}_{AA} - \mathfrak{M}_{AB})r_0\varepsilon \quad (4.26) \end{aligned}$$

where  $\mathfrak{M}_{AA}r_0$  represents the magnetoelastic anisotropy at A sites due to other A sites whereas  $\mathfrak{M}_{AB}r_0$  represents the magnetoelastic anisotropy at A sites due to B sites. As  $\mathfrak{Z}_{AA}$  and  $\mathfrak{M}_{AA}r_0$  can be expected to be of the same order of magnitude [39], and as  $\varepsilon$  is typically of the order of a percent, it appears that strains will not greatly modify the interface anisotropy. This is why, in our analysis of interface anisotropy in the Fe / W system (chapter 5) the strain dependence of interface anisotropy (expression (4.26)) will be neglected.

Note finally, that in an extension of the Néel model, the influence of surface roughness on anisotropy may be evaluated. Lowering of anisotropy is obtained [41], in agreement with experimental results.

#### •Band structure calculations

##### •Free standing monolayer

Bruno has calculated the band structure of 3d monolayers by means of a tight binding approximation [42]. An important parameter is the splitting ( $\Delta_{\text{crys}}$ ) between the in-plane orbitals and the out of plane orbitals.  $\Delta_{\text{crys}}$  arises due to the fact that the Coulombian interactions are greater in the more localised out-of-plane orbitals compared with the less localised in-plane orbitals. The monolayer anisotropy energy and orbital moment are then obtained by calculating the effect of spin orbit coupling by means of perturbation theory. The calculations show that the anisotropy energy depends mainly on band filling and less on details of the band structure.

Similar results have been obtained by means of ab initio FLAPW band structure calculations for monolayers [43]. The results are schematised in figure 4.8 as a function of band filling, where  $E_a$  is the total anisotropy energy between the film normal and the



film plane ( $E_a > 0$  corresponds to perpendicular magnetisation),  $\Delta E^{dd}$  is the contribution to  $E_a$  arising from mixing between occupied minority band states and un-occupied minority band states due to spin orbit coupling, and  $\Delta E^{ud}$  corresponds to mixing between occupied majority band states and unoccupied minority band states.  $\Delta E^{dd}$  is greater than  $\Delta E^{ud}$  showing that the dominant contribution to anisotropy arises from minority band states only. In perturbation calculations, this result is transparent for strong ferromagnets. The contribution to the anisotropy due to the coupling between two states is inversely proportional to their energy difference. As coupling occurs between occupied and un-occupied states, this contribution will be maximum for states close to the Fermi level.

Figure 4.8 shows that as the band filling increases, the easy anisotropy orientation passes from the normal to the plane and back to the film normal. For Fe, the number of valence electrons is 8, which corresponds approximately to a band filling at which the anisotropy changes sign. In fact, different ab-initio calculations are in agreement that a free standing monolayer of Fe has a relatively weak easy axis along the film normal (table 4.4). Ab-initio calculations show that free-standing Co monolayers have a strong in-plane anisotropy (table 4.4).

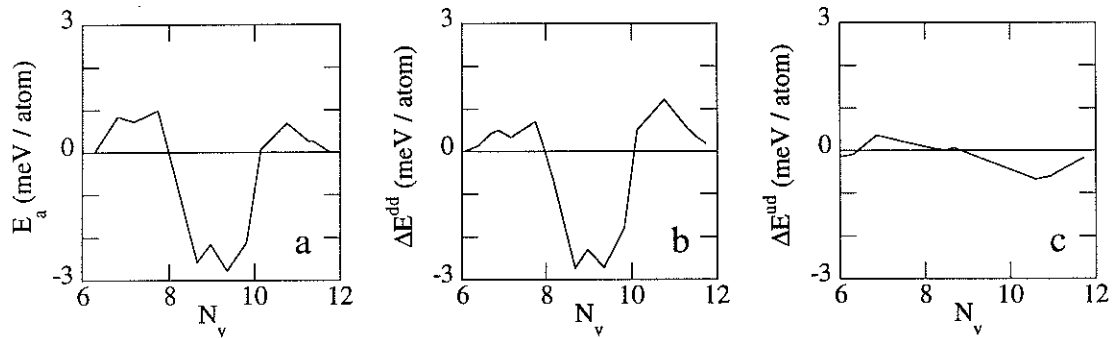


Fig. 4.8 - Ab-initio anisotropy calculations for an Fe (001) monolayer (lattice parameter 3.16 Å) as a function of the number of valence electrons ( $N_v$ ); a -  $E_a$ , b -  $\Delta E^{dd}$  and c -  $\Delta E^{ud}$  (see text for definition), from reference [43].

The influence of strain has also been investigated by calculating the anisotropy energy of an Fe monolayer as a function of lattice spacing [43]. No change in the sign of the anisotropy is found for expansions up to 10 % and contractions down to 9 % from the lattice parameter of bulk Fe. The former leads to a 27 % decrease in anisotropy (0.27 meV / atom) and the latter leads to 13 % increase (0.42 meV / atom) compared with an un-strained monolayer.

Finally, the angular dependence of surface anisotropy calculated by means of ab-initio calculations is in agreement with Néel's phenomenological expression, i.e. expression (4.14) [43].

•Interface anisotropy

The influence of an interface was investigated by performing ab-initio calculations for (Co / X) multilayers, where X = Cu, Ag or Pd by means of the linear muffin tin orbitals (LMTO) method in the atomic spheres approximation using the local spin density approximation [44]. The easy axis of anisotropy is found to be perpendicular in all these systems (table 4.4). The strength of the perpendicular anisotropy is found to be highest for Pd and less for Ag and Cu.

Recent calculations [45] have found, on the other hand that Cu / Co systems exhibit an easy plane interface anisotropy (table 4.4). These calculations [45] show that  $\Delta E^{\text{ud}}$  is relatively unaffected by the presence of the interface and that the anisotropy change compared with a free monolayer arises mainly from changes in  $\Delta E^{\text{dd}}$ .

System	X	$2K'_s$ (meV / atom)	a (Å)	Ref.
X / Co / X	UHV	-3.60	2.9	[46]
	UHV	-1.35	2.6	[47]
	Pd (111)	+0.84(6)	2.8	[44]
	Pd (001)	+0.46(22)	2.8	[48]
	Cu (111)	+0.20	2.6	[44]
	Cu (001)	-0.01	2.6	[45]
	Ag (111)	+0.15	2.8	[44]
X / Fe / X	UHV (001)	+0.38	2.9	[47]
	UHV (001)	+0.47	2.6	[49]
	Pd (111)	+0.43	2.7	[50]
	Pt (111)	-0.03	2.7	[50]
	Ag (111)	+0.57	2.9	[50]
	Au (111)	+1.03	2.9	[50]

Table 4.4 - Ab-initio calculations for interface anisotropy for Fe and Co systems from different sources (references indicated in square brackets).

### 4.3.5 Discussion

Due to the difficulties in both theoretical and experimental evaluation of surface anisotropy it is not possible to make a quantitative comparison of the magnitude of surface / interface anisotropy between experiment and theory. We shall therefore only discuss the sign of anisotropy in the following.

For the case of a free surface, theoretical calculations and experimental findings are in agreement that Fe has a perpendicular easy axis whereas Co and Ni have easy plane anisotropy (compare table 4.3 with 4.4).

For the case of X / Fe and X / Ni interfaces, it appears that in most cases no difference in the easy axis of magnetisation compared with a free surface is observed experimentally, which is in good agreement with theoretical results. One exception is W where in both Ni and Fe it leads to an easy axis switching compared with a free surface.

For the case of Co, however the easy axis of X / Co interfaces is often found to be different compared with a free Co surface. Due to the fact that most Co films investigated to-date have been deposited on substrates or buffer layers with larger lattice parameters one can assume that if the films are strained then the strain is expansive. An expansive strain will favour the perpendicular direction. One can conclude that the observation of perpendicular magnetisation is not conclusive proof of perpendicular interface anisotropy especially for the case of Au / Co and Ag / Co.

Pd is found, both theoretically and experimentally, to cause the easy axis of Co to switch to the perpendicular direction compared with a free Co surface.

### 4.3.6 Concluding remarks

- It remains an experimental challenge to evaluate  $K_s$  (or  $K'_s$ ) in systems where anisotropy analysis in the  $d < d_c$  range is not possible.
- A correct evaluation of surface anisotropy (and not effective surface anisotropy) is indispensable in order to compare experimental results with theory.

## 4.4 Thermal excitations

### 4.4.1 Introduction

The understanding of magnetic order in 2D is a fundamental problem which has attracted much theoretical work for many years. In the past, experimental work was restricted to compounds with a particular crystallographic structure where the exchange interactions along one direction are much weaker than exchange interactions in the plane perpendicular to this direction. For magnetic studies, such compounds constitute pseudo 2D systems. The possibility of preparing magnetic films of monolayer thicknesses opens up new vistas for this subject.

### 4.4.2 Experimental results

One of the most universal properties of ultra-thin films is that the thermal variation of the magnetisation and ordering temperatures are thickness dependent. For example the 300 K value of the reduced magnetisation of Ni (111) on Re (0001) is shown in figure 4.9a as a function of film thickness. For thicknesses from 60 ml down to 15 ml, it decreases slowly with decreasing thickness, whereas for  $d < 15$  ml, it decreases rapidly. The Curie temperature ( $T_c$ ) shows a similar thickness dependence (fig. 4.9b). At 52 ml  $T_c$  is 616 K, to be compared with 627 K for bulk Ni, whereas for  $d = 3.2$  ml it is reduced to 340 K.

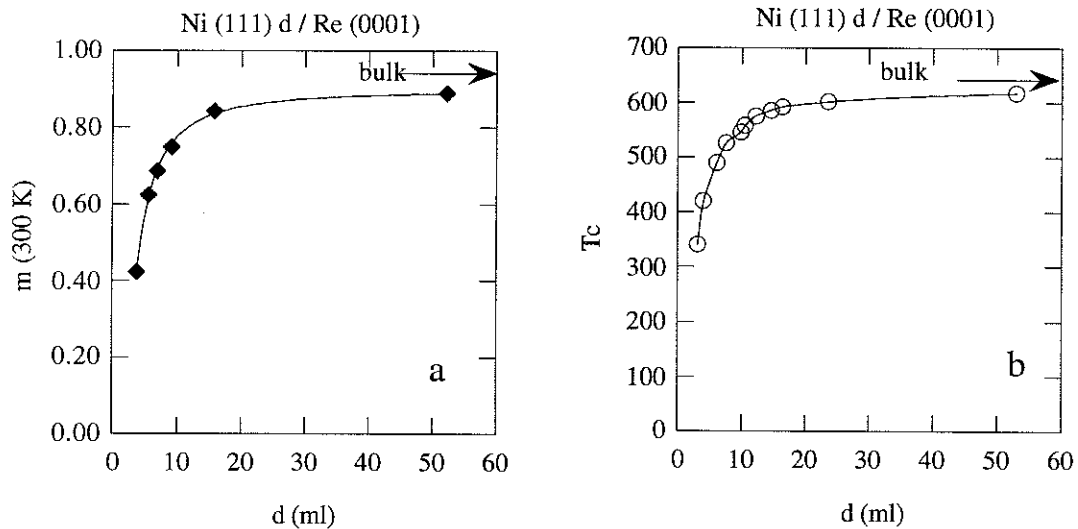


Fig. 4.9a Thickness ( $d$ ) dependence of the reduced magnetisation at 300 K ( $m$ ) and b - Curie temperature ( $T_c$ ) for Ni (111) deposited on Re (0001) ( data from reference [51])

Many studies have been devoted to Fe films, where it is possible to perform Mössbauer studies using  $^{57}\text{Fe}$  enriched films. The temperature dependence of the reduced hyperfine field of Fe (110) films on W (110) and coated by Ag is shown in figure 4.10 (from ref. [52]). The 300 K values increase from 0.89 for  $d = 3.2$  ml to 0.96 for  $d = 20.5$  ml and to 0.97 for bulk Fe.

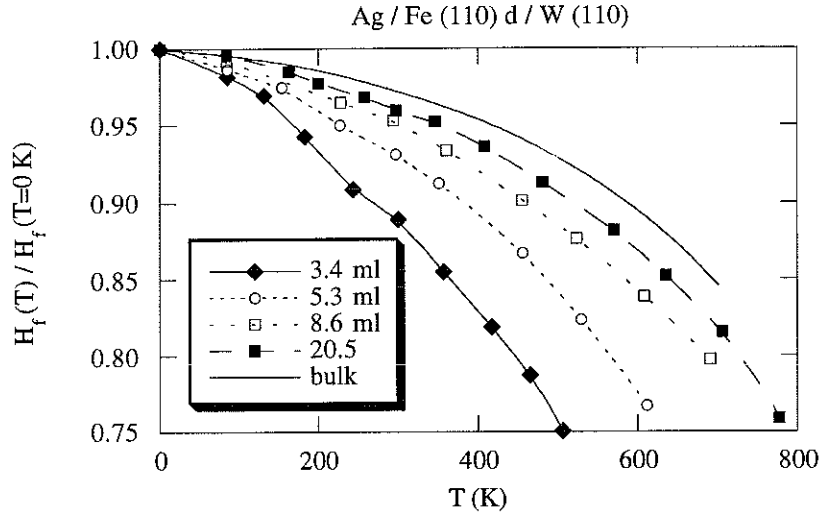


Fig. 4.10 - Reduced hyperfine field as a function of temperature for Ag / Fe (110) / W films of varying thickness ( $d$ ) (from reference [52]).

Magnetic studies have also been performed on monolayer films of Fe and Co. For a monolayer of Fe (110) on W (110) the Curie temperature was found to be 210 K [53] and when coated by Ag, the Curie temperature was found to increase to 300 K. SPLEED measurements on a monolayer Fe (100) film on Au (100) revealed the Curie temperature to be 300 K [54].

Contradictory results have been reported for monolayer Co (001) deposited on Cu (001), which highlights the experimental difficulty inherent in such measurements. Spin polarised photoemission investigations revealed that the Curie temperature was higher than 300 K, and that the spin polarisation did not show a temperature dependence between 100 K and 450 K [55]. Kerr magnetometry studies, on the other hand, showed that the Curie temperature was much less than 300 K [56].

Magnetic order in the sub-monolayer range has recently been investigated [57] in Fe (110) on W (110). The Curie temperature was found to vary monotonously with film coverage and was very sensitive to substrate deposition temperature, as explained in figure 4.11.

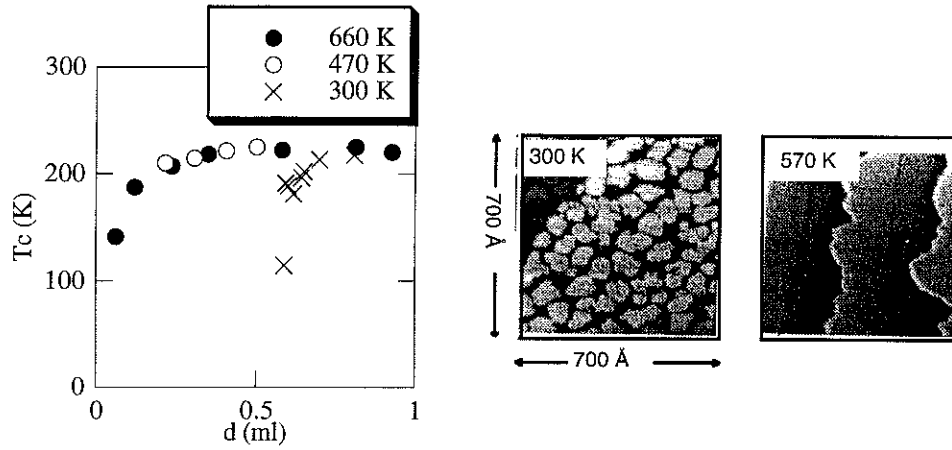


Fig. 4.11 - left- The Curie temperature as a function of sub-monolayer coverage ( $d$ ) for depositions at substrate temperature from 300 K to 660 K. The difference in the high temperature and low temperature depositions can be understood by examining SEM micrographs (right). At low temperatures, the sub-monolayer nucleates through islands and for higher temperatures the sub-monolayer grows in a stripe-like fashion on the bulk W substrate due to its stepped morphology (from ref. [57]).

#### 4.4.3 Theoretical results

In this section we shall examine thermal excitations from a theoretical perspective. First of all we shall discuss the case of a single monolayer. Then we shall address the problem of the thickness at which one expects the thermal excitations to change from 2D excitations to 3D excitations.

The thermal variation of the reduced magnetisation of a monolayer can be calculated from (4.8) for a 2D lattice, yielding :

$$\frac{M(T)}{M(0)}(2D) = 1 - \frac{1}{M(0)} \frac{1}{(2\pi)^2} \int_0^\infty \frac{4\pi q dq}{\exp(Dq^2 / k_B T) - 1} \quad (4.27)$$

The integral of (4.27) diverges logarithmically at the lower limit and therefore implying the existence of a non-null density of excitation states at 0K. This was interpreted by Bloch [58] to mean that no long range ferromagnetic order exists in a 2D lattice at finite temperatures. A more rigorous proof of the absence of long range ferromagnetic order at finite temperatures in 1D and 2D isotropic Heisenberg systems was later given by Mermin and Wagner [59].

As shown by the experimental results described in the above, magnetic order exists for a monolayer. It is now believed that the existence of 2D long range order results from dipolar interactions and anisotropy [60]. A simple physical picture to understand this phenomenon has been proposed by Arrot and Heinrich [61]. In a hypothetical 2D Heisenberg system with neither dipolar nor anisotropy interactions, large areas of spin

fluctuations can exist as their energy is finite and independent of their size thus impeding the stabilisation of long range ferromagnetic order. When an uniaxial anisotropy is considered, the energy of these spin fluctuations areas becomes proportional to the square of their radius and long range order is established.

These ideas can be seen mathematically by evaluating (4.27) in the presence of an uniaxial effective anisotropy field  $H_a$ , which gives:

$$\begin{aligned}\frac{M(T)}{M(0)}(2D, H) &= 1 - \frac{1}{M(0)} \frac{a^2}{(2\pi)^2} \int_0^\infty \frac{4\pi q dq}{\exp[Dq^2 / k_B T + (2\mu_B H_a / k_B T)] - 1} \\ &= 1 + \frac{a^2 k_B T}{2\pi M(0) D} \ln[1 - \exp(-2\mu_B H_a / k_B T)]\end{aligned}\quad (4.28)$$

showing that the presence of an easy axis uniaxial anisotropy removes the logarithmic divergence by opening a gap at the bottom of the spin wave spectrum.

An exact solution for the thermal variation of the reduced magnetisation of a 2D square lattice, taking into account both anisotropy and dipolar interactions, has recently been derived [60]. For the case of an uniaxial anisotropy favouring the film normal ( $K'_{\text{tot}} > 0$ , where  $K'_{\text{tot}} = K'_s - K_{\text{dip}}$ ), the thermal variation of  $m$  is :

$$\begin{aligned}m &= 1 - \left( \frac{1}{4\pi S} \frac{a^2 K_B T}{D} \ln \left[ 1 - \exp \left[ \frac{-K'_{\text{tot}}}{K_B T} \right] \right]^{-1} \right) \\ &= 1 - \left( Y \cdot T \ln \left[ 1 - \exp \left[ \frac{-Z}{T} \right] \right]^{-1} \right)\end{aligned}\quad (4.29)$$

where  $S$  is the spin per atom. For the case of  $K'_{\text{tot}} < 0$  (i.e. easy plane anisotropy) without the presence of in-plane surface anisotropy, the long range dipolar interactions are found to give rise to a pseudo-gap at the bottom of the spin-wave spectrum. In this case,  $m$  shows a faster thermal variation compared with the case of  $K'_s > 0$ . The influence of an in-plane surface anisotropy ( $K_s$ ) has not been examined in the literature to-date.

The thermal variation of  $m$  as a function of film thickness attracted much theoretical work in the sixties and seventies, with the results differing from author to author [62]. In the absence of suitable calculations, most experimental work is analysed by fitting  $m(T)$  to expression (4.9) and examining the thickness dependence of  $B$  [62]. The essential features of the thickness dependence of  $m$  can however be understood by

means of spin wave theory. In a thin film the excitation spectrum will vary as a function of film thickness, from 2D behaviour for films of a monolayer thickness to 3D behaviour for thicker films. In a thin film of  $N$  layers with interplanar spacing  $a'$ , the dispersion curve along the film normal,  $q_z$  is discrete. It can be expressed as:

$$q_z = \frac{2\pi n}{Na'} \quad (4.30)$$

where  $n$ , an integer which varies from 0 to  $N-1$ , represents the magnon excitation branch number. The  $n = 0$  branch corresponds to 2D excitations and the progressive population of  $n > 0$  branches corresponds to a transition from 2D excitations to 3D excitations. The low energy dispersion of the film can therefore be written as :

$$E_q = D \left( q_x^2 + q_y^2 + \left( \frac{2\pi n}{Nd} \right)^2 \right) + E_a \quad (4.31)$$

where  $E_a$  is the anisotropy energy in units of energy per atom. For the simplest case of perpendicular anisotropy ( $K'_{\text{tot}} > 0$ ) and assuming that only surface anisotropies are present, then :

$$E_a = \frac{2K'_s v_{\text{at}}}{Nd} \quad (4.32)$$

Equation (4.31) is phenomenological and a rigorous proof requires ab-initio calculations. We have calculated the spin wave dispersion curve as a function of thickness for Fe (110) films by assuming  $D = 330 \text{ meV} \cdot \text{\AA}^2 / \text{atom}$  (bulk value at 0 K ; from ref. [5]),  $a' = 2.0 \text{ \AA}$  and  $K'_s = 0.2 \text{ meV} / \text{atom}$  as shown in figure 4.12.

For a monolayer film (fig. 4.12a) only an  $m = 0$  branch exists (fig. 4.12a). For a two monolayer film (fig. 4.12b), the energy gap between the  $m = 0$  branch and the  $m = 1$  branch is 815 meV (9442 K). For a 5 monolayer film, there are five excitation branches (fig. 4.12c). The energy gap between the  $n = 0$  branch and the  $n = 1$  branch is now 32 meV (370 K). It therefore appears that 2D excitations will prevail up to 300 K even for thicknesses of a few monolayers. The influence of the above excitation spectra on the thermal variation of the reduced magnetisation can be evaluated from :

$$m = 1 - \frac{1}{z} \sum_{q,n} \frac{1}{\exp(E_q / k_B T) - 1} \quad (4.33)$$

where  $E_q$  is given by (4.31) and  $z$  is a normalisation factor. We evaluated (4.33) by summing  $q$  over the first Brillouin zone. In the x-y plane, the summation over  $q$  was taken to be continuous and was performed over a disc whose area is equal to the area of the first 2D Brillouin zone.



The calculated thermal variation of  $m$  from 0 K to 300 K is shown in figure 4.13 for a 1, 2 and 5 monolayer film. As the gap between the  $n = 0$  branch and the  $n = 1$  branch is  $> 300$  K, the  $n = 0$  branch contributes predominantly to the thermal variation of  $m$  and thus the number of excitations is approximately constant. Figure 4.13, however, shows that the thermal variation of  $m$  is thickness dependent. This arises because  $m$  is actually determined by the number of excitations per atom in each film.

Due to the reduction in the co-ordination at the surface, one can expect surface exchange weakening to exist. The simplest way of analysing this is to assume that the surface exchange scales directly with the co-ordination and that the average value of  $D$  in all layers for a bcc lattice is given by:

$$D(N) = \frac{N-1/2}{N} D_b \quad (4.34)$$

The influence of introducing this surface exchange weakening can be seen by comparing figure 4.14 with 4.13. It leads to a weakening of  $m$  at small thicknesses only. At 30 K, for example, for the 1 ml film, the calculation without surface exchange weakening gives a value of  $m = 0.98$  compared with  $m = 0.96$  for surface exchange weakening. For the 5 ml film, the difference is negligible (0.993 compared with 0.992).

In reality,  $D$  and  $E_a$  are temperature dependent because as  $m$  decreases both  $D$  and  $E_a$  decrease consequently. This dependence can be expressed as  $D(T) = mD(0)$  and  $E_s(T) = m^3 E_a(0)$ . In the temperature range over which the non-interacting spin wave theory is applicable ( $T < T_c / 3$ ), however, the temperature dependence of  $D$  and  $E_a$  is relatively weak and calculations for  $D$  and  $E_a$  varying with  $m$  yield similar results as calculations with  $D$  and  $E_a$  constant.

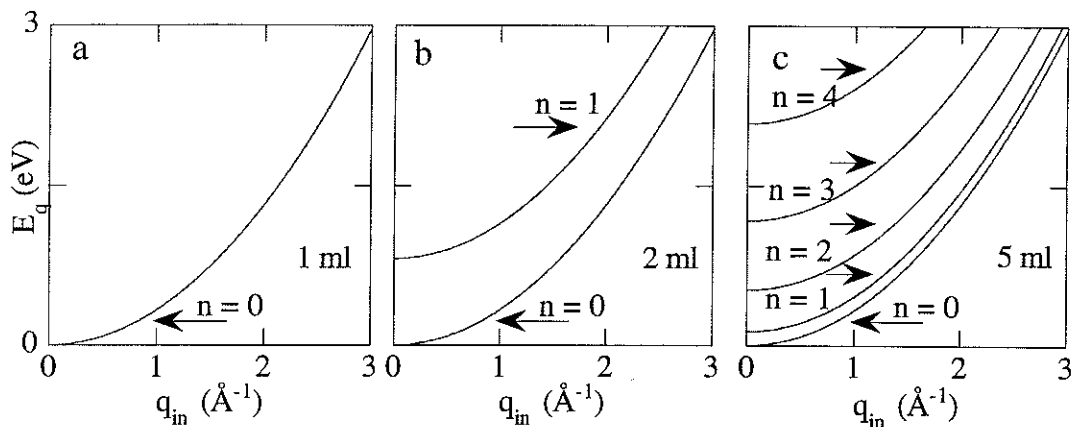


Fig. 4.12 - Spin wave dispersion curves for a - a monolayer, b - a two-layer film with the ground state ( $n=0$ ) and the first excited state ( $n=1$ ) and c - a 5 layer film with branches from  $n = 0$  to  $n = 4$ .

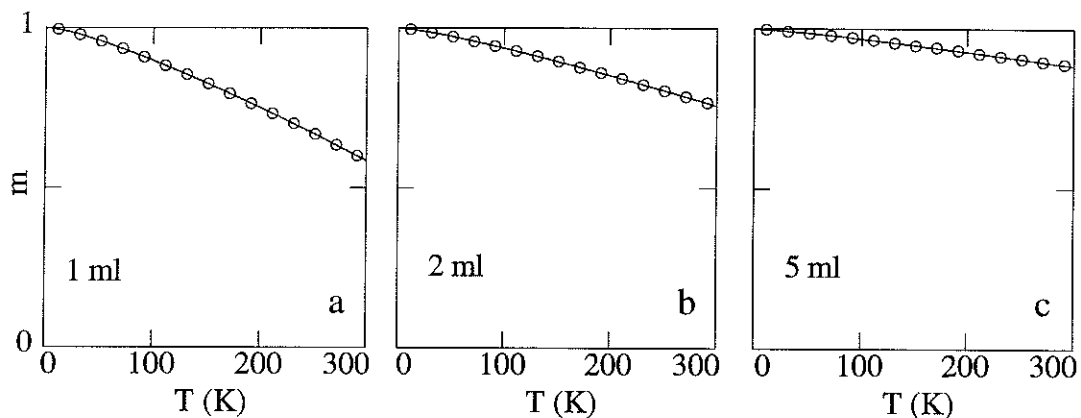


Fig. 4.13 - Thermal variation of the reduced magnetisation ( $m$ ) for a - one monolayer, b- two-layer and c- 5 monolayer film calculated from the spin wave dispersion curve shown in figure 4.12.

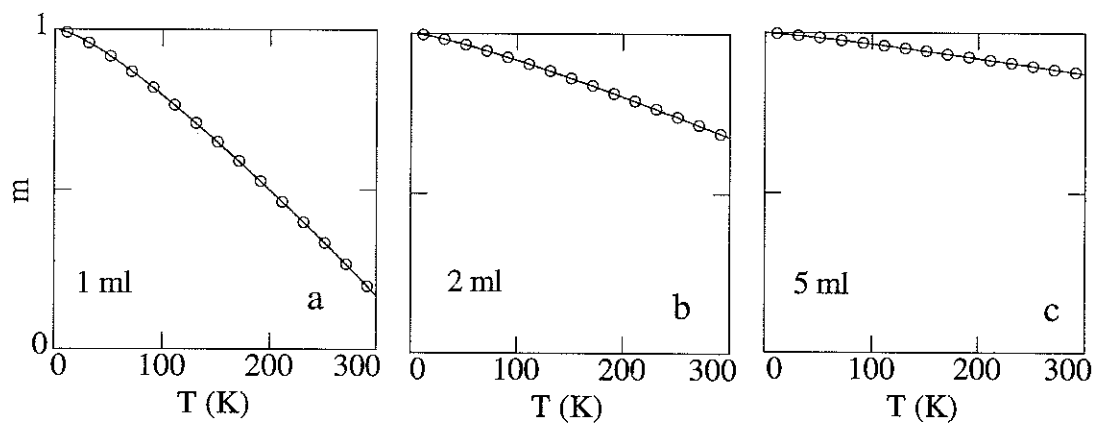


Fig. 4.14 - Thermal variation of the reduced magnetisation ( $m$ ) as in fig. 4.13 with the inclusion of surface exchange weakening.

Finally, it is interesting to note that at very low temperatures the magnetisation in a 1 ml film can be more stable than a 5 ml film, as shown in figure 4.15b. From 0 - 2 K, the thinner films have a higher value of  $m$ . Between 2 K and 5 K a transition occurs and the order is reversed to  $m$  being more stable in the thicker films. This can be understood by examining the spin wave dispersion of the lowest lying branch ( $m=0$ ) for different thicknesses (fig. 4.16a). As the film thickness decreases, the anisotropy energy gap increases. As the dominant mechanism for the stabilisation of  $m$  at very low temperatures is the anisotropy gap then the films with the higher anisotropy exhibit a higher magnetisation. For temperatures at which the thermal energy is greater than the anisotropy energy, then the value of  $m$  at a given temperature increases with the number of layers.

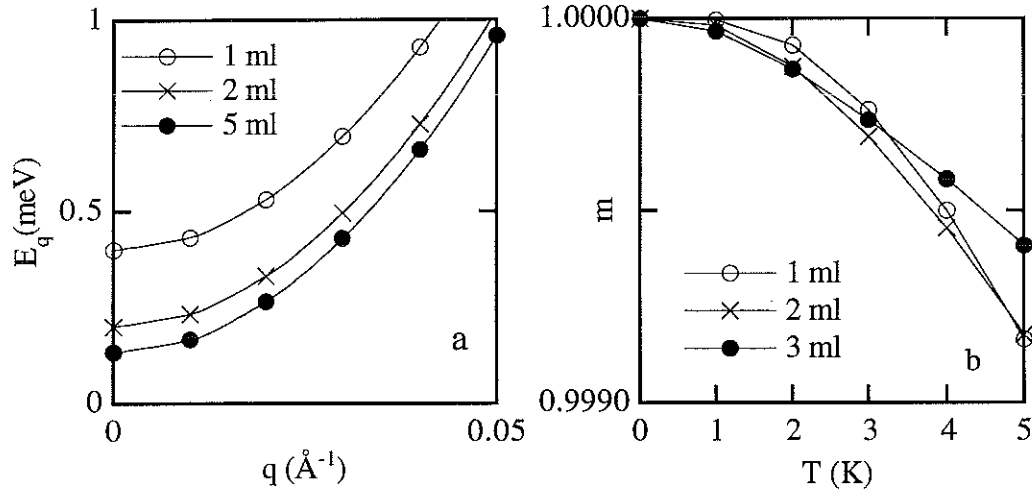


Fig. 4.15a - Close-up of the  $m = 0$  excitation branch of the spin wave dispersion curves in fig. 4.14 showing the thickness dependence of the anisotropy gap and b- close-up of the corresponding temperature dependence of  $m$ .

## 4.5 Conclusion

In this chapter we have discussed ground state moments, anisotropy and thermal excitations in ultra-thin transition metal films. At the surfaces of a transition metal film, the energy band of the 3d electrons is modified. As the range of intra-atomic and inter-atomic exchange interactions are of the order of atomic distances these modifications concern mainly the surface layers. For the case of free surfaces, it results in an enhanced ground state moment and in an enhanced anisotropy energy per surface atom. For the case of monolayer films, these enhancements are even greater. Typically moment enhancement is of the order of some percent whereas anisotropy enhancement is of the order of a thousand percent. The total magnetic moment in a thin film can therefore be expected to be significantly different from the bulk value for thicknesses up to a few monolayers whereas the total anisotropy can be expected to be different for thicknesses up to some tens of monolayers. Moment enhancement follows the following order  $\text{Fe} > \text{Co} > \text{Ni}$ . The easy axis of magnetisation for free surfaces is perpendicular for Fe and in plane for Co and Ni.

At interfaces the above phenomenon may be influenced by hybridisation effects. These may lead to a reduction in ground state moments and changes in the anisotropy energy compared with a free surface. In particular, in some cases hybridisation effects result in a switching of the easy axis of magnetisation compared with a free surface.

The experimental study of the above surface effects is further complicated by interface roughness and strains. Interface roughness can influence the ground state moment and the anisotropy. Lattice strains influence the magnetic properties of all layers in the film, including the surface / interface layers.

The thermodynamics of ferromagnetism in thin films is strongly thickness dependent. As the characteristic length scale of thermal excitations is of the order of some tens of monolayers for temperatures up to 300 K the thermal variation of the magnetisation differs from the bulk value for film thicknesses up to some tens of monolayers. For a monolayer, long range ferromagnetic order is stabilised by anisotropy and dipolar interactions. As the film thickness increases ferromagnetic order becomes progressively more stable. At low thicknesses, the temperature dependence of the magnetisation is determined by 2D excitations over a large temperature range.

## 4.6 References

---

- [1] V. L. Moruzzi, A. R. Williams and J. F. Janak,  
Phys. Rev. B15 (1977) 1854.
- [2] B. Coqblin,  
“The electronic structure of rare earth metals and alloys” , pp 262  
Academic Press; London (1977).
- [3] C. Kittel,  
“Physique de l’état solide”, Dunod, Paris (1983).
- [4] T. Kaneyoshi  
“Introduction to surface magnetism”, pp 150, CRC press, USA (1991).
- [5] G. Shirane, V. J. Minkiewicz and R. Nathans,  
J. Appl. Phys., 39 (1968) 383.
- [6] F. Gautier,  
“Metallic Multilayers”, pp 374, Mat. Sci. Forum, Vol 60, Trans Tech Publishers,  
Switzerland (1990)
- [7] E. Tamura, R. Feder, G. Waller and U. Gradmann,  
Phys. Stat. Solid, 157b (1990) 627.
- [8] H. J. Elmers, G. Liu and U. Gradmann,  
Phys. Rev. Lett. 63 (1989) 566.
- [9] C. Turtur and G. Bayreuther,  
Phys. Rev. Lett., 72 (1994) 1557.
- [10] G. P. Felcher,  
Phys. Rev. B24 (1981) 1595.  
  
S. J. Blundell and J. A. C. Bland,  
J.M.M.M., 121 (1993) 185.
- [11] J.A.C. Bland, C. Daboo, B. Heinrich and Z. Celinski,  
Proceedings of 14<sup>th</sup> Int. Colloq. on Magnetic Films and Surfaces, Düsseldorf, August  
1994, pp. 124.

- 
- [12] V. V. Pasyuk, H. J. Lauter, M. T. Johnson, F.J.A. den Broeder, E. Janssen, J.A.C. Bland, A.V. Petrenko and J. M. Gay,  
J.M.M.M., 121 (1993) 180.
- [13] U. Gradmann,  
J.M.M.M., 100 (1991) 481.
- [14] A. J. Freeman and Ru-qian Wu,  
J.M.M.M., 100 (1991) 497.
- [15] S. Ohnishi, A. J. Freeman and M. Weinert,  
Phys. Rev. B28 (1983) 6741.
- [16] W. Karas, J. Noffke and L. Fritsche,  
J. de Chim. phys., 86 (1988) 861.
- [17] S. Ohnishi, A. J. Freeman and M. Weinert,  
Phys. Rev. B28 (1988) 6741.
- [18] R. H. Victoria, L. M. Falicov and S. Ishida,  
Phys. Rev. B30 (1984) 3896.
- [19] C. L. Fu and A. J. Freeman,  
J.M.M.M., 69 (1987) L1.
- [20] W. Ruqian, W. Dingsheng and A. J. Freeman,  
Mat. Res. Soc. Symp. Proc., 313 (1993) 541.
- [21] R. H. Victora and L. M. Falicov,  
Phys. Rev. B31 (1985) 7335.
- [22] H. Chen, N. E. Brener and J. Callaway,  
Phys. Rev. B40 (1990) 1443.
- [23] C. Chappert and P. Bruno,  
J. Appl. Phys. 64 (1988) 5736.
- [24] E. du Trémolet de Lacheisserie,  
“Magnetostriction”, page 68, CRC Press, USA, 1993.
- [25] H. J. Elmers and U. Gradmann,  
Appl. Phys., A51 (1990) 255.

- 
- [26] U. Gradmann,  
Ann. Phys., 17 (1966) 91.
- [27] P. F. Carcia, A. D. Meinhaldt and A. Suna,  
Appl. Phys. Lett., 47 (1985) 178.
- [28] G. A. Prinz, G. G. Rado and J. J. Krebs,  
J. Appl. Phys., 53 (1982) 2087.
- [29] G. T. Rado,  
Phys. Rev. B26 (2087) 1982.
- [30] M. T. Johnson, R. Jungblut and F.J.A. den Broeder,  
Proceedings of 14<sup>th</sup> Int. Colloq. on Magnetic Films and Surfaces, Düsseldorf, August  
1994, pp. 233.
- [31] see chapter 1 by U. Gradmann in "Handbook of magnetic materials", vol. 7,  
K.H.J. Bushow (ed.), (North-Holland publishers), 1993.
- [32] F.J.A. den Broeder, W. Hoving and P.J.H. Bloemen,  
J.M.M.M., 93 (1991) 562.
- [33] B. N. Engel, M. H. Wiedmann, R. A. Van Leeuwen and C. M. Falco,  
J.M.M.M., 126 (1993) 532.
- [34] F. J. A. den Broeder, D. Kuiper, A. P. van de Mosselaer and W. Hoving,  
Phys. Rev. Lett., 60 (1988) 2769.
- [35] M. Albrecht, U. Gradmann, T. Furubayashi and W.A. Harrison,  
Euro. Phys. Lett., 20 (1992) 65.
- [36] M. T. Johnson, J. J. de Vries, N.W.E. Mc Gee,  
J. aan de Stegge and F.J.A. den Broeder,  
Phys. Rev. Lett., 69 (1992) 3575.
- [37] P. Krams, F. Lauks, R. L. Stamps, B. Hillebrands and G. Güntherodt,  
Phys. Rev. Lett., 69 (1992) 3674.
- [38] P. Beauvillain, C. Chappert, V. Grolier, R. Mège,  
S. Ould-Mahfoud, J.P. Renard and P. Veillet,  
J.M.M.M., 121 (1993) 503

- 
- [39] L. Néel,  
Compt. Rend., 237 (1953) 1468.
- [40] E. du Trémolet de Lacheisserie and O.F.K. Mc Grath,  
submitted to J.M.M.M.
- [41] P. Bruno and J. P. Renard,  
Appl. Phys. A49 (1989) 499.
- [42] P. Bruno,  
Phys. Rev. B39 (1989) 865.
- [43] D. W. Wang; R. Wu and A. J. Freeman,  
Phys. Rev. B47 (1993) 14932.
- [44] G. H. O. Daalderop, P. J. Kelly and M. F. H. Schuurmanns,  
Phys. Rev. B42 (7270) 1990.
- [45] D. W. Wang; R. Wu and A. J. Freeman,  
J.M.M.M., 129 (1994) 237.
- [46] J. G. Gay and R. Ritcher,  
J. Appl. Phys., 61 (1987) 3362.
- [47] D. S. Wang, R. Wu and A. J. Freeman,  
Phys. Rev. Lett., 70 (1993) 869.
- [48] D. S. Wang, R. Wu and A. J. Freeman,  
Phys. Rev. B48 (15886) 1993.
- [49] D. S. Wang, R. Wu and A. J. Freeman,  
J. Appl. Phys., 73 (1993) 6745.
- [50] K. Kyuno, R. Yamamoto and S. Asano,  
J.M.M.M., 126 (1993) 239.
- [51] R. Bergholz and U. Gradmann,  
J.M.M.M., 45 (1984) 389.
- [52] J. Korecki, M. Przybylski and U. Gradmann,  
J. M.M.M., 89 (1990) 325.



- 
- [53] M. Przybylski and U. Gradmann,  
Phys. Rev. Lett., 59 (1987) 1152.
- [54] W. Duerr, M. Taborelli, O. Paul, R. Germar, W. Gudat, D. Pescia and M. Landolt,  
Phys. Rev. Lett., 62 (1989) 206.
- [55] D. Pescia, G. Zampieri, M. Stamponi, G.L. Bona, R. F. Willis and F. Meier,  
Phys. Rev. Lett., 58 (1987) 933.
- [56] C. M. Schneider, P. Bressler, P. Schuster and J. Kirshner,  
Phys. Rev. Lett., 64 (1990) 1059.
- [57] H. J. Elmers, J. Hauschild, H. Höche, U. Gradmann,  
H. Bethge, D. Heuer and U. Köhler,  
Phys. Rev. Lett., 73 (1994) 898.
- [58] F. Bloch,  
Z. Phys. 61 (1930) 206.
- [59] N. D. Mermin and H. Wagner,  
Phys. Rev. Lett., 17 (1966) 1133.
- [60] P. Bruno,  
Phys. Rev. B43 (1991) 6015.
- [61] A. S. Arrot and B. Heinrich,  
J.M.M.M., 93 (1191) 571.
- [62] for a discussion see G. Luggert and G. Bayreuther,  
Phys. Rev. B38 (1988) 11068 and references therein.



# CHAPTER FIVE

## GROUND STATE MAGNETIC MOMENT, ANISOTROPY AND THERMAL EXCITATIONS OF Fe in W / Fe / W.

### Table of contents to chapter 5

5.1 Introduction	139
5.2 Ground state moment	140
5.2.1 PNR - Introduction	140
5.2.2 Experimental	141
5.2.3 Experimental results and data analysis	143
5.2.4 Discussion	146
5.3 In-plane anisotropy in W / Fe (110) / W	148
5.3.1 Results	148
5.3.2 Determination of total in-plane anisotropy constants	150
5.3.3 Derivation of constants associated with different anisotropy sources	152
5.3.4 Evaluation of constants associated with different anisotropy sources	153
5.3.5 Discussion	157
5.4 Thermal excitations	162
5.4.1 Results	162
5.4.2 Discussion	163
5.5 Discussion and conclusion to chapter 5	166
5.6 References to chapter 5	167

## RÉSUMÉ

Dans ce chapitre nous présentons une analyse du moment magnétique, de l'anisotropie planaire et des excitations thermiques du Fe dans des couches de W / Fe / W d'épaisseur en Fe variable. L'amplitude du moment magnétique à 0K est déterminée par des mesures de neutrons polarisés et des mesures de SQUID. Pour une couche de Fe de trois plans atomiques d'épaisseur, le moment magnétique à 0K est  $2.1 \pm 0.1 \mu_B$ . L'anisotropie planaire est mesurée par un magnétomètre à effet Kerr transversal et SQUID. Un axe de facile aimantation est observé dans toutes les couches. Pour une couche de 120 Å l'axe facile est l'axe [001] mais pour les couches de 90 Å et 20 Å c'est l'axe  $[1\bar{1}0]$  qui est facile. Pour analyser l'anisotropie nous développons un modèle dans lequel les anisotropies de volume sont évaluées à partir des valeurs du massif à 0K renormalisées à l'aimantation de la couche à la température considérée. Nous montrons que l'anisotropie de surface est à l'origine du basculement de l'axe de facile aimantation. Notre technique d'analyse est aussi appliquée à d'autres résultats expérimentaux de la littérature. A la fin nous discutons brièvement de la variation thermique de l'aimantation dans ces couches.

## SUMMARY

In this chapter we analyse the ground state moment, in-plane anisotropy and thermal excitations of Fe in W / Fe (110) / W films of varying Fe thickness. The ground state moment of Fe is determined by means of PNR at 300 K and SQUID measurements. For the case of a three layer Fe film the ground state moment is found to be  $2.1 \pm 0.1 \mu_B$ . The in-plane anisotropy is measured by means of transverse Kerr and SQUID magnetometry. An in-plane easy axis of magnetisation is observed in all films. This easy axis switches from the [001] axis for the 120 Å film to the  $[1\bar{1}0]$  for the 90 Å and 20 Å film. The anisotropy is analysed within a model where the various non-surface anisotropies are evaluated from bulk 0 K data re-normalised to the film magnetisation at the considered temperature. Surface anisotropy is found to be the sole cause of the observed easy axis switching. The analysis technique is further discussed by analysing published experimental data. Finally, the thermal variation of the magnetisation is briefly discussed.

## 5.1 Introduction

In the previous chapter we discussed the ground state moments, anisotropy and thermal excitations in ultra-thin films from a general perspective. In this chapter we investigate these three properties in W / Fe (110) / W thin films of varying Fe thicknesses.

In the first section, we present an experimental investigation of the magnetic moment by polarised neutron reflectometry.

In the second section we present the results of an experimental investigation of the in-plane anisotropy by transverse Kerr and SQUID magnetometry. We analyse our results and extract a value of the in-plane surface anisotropy constants.

In the final section we discuss the thermal variation of the magnetisation, as measured by SQUID magnetometry.

## 5.2 Ground state moment

As discussed in the previous chapter, the reduction of atomic co-ordination at the surface of a magnetic thin film is expected to give rise to an enhanced or reduced magnetic moment per atom at the surface layers compared with the volume layers. For the case of W / Fe (110) / W tri-layers, an interface Fe atom has 6 Fe nearest neighbours and 2 W nearest neighbours, whereas an atom in a volume layer has 8 Fe nearest neighbours.

In order to investigate this phenomenon experimentally, PNR experiments were performed on the SPN spectrometer at the IBR-2 reactor in Dubna, Russia. The objective of the experiments was to determine the magnetic moment profile at 300 K. Three W / Fe (110) d / W films were investigated, where d = 6 Å, 20 Å and 90 Å. In the following we shall describe these experiments and discuss the results. Firstly we shall briefly explain the concept of PNR experiments, then we shall describe the experimental set-up employed followed by a presentation of the experimental results and data analysis. The measured values were extrapolated to 0 K, by SQUID magnetometry, and the extrapolated value of the 6 Å film is discussed by comparing it with previous experimental and theoretical work on similar systems.

### 5.2.1 PNR - Introduction

When a neutron beam is incident on a surface at grazing incidence it is specularly reflected, analogous to x-ray specular reflection. The refractive index of the surface can be written, neglecting absorption effects, as [1] :

$$\begin{aligned} n^{+/-} &= n_n \pm n_m \\ &= 1 - \frac{\lambda^2}{2\pi} \left[ \frac{b(z)}{V(z)} \pm \frac{C\mu(z)}{V(z)} \right] \end{aligned}$$

$$\text{where } C = \frac{2\pi\mu_n m}{h} = 2.695 \times 10^{-5} \text{ Å} \cdot \mu_B^{-1} \quad (5.1)$$

and  $\lambda$  is the neutron wavelength,  $V$  is the atomic volume at a distance  $z$  from the surface,  $b(z)$  and  $C\mu(z)$  are the nuclear and magnetic scattering length profiles respectively.  $b(z) / V(z)$  and  $C\mu(z) / V(z)$  are the scattering lengths per unit volume and are the physical parameters involved in the reflectivity process. The “+” sign refers to the case of the neutron polarisation being parallel to the moment and the “-” sign refers to the case of the neutron polarisation being anti-parallel. The reflectivity profiles  $R^+$  and  $R^-$  are therefore functions ( $f$ ) of the nuclear  $b(z) / V(z)$  and magnetic profiles  $C\mu(z) / V(z)$  :

$$R^{+/-}(q) = f \left[ \frac{b(z)}{V(z)} + / - \frac{C\mu(z)}{V(z)} \right]$$

where

$$q = \frac{4\pi(\sin \theta)}{\lambda} \quad (5.2)$$

and  $\theta$  is the angle of incidence. For a description of the exact form of  $f$  see references [1] [2] and [3]. During PNR experiments one therefore measures  $R^+$  and  $R^-$  in order to extrapolate  $b(z)$  and  $\mu(z)$ .

### 5.2.2 Experimental

The experimental set-up of the SPN spectrometer at the IBR-2 reactor in Dubna, Russia is schematised in figure 5.1. The neutron source is a pulsed source and the spectrometer works at fixed angle of incidence with varying neutron wavelength, i.e. time-of-flight spectrometer. A double disc chopper suppresses the background from the satellite reactor pulses and defines the wavelength band (from 0.7 Å to 12 Å). The conical neutron guide forms the beam before the polariser and increases the effective aperture of the instrument. The neutron beam polariser consists of iron-cobalt magnetic mirrors with a titanium-gadolinium anti-reflecting under layer. The efficiency of the polariser, averaged over the neutron spectrum is about 95 %. The maximum integral neutron flux at the polariser exit was  $1.2 \times 10^6 \text{ n.s}^{-1}.\text{cm}^{-2}$ . An array of permanent magnets serves as a guiding field (120 Oe) for the polarised beam. The neutron beam flipper selects a given spin state (+ or -) and has an efficiency of 99.5 %. The horizontal beam collimation is adjusted by means of a cadmium slit at the exit of the polariser.

The sample holder is located at 29 m from the source. The film is fixed in a vertical position. The angle of incidence of the neutron beam is varied by rotating the film holder (from  $-10^{-2}$  to  $+10^{-2}$  rad with an accuracy of  $10^{-5}$  rad). An electro-magnet enables fields up to 11 kOe to be applied at the film position. The detector is a  $\text{He}^3$  detector surrounded by boron-carbide shielding and positioned at 2.5 m from the sample holder.

All measurements were performed at 300 K. The films were oriented onto the sample holder so that their easy axis of magnetisation was parallel to the applied field (500 Oe). The  $R^+$  and  $R^-$  reflectivities were measured by alternating the spin flipper every five minutes. The total count time was 24 hours.

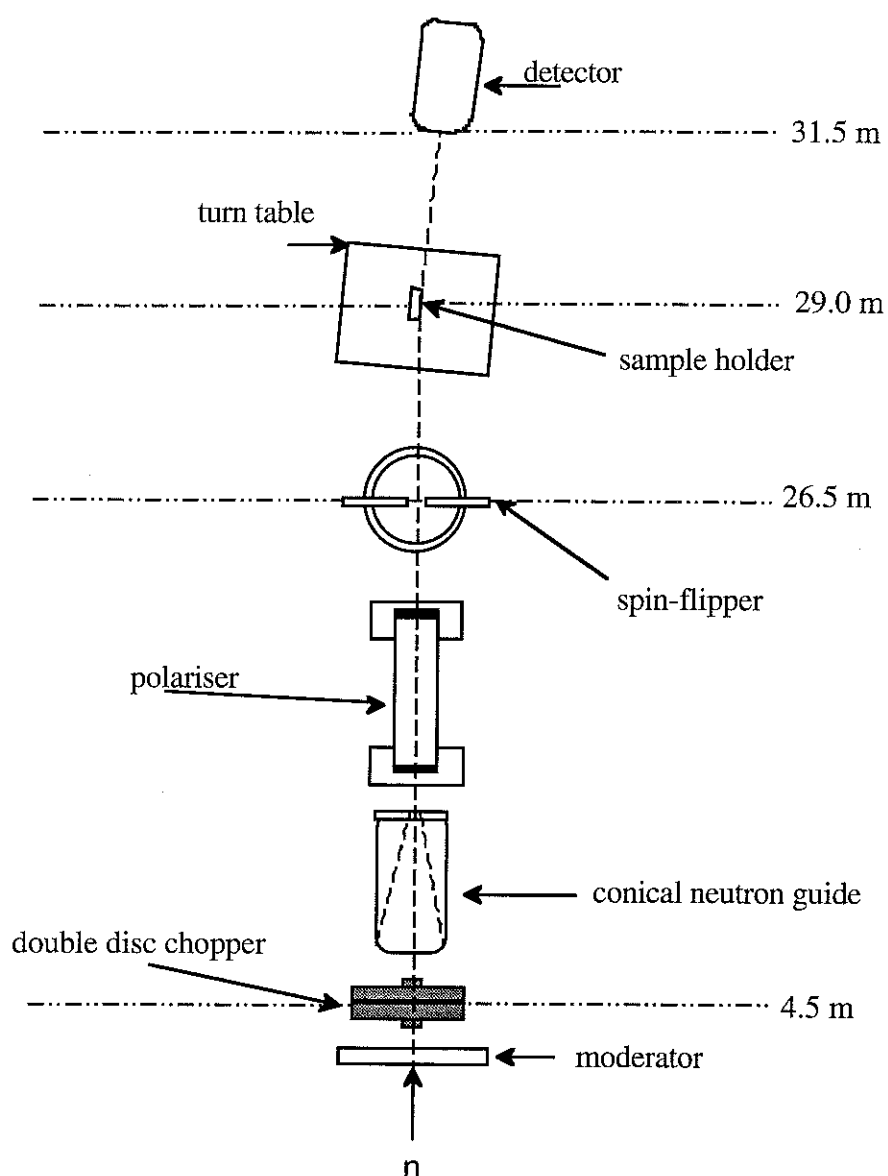


Fig. 5.1 Schematic drawing (bird's eye view) of the PNR experimental set-up. The drawing is not to scale but the distance of certain components from the source is indicated.



### 5.2.3 Experimental results and data analysis

The  $R^+$  and  $R^-$  data, corrected for the imperfect polarisation of the neutron beam, is shown in figure 5.2a and 5.2b respectively for the 6 Å Fe film. The data is analysed by calculating the spin dependent reflectivities by means of a transfer matrix method [4]. The fitting parameters are  $b(z) / V(z) + \mu(z) / V(z)$  for  $R^+$  and  $b(z) / V(z) - \mu(z) / V(z)$  for  $R^-$ . The starting values of  $b / V$  were taken from bulk data ( $b / V(\text{Fe}) = 8.030 \times 10^{-6} \text{ Å}^{-2}$  and  $b / V(\text{W}) = 3.084 \times 10^{-6} \text{ Å}^{-2}$  [5]) and the value of  $b / V$  at a given depth from the surface ( $b(z) / V(z)$ ) was deduced from X-ray reflectivity thickness analysis (see chapter 3). The starting values of  $C\mu / V$  were taken from Fe bulk moments ( $\mu = 2.2\mu_B$ ). The fitting parameters were adjusted until the best fit to the experimental data was obtained (fig. 5.2a and 5.2b). As can be seen from expression (5.2), one can concentrate on magnetic effects by plotting the flipping ratio  $R^+/R^-$  as shown in figure 5.2c. The best fits to the data (fig. 5.2 a - c) were obtained from the  $b(z) \pm \mu(z)$  profiles shown in figure 5.3. The obtained thicknesses are in good agreement with the X-ray analysis (compare fig. 3.17a with fig. 5.3a). In particular the Fe thickness is found to be  $6 \pm 1 \text{ Å}$ .

Interface roughness was accounted for by making step like variations in  $b(z) / V(z) \pm \mu(z) / V(z)$  at each interface. The best fit was obtained by assuming that there is a 5 Å intermixed layer either side of the 6 Å Fe layer. The obtained value of  $b(z) / V(z)$  for this model corresponds to 20 % Fe and 80 % W. In addition the obtained value of  $C\mu(z) / V(z)$  was 0, thus indicating that this intermixed region is non-magnetic (fig. 5.3b).

Finally, the deduced value of  $C\mu / V$  in the Fe layer is  $4.0 \pm 0.1 \times 10^{-6} \text{ Å}^{-2}$  (fig. 5.3b), which corresponds to a moment of  $1.80 \pm 0.05 \mu_B / \text{atom}$ . The statistics are not sufficient to determine a profile of the Fe moment in the three layers and  $C\mu(z) / V(z)$  is assumed to be constant in these three layers.

In order to compare the above results with theoretical calculations one must extrapolate the 300 K value to 0 K. The thermal variation of the total film moment was measured by means of a SQUID magnetometer. The film was oriented onto the sample holder with the easy axis to within  $0.5^\circ$  of the field direction. A constant field of 1 kOe was applied and the magnetisation was measured from 4.2 K to 300 K (fig. 5.2). The total moment of the film is found to decrease from  $1.85 \pm 0.05 \times 10^{-5} \text{ emu}$  at 4.2 K to  $1.57 \pm 0.05 \times 10^{-5} \text{ emu}$  at 300 K. Assuming that the thermal decrease from 0 K to 4.2 K is negligible then the 300K moment, as determined from the neutron data ( $1.80 \pm 0.05 \mu_B$ ) can be extrapolated to  $2.1 \pm 0.1 \mu_B$  at 0K.

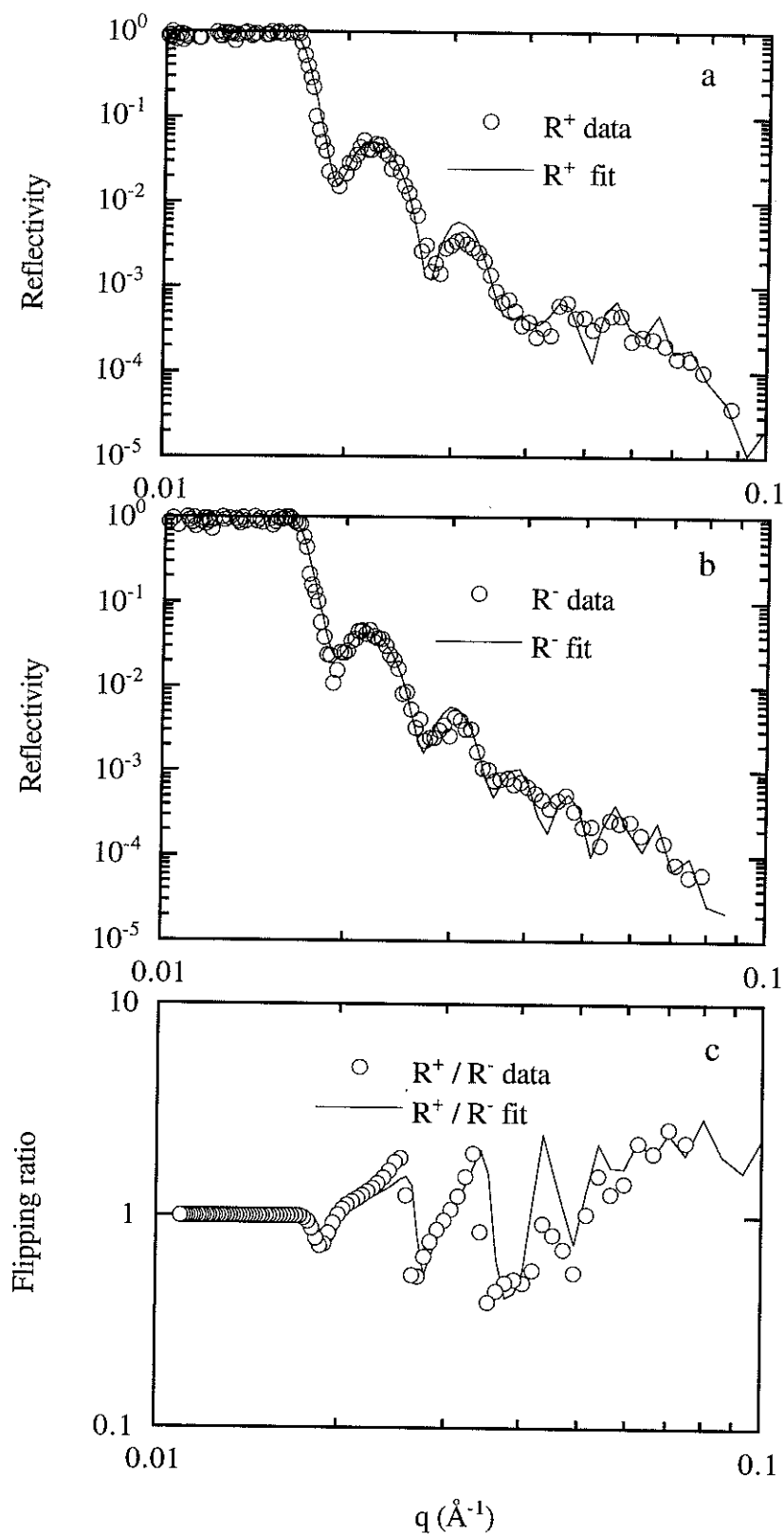


Fig. 5.2 - Specular neutron reflectivity data and fits for ; a - neutrons polarised parallel to the magnetisation ( $R^+$ ), b - neutrons polarised anti-parallel ( $R^-$ ) and c - flipping ratio ( $R^+/R^-$ ).

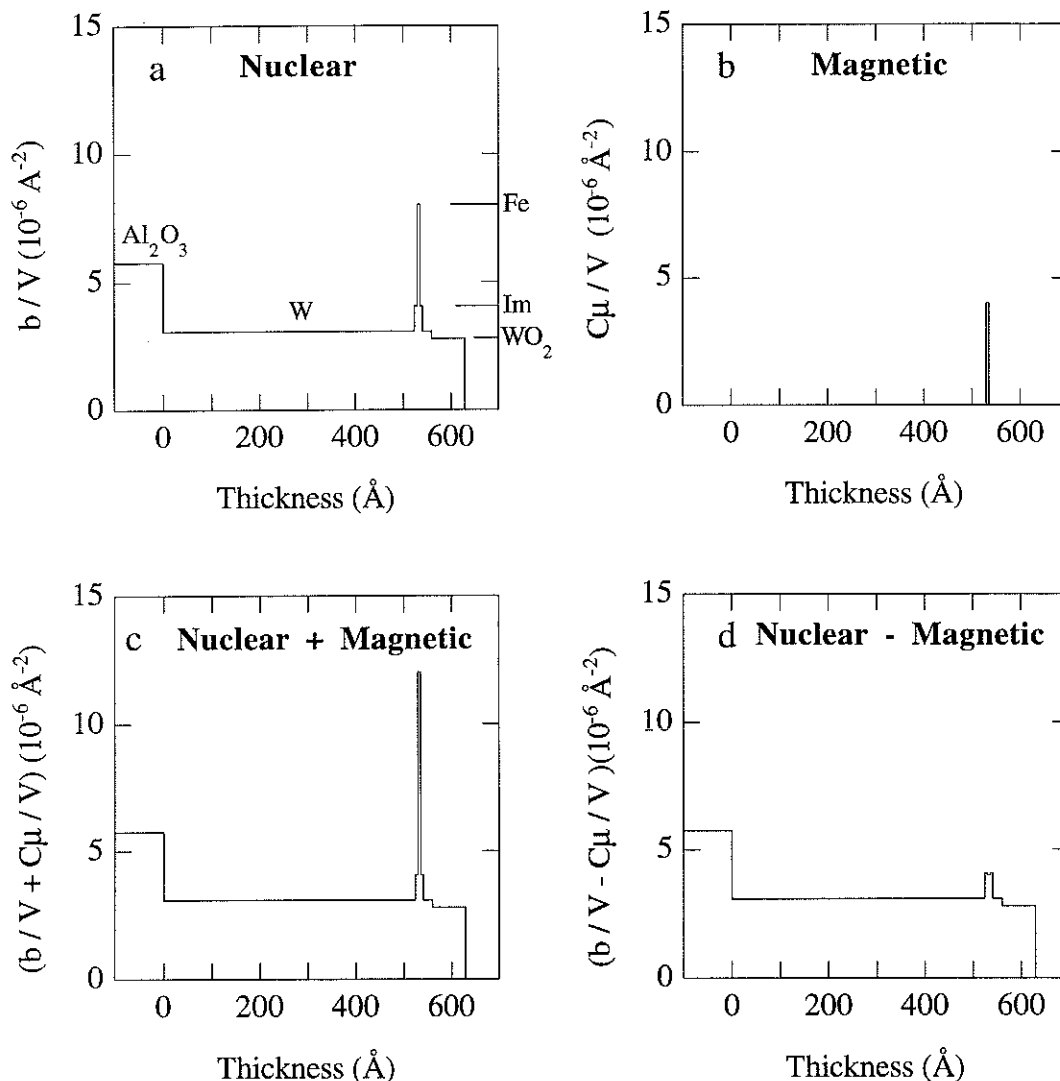


Fig. 5.3a- thickness profiles of  $b_n/V$ , the values correspond to bulk values of W and Fe. At each side of the Fe interface, there is an intermixed region (labelled Im) which is 80 % W and 20 % Fe and 90 Å of the W surface layer is found to be oxidised ; b - the thickness profile of the magnetic moment where only the three layers of Fe are found to possess a moment of  $1.8 \mu_B$  at 300 K ; c - the total fitting parameters for  $R^+$  reflectivity  $(b_n + C\mu)/V$  and d - for  $R^-$  reflectivity  $(b_n - C\mu)/V$ .

Similar experiments performed on the 20 Å and 90 Å Fe film indicated that the average ground state moment in these films was identical to the bulk moment ( $2.22 \mu_B$  [6]). The thickness of these films was such that we could not detect, to within reasonable error, the interface moment. This can be understood by the fact that in the three layer film, the difference between the measured moment and the bulk value is  $0.1 \mu_B$ . In the 20 Å film, the contribution of the interface moments to the total moment is 10 %. If the interface moments have the same value in the 20 Å film compared with the 6 Å film, then the difference between the total film moment and the bulk is  $0.01 \mu_B$  which is much less than the experimental error.

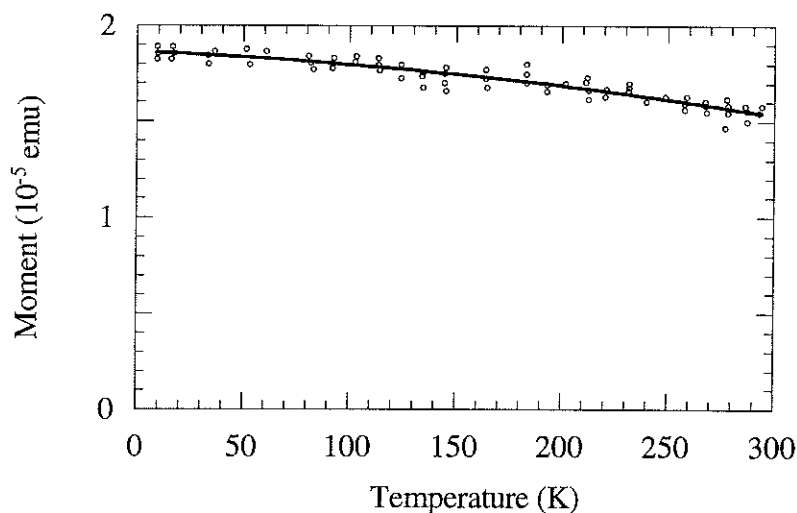


Fig. 5.4 - Thermal variation of the total magnetic moment with an applied field of 1 kOe.

#### 5.2.4 Discussion

The above results are reported graphically in figure 5.5a. It is interesting to compare these results with those of a similar system where the average moment in a monolayer and two-layer thick Fe (110) film deposited on W (110) was deduced from magnetisation measurements and quartz microbalance thickness measurements [7]. The ground state moment was found to be  $2.53 \mu_B$  and  $2.46 \mu_B$  for the one monolayer and two monolayer film respectively (fig. 5.5b and 5.5c).

Ab-initio calculations for a seven layer free standing Fe (110) film [8] show that the ground state magnetic moment at the surface layers is expected to be  $2.65 \mu_B$  (figure 5.5d), which corresponds to a 19% increase with respect to the bulk. Calculations for a monolayer of Fe (110) deposited on W [9], however, show that the ground state moment of Fe is  $2.18 \mu_B$  (figure 5.5e), which corresponds to a 2% reduction compared with the bulk or an 18% reduction compared with a free surface. The moment reduction at a W / Fe interface is due to hybridisation effects. Coating of the film with Ag has a negligible effect (compare 5.5e with 5.5f) as Ag / Fe hybridisation effects are negligible.

Our experimental results confirm that the moment of Fe is reduced at a W / Fe interface. As calculations do not exist for W / Fe / W, a quantitative comparison between our results and theory is not however possible. One may note, however, that the value of the Fe moment found in W / Fe / W is less than the moment calculated for an un-coated monolayer of Fe on W.










PNR	a		$2.1 \pm 0.1 \mu_B$
magnetometry	b		$2.53 \pm 0.12 \mu_B$
	c		$2.46 \pm 0.15 \mu_B$
theoretical	d		$2.65 \mu_B$ $2.25 \mu_B$
	e		$2.18 \mu_B$
	f		$2.17 \mu_B$
 = W  = 1 ml Fe (110)  = Ag			

Fig. 5.5- Schematic representation of the ground state moment (in units of  $\mu_B$ ) in various ultra-thin Fe films; a - polarised neutron data (PNR) (this work), b-c - magnetometry data (from [7]), and d - f theoretical calculations ( d from [8] and e and f from [9]).

### 5.3 In-plane anisotropy in W / Fe (110) / W

In this section we discuss the in-plane anisotropy of Fe in W / Fe (110) d / W (110) , where  $d = 20 \text{ \AA}$ ,  $90 \text{ \AA}$  and  $120 \text{ \AA}$ . As discussed in chapter four, the magnetic anisotropy of ultra-thin films is a complex phenomenon and requires a subtle analysis. The objective of our study was to extract from experimental data the in-plane surface anisotropy constant and not limit our analysis to simply an effective surface anisotropy constant.

#### 5.3.1 Results

Magnetisation measurements were first performed at room temperature with a transverse Kerr magnetometer. During these measurements hysteresis cycles were recorded for fields applied every  $5^\circ$ .

For the  $120 \text{ \AA}$  film, the hysteresis cycle obtained when  $H$  is parallel to the  $[001]$  axis is characteristic of an easy axis cycle (fig. 5.6c). It can be inferred from this that the  $[001]$  direction is an easy axis of magnetisation as in bulk Fe. Measurements performed for  $H$  applied at different angles revealed that the  $[1\bar{1}0]$  is the hardest axis. For  $H$  applied along this direction, the magnetisation varies initially linearly with  $H$ , as expected for an applied field at  $90^\circ$  to an easy axis. At a critical field of 130 Oe there is a transition towards saturation.

For the  $90 \text{ \AA}$  and  $20 \text{ \AA}$  film, it is observed, on the other hand, that the easy axis of magnetisation is the  $[1\bar{1}0]$  axis (fig. 5.6b and 5.6a respectively).

For the  $90 \text{ \AA}$  film, the initial variation of magnetisation is linear with applied field along the  $[001]$  axis and a transition occurs at 13 Oe (fig. 5.6b), which illustrates the weak anisotropy in this film.

For the  $20 \text{ \AA}$  film, and for an applied field parallel to the  $[001]$  axis, the magnetisation exhibits an upward curvature, it saturates at  $H = 1400 \text{ Oe}$  (fig. 5.6a) which indicates the presence of large in-plane anisotropy.

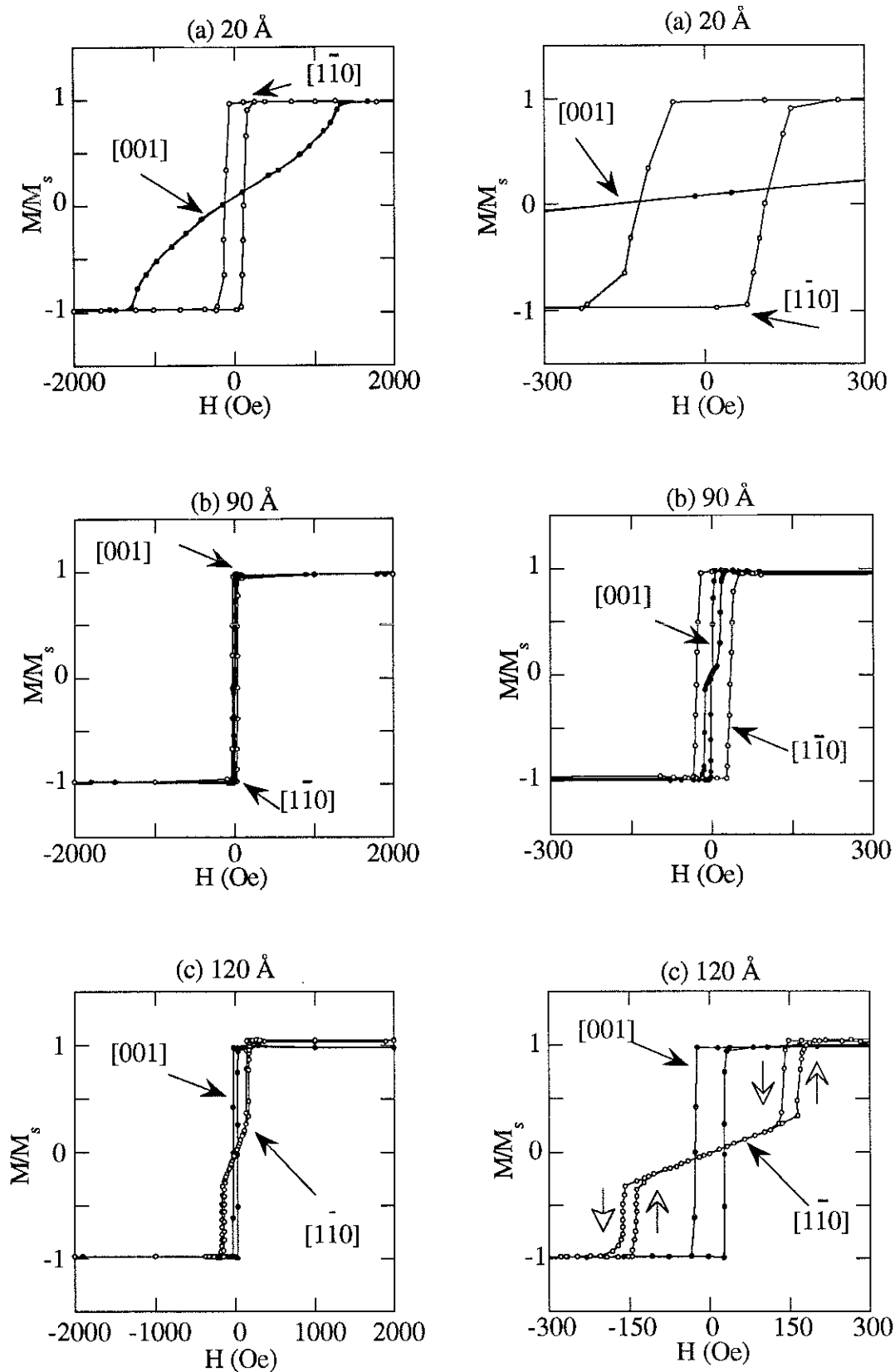


Fig. 5.6 - Transverse Kerr hysteresis loops taken with an applied field ( $H$ ) parallel to the  $[001]$  and  $[1\bar{1}0]$  crystallographic axes for a 20 Å (a), 90 Å (b) and 120 Å (c) Fe film.

Having established the presence of an in-plane easy and hard axis of magnetisation at room temperature, the temperature dependence of the anisotropy was measured by means of a SQUID magnetometer. For these measurements the films were oriented by Laue diffraction so that the applied field was at less than  $0.5^\circ$  from the hard axis of magnetisation. The field dependence of the magnetisation was measured at 10 K, 100 K, 200 K and 300 K for the 20 Å and 120 Å film. The temperature dependence of the 90 Å film could not be measured as the anisotropy field is less than the minimum field step size of the SQUID.

### 5.3.2 Determination of total in-plane anisotropy constants

Due to the in-plane two-fold symmetry of the (110) plane, the anisotropy energy can be written phenomenologically, to fourth order as :

$$E_a = A\sin^2\theta + B\sin^4\theta \quad (5.3)$$

where it is assumed that the moments rotate in-plane which is plausible for an applied field in-plane due to predominance of shape anisotropy.  $\theta$  is the angle of the magnetisation with respect to the [001] axis and A and B are phenomenological second and fourth order anisotropy constants respectively. For an applied field, (5.3) becomes:

for  $H \parallel [001]$  then  $M = M_s \cos\theta$

$$\Rightarrow E_a = A\sin^2\theta + B\sin^4\theta - M_s H \cos\theta \quad (5.4a)$$

for  $H \parallel [1\bar{1}0]$  then  $M = M_s \sin\theta$

$$\Rightarrow E_a = A\sin^2\theta + B\sin^4\theta - M_s H \sin\theta \quad (5.4b)$$

The A and B anisotropy constants can be evaluated by finding, at each H, the angle  $\theta$  which corresponds to the minimum of 5.4a and 5.5b for  $H \parallel$  to the [001] and [1-10] axes respectively.

In general, the experimentally observed hysteresis is much less than that calculated by means of a coherent rotation model. One should therefore fit the experimental anhysteresis loops to the theoretical anhysteresis loops. The experimental anhysteresis loops can be estimated by averaging the upward and downward branches of the experimental loops.

For a given H, the energy minima of  $\theta$  are given by :



$$H // [001] \quad \Rightarrow \quad H = \left(-\frac{2A}{M_s} - \frac{4B}{M_s}\right)\cos\theta + \frac{4B}{M_s}\cos^3\theta \quad (5.5a)$$

$$H // [1\bar{1}0] \quad \Rightarrow \quad H = \frac{2A}{M_s}\sin\theta + \frac{4B}{M_s}\sin^3\theta \quad (5.5b)$$

In addition, depending on the relative values of A and B, it is possible that there is a local energy minimum at saturation, i.e. the solutions  $\cos\theta = 1$  and  $\sin\theta = 1$  for  $H // [001]$  and  $H // [1\bar{1}0]$  respectively must also be considered. The theoretical anhysteresis loops is given by the value of  $\theta$  which corresponds to the absolute energy minimum at the value of H in question.

The fitting procedure is as follows. For the 20Å film, the magnetisation curve does not show any hysteresis nor transitions thus indicating that  $\cos\theta = 0$  ( $\equiv M / M_s = 1$ ) is not an energy minimum. The magnetisation curve is calculated from 5.5a by varying the  $A / M_s$  and  $B / M_s$  parameters until the best fit to the experimental data is obtained, as shown in figure 5.7.

For the 90Å and 120Å film, the magnetisation increases approximately linearly with H up to a certain value ( $H^*$  = average between upward and downward transition branch) at which point a jump to saturation is observed. For  $0 < H < H^*$ , the theoretical anhysteresis curve is given by 5.5. The A and B anisotropy constants can be estimated to a first approximation by assuming that the slope of the experimental anhysteresis curve for  $0 < H < H^*$  is inversely proportional to  $(-2A - 4B) / M_s$  and to  $2A / M_s$  for  $H // [001]$  and  $H // [1\bar{1}0]$  respectively, as seen from (5.5a) and (5.5b). At  $H^*$ , assuming that the energy minimum at non-saturation equals the energy minimum at saturation, it follows that (from 5.4 and 5.5) :

$$\begin{aligned} \text{for } H // [001] \quad & H^*M_s = -A(1+m^2) - B(1+2m^2 + 3m^4) \\ \text{for } H // [1\bar{1}0] \quad & H^*M_s = A(1+m^2) + B(1+3m^4) \end{aligned}$$

where m is the minimum value of  $M / M_s$  at  $H^*$ . From the value of the slope, the value of  $H^*$  and the value of m, the  $A / M_s$  and  $B / M_s$  parameters can therefore be firstly deduced. They are then refined by imputing them into (5.5) and adjusting them until the best fit with the experimental data in the  $0 < H < H^*$  region is obtained.

The value of  $M_s$  for each film and temperature is calculated from the value of the total magnetic moment from SQUID measurements along the easy axis and x-ray reflectivity thickness measurements. The thus deduced values of A, B and  $M_s$  are collected in table 5.1.

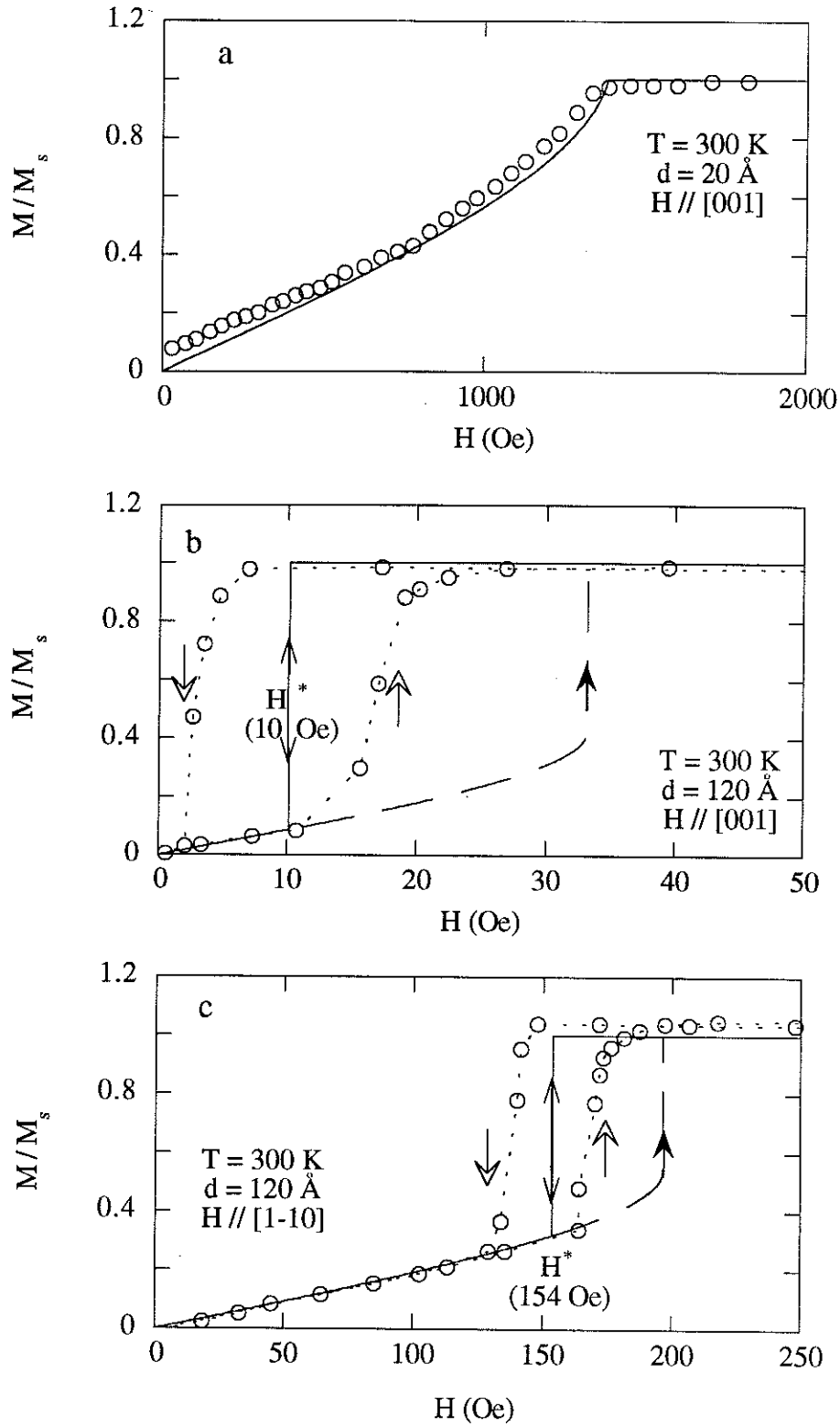


Fig. 5.7 - Fits of the hysteresis loops of all films at 300 K in order to evaluate the A and B anisotropy constants ; the continuous lines are the anhysteresis fits, the dashed lines are the upward hysteresis fits and the open circles are the experimental data points.

		20 Å	90Å	120Å
10 K	A ( $10^5 \text{ erg.cm}^{-3}$ )	-16(1)		+6.5 (0.5)
	B ( $10^5 \text{ erg.cm}^{-3}$ )	-3 (1)		-2.5 (0.75)
	$M_s$ (emu.cm $^{-3}$ )	1740		1740
100 K	A ( $10^5 \text{ erg.cm}^{-3}$ )	-15 (1)		+6.0 (0.5)
	B ( $10^5 \text{ erg.cm}^{-3}$ )	-3 (1)		-2.5 (0.75)
	$M_s$ (emu.cm $^{-3}$ )	1706		1733
200 K	A ( $10^5 \text{ erg.cm}^{-3}$ )	-14 (1)		+5.0 (0.5)
	B ( $10^5 \text{ erg.cm}^{-3}$ )	-2 (1)		-2.5 (0.75)
	$M_s$ (emu.cm $^{-3}$ )	1677		1719
300 K	A ( $10^5 \text{ erg.cm}^{-3}$ )	-12 (1)	+0.9 (0.5)	+4.6 (0.5)
	B ( $10^5 \text{ erg.cm}^{-3}$ )	-2 (1)	-1.0 (0.5)	-2.4 (0.5)
	$M_s$ (emu.cm $^{-3}$ )	1660	1672	1694

Table 5.1 - The deduced anisotropy constants (A and B) and  $M_s$  as a function of temperature for W / Fe / W films of thicknesses ranging from 20 Å to 120 Å.

Having evaluated the total anisotropy constants, the problem is now to evaluate the various anisotropy sources.

### 5.3.3 Derivation of constants associated with different anisotropy sources

#### - Volume term

The anisotropy energy of a cubic structure is given in (4.4). As the easy axis of magnetisation was found to lie in the plane of the films and due to the presence of shape anisotropy, one can assume that rotation of the magnetisation from the easy axis to the hard axis occurs without the magnetisation vector ( $\mathbf{M}$ ) leaving the plane. The projections of  $\mathbf{M}$  onto the cube edges can therefore be written as:

$$\alpha_1 = \cos \theta, \quad \alpha_2 = \frac{\sqrt{2}}{2} \sin \theta, \quad \alpha_3 = -\frac{\sqrt{2}}{2} \sin \theta \quad (5.6)$$

where  $\theta$  is defined as the angle between  $\mathbf{M}$  and the [001] axis. The corresponding anisotropy energy ( $E_a$ ) is :

$$E_a = K_1 \sin^2 \theta - \frac{3}{4} K_1 \sin^4 \theta \quad (5.7)$$

The first term on the right hand side of equation (5.7) is a second order symmetry term ( $\sin^2 \theta$ ) although the energy is of fourth order ( $K_1$ ). It appears due to the fact that the symmetry of the (110) plane is not square but rectangular.

#### - Magnetoelastic term

The magnetoelastic anisotropy for a (110) film, to second order, is given in (4.18). For the 20Å film  $\epsilon_{in}$  was measured by RHEED at 300 K as 1.7% (see chapter 3). It has been reported that the lattice parameter of Fe (110) on W (110) does not relax completely and that a residual in-plane strain of 0.39% exists for thick films [22]. As this value falls within the error of our RHEED measurements (1%) we therefore assume a value of  $\epsilon_{in}$  of 0.39% for the 90Å and 120Å film at 300K. Due to the 2D character of the RHEED diffraction patterns,  $\epsilon_{out}$  could not be measured. It can be evaluated by minimising the total elastic energy with respect to strain, yielding :

$$\epsilon_{out} = \epsilon_{in} \left( \frac{4C^\alpha - 5C^\gamma - 3C^\epsilon}{2C^\alpha - 3C^\gamma + 3C^\epsilon} \right) \quad (5.8)$$

where  $c^\alpha$ ,  $c^\gamma$  and  $c^\epsilon$  are the isotropic, strain and shear elastic constants respectively. (Note : In the literature, Voigt's notation is often employed for the elastic constants. The elastic constants in (5.8) are related through ;  $C^\alpha = C_{11} + 2C_{12}$ ,  $C^\gamma = C_{11} - C_{12}$  and  $C^\epsilon = 2C_{44}$  ( see reference [10])). Expression (5.8) was evaluated by taking bulk values of the elastic constants from reference [11].

#### Surface term

The surface anisotropy energy for a cubic (110) film is given in 4.16. For in-plane anisotropy ( $\phi = 90^\circ$ ) and neglecting constant terms, it becomes to second order :

$$E_s = K_s \sin^2 \theta \quad (5.9)$$

### 5.3.4 Evaluation of constants associated with different anisotropy sources

#### evaluation of $K_1$ and $B\gamma^2$ and $B\epsilon^2$

As discussed in chapter four, it is not possible to evaluate  $K_S$  from a plot of the total anisotropy as a function of film thickness as the strain in the above films varies with thickness. In the following, we therefore propose to deduce a value of  $K_S$  by evaluating  $K_1$  and  $K_{me1}$ . It would appear, at first sight, reasonable to assume that  $K_1$  and  $K_{me1}$  can be evaluated from bulk data. At 300 K, however, the magnetic state of a thin film is different from that of a bulk material. In fact, the reduction of the anisotropy and magnetoelastic properties of a material at 300 K compared with 0 K arise from thermal disorder. As discussed by Callen and Callen [12], the thermal variation of  $K_1$  and  $B\gamma^2$  and  $B\epsilon^2$  are due to the thermal disorder of the moments and fundamentally these quantities are in fact functions of the magnetisation.

It appears therefore, that the most reasonable hypothesis is to assume i) that the parameters  $K_1$ ,  $B\gamma^2$  and  $B\epsilon^2$  have the same values at 0 K as in the bulk but as temperature increases, the values in a thin film differ from those in the bulk because the temperature dependence of the magnetisation is thickness dependent (as discussed in chapter 4). It is further assumed that ii) the magnetisation dependence of  $K_1$ ,  $B\gamma^2$  and  $B\epsilon^2$  is as in the bulk. This can be expressed mathematically as :

$$\begin{aligned}\frac{K_1(T)}{K_1(T=0)} &= f\left(\frac{M(T)}{M(T=0)}\right) = f(m) \\ \frac{B\gamma^2(T)}{B\gamma^2(T=0)} &= f'(m) \\ \frac{B\epsilon^2(T)}{B\epsilon^2(T=0)} &= f''(m)\end{aligned}\tag{5.10}$$

The magnetisation dependence of  $f$ ,  $f'$  and  $f''$  as deduced from bulk measurements is shown in figure 5.8.

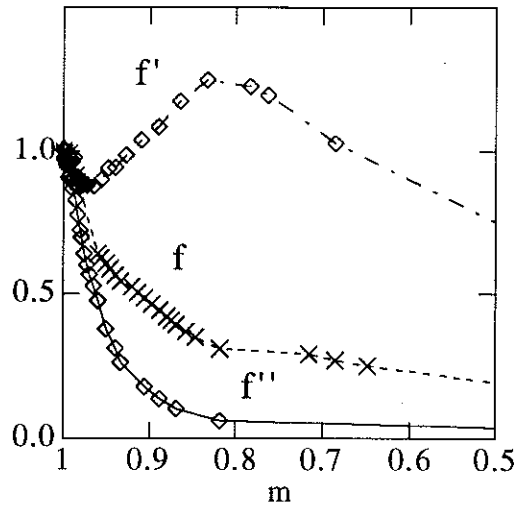


Fig. 5.8. - The bulk magnetisation dependence of  $K_1$ ,  $B\gamma^2$  and  $B\epsilon^2$  showing the functions  $f$ ,  $f'$  and  $f''$  as explained in the text. Bulk magnetisation data taken from [13],  $K_1$  data taken from [14] and [15] and  $B\gamma^2$  and  $B\epsilon^2$  taken from [16].

The value of  $m$  was measured at temperatures from 10 K to 300 K for all films (see section 5.4), from which  $K_1$ ,  $B\gamma^2$  and  $B\epsilon^2$  were evaluated by employing (5.10). The deduced values of  $K_1$ ,  $B\gamma^2$  and  $B\epsilon^2$  are shown in figure 5.9.

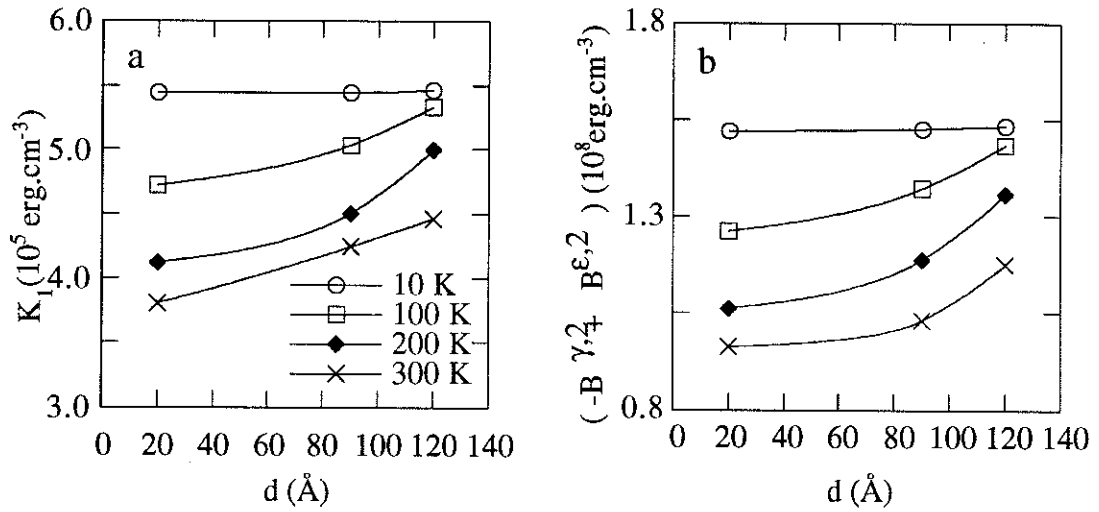


Fig. 5.9 - The evaluated thickness dependence of  $K_1$  (a) and  $(-B\gamma^2 + B\epsilon^2)$  (b) for 10 K to 300 K.

### evaluation of $K_{mel}$

$K_{mel}$  was evaluated at 300 K from expressions (4.18), (5.8), the deduced value of  $B\gamma^2$ ,  $B\epsilon^2$  (fig. 5.9) and the value of  $\epsilon_{in}$  at 300 K. The evaluation of  $K_{mel}$  for  $T < 300$  K rests on the evaluation of  $\epsilon_{in}$  for  $T < 300$  K. Measurement of  $\epsilon_{in}(T)$  was not however possible from RHEED and we therefore assume it to be constant with temperature. The thus deduced thickness dependence of  $K_{mel}$  is shown in figure 5.10b for temperatures from 10 K to 300 K.

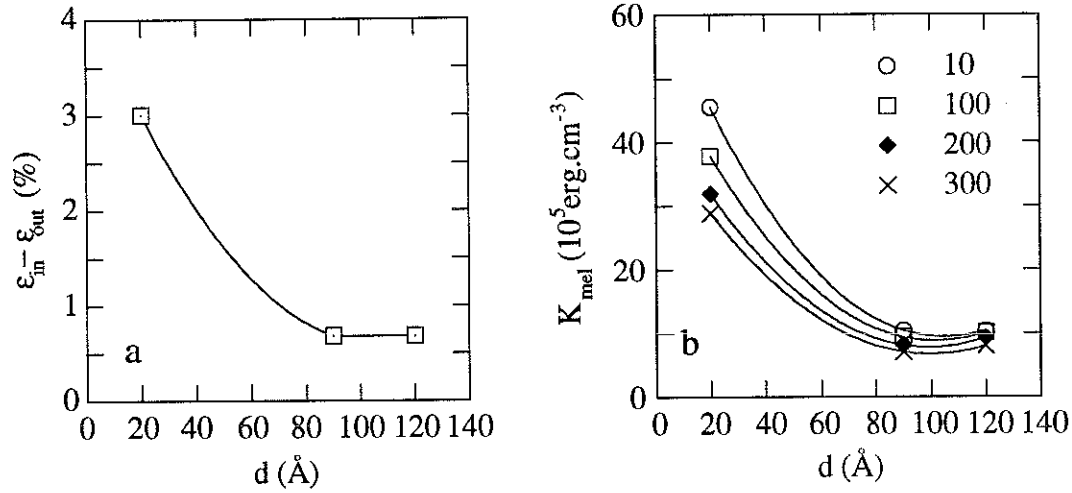


Fig. 5.10 - Thickness dependence of a -  $\epsilon_{in} - \epsilon_{out}$  for all temperatures and b - thickness and temperature dependence of  $K_{mel}$

### evaluation of $K_s$

$K_s$  can be evaluated to second order from (5.3), (5.7), (4.18) and (5.9) by writing :

$$\frac{2K_s}{d} = A - K_1 - K_{mel} \quad (5.11)$$

The deduced thickness dependence of  $K_s$  at 300 K is shown in figure 5.11a, and the deduced temperature dependence of  $K_s$  for the 20 Å and 120 Å film is shown in figure 5.11b and 5.11c respectively.

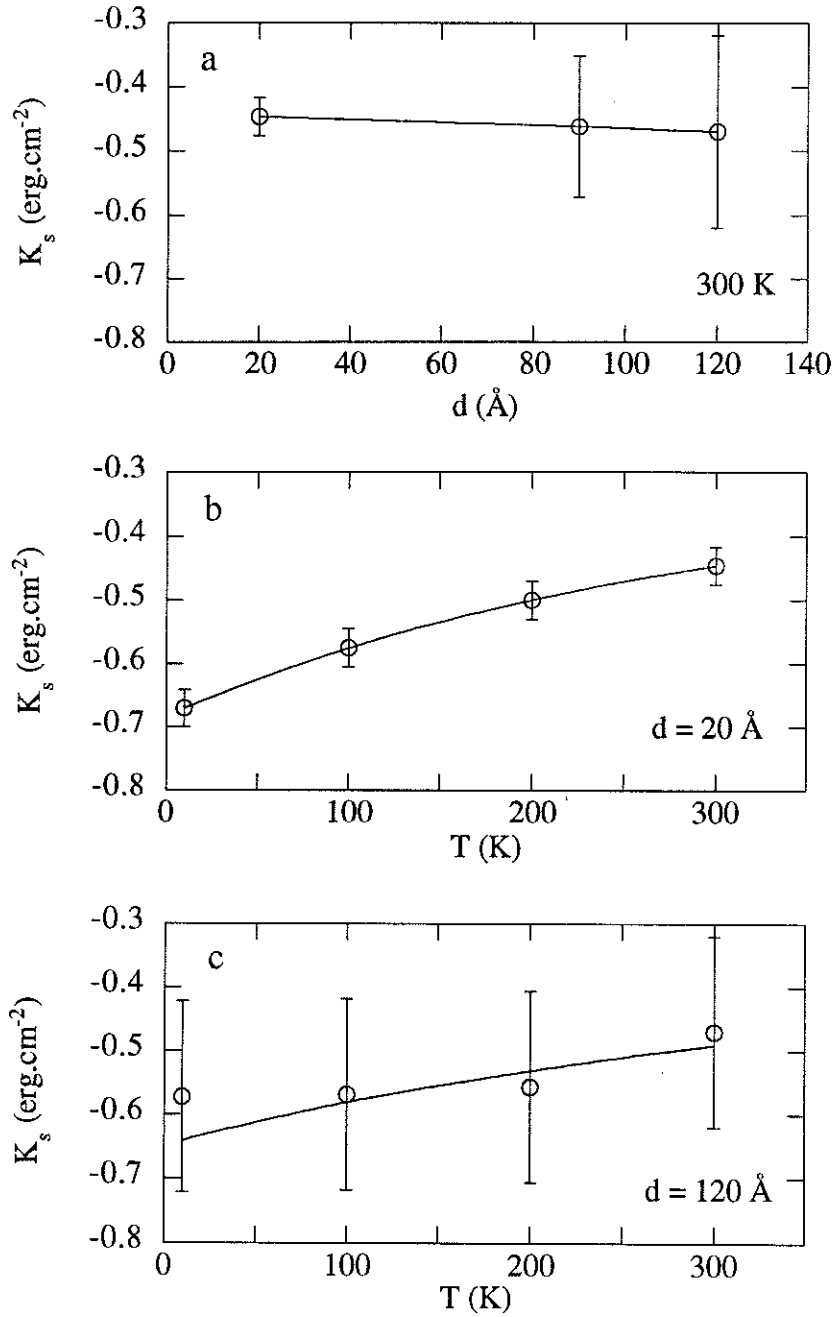


Fig. 5.11 a - Deduced values of  $K_s$  as a function of film thickness, b - temperature dependence of  $K_s$  for the 20 Å film and c - for the 120 Å film.

### 5.3.5 Discussion

#### • analysis technique

The usual analysis of thin film anisotropy employed in the literature assumes that all anisotropy constants are thickness independent even for thicknesses down to a monolayer. The Curie temperature, however is often found to be less than 300 K for monolayer thicknesses. This fact alone makes it hard to believe that a film of say a 100 Å will have the same anisotropy constants as a film of 10 Å.



The analysis which we employed is rather long winded and rests on certain hypothesis. It has enabled us to evaluate  $K_s$  for each film and not an effective surface anisotropy constant averaged over all films. In addition, not only do we take into account the thickness dependence of strain but we also take into account dimensionality effects.

Before discussing our experimental results, it is instructive to apply our analysis technique to published experimental data for surface anisotropy. Take, for example the case of Ni (001) on Cu, as shown in figure 4.6 and assume a strain of 2.5 % for  $d < d_c$  with a  $1/d$  relaxation for  $d > d_c$  ( $d_c = 47\text{\AA}$ ).

The total anisotropy constant for this film ( $K'_{tot}$ ) is given by :

$$K'_{tot} = K'_{mel} + K_{dip} + \frac{2K'_s}{d} \quad (5.12)$$

where  $K'_{mel}$  is given by (4.17) and  $K_{dip}$  is given by (4.14) and where  $K_1$  is neglected as it is two orders of magnitude less than all the other anisotropy terms. Minimisation of the elastic energy yields :

$$\begin{aligned} \epsilon_{out} - \epsilon_{in} &= \epsilon_{in} \left( \frac{3C\gamma}{C\alpha + 2C\gamma} \right) \\ &= \epsilon_{in} (2.2) \end{aligned} \quad (5.13)$$

taking bulk elastic constants of Ni from reference [17]. The bulk value of  $B\gamma^2$  of Ni is found to follow  $1.05 \times 10^8 m^2$  (erg.cm<sup>-3</sup>) [18], where  $m$  is the reduced magnetisation. Similarly  $K_{dip}$  can be evaluated from  $K_{dip} = K_{dip}(\text{bulk } 0\text{ K}).m^2$  where  $K_{dip}(\text{bulk}, 0\text{ K}) = 1.6 \times 10^6$  erg.cm<sup>-3</sup>[19]. In order to analyse the data we need to know the thickness dependence of  $m$  at 300 K for this film. As this is not available, we took, for illustrative purposes the data of figure 4.9a, which refers to Ni (111) on Re (0001).

The thickness dependence of the evaluated magnitudes of  $K'_{mel}$  and  $K_{dip}$  is shown in figure 5.12b. Note in particular, that  $K'_{mel}$  is not constant for  $d < d_c$ , as is usually assumed but shows a slow curvature towards zero. Similarly,  $K_{dip}$  decreases at low thicknesses. This is due to the thickness dependence of  $m$  (300 K).

$K'_s$  was extracted from the measured value of  $K'_{tot}$  and the deduced values of  $K'_{mel}$  and  $K_{dip}$  by means of (5.12). The deduced thickness dependence of  $K'_s$  is shown in figure (5.12a). The large fluctuations in the values of  $K'_s$  arise from small fluctuations in the experimental data. At large film thicknesses it is  $-0.4$  erg.cm<sup>-2</sup>. As the film thickness decreases it shows a slow curvature towards zero. By  $20\text{\AA}$ ,  $K'_s$  is approximately  $-0.2$  erg.cm<sup>-2</sup>. The decrease of  $K'_s$  with film thickness can be simply understood, in the spirit of our analysis, by supposing that it is a function of magnetisation (or more precisely, surface magnetisation). This experimental result brings credit to our analysis.

The value of  $K'_s$  deduced in chapter 4 from a thickness plot and assuming that  $K_{\text{dip}}$  and  $K'_{\text{mel}}$  are constant for  $d < d_c$  (fig. 4.6) is  $-0.35 \text{ erg.cm}^{-2}$ . This is the same order of magnitude as the values which are shown 5.12a.

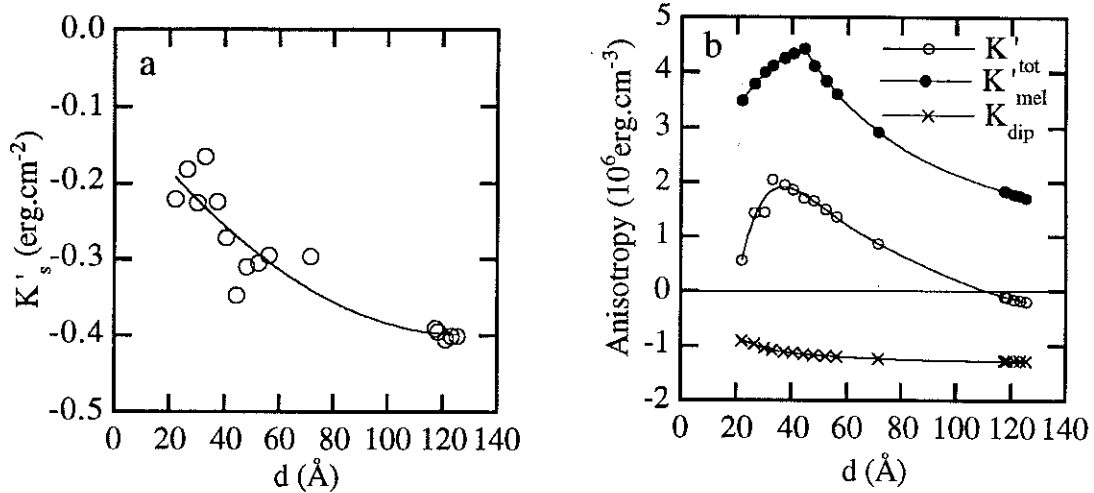


Fig. 5.12 - Analysis of the experimental data of figure 4.6 ;  $K'_s$  as a function of  $d$  and b -  $K'_{\text{tot}}$ ,  $K'_{\text{mel}}$  and  $K_{\text{dip}}$  as a function of  $d$ .

It must be stressed that as the exact values of  $m$  (300 K) are not known for these films, the above is illustrative only. The above analysis shows that all anisotropy constants are thickness dependent. That the slope of  $K'_s d$  for  $d < d_c$  (fig. 4.6) gives a similar value of  $K'_s$  arises from the fact that all anisotropy constants show a similar magnetisation dependence. This however would not be the case for other orientations, such as Ni (111) because  $B\mathcal{E},^2$  shows a faster magnetisation dependence than  $B\gamma^2$  [19]. In this case, an extrapolation of data for  $d < d_c$  would lead to an even greater error in the evaluation of  $K'_s$ .

A curvature of the total anisotropy towards zero for thicknesses less than  $10 \text{ \AA}$  has been observed in Co / Au multilayers and although it was explained by a deterioration in the quality of the surface layers at low thicknesses [20] it can also be explained by dimensionality effects, as discussed above. This can be verified experimentally by measuring the total anisotropy at 10 K, say, where the curvature should be much less marked. Finally, the validity of re-normalising the anisotropy constants to  $m$  has been recently confirmed where anomalies in magnetoelastic measurements at 300 K in thin Ni films were explained by re-normalising the data to  $m$  [21].

• W / Fe / W results

We would now like to discuss our results for the W / Fe / W system. The first important point is that as  $K_s$  is the only negative term it is the sole cause of the in-plane easy axis switching observed at small film thicknesses. A good agreement between the value of  $K_s$  is observed in all films. In both the 20 Å and 120 Å film,  $K_s$  decreases with increasing temperature.

The in-plane anisotropy of X / Fe (110) / W (110) has been previously analysed [22] for Fe thicknesses greater than 70 Å, where the effective in-plane surface anisotropy constant was evaluated from thickness plots. These results are compared with our results in table 5.2.

X / Fe (110) / W	X		$K_s$ (300 K) erg.cm <sup>-2</sup>	
	W	(20 Å)	-0.45 (3)	this work
		(90 Å)	-0.46 (11)	this work
		(120 Å)	-0.47 (15)	this work
	UHV	70 Å < d < 100 Å	-0.30 (2)	ref. [20]
	Ag	100 Å < d < 200 Å	-0.23 (2)	ref. [20]
	Cu	100 Å < d < 200 Å	-0.29 (7)	ref. [20]

*Table 5.2 A comparison of  $K_s$  at 300 K for Fe (110) on W (110) with different coatings.*

In all of the above samples one finds similar values of  $K_s$ . As symmetrical interfaces have not been previously studied in Fe (110) samples with in-plane surface anisotropy a more quantitative discussion is not possible.

## 5.4 Thermal excitations

In this section, the thermal excitations in the W / Fe / W films are briefly discussed.

### 5.4.1 Results

The thermal variation of the spontaneous magnetisation was measured by means of a SQUID magnetometer. The films were oriented so that the applied field was parallel to the easy axis of magnetisation to within less than  $1^\circ$ . Prior to the measurements a field of 60 kOe was applied to saturate the film. During the measurements a field of 1 kOe was applied to ensure that the sample remained in the saturated state. The thus measured thermal variation of the magnetisation is shown in figure 5.13 for all thicknesses; bulk measurements are included for comparison.

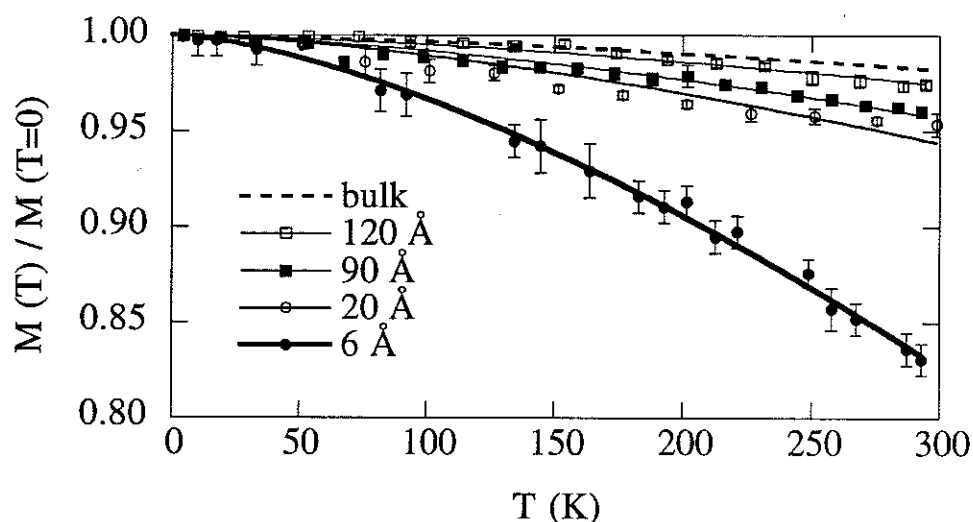


Fig. 5.13 - Thermal variation of the reduced magnetisation ( $m$ ) for W / Fe (110) / W for films of different thicknesses as measured by SQUID magnetometry (points see legend). The results of best fits to equation (5.14) are shown in continuous lines.

### 5.4.2 Discussion

In the above thickness range, the thermal variation of  $m$  can be expected to be intermediate between a 2D behaviour and a 3D behaviour (see section 4.4).

For a 3D behaviour, the thermal variation of  $m$  is (see expression (4.9)) :

$$m = \frac{M(T)}{M(T=0)} = 1 - BT^{3/2} \quad (5.14)$$

The above results were fitted to (5.14) as shown in figure 5.13. The thus deduced value of  $B$  is plotted in figure 5.14 as a function of reciprocal thickness ( $1/d$ ). The value of  $B$  is found to increase as the film thickness decreases. For the 120 Å film (60 monolayers),  $B$  is found to be  $5.76 \times 10^{-5} \text{ K}^{-3/2}$  which is 1.4 times that of bulk Fe. For the 6 Å film,  $B$  is found to be almost 10 times greater than in bulk Fe.

The above results can be compared with Mössbauer data for Fe (110) films deposited on W and protected by Ag (7 Å, 11 Å, 17 Å and 41 Å) [23]. The deduced thickness dependence of  $B$  for these films is compared with our films in figure 5.14.

In both systems  $B$  is found to vary approximately as  $1/d$ . For small thicknesses the Ag coated films show a slower thermal variation of magnetisation compared with the W coated films. This suggests that Ag coatings leads to an enhancement of the interface exchange interactions compared with W coatings. This is consistent with Mössbauer studies on a monolayer Fe (110) film deposited on W (110) [24] where coating by Ag lead to an increase in the Curie temperature from 210 K to 300 K.

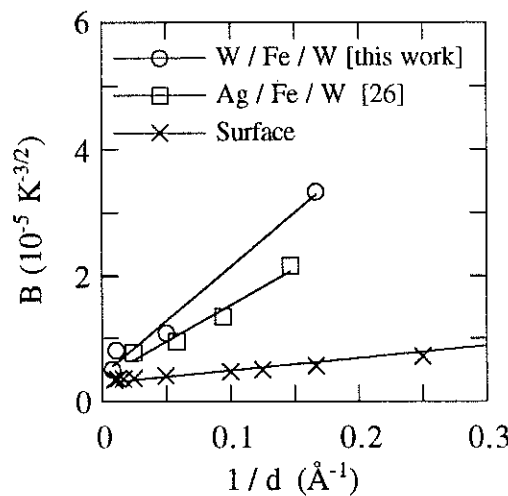


Fig. 5.14 - Thickness dependence of the spin wave pre-factor.

As discussed in chapter four, the thickness dependence of the thermal variation of magnetisation can be expected to arise due to surface effects and dimensionality effects.

The influence of surface effects can be evaluated by assuming that  $B$  in all layers is equal to the bulk value ( $B_b = 3.4 \times 10^{-6} \text{ K}^{-3/2}$  [25]) except at the surface. If one assumes that the reduction of exchange at the surface scales with the co-ordination reduction, then  $B_s = 1.5 B_b$  is expected. Alternatively, it has been proposed that  $B_s = 2 B_b$  because the surface is an anti-node for each spin wave [26]. Assuming a worst case scenario of  $B_s = 2B_b$  then the average value of  $B$  in a film of  $N$  monolayers is :

$$B_{av} = \frac{(N+2)}{N} B_b \quad (5.15)$$

The thus evaluated thickness dependence of  $B$  is shown in figure 5.14 (marked "surface" on plot). Comparison with the experimental data shows that surface effects are not the dominant mechanism for the thermal variation of the magnetisation in ultra-thin films. This is in agreement with our spin wave calculations in chapter four.

As discussed in chapter four, the thermal excitations in the  $6\text{\AA}$  film can be expected to be predominantly 2D in character. It is therefore interesting to try and fit the  $m(T)$  plot of the  $6\text{\AA}$  film to that expected for 2D thermal excitations, which from (4.29) is given by :

$$\begin{aligned} m &= 1 - \left( \frac{1}{4\pi S} \frac{a^2 K_B T}{D} \ln \left[ 1 - \exp \left[ \frac{-E_{\text{gap}}}{K_B T} \right] \right] \right)^{-1} \\ &= 1 - \left( Y \cdot T \ln \left[ 1 - \exp \left[ \frac{-Z}{T} \right] \right] \right)^{-1} \end{aligned} \quad (5.16)$$

where  $E_{\text{gap}}$  is now the anisotropy energy for rotations about the  $[1\bar{1}0]$  axis. The results of the best fit to (5.16) are shown in figure 5.15 (marked 2D on plot). The obtained values are :  $Y = 2.5 \pm 1 \times 10^{-4} \text{ K}^{-1}$  and  $Z = 30 \pm 20 \text{ K}$ . From (5.16) it follows that  $D = 125 \text{ meV} \cdot \text{\AA}^2$  which corresponds to a 55% reduction compared with the bulk value at 300 K. This value appears reasonable. The fitting is less sensitive to the anisotropy gap and the deduced value of  $2.5 \pm 1.7 \text{ meV / atom}$  is at least one order of magnitude too large. For example, the shape anisotropy of the film is of the order of  $0.1 \text{ meV / atom}$ . Of course, (5.16) does not take into account the stabilisation of  $m$  due to the fact that the film is 3 monolayers thick and not 1 monolayer.

The fit obtained by (5.16) (2D) is compared with that obtained by (5.14) (3D) in figure 5.15, showing that both expressions give a good account of the experimental data. In

addition both expressions give exactly the same result in the temperature range 100 K to 300 K. The two models start to deviate from each other for  $T < 100$  K. The maximum deviation between the two models corresponds to a magnetic moment difference of  $10^{-8}$  emu. It therefore appears difficult to distinguish experimentally between a 2D and a 3D spin wave behaviour. The experimental accuracy of the data is not sufficient for a more quantitative discussion, especially for the case of the thicker films (20 Å, 90 Å and 120 Å).

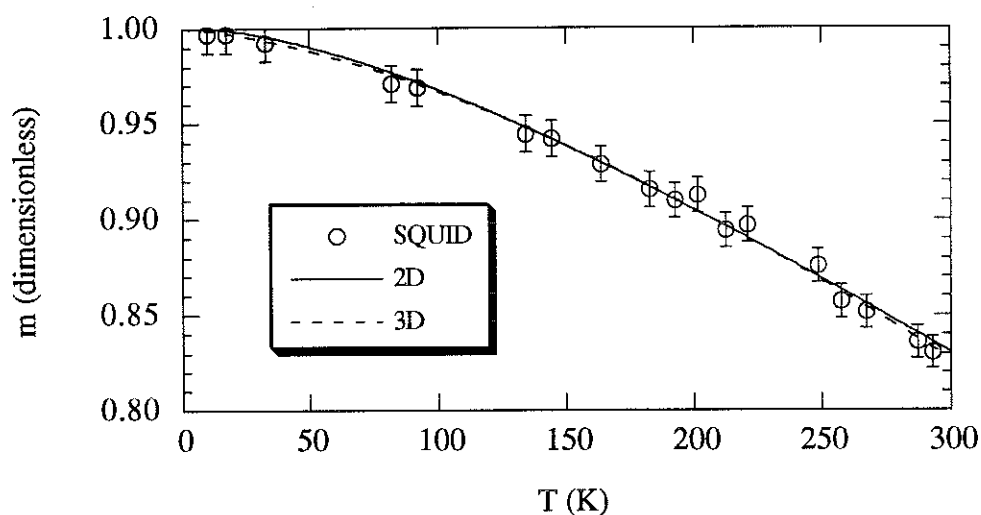


Fig. 5.15- The thermal variation of the reduced magnetisation for a 6 Å (3 ML) film fitted to a 2D expression (5.16) and fitted to a 3D expression (5.14).

## 5.5 Discussion and conclusion to chapter 5

In this chapter we have analysed the ground state moment, in-plane anisotropy and thermal excitations of W / Fe (110) / W films.

An absolute value of the average moment of a three layer Fe film in W / Fe / W has been determined by PNR at 300 K. The 300 K value ( $1.80 \pm 0.05 \mu\text{B}$ ) was extrapolated to  $2.1 \pm 0.1 \mu\text{B}$  at 0K, by means of SQUID measurements. These experiments provide the first experimental verification of band structure calculation predictions that at a W / Fe interface, the Fe moment is significantly reduced compared with a free Fe surface due to hybridisation effects.

The in-plane anisotropy was measured by means of transverse Kerr and SQUID magnetometry. An in-plane easy axis of magnetisation was observed in all films. This easy axis was found to switch from the [001] axis for the 120 Å film to the  $[1\bar{1}0]$  for the 90 Å and 20 Å film.

The anisotropy has been analysed within a model where the various non-surface anisotropies are evaluated from bulk 0 K data re-normalised to the film magnetisation at the considered temperature. The advantage of this technique is that it enables the surface anisotropy, and not an effective surface anisotropy to be evaluated. In addition, it enables a value of the surface anisotropy to be evaluated for each film. The validity of this approach does not, as yet, have a direct experimental justification. However, the consistency of the obtained results give it credit. It must be stressed that the usual assumption that all anisotropy constants are thickness independent neither has an experimental confirmation. More importantly, it does not have a sound physical basis.

In the case of W / Fe / W, we show that surface anisotropy is the sole cause of the observed easy axis switching.  $K_s$  is found to vary from -0.46, for the 20 Å film to -0.20 for the 120 Å film at 300 K. It is found to increase as temperature decreases.

The thermal excitations in the films were shown to be thickness dependent. The thickness dependence was attributed to dimensionality effects and not surface effects. It appears that Fe at a W / Fe interface shows a weaker exchange compared with Ag / Fe interfaces.



## 5.6 References to chapter 5

---

- [1] G. P. Felcher,  
Phys. Rev. B24 (1981) 1595.
- [2] S. K. Mendriatta and M. Blume,  
Phys. Rev. B14 (1976) 144.
- [3] J. Penfold and R. K. Thomas,  
J. Phys : Condens. Matter, 2 (1990) 1369.
- [4] S. J. Blundell and J. A. C. Bland,  
J.M.M.M., 121 (1993) 185.
- [5] J. Penfold,  
“Neutron, X-ray and Light scattering”, P. Linder and T. Zemb (eds.), Elsevier  
Sci. Publ., 1991, pp. 223.
- [6] J. P. Rebouillat,  
Thèse de docteur es-sciences, L’Université scientifique de Grenoble, 1972.
- [7] H. J. Elmers, G. Liu and U. Gradmann,  
Phys. Rev. Lett. 63 (1989) 566.
- [8] C. L. Fu and A. J. Freeman,  
JMMM, 69 (1987) L1.
- [9] S. C. Hong, A. J. Freeman and C. L. Fu,  
Phys. Rev. B38 (1988) 12156.
- [10] E. du Trémolet de Lacheisserie,  
“Magnetostriction”, page 68, CRC Press, USA, 1993.
- [11] J. A. Rayne and B. S. Chandrasekhar,  
Phys. Rev. 122 (1961) 1714.
- [12] E. R. Callen and H. B. Callen,  
Phys. Rev. 139 (1965) A455.
- [13] J. Crangle and G. D. Goodman,  
Proc. Roy. Soc. London, A321 (1971) 477.

- 
- [14] P. Escudier,  
Thèse de docteur es-sciences, l'Université scientifique de Grenoble, 1973.
- [15] A. H. Morrish, "The physical principles of magnetism", page 320,  
R. E. Kriger Publishers, Florida, 1983.
- [16] E. du Trémolet de Lacheisserie and R. M. Monterossa,  
JMMM, 31 (1983) 837.
- [17] G. A. Alers, J. R. Neighbours and H. Sato,  
J. Phys. Chem. Solids, 13 (1960) 40.
- [18] E. du Trémolet de Lacheisserie and J. Rouchy,  
J.M.M.M., 28 (1982) 77.
- [19] C. Kittel,  
"Physique de l'état solide", Dunod, Paris (1983).
- [20] F. J. A. den Broeder, D. Kuiper, A. P. van de Mosselaer and W. Hoving,  
Phys. Rev. Lett., 60 (1988) 2769.
- [21] O. F. K. Mc Grath and E. du Trémolet de Lacheisserie,  
to be published
- [22] H. J. Elmers and U. Gradmann,  
Appl. Phys. A51 (1990) 255.
- [23] J. Korecki, M. Przybylski and U. Gradmann,  
JMMM 89 (1990) 325.
- [24] M. Przybylski and U. Gradmann,  
Phys. Rev. Lett., 59 (1987) 1152.
- [25] B. E. Argyle, S.H. Charap, and E.W. Pugh,  
Phys. Rev. 132 (1963) 2051.
- [26] G. T. Rado,  
Bull. Am. Phys. Soc., 2 (1957) 127

# CHAPTER SIX

## EXCHANGE COUPLING IN EPITAXIAL Gd / Fe BI-LAYERS

### Table of contents to chapter 6

6.1 Introduction	171
6.1.1 Introduction to magnetism in R-T intermetallics	171
6.1.2 Literature review of interfacial coupling in R-T multilayers	172
6.2 Experimental results	175
6.2.1 Magnetometry results	175
6.2.2 PNR Results	176
6.3 Discussion	182
6.4 Conclusion	185
6.5 References	186

## RÉSUMÉ

Dans ce chapitre nous présentons des résultats d'une étude du couplage interfacial dans une couche de Y (0001) / 60 Å Gd (0001) / 120 Å Fe (110) / W (110). Ce couplage est étudié en analysant des résultats de mesures du moment magnétique par un magnétomètre à échantillon vibrant (MEV) et les résultats des mesures de réflectivité de neutrons polarisés (RNP) avec analyse de polarisation. Les mesures de MEV montrent que les moments du Fe et les moments du Gd ne sont ni complètement parallèles ni complètement antiparallèle. Une saturation complète de l'échantillon n'est même pas observée pour des champs aussi intenses que 80 kOe. Les mesures de RNP montrent en effet que les moments du Gd adoptent une configuration en éventail. On interprète ces résultats par un couplage interfacial 3d-5d à l'interface Fe / Gd qui donne lieu à une polarisation oscillante de la bande 5d du Gd et par conséquent un échange oscillant dans la couche de Gd.

## SUMMARY

In this chapter we present the results of a study of the interfacial exchange coupling in a Y (0001) / 60 Å Gd (0001) / 120 Å Fe (110) / W (110) film. The interfacial coupling is studied by analysing VSM (Vibrating sample magnetometer) and PNR with spin analysis results. The VSM measurements show that the spin configuration in fields of 300 Oe corresponds to neither a parallel nor an anti-parallel alignment of the Fe and Gd layers and complete saturation does not occur for fields even as high as 80 kOe. PNR results show the presence of a fanned configuration of the Gd moments. These results are interpreted as being due to 3d-5d interfacial coupling at the Gd / Fe interface which leads to an oscillatory polarisation of the 5d Gd band and hence oscillatory exchange coupling through the Gd layers.

## 6.1 Introduction

In the previous two chapters we have discussed the magnetic properties of single films. In this chapter we discuss exchange coupling between two magnetic films. One can distinguish between two forms of exchange coupling between films: interlayer coupling and interfacial coupling. The former refers to coupling between two magnetic films separated by a non-magnetic spacer. The latter refers to coupling across the interface between two films in direct contact with each other.

Interlayer coupling has been extensively studied over the past few years and a review of this subject can be found in reference [1]. The most significant result of these studies is that the interlayer exchange coupling is often found to be oscillatory.

A subject of particular interest which has attracted much less attention is intermetallic interfacial exchange coupling between a rare-earth (R) and a transition metal (T). The interest of such studies can be seen by examining the results of studies on bulk intermetallic compounds. The original magnetic properties (high  $T_C$ , high anisotropy and coercivity ...) observed in these compounds results from the interplay between mainly 3d-3d exchange interactions, 3d-4f exchange interactions and crystalline electric field (CEF) interactions at the 4f sites. A bi-layer of, for example, R / Fe constitutes a model system for studying these various interactions. In the case where R is Gd, analysis becomes easier as the CEF interactions are small due to the sphericity of the Gd 4f shell.

Such studies have been performed in the past on polycrystalline films. In order to get a more complete understanding of this phenomenon we undertook an investigation of the interfacial exchange coupling in single crystalline Gd / Fe bi-layers. In this chapter we describe the results of such an investigation of a Y (0001) / 60 Å Gd (0001) / 120 Å Fe (110) / W (110) film.

Before discussing our own results we present a short description of the main properties of R - M bulk alloys and give a brief review of the literature in the following section.

### 6.1.1 Introduction to magnetism in R-T intermetallics

It is a well established fact that in RT intermetallic alloys the coupling between the R and T spin moments is always anti-ferromagnetic. In RT alloys, where R is a light rare earth,  $J = L - S$  with  $L > S$  (see chapter four) which implies that the total R moment ( $g\mu_B J$ ) is coupled anti-ferromagnetically to the R spin moment and thus ferromagnetically to the T moment. For alloys where R is a heavy rare earth, on the opposite,  $J = L + S$  and anti-ferromagnetic coupling between the R and T moments occurs.

In a large series of compounds, it appears that the exchange energy between one R and one M spin moment varies by a factor which is less than two as their electronic

environment is changed from one compound to another [2]. The total R-T exchange energy must be obtained by summing over all R-T pairs in a given system. The exchange energy for  $\text{GdFe}_2$  compounds, for example, is of the order of 300 K, in units of temperature.

A microscopic explanation of R-T exchange interactions was initially proposed by Campbell [3] and elaborated more recently by Brooks [4]. Exchange coupling between 3d and 4f electrons is mediated through 5d electrons. At the R site, 4f-5d direct positive exchange occurs. The interactions between 5d and 3d electrons involves 3d-5d band hybridisation. As the 5d band is higher in energy than the 3d band, 3d-5d hybridisation is stronger for the minority 3d sub-band than the lower lying majority 3d sub-band. The result is that the hybridised minority d band has more 5d character than the hybridised majority d band. Consequently, the coupling between 3d-4f spins is anti-ferromagnetic, as observed experimentally.

Although the fundamental mechanism of 3d-4f exchange appears to be understood, the range of these interactions cannot be deduced from measurements of bulk alloys. Bilayers, such as Gd / Fe, constitute a model system for studying this phenomenon.

#### **6.1.2 Literature review of interfacial coupling in R-T multilayers**

Polycrystalline Gd / Fe multilayers were first prepared by electron beam evaporation on glass substrates [5]. The thermal variation of the magnetisation ( $M(T)$ ) in applied fields of 5 kOe was examined. In multilayers where the Fe thickness was greater than the Gd thickness,  $M(T)$  was found to increase with temperature (fig. 6.1a), whereas in multilayers where the Gd thickness was greater  $M(T)$  was found to initially decrease with temperature until 220 K and then rise again (fig. 6.1b). These results show that the Gd and Fe layers are coupled anti-ferromagnetically, in agreement with the anti-ferromagnetic coupling observed between Gd and Fe in  $\text{GdFe}$  bulk alloys. As the thermal variation of Gd is faster than that of Fe, in the case of Fe aligned multilayers,  $M(T)$  increases with increasing  $T$ . For the case of Gd aligned multilayers,  $M(T)$  decreases with increasing  $T$  until a compensation point is reached at which the magnetisation of Gd is equal to that of Fe.

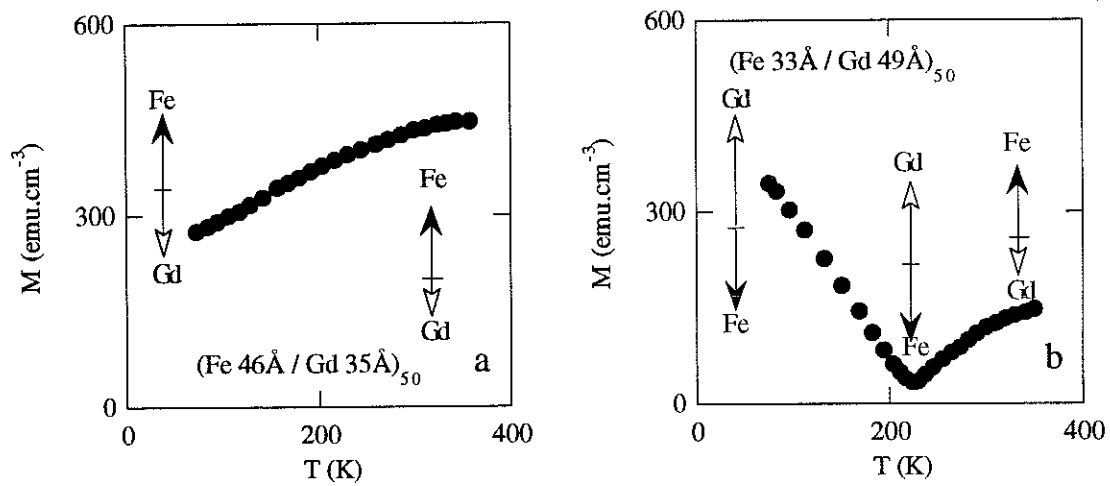


Fig. 6.1 The thermal variation of the magnetisation in Gd / Fe multilayers ; a- Fe aligned state and b - Gd aligned state (from [5]).

The interfacial coupling in a Gd (84 Å) / Fe (42 Å) polycrystalline multilayer has been studied by magnetometry [6] and polarised neutron low angle diffraction [7]. Again, an aligned Gd state is observed at low temperatures which remained stable to up a critical applied field ( $H_C = 3.6$  kOe). At  $H = H_C$ , a transition occurs towards a canted state where both the Gd and Fe moments make a large angle with respect to  $H$  (fig. 6.2). As  $H$  is increased further, the Gd and Fe layers slowly rotate into the field direction (fig. 6.2) as the applied field is in competition with Gd-Fe interfacial exchange coupling. This process is reminiscent of a spin-flop transition in anti-ferromagnets. It has also been detected by magnetoresistance measurements [8].

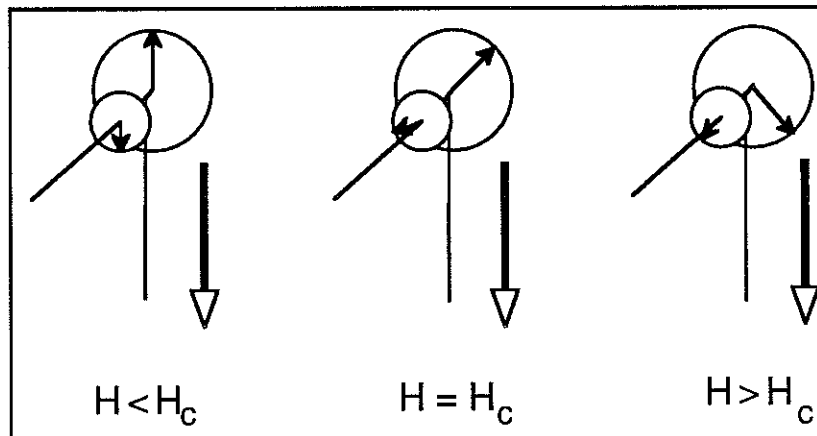


Fig. 6.2 - Schematic representation of the field dependence of the Gd layers (large circles) and Fe layers (small circles) in Gd / Fe polycrystalline multilayers .

Interfacial coupling in Er / Fe polycrystalline multilayers has recently been investigated [9]. The Fe and Er films were found to align parallel in an applied field. The interfaces were found to consist of a ErFe alloy and to be ferrimagnetic.

Interfacial coupling between R and Fe has been investigated by numerical simulations [10] [11], where R is Gd. In these simulations, ferromagnetic exchange was assumed within the Gd and Fe layers ( $J = J_{Fe}$  in the Fe layers and  $J = J_{Gd}$  in the Gd layers). Antiferromagnetic coupling was assumed between the Gd and Fe layers at the interface ( $J = J_{Fe-Gd} < 0$ ).

This model reproduces the main experimental features of Gd / Fe polycrystalline multilayers. The most important parameter for the simulations is  $J_{Fe-Gd}$ . The calculated interface angle for  $H > H_c$  and the calculated variation of  $H_c$  as a function of  $J_{Fe-Gd}$  is shown in figure 6.3a and 6.3b respectively. A significant deviation from  $180^\circ$  coupling is only found for values of  $J_{Fe-Gd} < -0.15 J_{Fe}$ . For  $J_{Fe-Gd} = -0.5 J_{Fe}$ , for example,  $H_c$  is approximately 35 kOe.

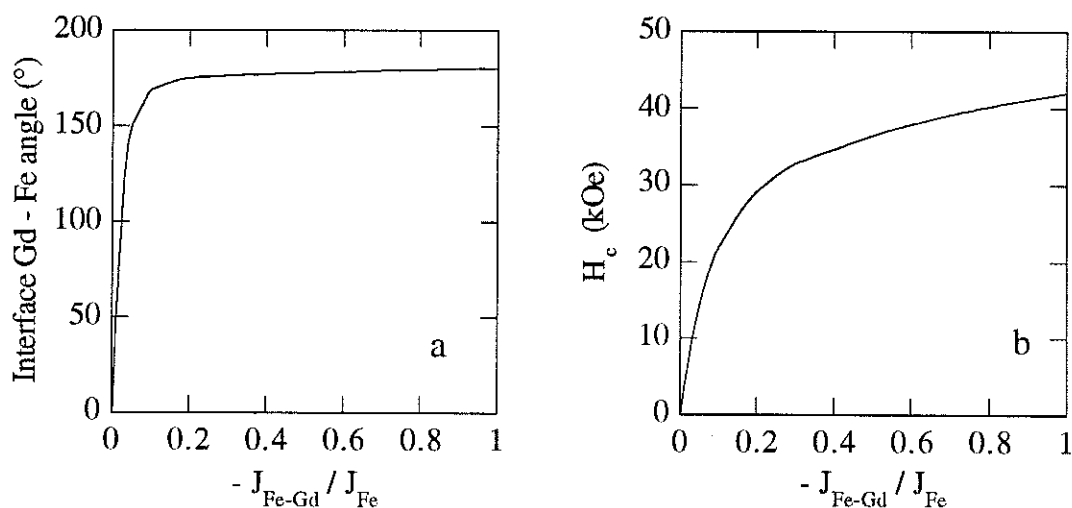


Fig. 6.3 - Results of numerical calculations for Gd / Fe multilayers (from ref. [10]) as a function of the ratio of the interfacial exchange ( $J_{Fe-Gd}$ ) to Fe exchange ( $J_{Fe}$ ) ; a - Interface angle between Gd and Fe and b- critical field ( $H_c$ ) for the transition into a twisted state.



## 6.2 Experimental results

In order to study intermetallic interfacial exchange coupling, epitaxial Gd / Fe bi-layers were prepared as described in chapter 3. In this section we present the results of an investigation of this phenomenon in a Y (0001) / Gd (0001) / Fe (110) / W (110) / Al<sub>2</sub>O<sub>3</sub> (1120) film. The thicknesses of the Gd and Fe layers are 60 Å and 120 Å respectively, as deduced from X-ray reflectivity measurements (see chapter 3). The interfacial coupling was studied by analysing VSM (Vibrating sample magnetometer) and PNR with spin analysis results.

### 6.2.1 Magnetometry results

The value of the total magnetic moment of the film was investigated by means of a VSM in fields up to 80 kOe and temperatures from 10 K to 300 K.

The in-plane low-field moment dependence along the  $[1\bar{1}0]$  and  $[001]$  axis is shown in figure 6.4a and 6.4b respectively. The coercive field is 40 Oe for both axes and does not vary between 10 K and 300 K. For applied fields greater than the coercive field, the field dependence of the total moment appears to be negligibly small.

A slight anisotropy difference is observed between the two directions. At 10 K the  $[1\bar{1}0]$  is an easy axis of magnetisation whereas at 300 K the  $[001]$  axis is easy. Following our analysis of anisotropy in W / Fe (110) / W in chapter 5, it is possible that the observed easy axis switching from the  $[1\bar{1}0]$  at low temperature to the  $[001]$  at high temperature can be attributed to the anisotropy of the Fe (110) layer. As the thermal variation of  $K_S$  is greater than that of  $K_1 + K_{me1}$  it appears that, at 10 K :

$$-2K_S / d > K_1 + K_{me1} \quad \Rightarrow \quad [1\bar{1}0] \text{ easy,}$$

whereas at 300 K :

$$-2K_S / d < K_1 + K_{me1} \quad \Rightarrow \quad [001] \text{ easy.}$$

It is instructive to try and deduce the spin configuration of Fe and Gd from the above measurements. Consider, for example, the measurements along the  $[1\bar{1}0]$  axis at 10 K. The value of the measured moment for  $H = 150$  Oe is  $2.3 \times 10^{-4}$  emu. The area of the sample in these measurements was  $0.16 \text{ cm}^2$  and therefore the volume of Fe is  $1.9 \times 10^{-7} \text{ cm}^3$  and the volume of Gd is  $9.6 \times 10^{-8} \text{ cm}^3$ . If one assumes that the magnetisation of Fe in the film at 10 K is the same as in the bulk ( $1740 \text{ emu.cm}^{-3}$  [12]) then the total Fe moment in the film is  $3.3 \times 10^{-4}$  emu. Similarly, taking a magnetisation of  $2010 \text{ emu.cm}^{-3}$  for Gd [12], one finds that the total Gd moment is  $1.9 \times 10^{-4}$  emu. As the measured value corresponds to neither the sum nor the difference of the expected Gd and Fe moments it appears that the spin configuration is neither completely anti-parallel nor parallel.

At 300 K the expected moment of Fe is  $3.27 \times 10^{-4}$  emu and as the measured moment is  $2.2 \times 10^{-4}$  emu it appears that the Gd layer still contributes significantly to the total moment of the bi-layer.

The high field moment dependence is shown in figure 6.5 for an applied field parallel to the  $[1\bar{1}0]$  of Fe at 300 K. From fields of 1 to 20 kOe, the moment varies very slowly as the field is increased. For fields greater than 20 kOe, the total moment increases with increasing field. Complete saturation does not appear to have occurred for fields even as high as 80 kOe. The same behaviour is found for measurements performed at temperatures of 10 K and for measurements with an applied field parallel to the  $[001]$  axis.

The above analysis indicates that the spin configuration of the bi-layer is complex.

### 6.2.2 PNR Results

In order to determine the spin configuration in the film, polarised neutron reflectivity with spin analysis was performed on the G2-2 spectrometer at the Orphée reactor at Saclay. This spectrometer is a new facility of the Laboratoire Léon Brillouin and is described in reference [13].

This spectrometer has a fixed wavelength with very high resolution ( $q_{\min}=10^{-3}\text{\AA}^{-1}$ ) with the possibility of performing experiments up to  $140^\circ$  with an angular resolution of  $0.001^\circ$ . The incident neutron beam is polarised by means of a polarising supermirror. A second polarising supermirror, placed in the path of the reflected beam enables the polarised state of reflected beam to be detected. Spin flippers, placed after the two polarisers enables a given spin state of the incident and reflected beam to be selected. Three reflectivity profiles can therefore be measured ;  $R^{++}$ ,  $R^{+-}$ ,  $R^{-+}$ .  $R^{++}$  ( $R^{--}$ ) corresponds to a + (-) polarised neutron which retains its spin state after reflection.  $R^{+-}$  corresponds to +(-) neutron which undergoes a spin flip during reflection.

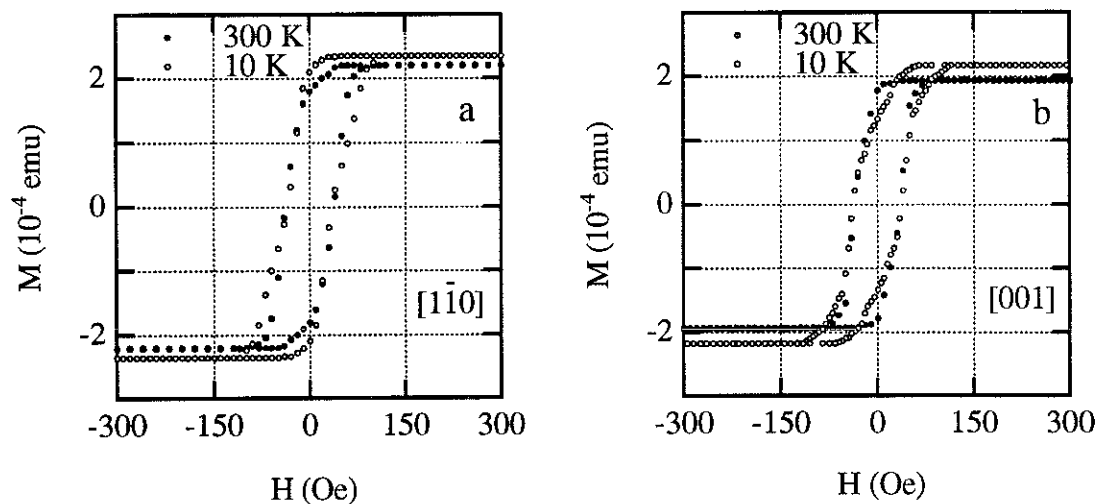


Fig. 6.4 - Low field moment measurements of a Gd / Fe bi-layer at 10 K and 300 K for an applied field parallel to the  $[1\bar{1}0]$  of Fe ( //  $[1\bar{1}00]$  of Gd) (a) and parallel to the  $[001]$  of Fe ( //  $[11\bar{2}0]$  of Gd).

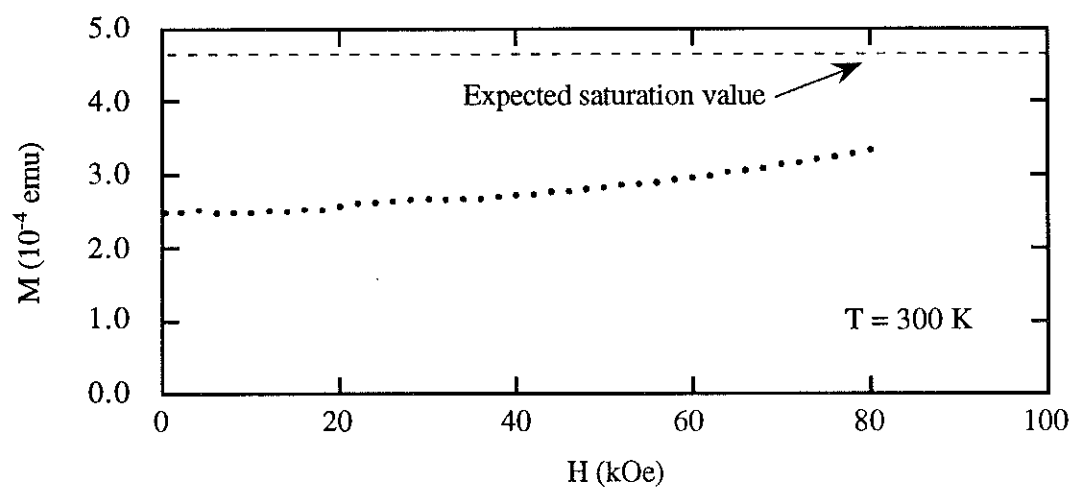


Fig. 6.5 - High field moment measurements of a Gd / Fe bi-layer at 300 K for an applied field parallel to the  $[1\bar{1}0]$  of Fe ( //  $[1\bar{1}00]$  of Gd).

During the measurements a small field is applied to define a quantification axis for the neutrons. For the case of an applied field in the plane of the sample non spin flip reflectivities ( $R^{++}$  and  $R^{--}$ ) are determined by nuclear scattering and magnetic scattering from the projection of the magnetisation along the quantification axis. Spin flip reflectivity ( $R^{+-}$ ) is determined by the component of the magnetisation which is perpendicular to the quantification axis. Note that the component of the magnetisation along  $q$  (perpendicular to the film plane) does not contribute to the reflection processes.

The neutron wavelength for the present work was 4.14 Å. The flipping ratio for the neutron beam, measured in the absence of the film, was 60 and the flux after analysis was  $10^4 \text{ n.s}^{-1} \cdot \text{cm}^{-2}$ . The  $R^{++}(q)$ ,  $R^{--}(q)$  and  $R^{+-}(q)$  reflectivity profiles were measured by varying the angle of incidence of the incident beam onto the sample ( $\theta - 2\theta$  scans, as for X-ray reflectivity measurements). The reflectivity profiles were measured at temperatures of 80 K, 300 K and 350 K. The sample was oriented so that the Fe  $[1\bar{1}0]$  axis was parallel to the applied field and hence the quantification axis. Measurements were performed with an applied field of 300 Oe.

The reflectivity profiles obtained at 300K are shown in figure 6.6. A large splitting between the  $R^{++}(q)$  and  $R^{--}(q)$  reflectivity profiles is observed which is proportional to the component of the magnetisation parallel to the quantification axis. Note the presence of a distinctive spin-flip reflectivity ( $R^{+-}$ ) which indicates that the magnetisation is not completely parallel nor anti-parallel to the applied field, in agreement with VSM measurements.

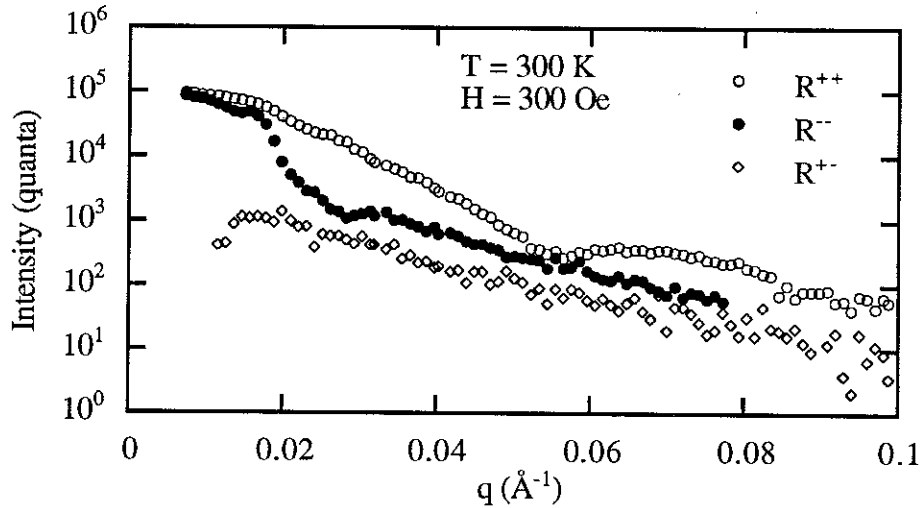


Fig. 6.6 - Spin flip (+-) and non spin flip (++ and --) polarised neutron reflectivities from an epitaxial Gd / Fe bi-layer with an applied field of 300 Oe along the  $[1\bar{1}0]$  axis of Fe at 300 K .

The calculation procedure for the spin flip and non spin flip reflectivity profiles is described in reference [13]. The fitting procedure is similar to that employed in chapter 5 for W / Fe / W. The starting values of  $b(z) / V(z)$  were taken from bulk values and X-ray thickness measurements. All interfaces were assumed to be abrupt and absorption by Gd was neglected. The magnitude and orientation of  $C\mu(z) / V(z)$  in the Fe and Gd layers were varied until the best simulation of the experimental reflectivities was obtained.

The calculated reflectivities are shown in figure 6.7. They reproduce the essential features of the experimental data. The calculation corresponds to an Fe moment of  $2.0 \pm 0.2 \mu_B$  which are all at  $-3^\circ \pm 2^\circ$  to the applied field. The average moment in all the Gd layers is found to be  $5.0 \pm 0.5 \mu_B$ . The moment is larger at the Fe interface and decreases through the Gd thickness ; a precise determination of the gradient would require better statistics. The exact form of the spin configuration in the Gd layer is obtained by calculating configurations which appear to be the most plausible from a physical point of view and by comparing them with the experimental data. One possibility is that at the interface the Gd is anti-parallel to the  $[1\bar{1}0]$  axis of Fe and rotates away from an anti-parallel alignment through the Gd thickness. The calculation gives approximately the first 20 Å at  $0^\circ$ , a progressive rotation of  $60^\circ$  through the next 20 Å and the last 20 Å remain at  $60^\circ$  to the applied field. As can be seen by comparing the  $R^{+-}(q)$  experimental data with the calculation (fig. 6.7c), this hypothesis gives a reasonable account of the experimental data.

Although the Gd configuration is approximate, other possibilities can be ruled out. For example, the case of no rotation would not give rise to a  $R^{+-}$  signal. The case of continuous rotation would give rise to slower variation of  $R^{+-}$  with increasing  $q$  than that observed experimentally (fig. 6.8).

The reflectivity profiles measured at 80 K are very similar to the data at 300 K; the average Gd moment is found to be  $7.0 \pm 0.5 \mu_B$  with a similar fan.

The reflectivity profile at 350 K is shown in figure 6.9. Fitting of the data is complicated by the fact that the Y (0001) protective coating has undergone a structural or chemical change. This can be attributed to either an oxidation effect with time or morphology change due to the applied temperature being higher than the deposition temperature. Preliminary data analysis indicates that the Gd layer is still magnetic and that the average Gd moment is  $2 \pm 0.5 \mu_B$ .

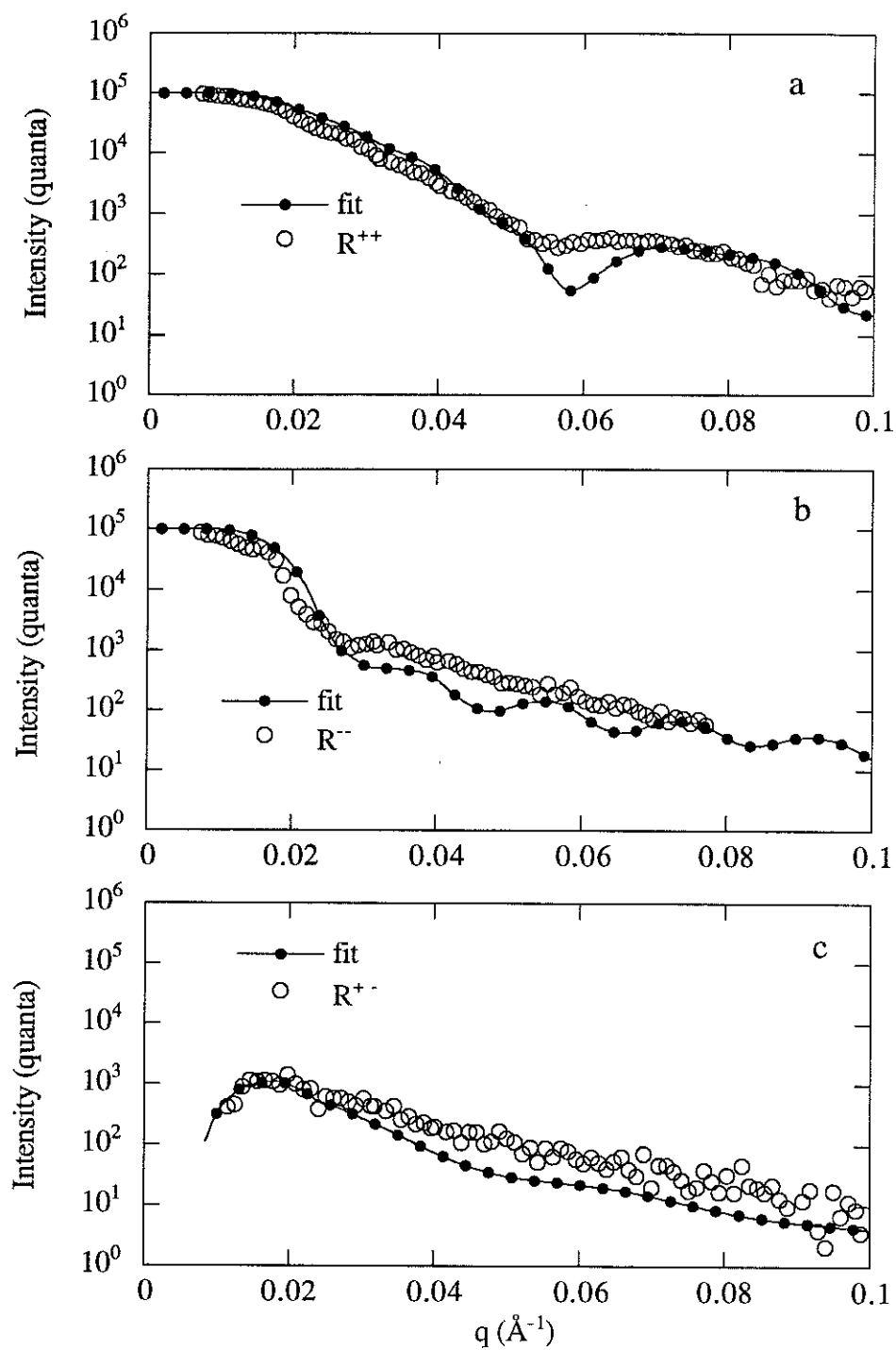


Fig. 6.7 - Comparison of reflectivity profile calculations with the experimental data ; a -  $R^{++}(q)$ , b -  $R^{-}(q)$  and c -  $R^{+-}(q)$  for an applied field of 300 Oe along the  $[1\bar{1}0]$  axis of Fe at 300 K.

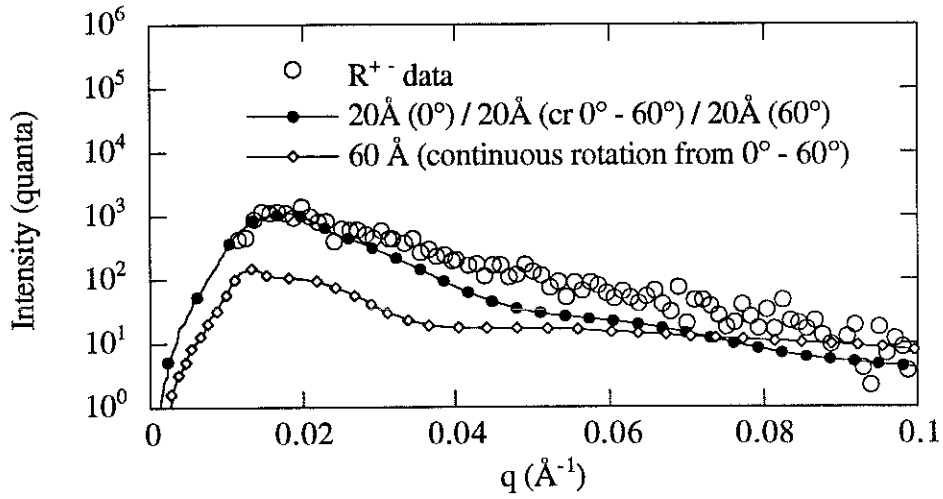


Fig. 6.8 - Comparison of experimental spin flip reflectivities for an applied field of 300 Oe at 300 K for the Gd / Fe bi-layer with calculated spin flip reflectivities. The open circles correspond to the experimental data ; the black circles correspond to the first 20 Å of Gd anti-parallel ( $0^\circ$ ) to Fe, the next 20 Å with a continuous rotation (c.r.) from  $0^\circ$  to  $60^\circ$  and the last 20 Å at  $60^\circ$  ; the open lozenges correspond to the case of a continuous rotation from  $0^\circ$  to  $60^\circ$  through the entire Gd thickness (60 Å).

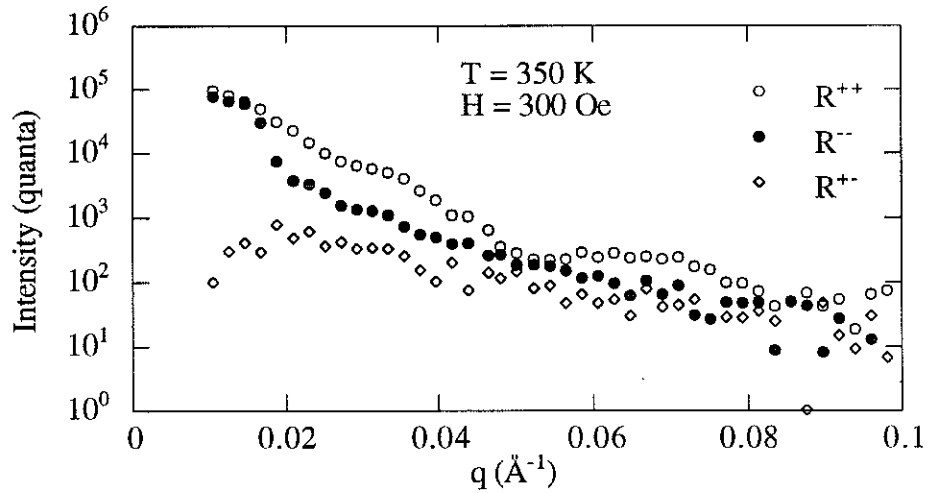


Fig. 6.9 - Spin flip (+-) and non spin flip (++ and --) polarised neutron reflectivities from an epitaxial Gd / Fe bi-layer with an applied field of 300 Oe along the  $[1\bar{1}0]$  axis of Fe at 350 K .

### 6.3 Discussion

From the magnitude and orientation of the Fe and Gd moments deduced from the neutron data at 300 K and  $H = 300$  Oe, we can calculate the projection of the total moment onto the field direction as  $2.2 \times 10^{-4}$  emu. This is in good agreement with the value measured by VSM (fig. 6.4). For the case of complete saturation at 300 K (Gd and Fe parallel to  $H$ ) one expects a total moment of  $4.6 \times 10^{-4}$  emu. From 6.4, we see that at 80 kOe, the total moment is 0.7 times the expected saturated moment.

It is interesting to compare the thermal variation of the Gd moment in the Gd / Fe bi-layer with the thermal variation of bulk Gd (fig. 6.10). The Gd in the bi-layer is found to vary more slowly with increasing temperature compared with bulk Gd. By extrapolation, the temperature at which the magnetic moment of the Gd in the bi-layer vanishes is approximately 370 K which is 70 K higher than the Curie temperature of bulk Gd. This increase can be attributed to Fe - Gd exchange interactions across the interface. This is in reasonable agreement with amorphous  $(\text{Gd } (40\text{\AA}) / \text{Fe } 40\text{\AA})_n$  multilayers where an enhancement of 50 K was estimated by X-ray dichroism [14]. Note that a monolayer of Gd on Fe was found to be magnetically polarised for temperatures up to 800 K [15].

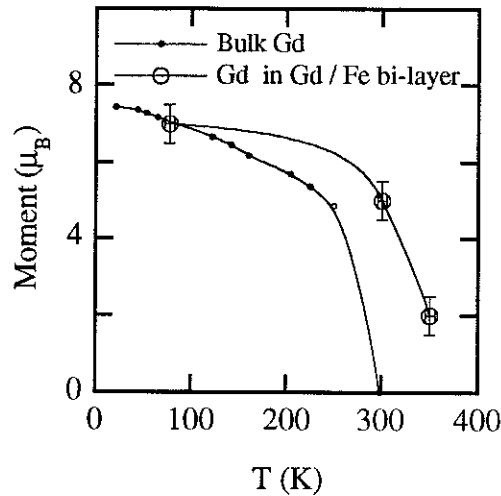


Fig. 6.10 - A comparison of the thermal variation of the Gd magnetic moment in a Gd / Fe bi-layer and in the bulk. (The thermal variation of the bulk reduced moment was taken from [16], the ground state moment of  $7.55 \mu_B$  was taken from [17]).



The observed spin configuration, for applied fields of 300 Oe along the  $[1\bar{1}0]$  of Fe at 300 K is schematised in figure 6.11. The question arises as to whether or not it is field induced and corresponds to the twisted state which occurs in Gd/Fe polycrystalline multilayers. If so, then the field induced transition occurs for fields less than 40 Oe as the VSM measurements (fig. 6.4a) do not show any transitions from 40 Oe to 300 Oe. For the bi-layer in this work, the critical field ( $H_C$ ) for field induced transitions is of the order of 50 kOe (assuming  $J_{\text{Fe-Gd}} = (J_{\text{Gd}} + J_{\text{Fe}}) / 2$ ). It appears therefore that the observed fanned state occurs in fields much less than that expected for field induced transitions into twisted states. In addition, the geometry of the observed fanned state does not correspond to the geometry expected for a field induced twisted state (compare fig. 6.11 with fig. 6.2).

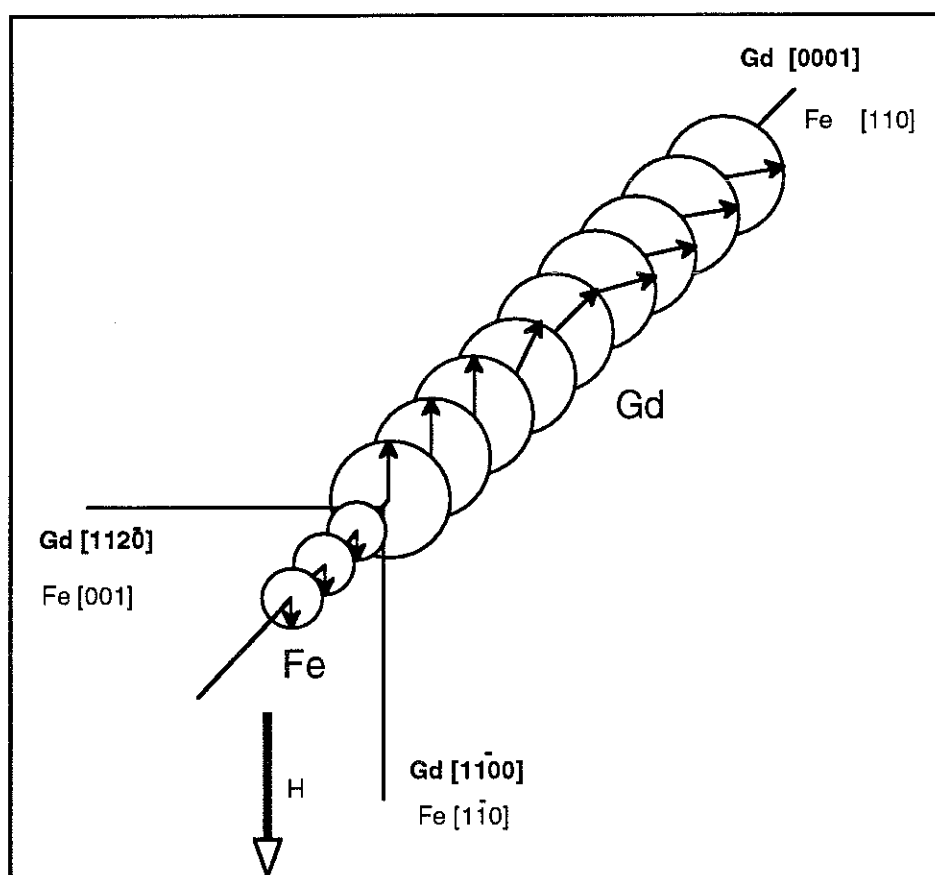


Fig. 6.11- Schematic representation of the observed spin configuration of a Gd / Fe bi-layer for an applied field of 300 Oe parallel to the  $[1\bar{1}0]$  of Fe at 300 K.

From qualitative arguments we suggest that the Gd configuration in this bi-layer can be understood by considering Gd-Gd exchange interactions within the Gd layer and Gd-Fe interfacial exchange interactions which are distance dependent. One can assume that Gd-Gd interactions, as in the bulk, favour ferromagnetic coupling between Gd moments. At the interface, Gd-Fe exchange interactions favour anti-ferromagnetic coupling as in bulk alloys. It can also, however, be assumed that as these interactions are mediated by 5d itinerant electrons, they are long ranged and oscillatory.

In the first Gd layers from the interface anti-ferromagnetic coupling between Fe and Gd satisfy both Gd-Gd and Fe-Gd exchange interactions. After a certain distance from the interface ( $d'$ ), however, the Fe-Gd interactions favour ferromagnetic coupling between Fe and Gd, as schematised in figure 6.12. This is because the 5d polarisation which results from 3d-5d hybridisation at the interface changes sign at this distance. The Fe-Gd interactions are then in competition with Gd-Gd exchange interactions which try and maintain a ferromagnetic coupling between neighbouring Gd layers. As in the case of a helimagnetic system, if the interaction with planes at distances greater than nearest neighbouring planes are sufficiently large the competition leads to a progressive rotation of the Gd moments. The turn angle between neighbouring Gd planes is  $10^\circ$  which shows that Gd-Gd interactions are largely dominant over Gd-Fe interactions. After a further distance ( $d''$ ) from the interface, the rotation in the Gd stops and the moments stay at a fixed angle with respect to the Fe layers. This can be understood by supposing that the Fe-Gd interactions have again changed sign or are negligibly small (fig. 6.12).

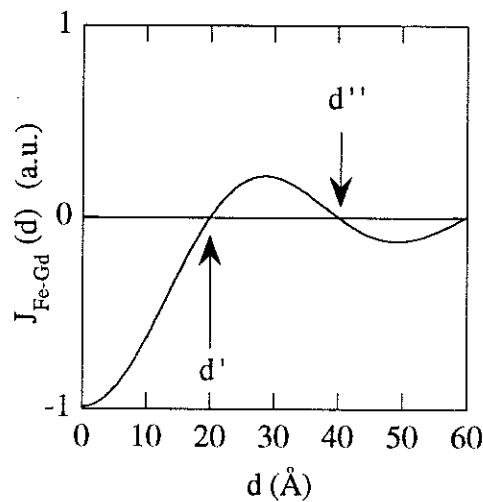


Fig. 6.12 - Hypothetical thickness dependence of the intermetallic interfacial exchange coupling ( $J_{Fe-Gd}$ ) in order to explain the experimental results.

## 6.4 Conclusion

We have discovered an original spin configuration in Gd / Fe epitaxial bi-layers by means of magnetometry and polarised neutron reflectivity investigations. We attributed the existence of oscillatory exchange coupling through the Gd layers to an oscillatory polarisation of the 5d Gd band arising from 3d-5d interfacial coupling at the Gd / Fe interface.

The results are however preliminary and of qualitative nature. Additional experimental and theoretical work is required to further clarify this phenomenon.

## 6.5 References

---

- [1] A. Fert and P. Bruno  
chapter 2.2 “Ultra-thin Magnetic Structures”, vol. 2  
B. Heinrich and G. A. Bland (eds.), Verlag publishers (1994).
- [2] N. H. Duc, T. D. Hein, D. Givord, J. J. M. Franse and F. R. de Boer,  
JMMM 123 (1993) 342.
- [3] I. Campbell,  
J. Phys. F, 2 (1972) L47.
- [4] M. S. S. Brooks, L. Nordström and B. Johansson,  
J. Appl. Phys., 69 (1991) 5683.
- [5] T. Morishita, Y. Togami and K. Tsushima,  
J. Phys. Soc. Jpn., 54 (1985) 37.
- [6] K. Cherifi, C. Dufour, Ph. Bauer, G. Marchal and Ph. Mangin,  
Phys. Rev. B44 (1991) 7733.
- [7] C. Dufour, K. Cheriffi, G. Marchal and Ph. Mangin,  
Phys. Rev. B47 (1993) 14572.
- [8] H. Fujimori, Y. Kamiguchi and Y. Hayakawa,  
J. Appl. Phys 67 (1990) 5716.
- [9] C. Dufour, M. Vergnat, Ph. Mangin and G. Marchal, M. Hennion and C. Vettier,  
J.M.M.M., 130 (1994) 305.
- [10] R. E. Camley,  
Phys. Rev. B39 (1989) 12316.
- [11] R. E. Camley and D. R. Tiley,  
Phys. Rev. B37 (1988) 3413.
- [12] C. Kittel,  
Physique de l'état solide, Dunod, 1983, pp 465.
- [13] C. Fermon,  
to be published in Physica B
- [14] F. Itoh, M. Nakamura and H. Sakurai,  
J.M.M.M., 126 (1993) 361.

- 
- [15] M. Taboreli, R. Allenspach, G. Boffa and M. Landolt,  
Phys. Rev. Lett., 56 (1986) 2869.
  - [16] J. F. Elliot, S. Legvold and F. H. Spedding,  
Phys. Rev. 91 (1953) 28.
  - [17] B. Coqblin,  
“The electronic structure of rare earth metals and alloys”, page 266,  
Academic Press, London 1977.









## CONCLUSION

Dans ce travail nous avons présenté les propriétés structurales et magnétiques des couches minces épitaxiées de W / Fe (110) / W et Gd (0001) / Fe (110) préparées par la technique de dépôt par laser pulsé.

Nous avons montré que la technique de dépôt par laser pulsé pouvait présenter certains avantages vis-à-vis d'autres techniques déjà établies. La souplesse de cette technique est telle qu'elle est particulièrement adaptée à l'élaboration des systèmes composés de plusieurs éléments. De plus, la qualité de nos couches peut être attribuée à la haute énergie des espèces évaporées, favorable à une croissance épitaxiale.

L'association de plusieurs techniques expérimentales a permis une caractérisation détaillée des couches préparées. Nous avons regardé l'influence des paramètres expérimentaux sur leur structure. Les conditions optimales de dépôt ont ainsi été déterminées.

Le moment magnétique du fer dans des couches de W / Fe / W a été déterminé par la technique de réflectométrie de neutrons polarisés. La valeur du moment du fer ( $2.1 \pm 0.1 \mu_B$  (0 K)), mesuré dans une couche de Fe de trois plans atomiques d'épaisseur, constitue la première vérification expérimentale de calculs théoriques prévoyant une réduction du moment du fer à l'interface Fe/W, par rapport à celui d'une surface libre de Fe, ceci en raison des effets d'hybridation.

Nous avons développé une technique d'analyse des résultats expérimentaux de l'anisotropie magnétique afin d'extrapoler une valeur réelle de l'anisotropie de surface. Cette technique permet la détermination de l'anisotropie de surface d'une couche quelle que soit son épaisseur. L'idée fondamentale de notre analyse est que l'anisotropie n'est pas directement fonction de la température mais de l'aimantation. A l'heure actuelle, les hypothèses sur lesquelles notre analyse s'appuie, bien que réalistes, n'ont pas encore pu être vérifiées. Il nous semble, néanmoins, que notre technique d'analyse est plus fondée que les techniques conventionnelles.

Une analyse des excitations thermiques des couches ultra minces a été abordée d'une part par des calculs phénoménologiques des ondes de spin, d'autre part par des mesures expérimentales de la variation thermique de l'aimantation dans des couches de W / Fe / W. Les calculs montrent que la variation thermique de l'aimantation dépend fortement de l'épaisseur de la couche, ce qui est observé expérimentalement.

Nous avons étudié le couplage d'échange entre une couche de 60 Å Gd (0001) et une couche de 120 Å Fe (110). Une expérience originale de réflectométrie de neutrons polarisés avec analyse de polarisation ainsi que des mesures de magnétométrie macroscopique nous ont permis de déterminer le profil de la configuration du spin avec l'épaisseur. D'un point de vue expérimental, ce travail figure parmi les premières études qui ont permis la détermination à la fois de l'amplitude et de l'orientation des moments, par neutrons polarisés. D'un point de vue scientifique, les résultats obtenus constituent la

première mise en évidence expérimentale d'un couplage intermétallique interfacial oscillant.

Ce travail nous ouvre des perspectives pour l'avenir.

#### Perspectives techniques

- La technique de dépôt par laser pulsé a besoin de plus de développement, notamment sur le problème de l'élimination des espèces trop énergétiques.
- Une meilleure connaissance de la rugosité interfaciale est nécessaire; le développement de la technique de réflectométrie de rayons X non spéculaire devrait répondre à ce besoin.
- Le développement de magnétomètres ultrasensibles et la recherche de substrats avec une faible susceptibilité magnétique seraient utiles.

#### Perspectives scientifiques

- La détermination du moment magnétique à l'état fondamental dans d'autres systèmes que W / Fe / W devrait conduire à une meilleure compréhension des effets d'interface.
- Des mesures de l'anisotropie dans des couches de faible épaisseur, à plusieurs températures, permettraient de tester la validité de notre analyse.
- Des études expérimentales et théoriques devraient être entreprises pour mieux comprendre le phénomène du couplage interfacial intermétallique.

D'un point de vue plus général des perspectives, il est à noter que la plupart du travail réalisé jusqu'à présent a concerné l'étude de couches minces de métaux de transition. Une étude systématique des propriétés magnétiques des terres rares en couches minces est donc nécessaire. On peut également s'attendre à un renforcement de l'anisotropie de surface dans ces systèmes, bien que probablement plus faible que dans les métaux de transition. Il est souvent prévu que le moment magnétique de surface à l'état fondamental d'une terre rare ne devrait pas être très différent de celui dans le massif, mais des modifications éventuelles du champ cristallin à la surface peuvent entraîner une réduction du moment magnétique. Puisque les interactions d'échange indirect dans les terres rares sont à plus longue portée que les interactions d'échange direct dans les métaux de transition, il est probable que la dépendance en épaisseur de la variation thermique de l'aimantation des terres rares soit très différente de celle dans les métaux de transition.

## CONCLUSION

In this work we have studied the structural and magnetic properties of W / Fe (110) / W and Gd (0001) / Fe (110) epitaxial films prepared by pulsed laser deposition.

We have shown that, by carefully choosing the operating parameters, the technique of pulsed laser deposition has certain advantages vis-à-vis the more established epitaxial deposition techniques. In particular, the versatility of the technique is such that it is ideally suited to the preparation of systems involving several elements. In addition, the quality of our films may be attributed to the high energy of the evaporated species which favours epitaxial growth.

By combining several characterisation techniques we were able to obtain a detailed structural characterisation of the prepared films. By examining the properties of films prepared under different experimental conditions we were able to optimise the experimental parameters for film preparation.

By means of polarised neutron reflectometry we were able to determine the ground state moment of Fe in W / Fe / W films. The value of the Fe moment ( $2.1 \pm 0.1 \mu_B$  (0 K)) obtained for a three monolayer thick Fe film provides the first experimental verification of band structure calculation predictions that at a W / Fe interface, the Fe moment is significantly reduced compared with a free Fe surface due to hybridisation effects.

Another important aspect of this thesis work was the development of thin film anisotropy analysis in order to determine a correct value for surface anisotropy. In particular, we have developed an analysis procedure which enables the surface anisotropy of a film of any thickness to be evaluated. The fundamental idea behind this approach is that the physical parameters which describe the anisotropy are not directly functions of temperature but functions of the magnetisation. Currently, the hypotheses upon which our approach rests, although realistic, are not proven experimentally. It however appears to us that it rests on physical grounds which are more sound than those inherent to the established procedure.

The thermal excitations in ultra-thin films have been partially discussed by means of phenomenological spin wave calculations and experimental results. The former show that the transition from 2D to 3D magnetism modifies greatly the temperature dependence of the magnetisation and this is confirmed experimentally.

Finally, the exchange coupling between a 60 Å Gd (0001) film and a 120 Å Fe (110) was studied. A unique neutron reflectivity experiment (spin polarised with polarisation analysis) was employed in order to determine the thickness profile (magnitude and orientation) of the magnetisation. From an experimental point of view this study constitutes one of the first studies by polarised neutron reflectometry where not only the

magnetic moment was deduced but also its orientation. From a scientific point of view, these results provide the first experimental evidence of the existence of oscillatory intermetallic interfacial exchange coupling.

Many perspectives for further technical and scientific work can be evoked.

#### Technical perspectives

- The technique of pulsed laser deposition requires further improvement, notably the elimination of overly energetic species.
- From the point of view of structural characterisation, a more detailed quantification of interface roughness is needed; development of the technique of non-specular X-ray reflectivity should meet this demand.
- Due to the difficulty of performing macroscopic magnetisation measurements of ultra-thin films there is a need for more sensitive magnetometers and low susceptibility substrates.

#### Scientific perspectives

- A determination of the ground state moment in systems similar to W / Fe / W should lead to a greater understanding of interface effects.
- Measurements of the anisotropy in films with small thicknesses at various temperatures should enable the validity of our anisotropy analysis to be tested.
- More experimental and theoretical work is required to further clarify intermetallic interfacial exchange coupling.

Finally, from an even more general perspective, it can be remarked that to-date the majority of studies of magnetism in ultra-thin films have been devoted to transition metals. An investigation of ultra-thin rare earth films is therefore required. One can expect that such films should exhibit an anisotropy enhancement at the surface although the degree of enhancement should be less than that of transition metals. Although it is often noted that the surface ground state moment of rare earths should not be significantly different compared with the bulk, it is possible that surface crystalline electric field perturbations could lead to a surface moment reduction. Due to the more long range character of indirect coupling one can also expect the thickness dependence of the thermal variation of magnetisation to be very different to that found in transition metals.



